2mly

Revised

X-750-73-55

PREPRINT

NASA TM X-70457

VIRGINIA PRECIPITATION SCATTER EXPERIMENT - DATA ANALYSIS

NOVEMBER 1972

REVISED OCTOBER 1973

GSFC

GODDARD SPACE FLIGHT CENTER

GREENBELT, MARYLAND

X-750-73-55

VIRGINIA PRECIPITATION SCATTER EXPERIMENT— DATA ANALYSIS

Robert K. Crane
MIT Lincoln Laboratory

November 1972

Goddard Space Flight Center
Greenbelt, Maryland

VIRGINIA PRECIPITATION SCATTER EXPERIMENT – DATA ANALYSIS

Robert K. Crane
MIT Lincoln Laboratory

ABSTRACT

The Virginia Precipitation Scatter Experiment provided a year of data for the construction of empirical distribution functions of transmission loss and scattering cross section per unit volume, data which show that interference due to rain scatter may occur between terrestrial and space services sharing a common frequency allocation. Data were obtained from scattering volumes at several heights up to 9 km at the intersection of beams from simulated earth and terrestrial station antennas at a frequency of 3.7 GHz (S-Band). Surface rain rate measurements were simultaneously made beneath the scattering volumes and at the transmitter and receiver sites. This report considers the analysis of the experimental data; a detailed description is given in a companion report, Virginia Precipitation Scatter Experiment—Experiment Description, NASA/GSFC X-750-73-54, August 1972.

Rain scatter and surface rain rate data were obtained from October 3, 1970 to October 2, 1971 using a bistatic radar system and tipping bucket rain gauges located in southeastern Virginia. The data showed that interference may occur between earth and terrestrial stations located within 80 km of each other either by mainlobe-to-mainlobe coupling or sidelobe-to-mainlobe coupling. The data further show that the distributions of scattering cross section per unit volume measured at several heights and estimated from surface rain gauge data were different. The density functions for the scattering cross section per unit volume values measured at a 3 km height and estimated from surface rain rate data were identical only for summer thundershowers. The data showed that the CCIR model used to estimate interference due to rain is inadequate because the cell size and change of scattering cross section per unit volume with height estimates of the model predict transmission loss values that are too low (more interference than will occur).

30 Oct. 1973

CONTENTS

CONTENTS (Continued)

ILLUSTRATIONS

ILLUSTRATIONS (Continued)

ILLUSTRATIONS (Continued)

ILLUSTRATIONS (Continued)

TABLES

30 Oct. 1973

TABLES (Continued)

30 Oct. 1973

TABLES (Continued)

VIRGINIA PRECIPITATION SCATTER EXPERIMENT—DATA ANALYSIS

1 INTRODUCTION

1.1 BACKGROUND

Interference between centimeter- or millimeter-wave communication systems operating at the same frequency and beyond each other's radio horizon may be caused by one or more of several propagation mechanisms: tropospheric scatter, terrain diffraction, ducting, and rain scatter. The Virginia Precipitation Scatter Experiment was conducted to provide data on rain scatter for use in preparing coordination procedures for the siting of earth terminals of the satellite services. Data were also obtained for preparation of procedures for estimating the probability of interference between systems operating in the same centimeter- or millimeter-wavelength bands. The general background for the design of the experiment and detailed descriptions of the bistatic radar and rain gauge systems used are given in the companion report, Virginia Precipitation Scatter Experiment—Experiment Description, Levine, et al. 1972 (Reference 1).* The present report considers only the analysis of data from the experiment.

1.2 EXPERIMENT OBJECTIVES

The Virginia Precipitation Scatter Experiment was designed to:

- Determine the extent of interference between terrestrial and space services ground stations due to rain scatter for the purpose of revising international and domestic coordination and interference calculation procedures.
- Provide empirically determined cumulative distributions of transmission loss for a 1-year measurement period for transmitter/receiver configurations typical of radio-relay and space-communication-system earth terminal interference problems.

*Citations to Reference 1 materials are prefixed R1: throughout this report.

- Provide empirically determined cumulative distributions of surface rain rate and equivalent reflectivity, Z_e, at several heights for use in assessing the effectiveness of estimation procedures established under NASA sponsorship or by other investigators.

- Determine whether the distribution function for scattering cross section may be simply related to the distribution function for surface rain rate.

The experimental data were obtained to demonstrate that interference from typical radio relay system installations would occur in satellite communication system terminals sited in accordance with procedures recommended by the CCIR (International Radio Consultative Committee) as given in CCIR Report 382 (1967; see also Sections R1:/1 and R1:/2.) The data also provided a year of measurements for the construction of empirical cumulative distributions of transmission loss for transmitter and receiver antenna spacings and orientations typical of radio relay and satellite communication systems with intersecting main beams. The experiment transmitter and receiver antennas were oriented to provide mainlobe intersections and to allow the received signal levels to be interpreted as bistatic radar scattering cross section per unit volume or as equivalent reflectivity measurements. Measurements were also made of the rain rate at the surface beneath the scattering volumes and at the transmitter and receiver terminals. Distributions of equivalent reflectivity, Z_e, and of reflectivity, Z, as computed from surface rain rate, R, using a Z/R relationship based upon previous drop-size measurements, were constructed for comparison with each other and with the results of distribution prediction procedures.

1.3 BRIEF DESCRIPTION OF EXPERIMENT

A comprehensive description of the bistatic radar and rain gauge systems used in the Virginia Precipitation Scatter Experiment is given in Reference 1. The salient features of the systems are summarized here for easy reference. A vertically polarized, continuous wave (cw) bistatic radar system was operated between October 3, 1970, and October 2, 1971, in southeastern Virginia, to acquire transmission loss and equivalent reflectivity data. Characteristics of the S-band bistatic radar system used in Phase II, June 4, 1971 through October 2, 1971, are listed below:

Frequency	3.672 GHz (8.164-cm wavelength)

Antenna 1 (receive)	30-foot (9.2-m) parabola with prime focus feed
Gain	48.0 dBi (relative to isotropic antenna)
Beamwidth	0.68°(0.012 rad) between half-power points
Polarization	vertical
Antenna 2 (transmit)	10-foot (3.0-m) parabola with prime focus feed
Gain	38.8 dBi
Beamwidth	2.0°(0.034 rad)
Polarization	vertical
Transmitted power	10 Watts
Transmitter line loss	4.4 dB (nominal)
Transmitted signal	cw with frequency stability of 5 parts in 10^{10} per day
Receiver bandwidth	2 kHz
Local oscillator frequency stability	5 parts in 10^{10} per day
Receiver system noise figure	8 dB
Detection	logarithmic with 50-dB dynamic range
Recording	analog magnetic tape and strip charts
Maximum measurable transmission loss	163 dB with 10-dB signal to noise ratio 154 dB for minimum useful signal level
Number of transmitters	four, located at 2 sites
Scatter volume size	0.15 by 0.15 by 1.76 km^3 to 0.32 by 0.32 by 2.61 km^3 at half-intensity points, depending upon transmitter
Distance from antenna 1 to scatter volume	12.8 to 26.8 km, depending upon transmitter
Distance from antenna 2 to scatter volume	51.1 to 78.1 km, depending upon transmitter
Minimum detectable scattering cross section per unit volume	10^{-9} m^{-1} for 10-dB signal to noise ratio 10^{-8} m^{-1} for minimum useful signal level

The radar used several separate transmitter sites and a single receiver site. Measurements were made at both 3.7 GHz (S-band) and 7.8 GHz (X-band) from October 3, 1970, through June 3, 1971, during the exploratory and transitional phases of the experiment. (These were Phases Ia and Ib, respectively.) During the remainder of the experiment, high-accuracy measurements were made at S-band only. The data used to prepare the empirical distributions were acquired with the S-band system, and only this system will be discussed in this report. Data from the X-band system and from two additional transmitter sites used in Phases Ia and Ib were reported separately by Hubbard, et al. (1971).

The transmitter and receiver antennas were located and oriented to represent a typical radio relay system and a space communication system terminal configuration. Although the experiment was designed to represent an extreme interference situation with main-beam intersections, the measurements are reported in terms of scattering cross section per unit volume. These measurements, together with assumptions of the spatial extent of the rain scattering volume, may be used to estimate transmission loss for any transmitter and receiver antenna spacing and orientation. For a volume of precipitation-particle scatterers and frequencies in the centimeter and millimeter bands, the transmission loss may be computed by using the bistatic radar equation (Crane, 1970 and 1971a). However, estimation of the distribution function of transmission loss for any combination of transmitter and receiver antenna size, location, and orientation, would require data on the joint distribution of scattering cross section per unit volume for all locations in space. In this experiment, distributions of scattering cross-section values for a particular set of scattering volume sizes and locations were measured and reported in terms of equivalent reflectivity (cross section per unit volume). The measurements are useful only for investigating the temporal behavior of equivalent reflectivity at two isolated points in space, one at a height of 3 km and the other at 6 km.

The receiving antenna of the bistatic radar system was located at the NASA/Langley Research Center in Hampton, Virginia. The transmitting antennas for Phase II were located at Eastville, Virginia (50.7 km distance and 57.7° azimuth with respect to the receiver) and at Fort Lee, near Petersburg, Virginia (85.2 km distance and 281.7° azimuth) as shown in Figure 1. The antenna orientation and scattering volume locations are given in Table 1. This table lists, from Table R1:/2-2 and R1:/3-5, the antenna orientation data for Phase II. The pointing errors were calculated using spherical geometry, a 1.23 effective earth's radius, and a computer program described by Crane (1971a, Section 5). Pointing errors are relatively insensitive (compared to measurement accuracy) to the assumed value for effective earth's radius.

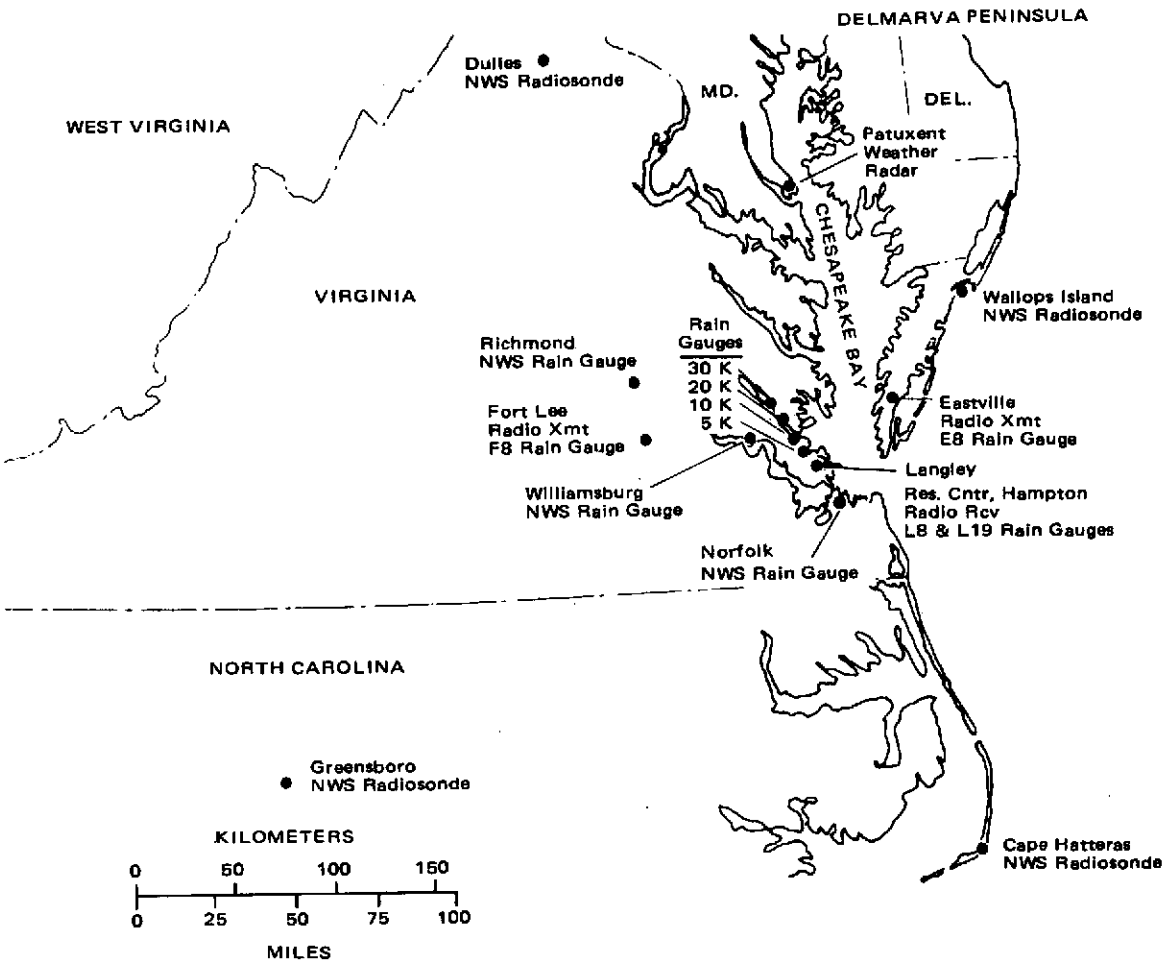

Figure 1. Experiment Area Map for Phase II

Table 1
Bistatic Radar-System Path Summary for Phase II

Path			Antenna Pointing		Scatter Volume Parameters						Transmit Antenna Pointing Errors		
No.	Site	Designation	Azimuth[2] (deg)	Elevation[2] (deg)	Height (km)	Distance to Transmitter (km)	Distance to Receiver (km)	Scattering Angle (deg)	Distance along Receive beam (km)	Distance Across Receive beam (km)	Azimuth (deg)	Elevation (deg)	Angle from Mainlobe Center (deg)
1[1]	E	GCE	237.3	0.8							-0.4		
3	E	10KE	252.1	3.6	3.0	51.1	12.9	99.4	1.76	0.15	+0.1	-0.4	0.4
4	E	20KE	265.2	6.2	6.1	54.7	25.7	112.7	2.02	0.31	0.0	-0.1	0.1
10	F	GCF	101.5	1.0									
11	F	10KF	94.0	2.1	3.0	78.1	12.8	60.4	3.06	0.15	-0.2	-0.1	0.2
12	F	20KF	84.6	4.4	6.3	72.2	26.8	70.0	2.61	0.32	+0.3	+0.1	0.3
	L		331.1	13.5									

1 For path numbering and description of all paths, see Table R1:/2-2.

2 Angles were best estimates for Phase II; see Table R1:/3-5.

Tipping-bucket rain gauges were located at the surface in the vicinity of the scattering volumes and at each of the transmitter and receiver sites used in Phase II. The gauges were of standard design as discussed in Sections R1:/2-2 and R1:/4 and were operated to provide 1-min average measurements of rain rates between 1 and 200 mm/hr. In addition to the data obtained from the experiment gauges, surface rate data were acquired from National Weather Service (NWS) tipping-bucket gauges at Norfolk, Virginia, and surface rain accumulation measurements were obtained from NWS gauges in the Tidewater District of Virginia and from Richmond. Weather radar data from both an S-band radar at the receiver site and the NWS radar at the Patuxent River NWS were also obtained to aid in the acquisition of data and in post-test analysis. The weather radar data were qualitative and used only for storm tracking and to assess synoptic weather conditions.

The bistatic radar and rain gauge data were processed in several ways. Hourly summary data were tabulated to aid in editing, to demonstrate that interference due to rain will occur, and to show that the measurements were not contaminated by other propagation phenomena. Detailed time histories were prepared of the measured equivalent reflectivities for each of the paths, and data for the same scattering volumes were compared to test antenna alignment and transmitter calibrations. Scattergrams comparing the minute-by-minute averaged values were also prepared for each scattering volume for the same purpose. Histograms of equivalent reflectivity for each path and of reflectivity computed from rain rate measurements for each gauge were generated for each storm event. Finally, empirical density and distribution functions were compiled for each phase of the experiment and for the year.

1.4 ORGANIZATION OF REPORT

The bistatic radar equation and Z/R relationship used in this report are considered in Section 2. Section 2.1 considers the problem of estimating the equivalent reflectivity from transmission loss measurements. The basic bistatic radar equation is derived in Section 2.1.1.1. The correction factors required to compensate for the receiver system are considered in the Sections 2.1.1.2 on logarithmic processing, 2.1.1.3 on Doppler spread, and 2.1.1.4 on the effects of change of the scattering process within the time interval used to make a measurement. This last section describes the possible errors involved in using sampling intervals of a minute or longer in obtaining data from transmission loss measurements. Section 2.1.1.5 considers the different data processing techniques used during the several phases of the experiment, the correction factors required for each of the processing schemes, and their precision.

Measurements of scattering cross section per unit volume require assumptions both about the fluctuations of the received signals and the operation of the receiver and data processing scheme in the presence of these fluctuations, (see Section 2.1.1) and about the distribution of scatterers in space and the response of antennas to the scattering. The latter problem, the definition of the scattering volume, is considered in Section 2.1.2. Finally, assumptions must be made about the scattering process to compute the equivalent reflectivity from the transmission loss measurements and about the distribution of raindrop sizes to compute the reflectivity from rain rate measurements. The relationship between the bistatic scattering cross section per unit volume and the equivalent reflectivity, together with the errors caused by the assumption of Rayleigh scattering for spheres or of the assumption of spherical drop shape are discussed in Section 2.1.3. The Z/R relationship is considered in Section 2.2.

Once the measurements were made, the problem of refining or improving the accuracy of the measurements remain. In Reference 1, the accuracies of the bistatic radar and rain gauge systems were presented. These accuracies were estimated before the data were analyzed in detail. The use of redundant measurements of the same Z_e values allowed the operation of the transmitter sites to be checked further. For the 10K paths, the uncertainty of the accuracy estimates given in Reference 1 could be reduced. The description of the various measurements and intercomparisons of measurements used to refine the accuracy estimates for transmitter operation are given in Section 3.1. Section 3.2 reconsiders the possible errors of the rain gauge measurements based upon a larger set of comparison data than were used in Reference 1.

Section 4 summarizes the measurements and presents the results. Section 4.1 presents data from the great circle path system that was used to test for possible contamination by propagation mechanisms other than rain. Section 4.2 considers several events in depth to examine possible departures from the assumptions made in Section 2. Section 4.3 presents the analysis of the observed number densities of equivalent reflectivity obtained from the transmission loss measurements and of reflectivity calculated from the rain rate measurements. The data presented in Section 4.3 are for Phase II. Data for the entire year are presented in Section 4.4. The results of the experiment are compared with earlier work and with prediction schemes in Section 5.

The appendixes contain tabular data: A—rain events and hours of observation, B—rain gauge accomodations, C—distribution and density functions for radar data, and D—distribution and density functions for rain gauges.

1.5 SUMMARY OF RESULTS

The data obtained during the high accuracy phase (Phase II) and for the entire year are summarized by the empirical distribution functions presented in this section. Figure 2 depicts the Z_e distribution function for 3-km height and the Z distribution function at the surface for the Phase II measurements. The distribution functions for Z_e values for both bistatic radar scatter paths with a scattering volume (common volume) at a height of 3 km (10KE and 10KF) are identical. Measurements made with the great circle path system showed no contamination of these data by other propagation mechanisms, and the data report only scattering by rain. The number density functions (histograms) for both paths were compared by means of a chi-square goodness-of-fit test at a 0.05 level of significance and found to be identical for Z_e values above 38 dBz* (see Section 4.3). The distributions of Z obtained from the surface rain gauge measurements were computed using a $Z = 270\ R^{1.3}$ relationship determined from drop size measurements made in North Carolina (Mueller and Sims, 1967a) and New Jersey (Mueller and Sims, 1967b). The rain gauge distributions were found to differ from each other and from the bistatic radar data distributions, using the chi-square goodness-of-fit test. When the data obtained during tropical storm Dora and hurricane Ginger were deleted from the Phase II data set, the resultant number density for the 10KE path was identical to that for the L8 gauge at the receiver site and to that for the 10K gauge at the 10K scattering volume subpoint for Z_e values greater than 42 dBz. The bistatic radar data were recalibrated (adjusted by 1 dB) before comparing number densities. The amount of adjustment was small in comparison with the measurement accuracy (±3 dB). Agreement was therefore obtained within the measurement accuracies of both the rain gauge and bistatic radar systems. For Z values above 42 dBz, the Z/R relationship used tends to underestimate Z by 1 dB, and the use of spherical drops in calculating Z tends to overestimate Z by 1 dB for the polarization used in the experiment. These effects thus tend to compensate for each other with a resultant Z/R relationship error that is small in comparison with the measurement errors and recalibration adjustment. Therefore the data for summer thundershowers show that in southeastern Virginia, the Z value distribution obtained using surface rain gauge data and an a priori determined Z/R relationship is identical to the Z_e values estimated from bistatic scatter data from a sufficiently small scattering volume at a height of 3 km.

* Z_e will be reported in terms of $z_e = 10 \log Z_e$, where Z_e is in units mm^6/m^3. To emphasize that z_e rather than Z_e is reported, the unit dBz will be used.

Data for the entire year together with the CCIR model used in interference calculations and coordination distance estimation are shown in Figures 3 and 4 for the 3- and 6-km heights, respectively. The CCIR model for rain climate 1 (CCIR, 1972) is applicable to the Tidewater District of Virginia. This model overestimates the Z_e values for the 10K path (3-km height) data. Since the model is a summary for a large section of the southeastern United States over which rain accumulations may vary significantly, departure from the model for a particular site and year is not unexpected. The data for the 20K path (6-km height) show a significant departure from both the CCIR model and the 10K path data (see Section 4.3). The CCIR model for the variation of reflectivity with height simply assumes that the Z_e value for a given number of minutes per year (percent of time) would be the same for all heights below 15 km in rain climate 1 for percentages of time smaller than 0.01. The measurements indicate that the Z_e values are nearly the same for the 6- and 3-km heights only for less than 0.002 percent of the year. The 10K data show good agreement with the model for all percentage values listed. The 20K data do not show good agreement with prediction for more than 0.002 percent of the year.

The data for both Phase II and the year show that for scattering volumes (mainlobe-to-mainlobe coupling) at 3- and 6-km altitudes, interference would occur when the thresholds established in Reference 1 are used. Figures 2 and 3 display the transmission loss for the nominal 10KE path using the Z_e and transmission loss relationship given in Table R1:/2-2. The transmission loss values, while representative of the interference problem simulated by the Virginia Precipitation Scatter Experiment, are not useful for general application to the interference prediction or coordination problem because additional information is required on cell size and variation of Z_e with height for a fixed percentage of the time. The great circle path data also show that mainlobe-to-sidelobe coupling also will cause interference when the thresholds established in Reference 1 are used.

The results of measurements for the year were compared (see Section 5) with the previous work of Doherty (1964), Carey and Kalagian (1970), and Buige and Rocci (1970). Doherty showed agreement between Z_e measurements and Z estimates based upon rain gauge data for scattering measurements made 250 m above the surface. The data for Phase II show that agreement may be obtained for heights up to 3 km (below the melting layer) but not at 6 km in thundershower rain. Carey and Kalagian found no agreement between the Z/R relationship derived from drop size measurements and their scattering measurements, and they proposed a new Z/R relationship for use in estimating interference. In contrast to their results, the Phase II data show good agreement using a Z/R relationship based upon drop size measurements. The data also show the prediction problem to be far more complex than assumed by Carey and Kalagian

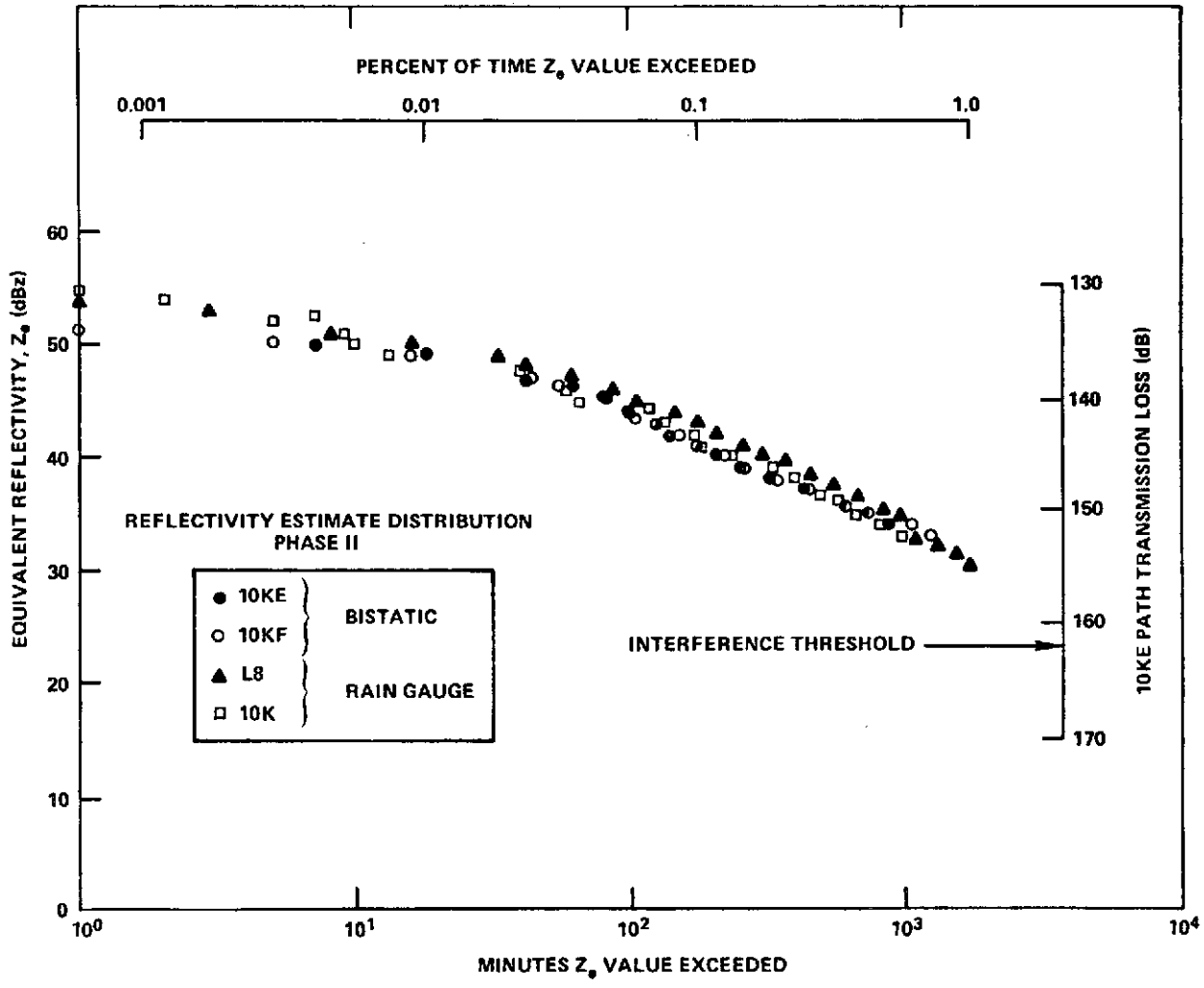

Figure 2. Reflectivity Estimate Distribution, Bistatic Radar and Gauge Data After Recalibration, Phase II

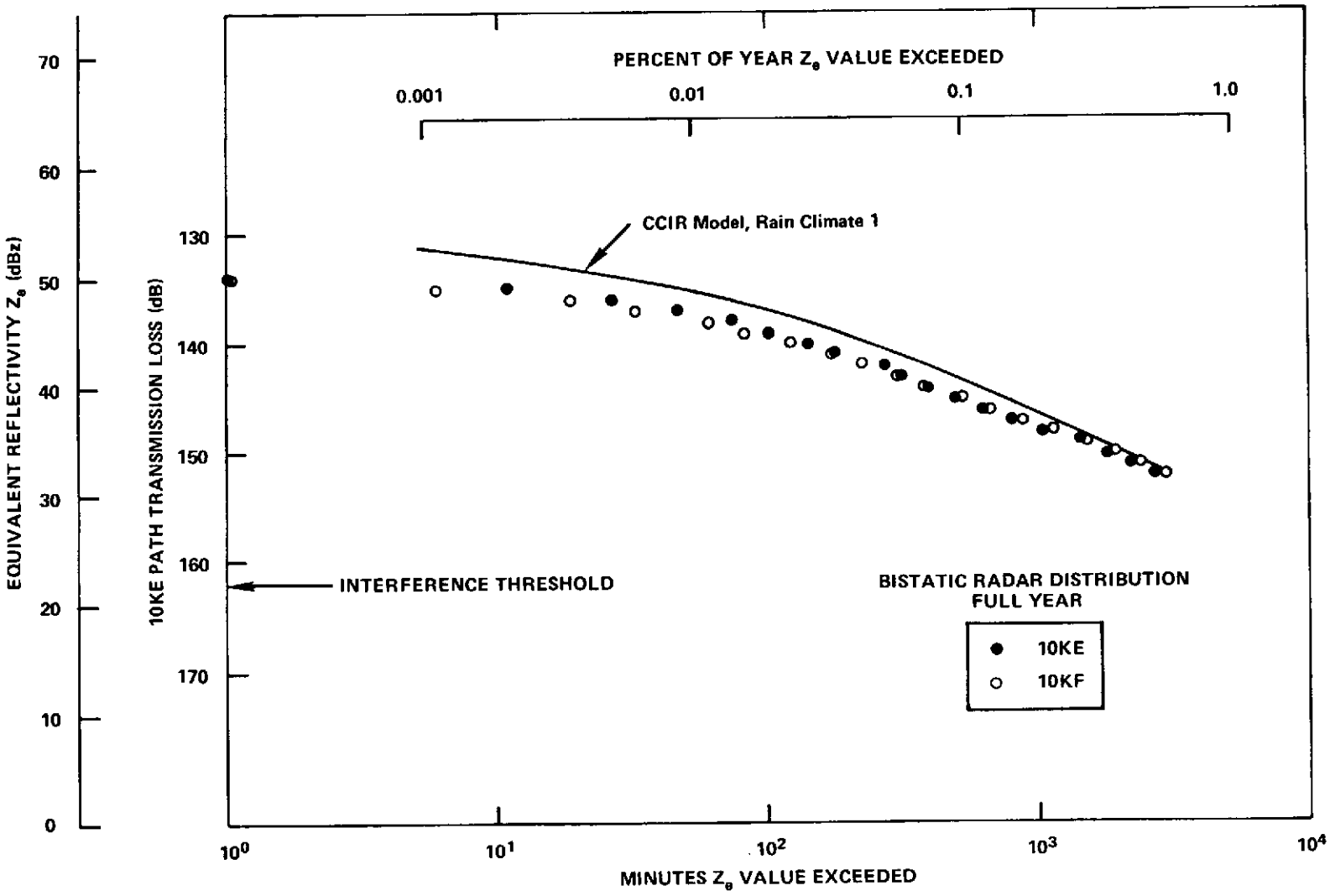

Figure 3. Reflectivity Estimate Distribution, 10K Paths
Bistatic Radar Data, Full Year

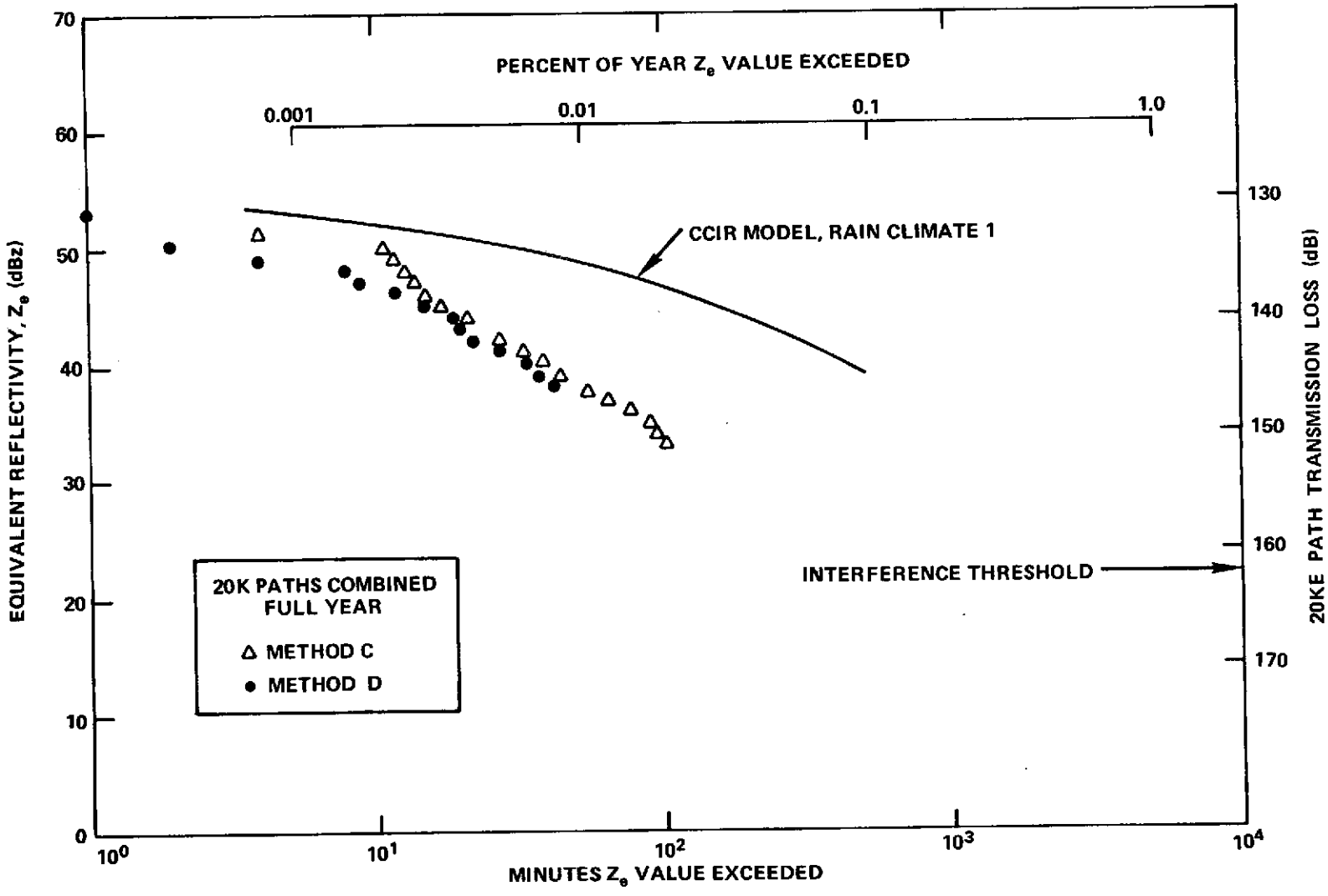

Figure 4. Reflectivity Estimate Distribution, 20K Paths Bistatic Radar Data, Full Year

in that prediction of Z at a point above the surface using surface data must take the rain, or synoptic, type into account and will change from location to location due to the change in the probability of occurrence of different synoptic types.

On the basis of an analysis of the relationship between the median logarithm of the received signal and the average received power for periods when the Z_e value is changing (nonstationary process), it appears that for less than 1 percent of the time the measured transmission loss distribution presented by Buige and Rocci was in agreement with an estimated distribution. The estimated distribution was based upon hourly rain gauge data obtained in the local area, the transformation to instantaneous rain rates recommended by Bussey (1950), and a Z/R relationship based upon drop size data obtained in New Jersey and North Carolina. Buige and Rocci in their analysis reached the opposite conclusion and proposed a new Z/R relationship. The use of a new relationship is not recommended, since the difference between the Z/R relationship determined using the transmission loss data and the relationship determined using drop size data may be due to the method used to estimate the Z_e value and not to the actual relationship between Z and R.

The empirical number density function for a year of data from the 10K gauge was within a factor of two of the number density predicted by the CCIR model for Z values below 50 dBz. After a 3-dB recalibration of the 10K gauge data to account for siting errors, the number density was still within a factor of two, with larger errors at low Z values rather than at high values. For fixed number density values, the Z values were within 3 dB of the values predicted by the CCIR model. This agreement is reasonable considering that only one year of data from one location is available for comparison. The CCIR model also shows less than a 6-dB difference in the Z values predicted by the distribution functions for a given percent of the year for all rain climates except a desert (rain climate 5).

Analysis of the scattering volume size correction factor (Section 2.1.2) shows that a 4 dB or greater change in the estimation of transmission loss may occur if the cell sizes are small in comparison with the assumed 3.5-km cell size used in the CCIR model.

The variation in Z_e value with height for the same percentage of the time indicated by the 10K and 20K scattering path measurements (3- and 6-km heights) shows that at 0.01 percent of the year, the effective reflectivity at 6 km is 10 dB lower than at 3 km. The CCIR model therefore is significantly in error by predicting a uniform Z_e value to a 15-km height in rain climate 1. The effect of Z_e variation with height is most important because tens of dB differences between the model and the actual value for a given percentage of the year and a height of, say, 12 km may occur.

1.6 CONCLUSIONS AND RECOMMENDATIONS

Analysis of data from the Virginia Precipitation Scatter Experiment has shown:

- Rain scatter can cause interference between terrestrial and space services ground stations either by mainlobe-to-mainlobe or sidelobe-to-mainlobe coupling.

- The CCIR surface rain rate distribution function model is within 3 dB of the empirical rain rate distribution function when both are compared in units of Z (using $Z = 270\ R^{1.3}$).

- Drop size distribution analysis for Virginia show a $Z - 270\ R^{1.3}$ relationship between Z and R should be used for showery rain rather than the $Z = 200\ R^{1.6}$ relationship adopted by the CCIR.

- For summer thundershowers the Z_e distribution (density function) measured at a height of 3 km is identical to the distribution (density function) measured at the surface after transformation from rain rate to Z using $Z = 270\ R^{1.3}$.

- For all rain types the Z_e distribution measured at a height of 3 km is not identical to the distribution of Z measured at the surface.

- For all categories and each separate rain type category, the Z_e value at a height of 6 km was overestimated by the surface Z values for percentages of the year in excess of 0.002. At 0.01 the surface value was 10 dB higher.

- The CCIR model that predicts the Z_e values for a fixed percentage of the year to be constant for heights up to some maximum value, which ranges from 7 km as a minimum to 15 km for the Virginia area (rain climate 1), is incorrect. At a height of 15 km the model may be in error by tens of decibels, causing coordination distances much larger than required.

- Rain cells appear to be smaller than the CCIR model estimate of 3.5 km, causing errors of as much as 4 dB in the estimate of transmission loss for intersecting beams.

On the basis of these conclusions it is recommended that radar studies of the horizontal extent and vertical development of rain be conducted. These studies should determine the conditional distributions of Z_e for a point at a particular height, given a Z value estimated from rain gauge data for a point on the surface, and the conditional distribution of cell size for a given Z_e at each height. The conditional distributions are required for adequate estimation of the transmission loss for intersecting beams. The current CCIR model will overestimate the scattering cross section and underestimate the transmission loss, resulting in coordination distances that are far too large. Conditional distribution information will permit an improved model with realistic coordination distances.

Additional studies of the occurrence and scattering properties of hail should be conducted. Hail is a rare phenomenon in most areas of the world. Hail was not observed during the Virginia Precipitation Scatter Experiment or during the Avon-to-Westford Experiment (Crane, 1971a; 1973). The Avon-to-Westford Experiment investigated the scattering angle dependence of bistatic scattering from hydrometeors and found that the data may be described by the Rayleigh approximations as assumed in the CCIR models for rain and snow within the ± 2.7 dB measurement accuracy of that experiment. Hail may cause a large (10-dB) departure from the scattering angle dependence given by the Rayleigh approximation. In regions where hail is plentiful, the Z_e values should be considerably higher than either those observed in this experiment or those computed by the CCIR model. The Z_e values for hail typically range from 55 to 70 dBz for frequencies in the 4 to 6 GHz range (Atlas, 1964).

2 ESTIMATION OF REFLECTIVITY

The Virginia Precipitation Scatter Experiment was designed to provide measurements both of scattering by rain and of surface rain rate. The object of the experiment was to determine whether the distribution function for scattering cross section may be simply related to the distribution function for surface rain rate. To provide a common basis for comparison, both the scattering cross section and rain rate values are reported in terms of reflectivity. The Z/R relationship between reflectivity and rain rate is considered in Section 2.2. Discussion of the relationship between reflectivity and received signal level for the bistatic radar system follows.

2.1 EQUIVALENT REFLECTIVITY MEASUREMENT USING BISTATIC RADAR

In Section R1:/2.2.1.3*, the bistatic radar system sensitivity is estimated from the radar equation, which relates the energy received to that transmitted and to the assumed properties of the scatterer. For use with a volume of randomly positioned scatterers, the effects of signal fluctuations must also be considered and, due to logarithmic signal processing in the receiver, correction factors must be provided. Correction factors are also required to account for fractional filling of the scattering volume by small, intense rain cells.

Equation R1:/(4) relates Z_e to the received power and other parameters of the radar equation. This equation is repeated here for convenience:

$$Z_e = \frac{P_r r_2 \sin\varphi}{P_t C_R G_2(\hat{r}_2)\theta_2} \tag{1}$$

where

$$C_R = \frac{1.86 \times 10^{-18} m\theta_1^2 G_1 \ell_1 \ell_2 |\kappa|^2}{\lambda^2}$$

and

P_t	=	transmitter power (W)
P_r	=	received power (W)
r_2	=	distance from antenna 2 (transmitter) to scattering volume (km)
C_R	=	equipment constant (defined above)
φ	=	scattering angle (rad)
$G_2(\hat{r}_2)$	=	gain of antenna 2 in the direction of the scattering volume

*Citations to Reference 1 materials are prefixed R1: throughout this report.

θ_2 = half-power beamwidth of antenna 2 (rad)

m = polarization mismatch factor (ratio ≤ 1)

θ_1 = half-power beamwidth of antenna 1 (rad)

$\ell_1 \ell_2$ = transmission loss factors for antennas 1 and 2 (ratio ≤ 1)

G_1 = peak gain (mainlobe) of antenna 1

$|\kappa|^2$ = $\left|\frac{\epsilon - 1}{\epsilon + 2}\right|^2$, where ϵ = dielectric constant for water

λ = wavelength (cm)

The correction factors for receiver processing, beam filling, data processing, and departure from Rayleigh scattering for spherical or spheroidal drop shapes are all multiplicative:

$$Z_e = \frac{P_r r_2 \sin\varphi}{C_p C_d C_s P_t C_R G_2(\hat{r}_2)\theta_2}$$

where

C_p = receiver and data processing corrections

C_d = beam filling corrections

C_s = correction for departures from Rayleigh scattering for spherical drops

Each of the correction factors and estimates of their accuracy are discussed in detail below.

2.1.1 Processing Correction Factor (C_p)

2.1.1.1 Bistatic Radar Equation—Calculation of the correction factor for signal fluctuations and receiver processing depends upon both the receiver parameters and assumptions about the random distribution of hydrometeor positions and velocities in the scattering volume. To simplify the derivation of the correction factors, the receiver output for a single isolated scatterer will be considered first, then scattering by an ensemble of independently positioned scatterers. The geometrical representation of the scattering problem is given in Figure 5. For a scatterer at position $\underset{\sim}{r}$ with respect to the transmitter and

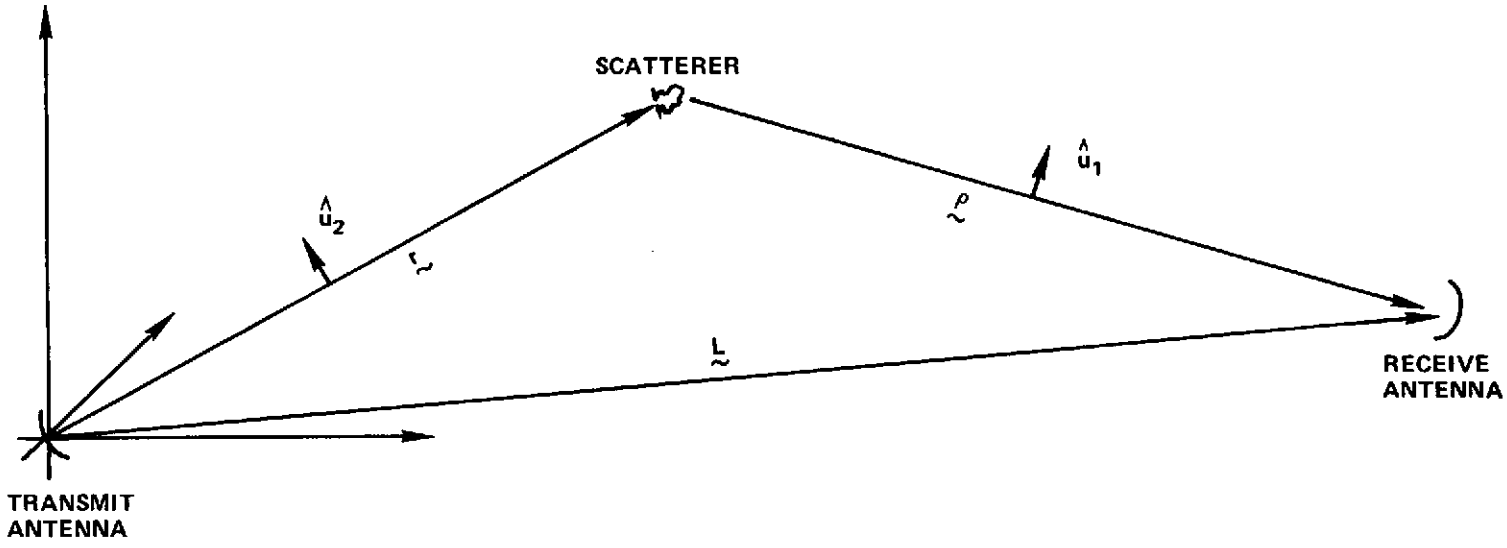

Figure 5. Scattering Geometry

$-\underset{\sim}{\rho}$ with respect to the receiver (Crane, 1966)

$$\underset{\sim}{E}^s(\underset{\sim}{L}) = \underset{\approx}{S}(\epsilon, a, \hat{r}, \hat{\rho}) \cdot \underset{\sim}{E}^i(\underset{\sim}{r}) \frac{e^{-ik \int_{\underset{\sim}{r}}^{\underset{\sim}{L}} n \, ds}}{ik\rho} \tag{2}$$

where*

$\underset{\sim}{E}^s(\underset{\sim}{L})$ = electric field vector at $\underset{\sim}{L}$

$\underset{\sim}{E}^i(\underset{\sim}{r})$ = electric field incident at $\underset{\sim}{r}$

$\underset{\sim}{r}, \underset{\sim}{\rho}, \underset{\sim}{L}$ = position vectors with magnitudes r, ρ, L and directions $\hat{r}$, $\hat{\rho}$, $\hat{L}$

$\underset{\approx}{S}(\epsilon, a, \hat{r}, \hat{\rho})$ = scattering amplitude tensor for a scatterer of dielectric constant ϵ, size parameter a, and directions of incident and scattered radiation $\hat{r}$, $\hat{\rho}$

$k = \frac{2\pi}{\lambda}$, where λ is wavelength

$\int_{\underset{\sim}{r}}^{\underset{\sim}{L}} n \, ds$ = line integral of the index of refraction, n, of the medium along the line-of-sight between $\underset{\sim}{r}$ and $\underset{\sim}{L}$, $\underset{\sim}{\rho} = \underset{\sim}{L} - \underset{\sim}{r}$

The field incident on the scatterer is given (Silver, 1949) as

$$\underset{\sim}{E}^i(\underset{\sim}{r}) = \sqrt{\frac{Z_o P_2' G_2}{2\pi}} \, f_2(\hat{r}) \, \hat{u}_2(\hat{r}) \frac{e^{-i\left[k \int_0^{\underset{\sim}{r}} n \, ds - \omega_c t\right]}}{r} \tag{3}$$

* In contrast to Equation (1), this equation is expressed in a consistent set of units. Specification of a particular set of mixed units is done as the last step of derivation.

30 Oct. 1973

where

Z_o	=	characteristic impedance of free space
P_2'	=	transmitter power delivered to antenna 2
G_2	=	transmit antenna gain at mainlobe peak
$f_2(\hat{r})$	=	normalized complex pattern function, $f_2^* f_2 = g_2$, where g_2 is the normalized gain function
$\hat{u}_2(\hat{r})$	=	unit vector in the direction of the electric field vector (unit polarization vector)
ω_c	=	$2\pi f_c = 2\pi \frac{c}{\lambda}$, where f_c is carrier frequency and c is speed of light in free space
t	=	time

The salient features of the bistatic radar system are depicted in the block diagram of Figure 6. The voltage input to the logarithmic amplifier and detector is given by

$$V = H(\omega - \omega_\ell) \sqrt{\frac{\lambda^2 G_1}{8\pi}}\, f_1(-\hat{\rho})\, \hat{u}_1(-\hat{\rho}) \cdot \underset{\sim}{E}(L)\underset{\sim}{}e^{-i\omega_\ell t} \qquad (4)$$

where

$H(\omega-\omega_\ell)$	=	bandpass response function of receiver system preceding logarithmic amplifier
ω	=	radian frequency (instantaneous) of received signal
ω_ℓ	=	$2\pi f_\ell$, where f_ℓ is local oscillator frequency
$G_1, f_1, \hat{u}_1$	=	gain, pattern function, and polarization vector for the receive antenna.

30 Oct. 1973

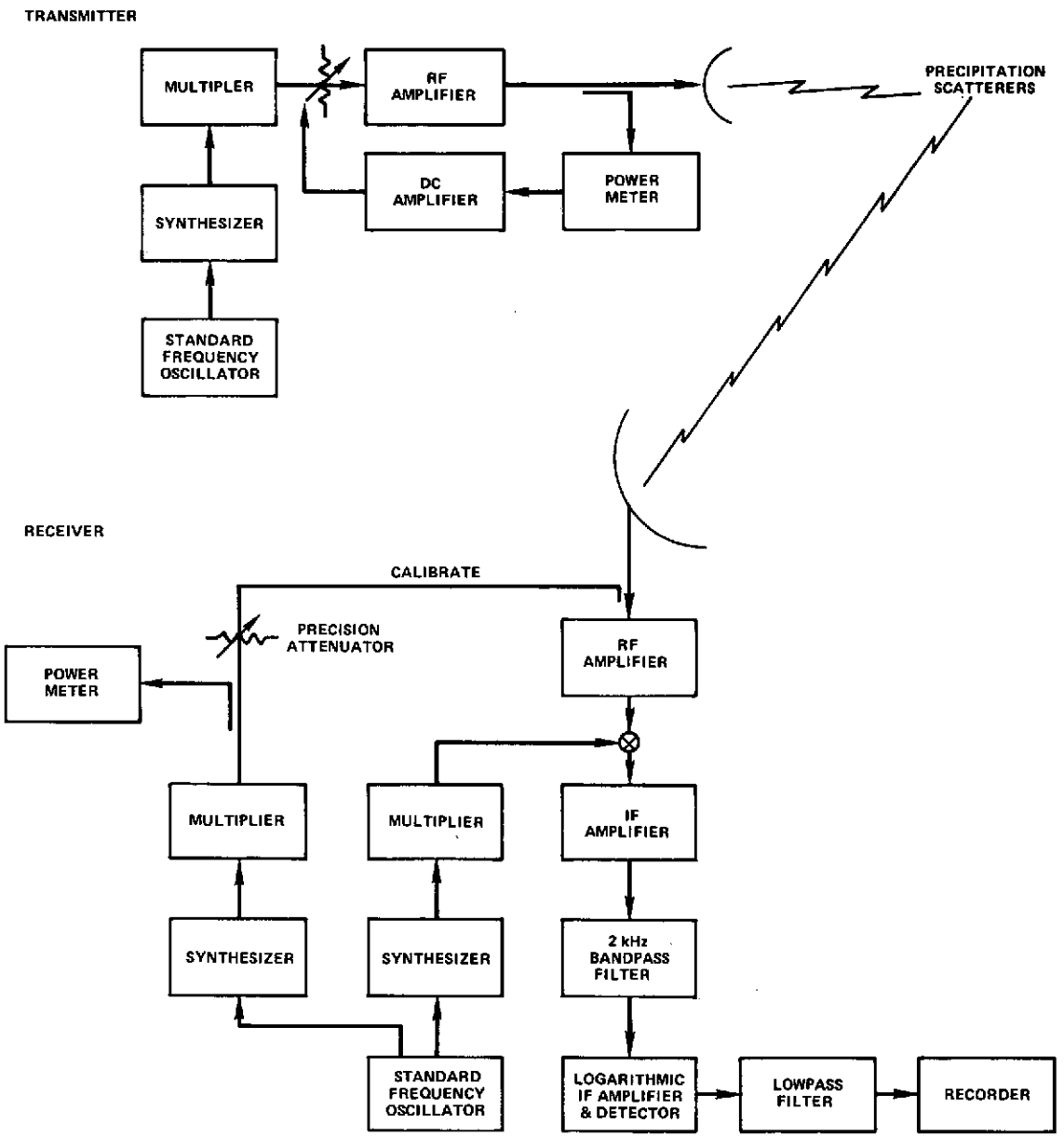

Figure 6. Bistatic Radar System Block Diagram

Equations (2) to (4) may be combined to provide a single equation relating the voltage at the input of the logarithmic receiver to the properties of the scatterer, $\underset{\approx}{S}(\epsilon, a, \hat{r}, \hat{\rho})$ and $\underset{\sim}{r}$:

$$V = \frac{CH(\omega - \omega_\ell) f_1 f_2 \hat{u}_1 \cdot \underset{\approx}{S} \cdot u_2 \exp -i\left[K(\underset{\sim}{r}) - (\omega_c - \omega_\ell)t\right]}{ikr\rho} \tag{5}$$

where

$$C = \frac{\lambda}{4\pi}\sqrt{G_1 G_2 P_2' Z_0} \text{ and } K(\underset{\sim}{r}) = k\left[\int_0^{\underset{\sim}{r}} n\,ds + \int_{\underset{\sim}{r}}^{\underset{\sim}{L}} n\,ds\right]$$

and some of the explicit functional dependences have been deleted. In this equation, $\underset{\sim}{r}$ moves with the scatterer. The equation may be rewritten using a fixed point in space, $\underset{\sim}{r}_0$, for the small duration of time during which the hydrometeor passes the point. During this interval, the position of the hydrometeor may be obtained from a Taylor series expansion of the hydrometeor position vector

$$\underset{\sim}{r} = \underset{\sim}{r}_0 + \frac{\partial \underset{\sim}{r}_0}{\partial t}(t - t_0) = \underset{\sim}{r}_0 + \underset{\sim}{v}(t - t_0)$$

$$K(\underset{\sim}{r}) = k\int_0^{\underset{\sim}{r}} n\,ds + k\int_{\underset{\sim}{r}}^{\underset{\sim}{L}} n\,ds = k\int_0^{\underset{\sim}{r}_o} n\,ds + k\int_{r_0}^{\underset{\sim}{L}} n\,ds + kn\left(\frac{\partial r}{\partial t} + \frac{\partial \rho}{\partial t}\right)(t - t_0)$$

where

$\underset{\sim}{r}_0$ = the fixed spatial position

$\underset{\sim}{v}$ = hydrometeor velocity

$t - t_0$ = duration of the small interval

The coefficient of $t - t_0$ is the Doppler frequency; this frequency in radians per second, ω_d, is

$$2\pi f_d = \omega_d = -kn\left(\frac{\partial r}{\partial t} + \frac{\partial \rho}{\partial t}\right)$$

For the geometry given in Figure 5

$$\frac{\partial r}{\partial t} = \frac{\underset{\sim}{r} \cdot \underset{\sim}{v}}{r} \quad , \quad \frac{\partial \rho}{\partial t} = \frac{\underset{\sim}{\rho} \cdot \underset{\sim}{v}}{\rho}$$

and

$$\omega_d = -\frac{kn}{\rho r}\left(r\underset{\sim}{\rho} + \rho\underset{\sim}{r}\right) \cdot \underset{\sim}{v} = 2\pi \underset{\sim}{\nu} \cdot \underset{\sim}{v} \tag{6}$$

where $\underset{\sim}{\nu}$ is the Doppler response function as defined by this equation.

For more than one scatterer, the received signals scattered by each must be summed. Using the assumption that, except for attenuation due to propagation through the scattering medium, the fields scattered by one hydrometeor and incident on another may be neglected in comparison with the incident field, the voltage at the logarithmic amplifier input may be obtained by summing Equation (5) for each drop. This assumption is called the distorted-wave Born approximation, or the single-scattering approximation, and is valid in the wavelength region of interest (Crane, 1971b). Since meteorological targets are composed of a large number of scatterers in a small volume, the summation may

be replaced by integration. Letting $\eta(a, \underset{\sim}{v}, \underset{\sim}{x})$ be the number density of scatterers at location $\underset{\sim}{x}$ with velocity $\underset{\sim}{v}$ and size parameter a

$$V = C \int_{\underset{\sim}{x}} \int_{\underset{\sim}{v}} \int_{a} \frac{H[W(\underset{\sim}{x}, \underset{\sim}{v})]\, f_1 f_2 \hat{u}_1 \cdot \underset{\approx}{S} \cdot \hat{u}_2 e^{-i[K(\underset{\sim}{x}) - W(\underset{\sim}{x},\underset{\sim}{v})t]} \eta(a, \underset{\sim}{v}, \underset{\sim}{x})}{ikx\,|\underset{\sim}{L} - \underset{\sim}{x}|} \, da \, d\underset{\sim}{v} \, d\underset{\sim}{x} \qquad (7)$$

where

$$W(\underset{\sim}{x}, \underset{\sim}{v}) = \omega_c + \omega_d - \omega_\ell$$

$$= \omega_c - \omega_\ell - \frac{kn}{x|\underset{\sim}{L} - \underset{\sim}{x}|} \left[x(\underset{\sim}{L} - \underset{\sim}{x}) + |\underset{\sim}{L} - \underset{\sim}{x}|\underset{\sim}{x}\right] \cdot \underset{\sim}{v}$$

The variable V is random because $\eta(a, v, x)$ is a random variable. Based on the assumption that hydrometeors are independently distributed in the scattering volume, η has a Poisson distribution for fixed a, $\underset{\sim}{v}$, and $\underset{\sim}{x}$ (Feller, 1966). For a Poisson process, the expectation and variance are given by

$$\langle \eta(a, \underset{\sim}{v}, \underset{\sim}{x}) \rangle = \bar{\eta}(a, \underset{\sim}{v}, \underset{\sim}{x})$$

$$\sigma_\eta^2 = \langle (\eta - \bar{\eta})^2 \rangle = \bar{\eta}(a, \underset{\sim}{v}, \underset{\sim}{x})$$

where $\langle\rangle$ represents ensemble averaging and $\bar{\eta}(a, \underset{\sim}{y}, \underset{\sim}{x})$ is the average (ensemble) number density. Since $\langle\rangle$ and integration are commutative

$$\langle V\rangle = c \int_{\underset{\sim}{x}} \int_{\underset{\sim}{y}} \int_{a} H f_1 f_2 \hat{u}_1 \cdot \underset{\approx}{S} \cdot \hat{u}_2 \frac{e^{-i(K - Wt)} \langle \eta(a, \underset{\sim}{y}, \underset{\sim}{x})\rangle \, da \, d\underset{\sim}{y} \, d\underset{\sim}{x}}{ikx|\underset{\sim}{L} - \underset{\sim}{x}|} \tag{8}$$

The functions in the integrand of Equation (8) are slowly varying with respect to $\underset{\sim}{x}$, except for $e^{-iK(\underset{\sim}{x})}$, which has rapidly oscillating real and imaginary parts. The integral therefore has a zero value and

$$\langle V\rangle = 0 = \langle \mathrm{Re}V\rangle + i\langle \mathrm{Im}V\rangle$$

Also, by letting

$$w = \mathrm{Re}V = \frac{1}{2}(V + V^*)$$

$$u = \mathrm{Im}V = \frac{1}{2i}(V - V^*)$$

the variance for w is given by

$$\sigma_w^2 = \langle w^2\rangle - \langle w\rangle^2 = \langle w^2\rangle = \frac{1}{4}\left[\langle VV\rangle + \langle V^* V^*\rangle + 2\langle VV^*\rangle\right]$$

$$\langle VV\rangle = C^2 \iiint\!\!\iiint\!\!\iint HH' f_1 f_1' f_2 f_2' (\hat{u}_1 \cdot \underset{\approx}{S} \cdot \hat{u}_2)(\hat{u}_1 \cdot \underset{\approx}{S} \cdot \hat{u}_2)'$$

$$\frac{e^{-i(K - Wt) - i(K - Wt)'} \langle \eta\eta'\rangle \, da \, da' \, d\underset{\sim}{y} \, d\underset{\sim}{y}' \, d\underset{\sim}{x} \, d\underset{\sim}{x}'}{ikxx' |\underset{\sim}{L} - \underset{\sim}{x}| \, |\underset{\sim}{L} - \underset{\sim}{x}'|}$$

30 Oct. 1973

where the primes refer to the a', $\underset{\sim}{v}'$, $\underset{\sim}{x}'$ coordinates. Because $\eta'(a', \underset{\sim}{v}', \underset{\sim}{x}')$ and $\eta(a, \underset{\sim}{v}, \underset{\sim}{x})$ are independent for $a \neq a'$, $\underset{\sim}{v} \neq \underset{\sim}{v}'$, and $\underset{\sim}{x} \neq \underset{\sim}{x}'$, then

$$\langle \eta\eta' \rangle = \langle \eta \rangle \langle \eta' \rangle \quad (a \neq a',\ \underset{\sim}{v} \neq \underset{\sim}{v}',\ \text{and}\ \underset{\sim}{x} \neq \underset{\sim}{x}')$$

$$= \langle \eta \rangle \quad (a = a',\ \underset{\sim}{v} = \underset{\sim}{v}',\ \text{and}\ \underset{\sim}{x} = \underset{\sim}{x}')$$

The sixfold integrals over $\langle \eta\ \eta' \rangle$ therefore reduce to a threefold integral with $a = a'$, $\underset{\sim}{v} = \underset{\sim}{v}'$, and $\underset{\sim}{x} = \underset{\sim}{x}'$ as a result of the oscillatory behavior of $\exp -i(K + K')$ for $\underset{\sim}{x} \neq \underset{\sim}{x}'$. The integrals for $\langle VV \rangle$ and $\langle V^* V^* \rangle$ also are zero for the same reason.

The variances of w and u are therefore given by

$$\sigma_w^2 = \sigma_u^2 = \frac{1}{2} \langle V^* V \rangle = \frac{1}{2} \langle P_r \rangle Z_o$$

$$= \frac{1}{2} C^2 \int_{\underset{\sim}{x}} \int_{\underset{\sim}{v}} \int_{a} \frac{H^* H g_1 g_2 |\hat{u}_1 \cdot \underset{\approx}{S} \cdot \hat{u}_2|^2 e^{-2\mathrm{Im}[K(\underset{\sim}{x})]} \overline{\eta}(a, \underset{\sim}{v}, \underset{\sim}{x})}{k^2 x^2 |\underset{\sim}{L} - \underset{\sim}{x}|^2} \, da \, d\underset{\sim}{v} \, d\underset{\sim}{x} \tag{9}$$

where P_r is received power and g_1, g_2 are the normalized gain functions for receive and transmit antennas, respectively. Equation (9) is the bistatic radar equation with the additional effects of receiver IF bandpass characteristics and particle motion included. This equation may be cast in the standard form by substitution for C:

$$\langle P_r \rangle = \frac{P_2' G_1 G_2 \lambda^2}{(4\pi)^2} \int_{\underset{\sim}{x}} \int_{\underset{\sim}{v}} \int_{a} \frac{H^* H g_1 g_2 |\hat{u}_1 \cdot \underset{\approx}{S} \cdot \hat{u}_2|^2 e^{-2\mathrm{Im}[K(\underset{\sim}{x})]} \bar{\eta}(a, \underset{\sim}{v}, \underset{\sim}{x})}{k^2 x^2 |\underset{\sim}{L} - \underset{\sim}{x}|^2} \, da \, d\underset{\sim}{v} \, d\underset{\sim}{x} \tag{10}$$

2.1.1.2 Logarithmic Processing—The logarithmic amplifier and detector output is proportional to the logarithm of the amplitude of V. The output of the logarithmic receiver was processed in several ways, depending upon the recording system used. Generally, the detected output was low-pass filtered; then it was either averaged or sampled and used for construction of within-the-minute empirical distribution functions. To evaluate the effect of processing on the output of the logarithmic detector, the distribution function of the output must be determined. As a starting point, the distribution function A for the amplitude of V is determined. The distribution function for η is assumed to be Poisson and, for a large number of hydrometeors per unit volume in the $a, \underset{\sim}{v}, \underset{\sim}{x}$ space, may also be approximated by a normal distribution function. Equation (7) is linear and η is independently distributed for different values of a, $\underset{\sim}{v}$, and $\underset{\sim}{x}$; consequently, w and u have independent Gaussian distributions:

$$p(u, w)\, du\, dw = p(u)p(w)\, du\, dw = \frac{e^{-u^2/2\sigma_u^2} e^{-w^2/2\sigma_w^2}}{2\pi\sqrt{\sigma_u^2 \sigma_w^2}} \, du\, dw$$

$$= \frac{e^{-(u^2 + w^2)/\langle V^* V \rangle}}{\pi \langle V^* V \rangle} \, du\, dw \tag{11}$$

From $A^2 = u^2 + w^2$ and $du\, dw = A\, dA\, d\Psi = \frac{dA^2\, d\Psi}{2}$, the density Equation (11), after integration over the polar angle Ψ, may be expressed by

$$p(A^2)\, dA^2 = \frac{e^{-A^2/\langle V*V\rangle}}{\langle V*V\rangle}\, dA^2 \tag{12}$$

The density function for $P_r = 10 \log P_r = 10 \log \frac{A^2}{Z_0}$ is found from Equation (12) by change of variable:*

$$p(P_r)\, dP_r = \frac{\mathrm{Ln}10}{10} \exp - \left[\frac{e^{(\mathrm{Ln}\,10/10)P_r}}{\langle P_r\rangle}\right] \exp\left[\left(\frac{\mathrm{Ln}\,10}{10}\right) P_r\right] \frac{dP_r}{\langle P_r\rangle} \tag{13}$$

The average value of P_r is found from Equation (13) to be

$$\langle P_r\rangle = \int P_r p(P_r)\, dP_r = \int 10 \log(A^2) p(A^2)\, dA^2$$

$$= 10 \log (0.561 \langle P_r\rangle) = -2.51 + 10 \log \langle P_r\rangle \tag{14}$$

*Ln = $\log_e$

30 Oct. 1973

The correction for logarithmic averaging therefore is 2.51 dB, which must be added to the measured average $\langle P_r \rangle$ to provide the best estimate of $\langle P_r \rangle$ expressed in dB.

2.1.1.3 Doppler Spread—During Phase I and for the 20K paths during Phase II, the average of P_r was not recorded, but had to be estimated from the recorded "instantaneous" data (~74 to 100-Hz low-pass-filtered output of the logarithmic detector). For Phase Ia, the output of the logarithmic detector was low-pass filtered and sampled to obtain empirical distributions of received signal levels within the minute. If the frequency spread of the received signal at the output of the logarithmic receiver was small in comparison with the 74-Hz low-pass filter, the sampled distribution would be the same as given by Equation (13). If the frequency spread is large in comparison with 74 Hz, an exponentially weighted integration of P_r is obtained and the resulting distribution tends toward the normal. (This temporal integration, assuming a stationary process, is equivalent to ensemble averaging.) Marshall and Hitschfeld (1953) calculated the distributions for the averages of a number of independent samples and showed that, with as few as 40 samples, the distribution is approximately normal, and with post-detection filtering and the assumption of ergodicity or that the time average is identical to the ensemble average, the measured distribution should tend toward a normal distribution.

The frequency spread at the output of the logarithmic amplifier depends upon the spread of the input. The input signal is frequency shifted by the average motion of the hydrometeors and spread by random fluctuations in hydrometeor velocity and by systematic changes in the Doppler frequency caused by changes in hydrometeor velocity or in the geometrical terms of the equation for Doppler frequency. Four causes of Doppler spread are of importance: turbulence, changes in hydrometeor fall velocity with the size parameter a, wind shear, and variation of the geometrical terms for different values of $\underset{\sim}{x}$ within the scattering volume. The components of $\underset{\sim}{\nu}$ (see Equation (6)) for the bistatic radar system are given in Table 2 along with the magnitude, ν, and postulated extreme Doppler shifts. The value of $\Delta\nu$ provides an estimate of the sensitivity of the system to variation in the geometrical terms. Using a $\Delta\nu$ value of 0.3 Hz/m/s, and an extreme wind speed of 50 m/s, the Doppler spread (at half-power per unit frequency) is estimated to be 15 Hz. Nathanson and Reilly (1967) reported that turbulence typically has a 1 m/s rms spread which, with ν = 20 Hz/m/s, causes a spread of 20 Hz. Fall velocities of rain range from less than 1 m/s to approximately 10 m/s, with an rms value of 8 m/s at 25 mm/hr (Atlas, 1964, Section 6.8) and causing a Doppler spread of less than 35 Hz. Donaldson et al. (1972) reported wind shear values as high as 0.025/s averaged over 150 m from Doppler radar measurements in thunderstorms.

Using these values and a ν value of 20 Hz/m/s, the Doppler spread due to wind shear is estimated to be less than 200 Hz. In comparison with other sources of Doppler spread, wind shear is dominant.

The frequency spread at the logarithmic detector output is much larger than at the input, because of harmonics generated by the process of taking the logarithm of the input signal. Assuming that at least third-order harmonics are present, even with no wind shear the detected output would have a frequency spread in excess of 140 Hz, or larger than the bandwidth of the low-pass filters used in the recording systems. The recorded signal therefore will not have the density distribution given by Equation (13), because of slight integration by the low-pass filter. The distribution function for the density function given in Equation (13) is depicted in Figure 7. The distribution function for 1 minute recorded on the 5K path in January 1971 is also shown in Figure 7. Data for the distribution were obtained by using a distribution analyzer, an analog to digital (A/D) converter, and computer processing as described elsewhere (method G, Table R1:/5-1 and p. R1:/81). The A/D converter sampled at a rate of 80/s, which was not high enough to reconstruct the recorded wave form. The distribution of the recorded signal was adequately sampled and after calibration using linear interpolation between the 10-dB calibration steps, has been reproduced in Figure 7. The measured data shown may be in error by as much as 1.5 dB in the region below -112 dBm due to nonlinearities in the transfer functions of the receiver and recording devices. The error is less than 0.5 dB over the rest of the relative amplitude scale.

2.1.1.4 Stationarity Considerations—The data selected for display were the only data recorded during Phase Ia that met criteria of both high median signal level, -99 dBm, and apparent constancy of average scattered signal power over the 1-min sampling interval, as observed by the position of the peaks of the upper and lower bounds of the fading signal shown on a strip chart (Z-fold). Generally, high-level data showed significant changes in the values of the bounds observed on the strip chart within a 1-min sampling interval and would not be useful in estimating the distribution function for a process that is postulated to be stationary over the sampling interval. The measured distribution shows that relatively more data points were recorded in the vicinity of the median than for the theoretical distribution. For the measurement range above a relative indicated power of -12 dB, the theoretical and measured values are within 1 dB. These results were expected for the detected and filtered signal, because the extreme values are moved slightly closer to the mean as a result of integration, but the general shape is maintained since the ratio of the expected frequency spread to filter bandwidth is not large.

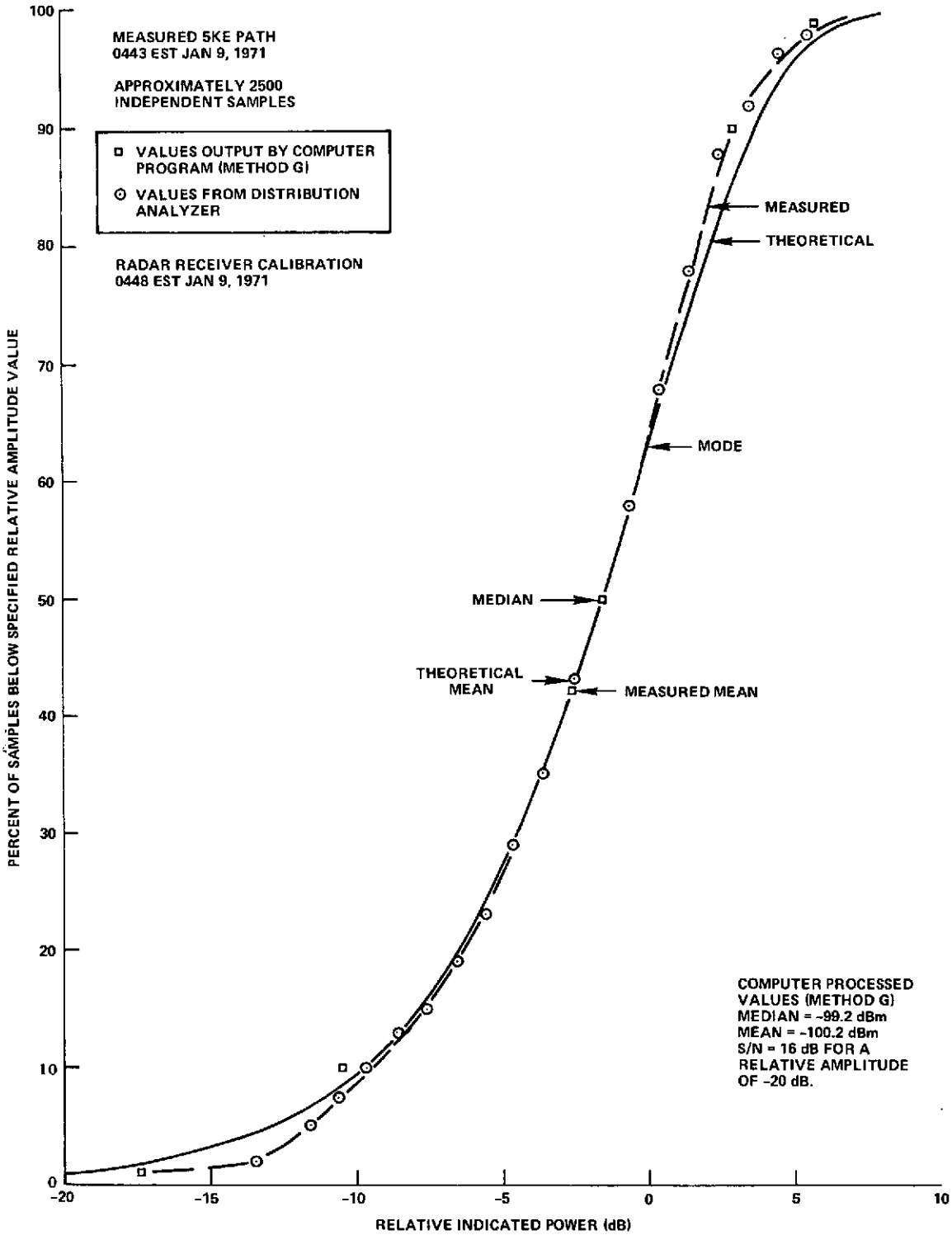

Figure 7. Within-Minute Received Power Distribution Function

Table 2
Bistatic Radar System Response to Hydrometeor Motion

Path	$^{1}\nu_s$ (Hz/m/s)	$^{1}\nu_w$ (Hz/m/s)	$^{1}\nu_v$ (Hz/m/s)	ν (Hz/m/s)	$\Delta\nu$ (Hz/m/s)	$^{2}f_{max}$ (Hz)	$^{2}f_{min}$ (Hz)
10KE	-6.8	-17.0	3.7	18.7	0.2	940	-890
20KE	-9.5	-17.5	4.3	20.4	0.3	1030	-970
10KF	-9.7	6.8	3.4	12.3	0.2	620	-570
20KF	-11.6	6.8	4.1	14.0	0.3	700	-640

[1] s - wind from the south, w - wind from the west, v - falling

[2] Maximum and minimum Doppler frequency for a 50 m/s wind at height computed for average rain fall velocity of 7 m/s.

The data obtained from the computer processing were in the form of median levels determined for each minute. The effect of the variation of the average value of the process during the 1-min sampling time may be estimated by postulating two independent processes, one for the mean of the process modeled by Equation (13) and the other for the distribution of P_r as a conditional distribution, given $\langle P_r \rangle$ (Rogers, 1969). Noting that the bounds of the fading signal tend to change linearly with time within the minute, and that changes of as much as 20 dB have been observed within a minute, then

$$p(P_r)dP_r = \int_{\langle P_1 \rangle}^{\langle P_2 \rangle} p(P_r \mid \langle P_r \rangle)\, p(\langle P_r \rangle)\, d\langle P_r \rangle \tag{15}$$

where $p(P_r \mid \langle P_r \rangle)$ is given by Equation (13) and, for a linear change in $\mathrm{Ln}\ \langle P_r \rangle$ within the minute, $p(\langle P_r \rangle)$ is given by

$$p(\langle P_r \rangle)\, d\langle P_r \rangle = \frac{1}{\langle P_r \rangle\, (\mathrm{Ln}\ \langle P_2 \rangle - \mathrm{Ln}\ \langle P_1 \rangle)}\, d\langle P_r \rangle \tag{16}$$

where $\langle P_2 \rangle$ is the maximum value of $\langle P_r \rangle$ within the minute and $\langle P_1 \rangle$ is the minimum value.

The distribution function for P_r can be determined by first finding the distribution function for A^2:

$$F(A^2) = \int_0^{A_2} p(A^2)dA^2 = \int_0^{A_2} e^{-x/\langle P_r \rangle Z_0} \frac{dx}{\langle P_r \rangle Z_0} = 1 - e^{-A^2/\langle P_r \rangle Z_0} \tag{17}$$

30 Oct. 1973

For $\langle P_r \rangle$ varying during the minute

$$F(A^2) = \int_0^{A_2} \int_{\langle P_1 \rangle Z_0}^{\langle P_2 \rangle Z_0} \frac{e^{-x/y}\, dx\, dy}{x^2 \mathrm{Ln}\,(\langle P_2 \rangle / \langle P_1 \rangle)}$$

$$= 1 - \frac{E_1(A^2/\langle P_2 \rangle Z_0) - E_1(A^2/\langle P_1 \rangle Z_0)}{\mathrm{Ln}\,(\langle P_2 \rangle / \langle P_1 \rangle)} \qquad (18)$$

where $E_1(x)$ is the exponential integral (Abramowitz and Stegun, 1964). The median value is found from Equation (18) for F = 0.5

$$F(A^2_m) = F\,(P_m Z_0) = 0.5$$

where A_m, P_m are the median amplitude and median instantaneous (assuming ergodicity) power values, respectively. P_m therefore is found by solving

$$E_1\left(\frac{P_m}{\Xi \langle P_1 \rangle}\right) - E_1\left(\frac{P_m}{\langle P_1 \rangle}\right) = \frac{\mathrm{Ln}\,\Xi}{2} \qquad (19)$$

where $\Xi = \langle P_2 \rangle / \langle P_1 \rangle$. For $\Xi = 1$ (no change), P_m must be determined by use of Equation (17). Consequently

$$e^{-P_m/\langle P_r \rangle} = 0.5$$

and

$$P_m = 10 \log (P_m) = 10 \log (\text{Ln } 2) + 10 \log \langle P_r \rangle$$

$$= -1.59 + 10 \log \langle P_r \rangle$$

For $\Xi > 1$, the expected average value for 1 min is given by

$$\langle \overline{P}_r \rangle = \int_{\langle P_1 \rangle}^{\Xi \langle P_1 \rangle} \frac{dx}{\text{Ln } \Xi} = \frac{\langle P_1 \rangle (\Xi - 1)}{\text{Ln } \Xi}$$

and

$$\langle P_1 \rangle = \langle \overline{P}_r \rangle \frac{\text{Ln } \Xi}{\Xi - 1} \tag{20}$$

For $\Xi = 10$ and $\Xi = 100$, corresponding to 10- and 20-dB changes within the minute, Equation (19) may be solved by trial and error. For $\Xi = 10$, $P_m = 2.05 \langle P_1 \rangle$ and $10 \log P_m = -2.80 + 10 \log \langle \overline{P}_r \rangle$. For $\Xi = 100$, $Pm = 5.95 \langle P_1 \rangle$ and $10 \log P_m = -5.58 + 10 \log \langle \overline{P}_r \rangle$. This model indicates that the median value differs from $\langle \overline{P}_r \rangle$ by as much as 5.6 dB for a 20-dB change in $\langle P_r \rangle$ during the minute. For the latter case the estimate of the time averaged value $\langle \overline{P}_r \rangle$ will be in error by 4 dB when the -1.6 dB ($\Xi = 1$) correction factor is used.

30 Oct. 1973

The mean value $\langle \bar{P}_r \rangle$ also depends upon Ξ :

$$\langle \bar{P}_r \rangle = \langle 10 \overline{\log (A^2)} \rangle = \int_0^{\infty} \int_{\langle P_1 \rangle}^{\Xi \langle P_1 \rangle} 10 (\log y) e^{-y/x} \frac{dy\ dx}{x^2 \mathrm{Ln}\ \Xi}$$

$$= 10 \log \left(0.561 \langle \bar{P}_r \rangle \frac{(\mathrm{Ln}\ \Xi)\ \sqrt{\Xi}}{\Xi - 1} \right) \qquad (21)$$

$$= -2.51 + 10 \log \langle \bar{P}_r \rangle \quad \text{for } (\Xi = 1)$$

$$= -3.43 + 10 \log \langle \bar{P}_r \rangle \quad (\Xi = 10)$$

$$= -5.83 + 10 \log \langle \bar{P}_r \rangle \quad (\Xi = 100)$$

For a 20-dB change in $\langle P_r \rangle$ during the minute, the correction factor for processing using the constant $\langle P_r \rangle$ hypothesis (Ξ=1) will be in error by 3.3 dB. The difference between the mean and median value estimates, P_m and $\langle \bar{P}_r \rangle$, is 0.9 dB for Ξ=1, 0.6 dB for Ξ=10, and 0.3 dB for Ξ=100. The observed values range from 1.0 to 0.2 (see Figure 7) in agreement with the above analysis.

2.1.1.5 Precision of Data Reduction--Data recorded during Phase II for the 10K paths were taken with a 0.7-Hz low pass filter and approximated the average of the logarithm of the received signal. For a Ξ of 100 for the minute, Ξ would be 2.5 for the 1/0.7s sample and the error due to nonstationarity of the process would be less than 0.2 dB. Using the ratio of the expected Doppler spread without windshear to 0.7 Hz to estimate the number of independent samples obtained by the radar, the instantaneous recorded signal represented

integration over at least 70 samples. From the analysis of Marshall and Hitschfeld (1953), for 70 samples the measured signal level will be within ±1 dB of the average 97.5 percent of the time. Using data processing methods A (see Section R1:/5.1), six samples of the recorded signal were processed, which reduced the uncertainty to ±0.4 dB for 97.5 percent of the time. Because each of the samples was quantized in 1-dB steps converted to linear values, averaged, and reexpressed in dBm, the 97.5 percent uncertainty is estimated to be ±1.4 dB. Using method B, a larger error exists, since the 1-min average of the logarithm is subjectively estimated. In this case, errors due to process nonstationarity may be large, because Ξ for the minute must be used with a resultant maximum error of 3.3 dB for $\Xi = 100$. The precision, or maximum uncertainty, in the estimate of the 1-min average of the logarithm of the received signal for method B was estimated to be ±3 dB from comparisons of the results of using methods A and B on the same data sets, as reported in Table R1:/5-1. This agrees with the difference in $\langle \overline{P}_r \rangle$ estimates for $\Xi = 2.5$ and $\Xi = 100$.

The other processing methods, C, D, E, and F, used the fading signal on the Z-fold as input. In each method the upper bound, and in D and E the lower bound also, of the fading signal must be determined. The selection of a bound is equivalent to fixing a percentage point on the distribution curve. The actual percentage point varied as a function of observer, chart speed, and ink flow from the recorder pen. The chart speed and ink flow rates varied little during most of the experiment. From a comparison between data processed using different methods, it was determined that the upper bound was usually estimated to be 10 dB above the mean and the lower bound to be 14 dB below the mean, corresponding to approximately 99.5 and 1.5 percent of the minute, respectively. The distribution function shows the upper bound to be relatively well defined in comparison with the lower bound. Method C, which uses the upper bound value only, was estimated to be more precise than methods D and E for this reason.

Method E was used for processing several events that had been automatically processed using method G. A comparison between the estimated average of the logarithm of the received power for each minute of data processed for the 10K paths is shown in Figure 8. These data show that a received-signal-level dependent correction factor should be used rather than the simple 2-dB correction factor given in Table R1:/5-1. The level-dependent correction factor was used in preparing the distribution of received signal level reported below and, from Figure 8, the precision of reading is estimated to be ±4 dB for method E. The 2-dB correction factor was retained for use with method C, where effect of scale nonlinearity which led to the variable correction factor was eliminated. Methods C and D were used only in processing the data for the 20K paths.

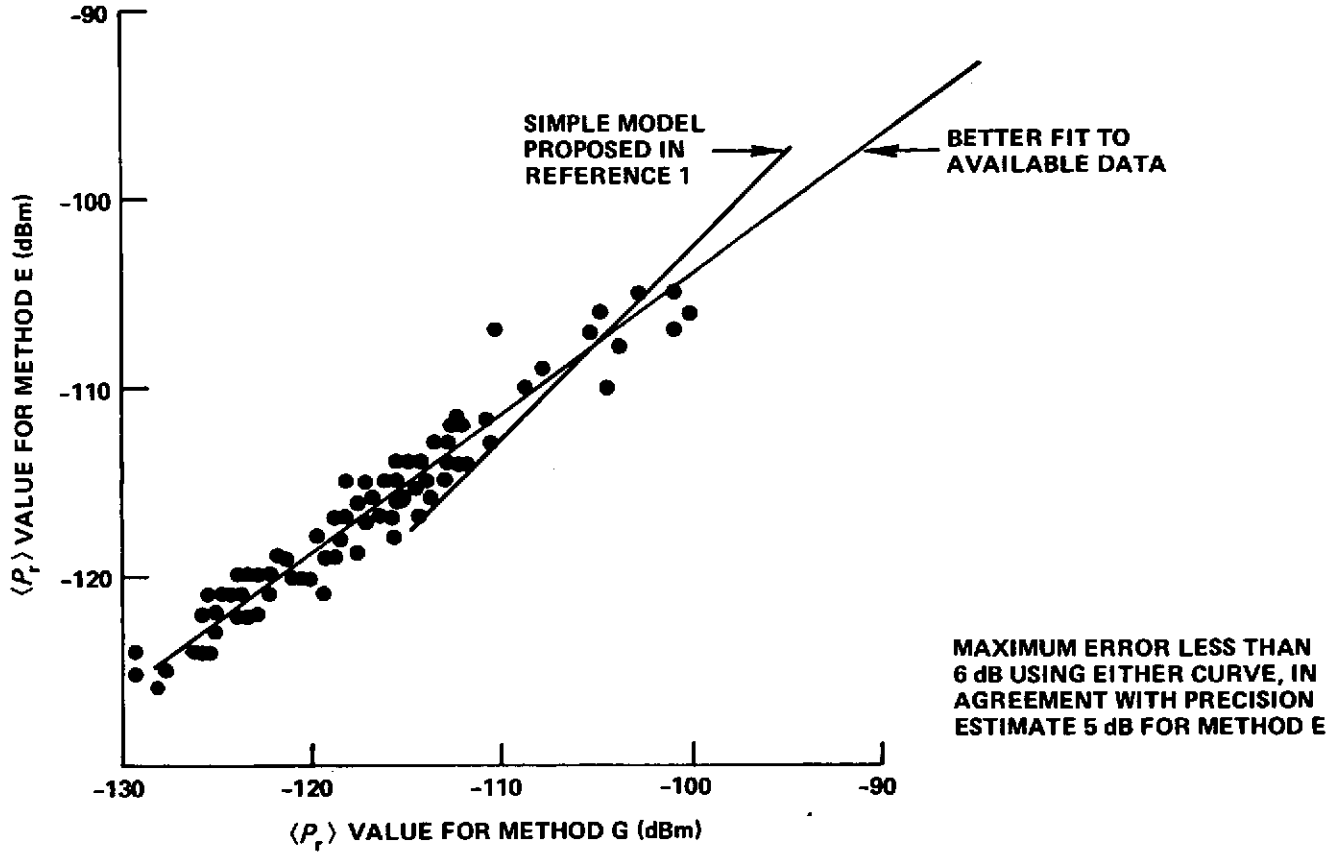

Figure 8. Comparison of Values Obtained Using Methods E and G

Measured distributions for the entire year for the 20K path as obtained using these methods are shown in Figure 4. The data obtained using the two methods agree within the estimated precision of each method. Method F was not used to process any of the data used in preparing distributions of received signal level.

The IF bandpass characteristics of the receiver system are discussed in Reference 1. For each of the paths, H*H varies by less than ±0.5 dB for frequencies within 500 Hz of the carrier frequency. Using the values of $\underset{\sim}{\nu}$ given in Table 2, less than ±0.5 dB variation occurs for wind speeds less than 24 m/s. An analysis of radiosonde data from four NWS stations surrounding the experiment area showed that the maximum Doppler shifts expected were 500 Hz on the 10KE path, 340 Hz on the 10KF path, 780 Hz on the 20KE path, and 500 Hz on the 20KF path. With the exception of the 20KE path, the variation in H*H is not a problem. For the 780-Hz shift, H*H is -1.3 dB with respect to its value at the carrier frequency. All Doppler shifts in excess of 500 Hz occurred during the winter months when no 20K data were obtained. Since the variation of H*H is less than 0.5 dB over the frequency band, the measurement error is increased by 0.5 dB and H*H is set equal to a constant (independent of ω_d). Because the Doppler shift varies from cell to cell, the error is used to increase the value of the repeatability estimates given in Table R1:/3-11.

The equation for use in reducing the bistatic radar data is obtained from Equation (10) by integrating over $\underset{\sim}{v}$ and a. Since H*H is a constant, only $\overline{\eta}$ depends upon $\underset{\sim}{v}$, and only $\overline{\eta}$ and $\underset{\approx}{S}$ depend on a. Because $\overline{\eta}$ is a number density

$$\int_{\underset{\sim}{v}} \overline{\eta}(a,\underset{\sim}{v},\underset{\sim}{x})\ d\underset{\sim}{v} = \overline{\eta}(a,\underset{\sim}{x})$$

and Equation (10) becomes

$$\langle P_r \rangle = \frac{P_2' G_1 G_2 \lambda^2 H^* H}{(4\pi)^2} \int_{\underset{\sim}{x}} \frac{g_1 g_2 \int_a |\hat{u}_1 \cdot \underset{\approx}{S} \cdot \hat{u}_2|^2 \overline{\eta}(a,\underset{\sim}{x})\ da\ e^{-2\mathrm{Im}[K(\underset{\sim}{x})]}\ d\underset{\sim}{x}}{k^2 x^2 |\underset{\sim}{L} - \underset{\sim}{x}|^2} \qquad (22)$$

The data processing correction factors , C_p, to be used with $\langle \overline{P}_r \rangle$ to estimate $\langle \overline{P}_r \rangle$ are summarized in Table 3. The values in the table were used in the preparation of received signal distribution functions and supersede those given in Table R1:/5-1.

2.1.2 Scattering Volume Size Correction Factor (C_d)

Equation (22) is the bistatic radar equation. It may be reexpressed in the usual form of Equation (1) as

$$\frac{\langle P_r \rangle}{P_t} = \frac{G_1 G_2 \ell_1 \ell_2 \lambda^2}{(4\pi)^3} \int_{vol} g_1 g_2 \beta(\underset{\sim}{x})\ 10^{-\frac{1}{10}\left[\int_0^{\underset{\sim}{x}} A\ ds + \int_{\underset{\sim}{x}}^{\underset{\sim}{L}} A\ ds\right]} \frac{d\underset{\sim}{x}}{x^2 |\underset{\sim}{L} - \underset{\sim}{x}|^2} \qquad (23)$$

where the scattering cross section per unit volume is

$$\beta(\underset{\sim}{x}) = \frac{4\pi}{k^2} \int_a |\hat{u}_1 \cdot \underset{\approx}{S}(a,\underset{\sim}{x}) \cdot \hat{u}_2|^2\ \overline{\eta}(a,\underset{\sim}{x})\ da \qquad (24)$$

Table 3
Data Processing Correction Factors (C_p)

Method[1]	Path	Phase	Correction[2] Factor (dB)	Precision Estimate (dB)
A	10K	II	+2.5	±1.4
B	10K	II	+2.5	±3.0
C	20K	II	+2.5[3]	±3.0
D	20K	II	+4.5	±4.0
E	10 and 20K	Ib	+2.5[4]	±4.0
F	Not used			
G	All	Ia	+2.0	+4.0, -1.0

1 See Table R1:/5-1 for method definitions.

2 Factors are to be added to $\langle \bar{P}_r \rangle$ to get 10 log $\langle \bar{P}_r \rangle$.

3 Additional -10 dB factor was applied to the data as read.

4 The correction curve given in Figure 8 was also used. This added 0 dB at -115 dBm and +5 dB at -100 dBm.

and total attenuation along the path is

$$\int_0^{\underset{\sim}{x}} A\,ds + \int_{\underset{\sim}{x}}^{\underset{\sim}{L}} A\,ds = \left(\frac{20\,k}{\log e}\right) \mathrm{Im}\left[\int_0^{\underset{\sim}{x}} n\,ds + \int_{\underset{\sim}{x}}^{\underset{\sim}{L}} n\,ds\right] = \left(\frac{20}{\log e}\right) [\mathrm{Im}K(\underset{\sim}{x})] \qquad (25)$$

where

A = specific attenuation

P_2' = $\ell_2 P_t$

P_t = transmitter power

ℓ_1 = H^*H = receiver line loss factor (< 1)

ℓ_2 = transmit line loss factor (< 1)

In radar measurements, $\beta(\underset{\sim}{x})$ is the parameter of interest and β may be obtained only from the solution of the integral equation, Equation (23).

Useful information also may be obtained by using β', the scattering cross section per unit volume averaged over the scattering volume as defined by

$$\beta'(\underset{\sim}{r}_2) = \frac{\int_{vol} g_1 g_2 \beta(\underset{\sim}{x})\; 10^{-\frac{1}{10}\left[\int_0^{\underset{\sim}{x}} A\,ds + \int_{\underset{\sim}{x}}^{\underset{\sim}{L}} A\,ds\right]} \frac{d\underset{\sim}{x}}{x^2 |\underset{\sim}{L} - \underset{\sim}{x}|^2}}{10^{-\frac{1}{10}\left[\int_0^{\underset{\sim}{r}_2} A\,ds + \int_{\underset{\sim}{r}_2}^{\underset{\sim}{L}} A\,ds\right]} \left(\frac{U}{r_2^2 |\underset{\sim}{L} - \underset{\sim}{r}_2|^2}\right)} \qquad (26)$$

where the scattering volume is

$$U = \int_{vol} \frac{g_1 g_2 r_2^2 \, |\underset{\sim}{L} - \underset{\sim}{r}_2|^2 \, d\underset{\sim}{x}}{x^2 \, |\underset{\sim}{L} - \underset{\sim}{x}|^2}$$

and $\underset{\sim}{r}_2$ is a central point in the scattering volume. However, $\beta'(\underset{\sim}{r}_2)$ is a useful approximation to $\beta(\underset{\sim}{r}_2)$ only when the scattering volume is small and well defined and the total attenuation along the path as calculated using $\underset{\sim}{r}_2$ is negligibly different from the possible values obtained for any point $\underset{\sim}{x}$ within the scattering volume. For the S-band measurements of the Virginia Precipitation Scatter Experiment, only the latter condition was met. Therefore, an additional cell size correction factor was required for a useful approximation to $\beta(\underset{\sim}{r}_2)$.

The receive antenna had a narrow beamwidth, as indicated in Section 1.3, and because the transmit and receive antenna beams intersect, the scattering volume may be approximately defined by the intersection of the receive antenna mainlobe and either the transmit antenna mainlobe or the rain cell, whichever gives the smaller volume. If the transmit antenna provides the smaller volume, the scattering volume is filled and β' is a good approximation to β. At the scattering volume, the smallest volume dimensions are determined by the receive antenna. The physical distance across the volume as measured between the half-power points on the receiver antenna pattern is approximately 0.2 to 0.3 km, as shown in Table 1. The receiver antenna pattern is nearly symmetrical about the peak of the mainlobe for angles from the mainlobe center line small compared with the half-power beamwidth. The natural coordinate system for computing U therefore is a spherical system with the direction of the mainlobe peak ($-\hat{\rho}$) as the polar direction:

$$U = r_2^2 \left|\underset{\sim}{L} - \underset{\sim}{r}_2\right|^2 \int_0^{\infty} \int_0^{\pi} \int_0^{2\pi} g_1(\theta) g_2(y, \theta, \psi) \frac{y^2 \sin\theta \, d\psi \, d\theta \, dy}{y^2 x^2}$$

The transmit antenna provides a limiting dimension along the receiver beam of 1.8 to 3.1 km as measured between the half-power points of the transmit antenna pattern. The variation in x^2 and g_2 with θ and ψ is very small over the range values of θ that correspond to the mainlobe, hence U may be approximated by

$$U \simeq r_2^2 \left| \underset{\sim}{L} - \underset{\sim}{r}_2 \right|^2 \int_0^{\infty} \frac{2\pi g_2(y)}{x^2} \int_0^{\pi} g_1(\theta) \sin\theta \, d\theta \, dy$$

The antenna gain function $g_1(\theta)$ is given in Figure R1:/3-6. If $g_1(\theta)$ is approximated by

$$g_1(\theta) = e^{-4(\mathrm{Ln}2)(\theta/\theta_1)^2}$$

where θ_1 is the half-power beamwidth, sin θ is approximated by θ ; and the limit of integration π is replaced by infinity, since the beamwidth is small:

$$U \simeq r_2^2 \left| \underset{\sim}{L} - \underset{\sim}{r}_2 \right|^2 \frac{\pi\theta_1^2}{4\,\mathrm{Ln}\,2} \int_0^{\infty} \frac{g_2(y)}{x^2} \, dy$$

Although the Gaussian approximation does not provide a good match to the measured gain function, it is satisfactory for estimation of $G_1 \int g_1 \, d\Omega$ over the solid angle subtended by the scattering volume when the solid angle is small in comparison with 4π steradians and larger than the mainlobe. Using the definition of antenna efficiency, the ratio C_θ between θ_1 and λ/D , with D

the diameter of the circular antenna aperture, and the Gaussian approximation, then

$$G_1 \int_{4\pi} g_1(\Omega)\, d\Omega \simeq \pi^2 \alpha \frac{D^2}{\lambda^2} \left(C_\theta \frac{\lambda}{\theta D} \right)^2 \frac{\pi}{4 \mathrm{Ln} 2} \tag{27}$$

$$\simeq 11.2\, \alpha\, C_\theta^{\,2}$$

where antenna efficiency is

$$\alpha = \frac{\lambda^2 G_1}{\pi^2 D^2}$$

and

$$C_\theta = \frac{\theta_1 D}{\lambda}$$

For the receive antenna, $G_1 = 48$ dB, $D = 9.1$ m, and $\theta_1 = 0.012$ rad, therefore $\alpha = 0.51$, $C_\theta = 1.34$ and

$$G_1 \int_{4\pi} g_1(\Omega)\, d\Omega \simeq 10.3$$

By definition, $G_1 \int_{4\pi} g_1(\Omega)\, d\Omega = 4\pi$, and the approximation is 80 percent of the theoretical value. The theoretical value applies only when the antenna is completely surrounded by scatterers. When the scattering volume subtends a small solid angle, the value of 4π can be used only as an upper bound on the integral.

A lower bound can also be estimated for the integral by using the measured antenna pattern. The envelope of the measured pattern is approximately -10 dBi for angles greater than 25°, 0 dBi for angles between 12° and 25°, +10 dBi for angles between 7° and 12°, and +15 dBi for angles between 3° and 7°. Using these approximate values to estimate the pattern for angles greater than 3° results in

$$G_1 \int_0^{3^\circ} \int_0^{2\pi} g_1 \sin\theta \, d\psi \, d\theta \geq 4\pi - 3.8 = 8.8$$

and

$$8.8 \leq G_1 \int_0^{\Omega_m} g_1(\Omega)\, d\Omega \leq 4\pi$$

where Ω_m is the maximum solid angle subtended by the scattering volume. Since the Gaussian assumption provides an estimate of the integral that lies midway between the upper and lower bounds and is less than 0.9 dB from either bound, it provides an adequate estimate of the integral. The accuracy is estimated to be ±0.5 dB, because neither the upper nor lower bound is expected to apply.

The remaining integral in the expression for U gives the weighted contribution of scatterers along the receive antenna beam. Using a Gaussian approximation for the gain function, as in Figure 9, the integral may be evaluated. The approximation provides a good fit to the antenna pattern for relative gain values within 20 dB of the peak value. The half width of the gain function represents a distance of between 1.8 and 3.1 km along the receiver beam, as shown in

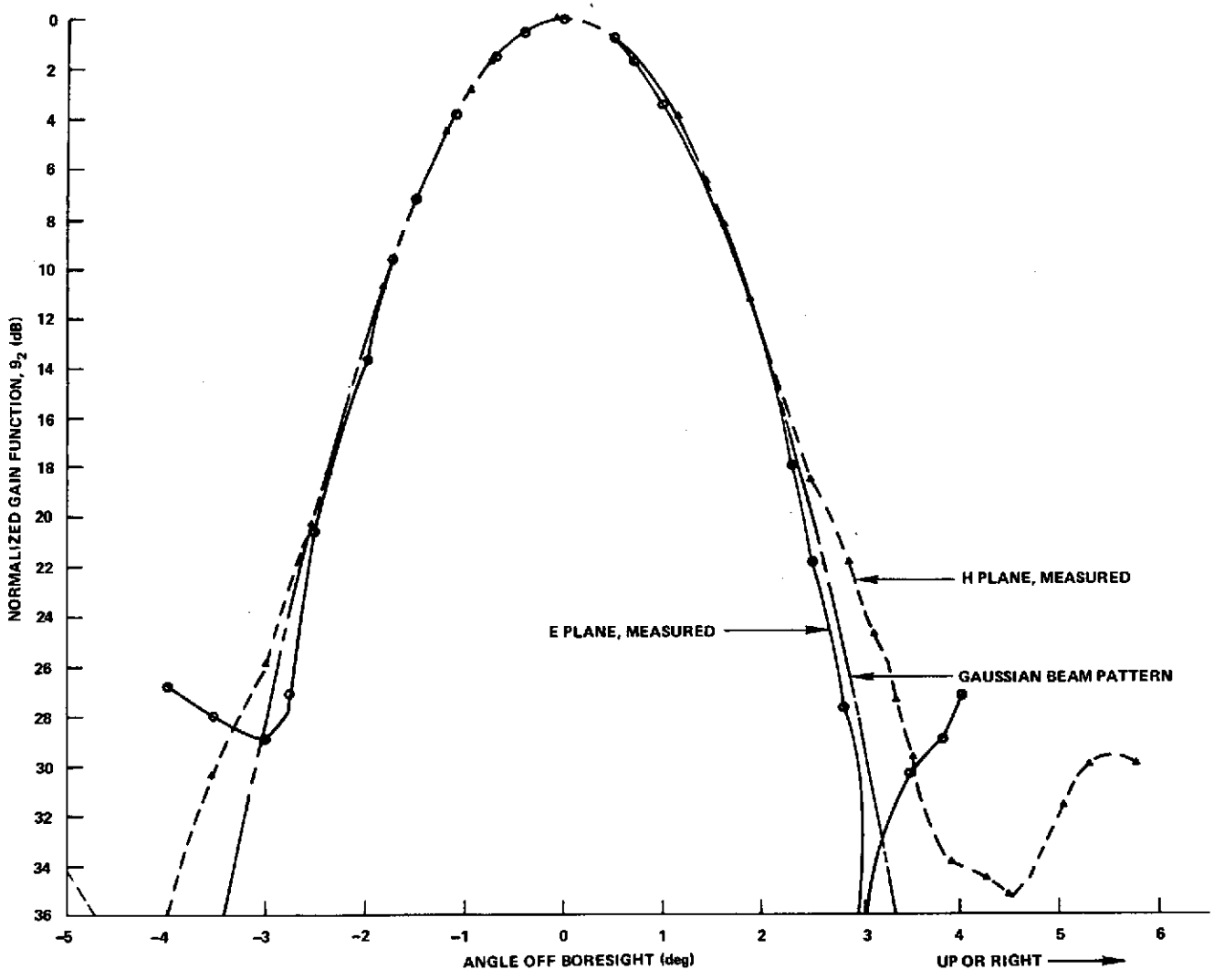

Figure 9. Eastville 10-KE Transmit Antenna Pattern

Figure 10 for the 10K scattering volume. Typical rain cell sizes are expected to lie between 2 and 4 km and to be comparable to the dimensions of the scattering volume along the beam.

To account for cell size, a modified scattering volume may be computed that uses the product of the antenna pattern and a Gaussian shaped rain cell to define the volume:

$$U = r_2^2 \left| \underset{\sim}{L} - \underset{\sim}{r}_2 \right|^2 \frac{\pi\theta_1^2}{4 \operatorname{Ln} 2} \int_{-\infty}^{\infty} \frac{\left[g_2(\hat{r}_2) e^{-4(\operatorname{Ln} 2)(y' \sin\varphi / r_2\theta_2)^2} \right] \left[e^{-4(\operatorname{Ln} 2)((y' - \delta)/d)^2} \right]}{x^2} dy'$$

where the first factor in the integrand describes the antenna pattern and the second describes a rain cell of half-width d. The origin of y' is taken as the direction of peak gain of the transmit antenna along the mainlobe of the receive antenna. The value of the gain function in this direction is $g_2(\hat{r}_2)$, φ is the scattering angle, and δ is the rain cell displacement from the origin of y'. Noting that x changes little within the scattering volume defined by the antenna pattern and rain cell, x^2 may be approximated by r_2^2 and, letting $\left| \underset{\sim}{L} - \hat{\underset{\sim}{r}}_2 \right|^2 = r_1^2$, then

$$U \simeq \frac{r_1^2 \pi\theta_1^2}{4 \operatorname{Ln} 2} g_2(\hat{r}_2) \int_{-\infty}^{\infty} e^{-4(\operatorname{Ln} 2)\left[(y' \sin\varphi / r_2\theta_\epsilon)^2 + ((y' - \delta)/d)^2 \right]} dy'$$

$$U \simeq \frac{r_1^2 r_2 \theta_2 g_2(\hat{r}_2) \theta_1^2 \pi\sqrt{\pi}}{\sin\varphi \; 8 \operatorname{Ln} 2 \sqrt{\operatorname{Ln} 2} \sqrt{1 + (r_2\theta_2/d \sin\varphi)^2}} \; e^{-4(\operatorname{Ln} 2)(\delta/d)^2 \left[\frac{1}{1 + \left(\frac{r_2\theta_2}{d \sin\varphi} \right)^2} \right]} = U' C_d$$

30 Oct. 1973

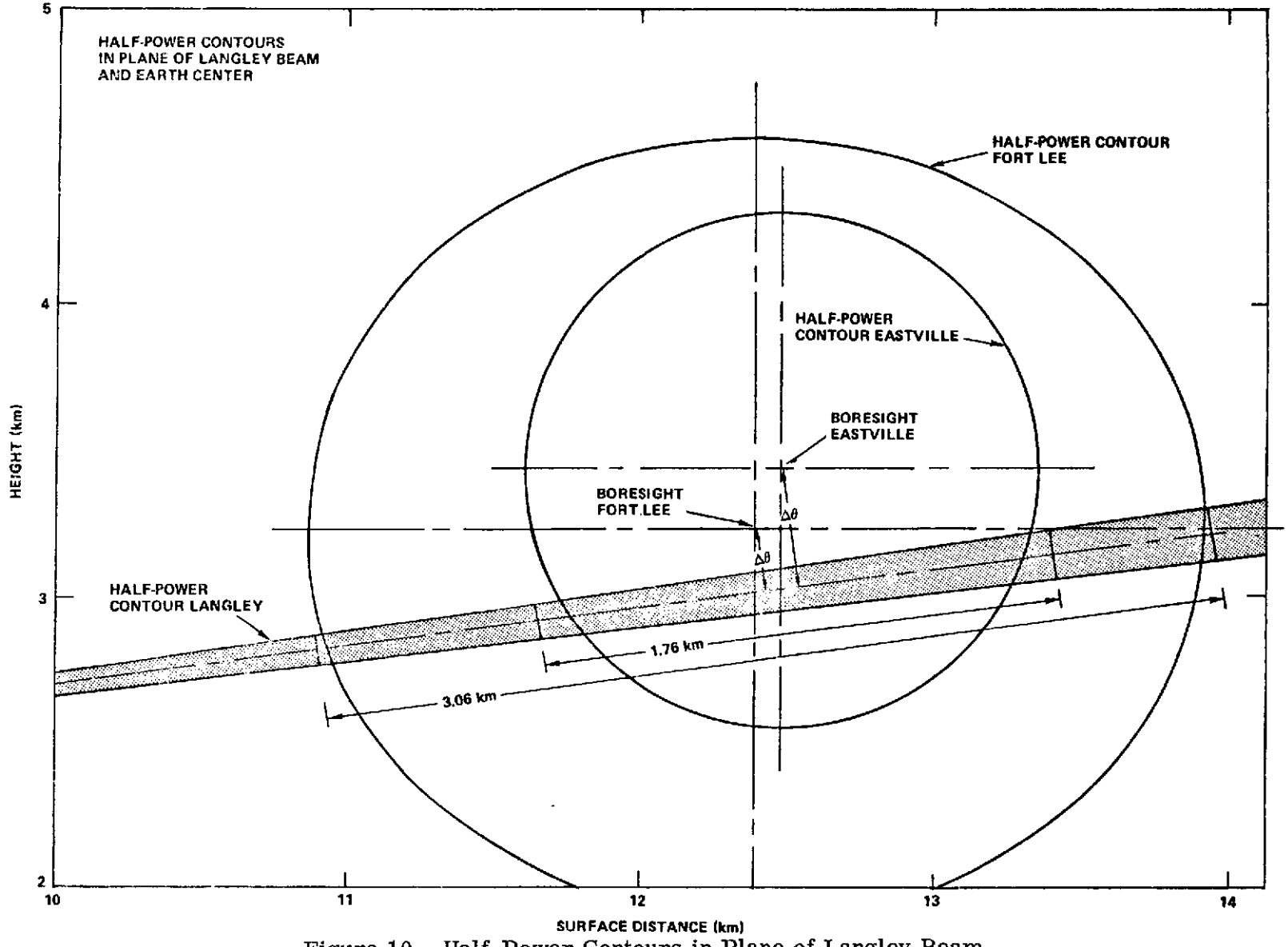

Figure 10. Half-Power Contours in Plane of Langley Beam and Earth Center

where

$$U' = \frac{r_1^2 r_2 \theta_2 g_2(\hat{r}_2) \theta_1^2 \pi\sqrt{\pi}}{\sin\varphi \, 8 \, \text{Ln} \, 2\sqrt{\text{Ln} \, 2}}$$

and the cell size correction factor (= 1 for d = ∞) is

$$C_d = \frac{e^{-4 (\text{Ln} 2)(\delta/d)^2 \left[\frac{1}{1 + (r_2\theta_2/d \sin\varphi)^2}\right]}}{\sqrt{1 + (r_2\theta_2/d \sin\varphi)^2}} \; e^{-4 (\text{Ln} 2)(\delta/d)^2 \left[\frac{1}{1 + (r_2\theta_2/d \sin\varphi)^2}\right]}$$

Then

$$\frac{\langle P_r \rangle}{P_t} = \frac{G_1 G_2 \ell_1 \ell_2 \lambda^2}{(4\pi)^3} \; \frac{\beta'(r_2) C_d U'}{r_1^2 r_2^2} \; 10^{-\frac{1}{10}\left[\int_0^{r_2} A \, ds + \int_{r_2}^{L} A \, ds\right]} \qquad (28)$$

The cell size corrections for the 10K and 20K paths are given in Figure 11 for values of d ranging from 1 to 10 km. The change in C_d with cell displacement is also shown. The point marked 10KE response first sidelobe gives the value that would be obtained if only the first sidelobe were filled. For the cell displacement that represents a cell centered on the first sidelobe, the part of

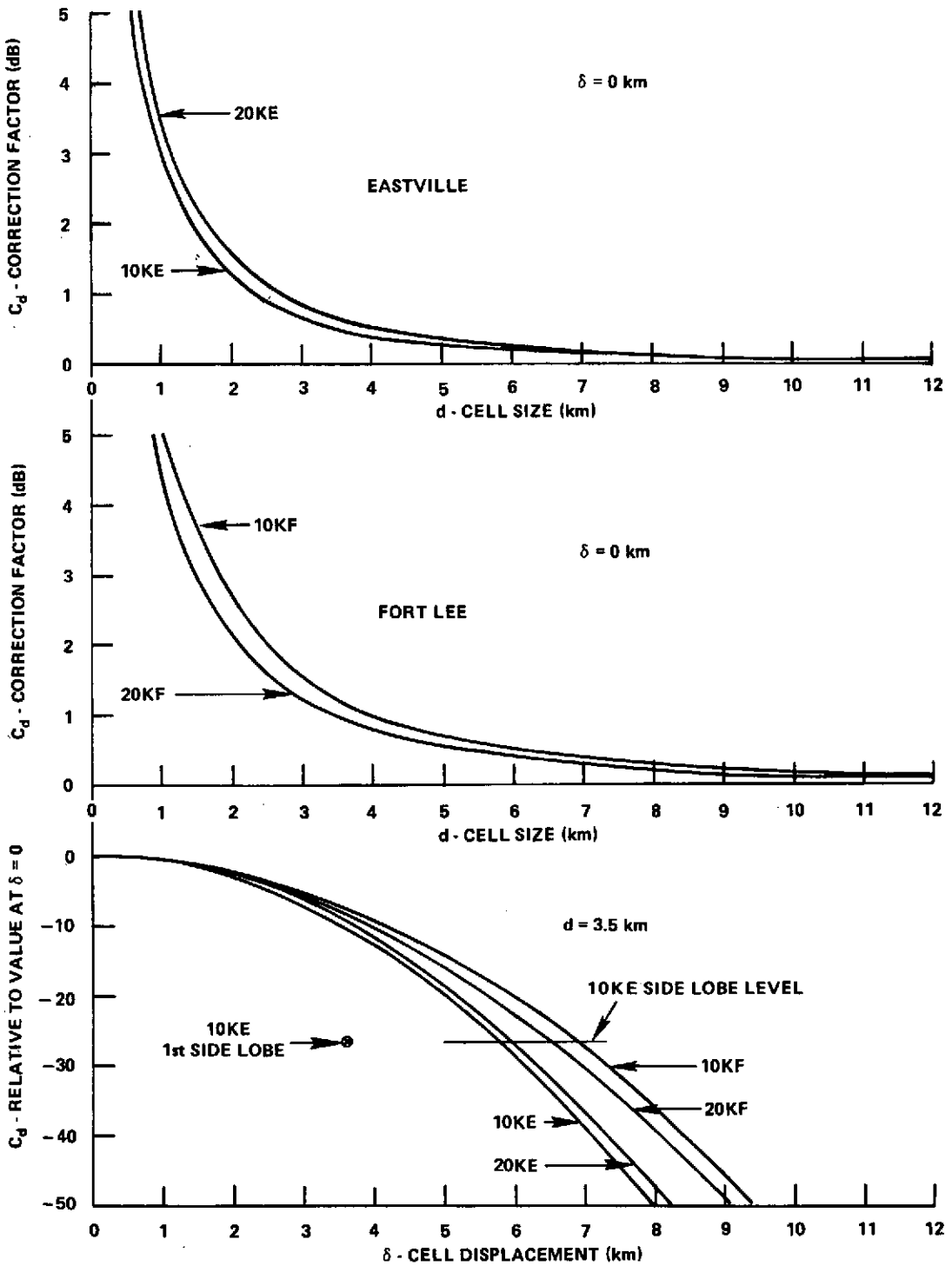

Figure 11. Correction for Cell Size

the cell that is still within the mainlobe contributes more to the scattering measurement.

2.1.3 Scattering Process Correction Factor (C_S)

The bistatic scattering cross section per unit volume is related to the scattering amplitude tensor by Equation (24), yielding

$$\beta(\underline{r}_2) = \frac{4\pi}{k^2} \int_a |\hat{u}_1(-\hat{\rho}) \cdot \underline{\underline{S}}(\epsilon, a, \hat{r}_2, \hat{\rho}) \cdot u_2(\hat{r}_2)|^2 \, \bar{\eta}(a, \underline{r}_2) \, da$$

For a plane wave incident on the scattering particle and for scattered fields computed in the far field of the scatterer, the scattering tensor may be represented by

$$\underline{\underline{S}}(\epsilon, a, \hat{r}_2, \hat{\rho}) = S_1 \hat{\xi}_1 \hat{\xi}_2 + S_2 \hat{\zeta}_1 \hat{\zeta}_2 + S_3 \hat{\zeta}_1 \hat{\xi}_2 + S_4 \hat{\xi}_1 \hat{\zeta}_2$$

where

$$\hat{\xi}_1 = \hat{\xi}_2 = \frac{\hat{r}_2 \times \hat{\rho}}{|\hat{r}_2 \times \hat{\rho}|} \quad \left(\underline{\ell} = \underline{\underline{L}} - \underline{r}_2 = -\underline{r}_1 \text{ and } \hat{r}_2 \cdot \hat{\rho} = \cos\varphi \right)$$

$$\hat{\zeta}_1 = \frac{\hat{r}_2 \times \hat{\xi}_1}{|\hat{r}_2 \times \xi_1|}$$

$$\hat{\zeta}_2 = \frac{\hat{\rho} \times \hat{\xi}_2}{|\hat{\rho} \times \hat{\xi}_2|}$$

The vectors $\underset{\sim}{r}_2$ and $\underset{\sim}{\rho}$ lie in the scattering plane; $\hat{\xi}_1$, $\hat{\xi}_2$ are unit vectors perpendicular to the scattering plane or the plane including the transmitter, the receiver, and the scatterer; $\hat{\zeta}_1$, $\hat{\zeta}_2$ are unit vectors in the scattering plane. The subscripts 1 and 2 refer to the transmitter and receiver, respectively. The amplitudes S_1 to S_4 are those considered by Van de Hulst (1957) for a variety of scatterers.

2.1.3.1 Rayleigh Approximation for Spheres—Raindrops are often assumed to have a spherical shape and for spherical dielectric scatterers, $S_3 = S_4 = 0$. The amplitudes S_1 and S_2 can be computed using Mie theory and, for frequencies below X-band and naturally occurring raindrop sizes, may be approximated by Rayleigh theory. In the Rayleigh limit

$$S_1 = ik^3a^3\kappa$$

$$S_2 = ik^3a^3\kappa \cos\varphi$$

where $\kappa = (\epsilon - 1)/(\epsilon - 2)$, ϵ is the complex dielectric constant of water and a is the drop radius.

Then

$$\underset{\approx}{S} = (\hat{\xi}_1\hat{\xi}_2 + \hat{\zeta}_1 \cos\varphi\, \hat{\zeta}_2)\, ik^3a^3\kappa$$

and

$$\beta(\underset{\sim}{r}_2) = 4\pi k^4 |\kappa|^2 |\hat{u}_1 \cdot (\hat{\xi}_1\hat{\xi}_2 + \hat{\zeta}_1 \cos\varphi\, \hat{\zeta}_2) \cdot \hat{u}_2|^2 \int_a a^6\, \overline{\eta}(a, \underset{\sim}{r}_2)\, da$$

$$= \frac{\pi^5}{\lambda^4} |\kappa|^2\, mZ\, (\underset{\sim}{r}_2) \qquad (29)$$

30 Oct. 1973

where

$$m \triangleq |\hat{u}_1 \cdot (\hat{\xi}_1 \hat{\xi}_2 + \hat{\zeta}_1 \cos \varphi \, \hat{\zeta}_2) \cdot \hat{u}_2|^2 \tag{30}$$

and the reflectivity is

$$Z(\underline{r}_2) \triangleq \int (2a)^6 \, \bar{\eta}(a, \underline{r}_2) \, da \tag{31}$$

2.1.3.2 Mie Scattering—Values of S_1 and S_2 computed by using Mie theory may be different from those given above, especially at frequencies above X-band. For linearly polarized waves with E-vector polarization either perpendicular, $\perp$, or parallel, $\parallel$, to the plane of polarization, Equation (29) for Rayleigh scattering simplifies to

$$\beta_\perp = \frac{\pi^5}{\lambda^4} |\kappa|^2 Z = \frac{4\pi}{k^2} S_1^* S_1$$

since

$$\hat{u}_1 \cdot \hat{\zeta}_1 = \hat{u}_2 \cdot \hat{\zeta}_2 = 0 \text{ and } m = 1$$

or

$$\beta_\parallel = \frac{\pi^5}{\lambda^4} |\kappa|^2 Z \cos^2 \varphi = \frac{4\pi}{k^2} S_2^* S_2$$

since

$$\hat{u}_1 \cdot \hat{\xi}_1 = \hat{u}_2 \cdot \hat{\xi}_2 = 0 \text{ and } m = \cos^2 \varphi$$

These equations may be used to relate S_1, S_2, and β for Mie scattering.

The scattering cross sections per unit volume, $\beta\perp$ and $\beta\,||$, were calculated using both Mie and Rayleigh theory and drop size distributions measured in Washington, D. C. as reported by Laws and Parsons (1943) and are given in Figure 12. The scales on the figure are β and φ as polar coordinates. The scattering angle φ varies from 0 to 180° and the right and left hand sides of the figure are identical. Scattering angles used for the 10K and 20K paths are shown. At these angles and for rain rates from 2 to 150 mm/hr, the ratio of $\beta\perp$ (Mie) to $\beta\perp$ (Rayleigh) varies from 0 to -0.6 dB for the Eastville paths and from +0.1 to +0.6 dB for the Ft. Lee paths. The antennas at the transmit and receive sites were vertically polarized, and for the scattering angles used, the m values were 0.95, 0.95, 0.93, 0.92 for the 10KE, 20KE, 10KF, and 20KF paths, respectively. Since m is near unity, $\beta\perp$ describes the dominant scattering process. The errors in using Z to approximate the scattering process are therefore small since the ratio of $\beta\perp$ (Mie)to $\beta\,||$ (Rayleigh) is less than ±0.6 dB for all paths.

2.1.3.3 Equivalent Reflectivity—In reporting measurements of scattering cross section per unit volume, it is convenient to express measured values approximately in terms of properties of the raindrop size distribution. The parameter Z is useful since, by Equation (31) it depends only on the drop radii, a, and drop number density, $\overline{\eta}$. Even when the Rayleigh approximation does not hold or when the dielectric constant is different as it is for ice particles, Equation (31) may be used to define an equivalent reflectivity

$$Z_e \triangleq \frac{\lambda^4 \beta'}{\pi^5 |\kappa|^2} \tag{32}$$

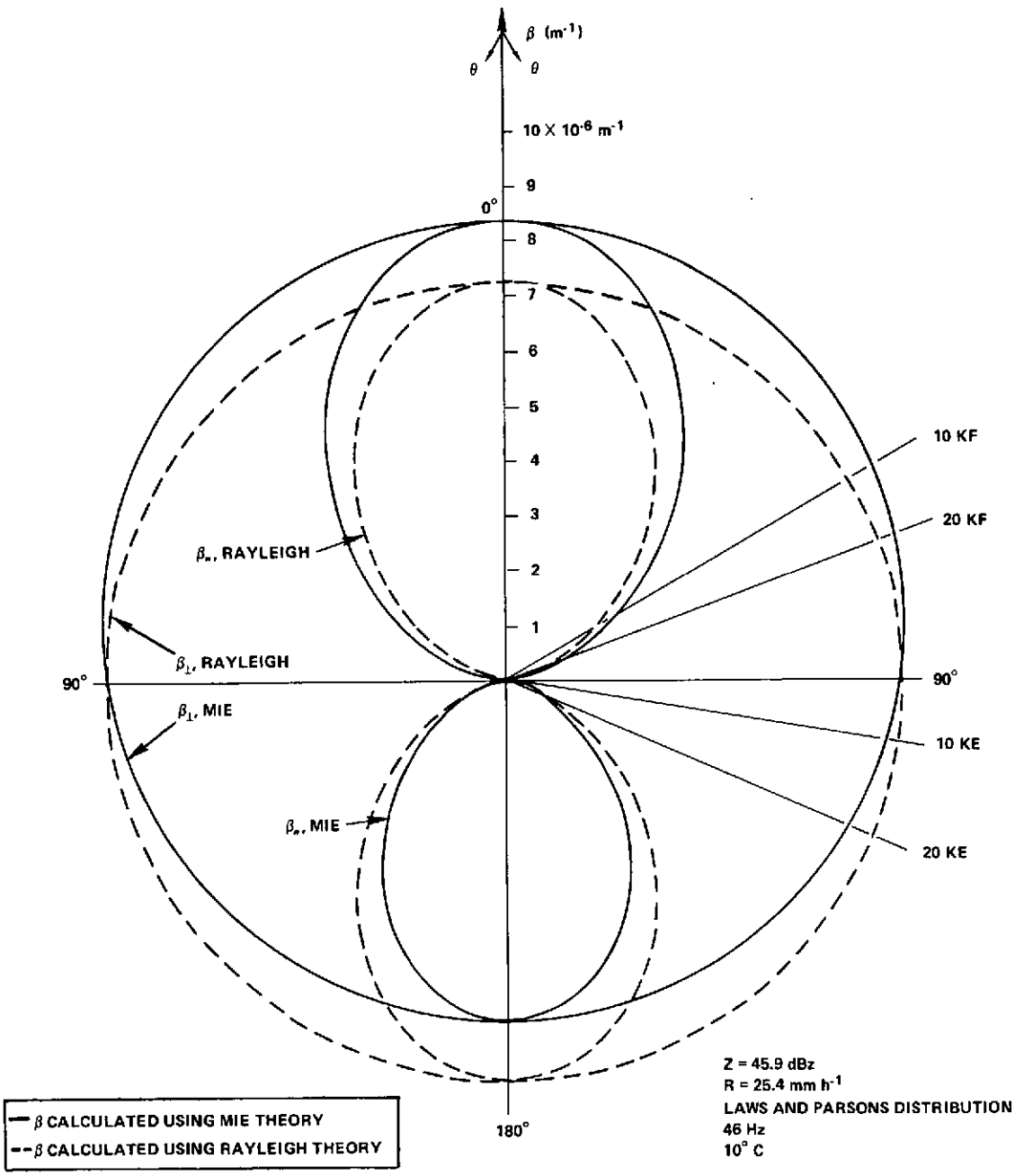

Figure 12. Bistatic Scattering Cross Section Per Unit Volume versus Scattering Angle

where $|\kappa|^2$ is for water at an assumed temperature and β' is the measured parameter given by Equation (28). This equation may then be reexpressed as

$$\frac{\langle P_r \rangle}{P_t} = \frac{C_R G_2(\hat{r}_2) Z_e D C_d}{r_2^2} \, 10^{-\frac{1}{10}\left[\int_0^{r_2} A \, ds + \int_{r_2}^{L} A \, ds\right]} \tag{33}$$

where

$$G_2(\hat{r}_2) = G_2 g_2(\hat{r}_2)$$

$$D = \frac{r_2 \theta_2}{\sin \varphi}$$

and

$$C_R = \frac{\pi^3 \sqrt{\pi}}{2^9 (\mathrm{Ln}\ 2) \sqrt{\mathrm{Ln}\ 2}} \frac{m\theta_1^2 G_1 \ell_1 \ell_2 |\kappa|^2}{\lambda^2} = \frac{G_1 \ell_1 \ell_2 \pi^2 m |\kappa|^2 U}{64 \lambda^2 r_1^2 D}$$

After expressing r_2 and D in kilometers, Z_e in mm^6/m^3, λ in centimeters, and evaluating, the numerical constant results in

$$C_R = 1.86 \times 10^{-18} \frac{m\theta_1^2 G_1 \ell_1 \ell_2 |\kappa|^2}{\lambda^2}$$

30 Oct. 1973

Equation (33) with A(s) = 0 and C_d = 1 is identical to Equation (1).

2.1.3.4 Rayleigh Approximation for Spheroids - Equation (29) was derived for the special case of spherical scatterers. Raindrops are, however, not spherical and additional correction factors are required. In the computations above, the Rayleigh approximation provided an estimate of the true (Mie) cross section value within ± 0.6 dB. Using Rayleigh theory and the slightly more general approximation that raindrops are oblate spheroids, the scattering amplitude tensor may be computed:

$$\underset{\approx}{S} = -ik^3(\hat{\rho} \times \hat{\rho} \times \hat{e}_1\alpha_1\hat{e}_1 + \hat{\rho} \times \hat{\rho} \times \hat{e}_2\alpha_2\hat{e}_2 + \hat{\rho} \times \hat{\rho} \times \hat{e}_3\alpha_3\hat{e}_3) \tag{34}$$

where

α_1, α_2, and α_3 are the nonzero diagonal elements of the polarizability tensor expressed in the principal-axis coordinate system

$\hat{e}_1$, $\hat{e}_2$, $\hat{e}_3$ are unit vectors along the principal axis

$\hat{\rho} = -\hat{r}_1$ are as defined above

For the oblate spheroid with $\hat{e}_1$ along the symmetry axis (Van de Hulst, 1957)

$$\alpha_i = \frac{a^3}{3}\left[\frac{1}{L_i + 1/(\epsilon - 1)}\right] = a^3\,\frac{\kappa}{3}\left(\frac{\epsilon + 2}{(\epsilon - 1)L_i + 1}\right)$$

where

$$L_1 = \left(\frac{1 + f^2}{f^2}\right)\left(1 - \frac{1}{f}\arctan f\right)$$

$$L_2 = L_3 = \frac{1 - L_1}{2}$$

$$f^2 = R^2 - 1$$

and R = ratio of major to minor axis of the spheroid.

Experimental observations of backscatter from rain by McCormick and Hendry (1972) have shown that from 60 to 90 percent of the raindrops have the same orientation angle. Radar measurements by McCormick and Hendry (1970) have also shown that the orientation angle is within a few degrees of vertical. Assuming that all the raindrops are vertically oriented, $\hat{e}_1 = \hat{z}$. For ease of computation, $\hat{e}_2$ is set perpendicular to $\hat{\rho}$ and, since $\hat{u}_1$ is perpendicular to $\hat{\rho}$

$$\hat{u}_1 \cdot \underset{\approx}{S} \cdot \hat{u}_2 = -ik^3 \int_L \left[(\hat{u}_1 \cdot \hat{e}_1)(\hat{u}_2 \cdot \hat{e}_1)\alpha_1 + (\hat{u}_1 \cdot \hat{e}_3)(\hat{u}_2 \cdot \hat{e}_3)\alpha_3\right] \qquad (35)$$

The factors in Equation (35) were computed for the 10K and 20K paths and are listed in Table 4. Using the tabulated values and noting that for the values of R that may occur in natural rain, $1 \leq R \leq 2$ and α_1 and α_3 have the same order of magnitude; hence the term in α_3 may be neglected

$$\beta \simeq 4\pi k^4 \left[(\hat{u}_1 \cdot \hat{z})(\hat{u}_2 \cdot \hat{z})\right]^2 \int \alpha_1^* \alpha_1 \overline{\eta}(a)\, da = \frac{\pi^5}{\lambda^4} m|\kappa|^2 Z_v = \frac{\pi^5}{\lambda^4} m|\kappa|^2 Z C_s \qquad (36)$$

Table 4
Coefficients of α_1 and α_3 in Scattering Amplitude Tensor of Equation (35)

Path	$\hat{u}_1 \cdot \hat{e}_1$	$\hat{u}_2 \cdot \hat{e}_1$	$(\hat{u}_1 \cdot \hat{e}_1)(\hat{u}_2 \cdot \hat{e}_1)$	$\hat{u}_1 \cdot \hat{e}_3$	$\hat{u}_2 \cdot \hat{e}_3$	$(\hat{u}_1 \cdot \hat{e}_3)(\hat{u}_2 \cdot \hat{e}_3)$	m
10KE	0.97	1.00	0.97	0.235	-0.044	-0.002	0.94
20KE	0.97	0.99	0.96	0.237	-0.035	-0.010	0.92
10KF	0.97	1.00	0.97	0.235	0.022	0.005	0.94
20KF	0.97	1.00	0.97	0.237	0.034	0.008	0.94

where

$$Z_v \simeq 2^6 \int \frac{\alpha_1^* \alpha_1 \eta(a)\, da}{|\kappa|^2}$$

and

$$m = [(\hat{u}_1 \cdot \hat{z})\,(\hat{u}_2 \cdot \hat{z})]^2$$

where Z_v is an effective reflectivity for the vertically oriented spheroidal raindrops.

Using Equation (36), the Laws and Parsons drop size distribution, and the variation of R with drop size measured by Pruppacher and Pitter (1971), the Z_V values for spheroidal drops for several rain rates were calculated and are listed in Table 5. From the tabular data it is seen that the measured Z_e for naturally occurring spheroidal drops may be 0.8 to 1.3 dB below the value predicted for spherical drops with the same drop size (volume) distribution, depending upon rain rate, for rates above 2.5 mm/hr.

2.2 REFLECTIVITY ESTIMATION USING RAIN GAUGE DATA (Z/R RELATIONSHIP)

The reflectivity is related to the drop size distribution through Equation (31) and to drop size and shape distributions through Equation (36). The rain rate is also related to the drop size distribution:

$$R = \int_a v_v(a) \frac{4\pi}{3} a^3 \bar{\eta}(a)\, da \qquad (37)$$

where

R = rain rate

v_v = fall velocity for drop of size a

Both Z and R are parametrically related to $\bar{\eta}$ (a). Observations of $\bar{\eta}$ (a) made at the surface (Mueller and Sims, 1967a) show that $\bar{\eta}$ (a) is a random variable that changes from one minute to the next and from one cubic meter of space to the next. Considered as functions of $\bar{\eta}$ (a), both Z and R are random variables, and a unique relationship between Z and R is not possible because they have different dependences on a. A statistical best estimate of Z, given R, is required for comparison of the rain gauge measurements with the bistatic radar data.

Several approaches have been tried to relate Z and R. Noting that both Z and R as given in Equations (31) and (37) are linear in $\bar{\eta}$, the expected or average R and Z may be related as

$$\langle \bar{R} \rangle = \int v_v(a) \frac{4\pi}{3} a^3 \langle \bar{\eta}(a) \rangle \, da \tag{38}$$

and

$$\langle \bar{Z} \rangle = \int (2a)^6 \langle \bar{\eta}(a) \rangle \, da \tag{39}$$

Laws and Parsons (1943) reported $\langle \bar{\eta}(a) \rangle$ stratified by rain rate for three years of data taken in Washington, D. C. The data were stratified by averaging all the distributions for different rain rate class intervals. Rain rates were determined by using rain gauges. Table 5 reports the $\langle \bar{Z} \rangle$ as Z and $\langle \bar{R} \rangle$ as rate for each of the rain rate class intervals. Each of the $\langle \bar{Z} \rangle$, $\langle \bar{R} \rangle$ values may be used to provide a power law relationship for the estimation of Z, given $\bar{R}$. Using linear least-squares fit to log $\langle \bar{Z} \rangle$ versus log $\langle \bar{R} \rangle$, the estimation equation

$$Z = 398 \, R^{1.41} \simeq 400 \, R^{1.4} \tag{40}$$

was obtained.

30 Oct. 1973

Table 5
Reflectivity Values for Spheres and Spheroids

R (mm/hr)	Z_v (dBz)	Z (dBz)	C_s Z_v / Z (dB)
0.25	17.1	17.4	-0.25
1.27	27.0	27.5	-0.57
2.5	31.2	31.9	-0.75
12.7	40.5	41.6	-1.14
25	44.6	45.9	-1.32
51	48.6	50.1	-1.48
102	52.6	54.2	-1.65
152	54.9	56.7	-1.78

Values were computed using Laws and Parsons (1943) drop size distribution, Pruppacher and Pitter (1971) ratio of major to minor axis versus drop size, and 10°C drop temperature.

Marshall and Palmer (1948) made drop size distribution measurements during one summer in Ottawa and reported their results both as exponential functions that provide a reasonable fit to $\langle\bar{\eta}(a)\rangle$ stratified by rain rate and as a Z/R relationship fit to Z and R computed for each $\bar{\eta}(a)$. Using exponential functions

$$Z = 296\ R^{1.47} \tag{41}$$

and using individual Z and R values

$$Z = 220\ R^{1.60} \tag{42}$$

The latter relationship, approximated by

$$Z = 200\ R^{1.6} \tag{43}$$

is the "standard relationship" generally used by radar meteorologists. Equation (43) was used in Section R1:/2. The difference in the Z/R relationships of Equations (41) and (42) is due to the use of $\langle\eta\rangle$ for Equation (41) and of individual $\bar{\eta}$ measurements for Equation (42). The difference between the Laws and Parsons relationship, Equation (40), and the three relationships based upon the Ottawa data, Equations (41) to (43), may be due to measurement technique, methods of processing and curve fitting, differences in synoptic rain types sampled, differences in climate, or natural variability of rain for the same climate and synoptic types.

Mueller and Sims have reported a series of measurements made with a drop camera in North Carolina (1967a) and in New Jersey (1967b). Their North Carolina site was in the mountains approximately 600 km west of the Langley receiver site reported here. Their New Jersey location was on the coast approximately 300 km north of the receiver. Z/R relationships were determined for at least one year of data at each of the sites, using log Z and log R values for each drop size distribution sample. The samples were made during an 11-s period once each minute and represent all the drops found in a cubic meter. The least squares fit straight line relationship between log Z and log R was used to calculate the Z/R relationship. For 4741 drop size distributions measured in North Carolina

$$Z = 263\ R^{1.30} \tag{44}$$

with a computed 67 percent rms deviation of Z values about the regression curve. For comparison, the North Carolina data had 101 percent rms deviation about the "standard" 200 $R^{1.6}$ curve, indicating that Equation (44) provided a slightly better fit to the data. For 3135 drop size distributions measured in New Jersey

$$Z = 282\ R^{1.29} \tag{45}$$

with a computed 63 percent rms deviation of Z values about the regression curve. For comparison, the New Jersey data had a 90 percent rms deviation about the Laws and Parsons 400 $R^{1.40}$ curve.

Figure 13 displays the Z and R values used to generate Equation (45) together with the Laws and Parsons curve, the standard 200 $R^{1.6}$ relationship, and the best fit approximation to both Equations (44) and (45):

$$Z = 270\ R^{1.3} \tag{46}$$

From this figure, it is seen that a wide variation in Z for a fixed value of R is possible, the range being over 20 dB (peak to peak) at 7 mm/hr. The empirical density function for the difference between the log Z values and the best estimate log Z values computed from Equation (45) is given in Figure 14. The density function for the deviations of log Z from estimates based upon the Laws and Parsons model of Equation (40) is given in Figure 15. The density functions show that the regression line, Equation (45) is the best estimate of log Z given log R, and that the distribution about the 400 $R^{1.4}$ line is highly skewed. The 1 to 99 percent confidence limits for the rms deviations computed using a chi-square test are ±2 percent for the regression line and ±3 percent for the 400 $R^{1.4}$ line, showing that the regression line provides a significant reduction in the estimation error when data for all measured rain rates are used. However, if $Z = 270\ R^{1.4}$ were used, the density function in Figure 15 would be centered and the rms deviation about the estimate would be 66 percent, which is not significantly different from the rms deviation about the regression line.

The data on Figure 13 show for rain rates above 20 mm/hr that the 400 $R^{1.4}$ and least squares lines appear to fit the data equally well. The average log Z and log R values computed for data stratified in rain rate class intervals of width 0.2 in log R are also plotted in the figure. These data points are closer to the least squares line than the 400 $R^{1.4}$ line. For rain rates below

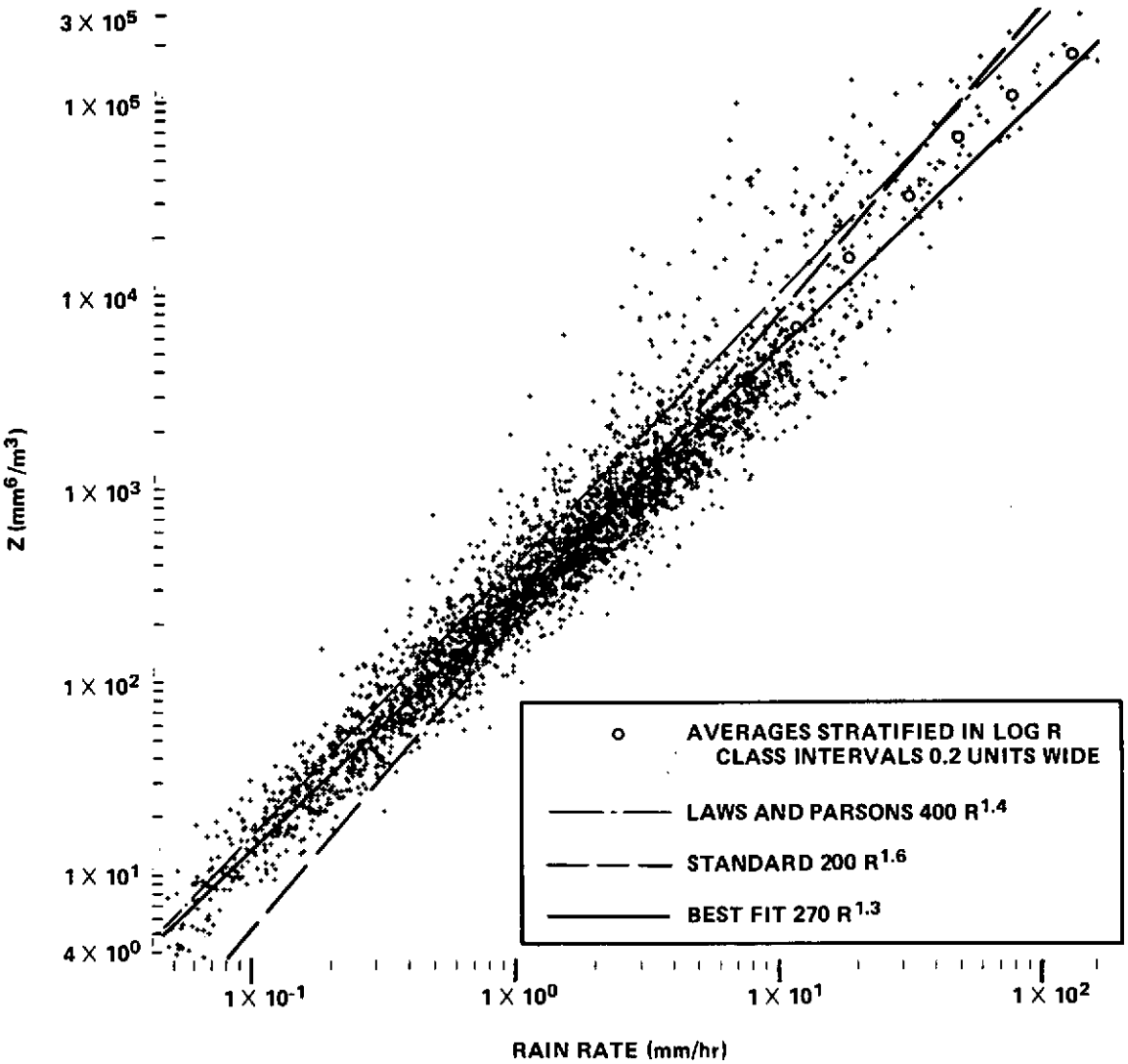

Figure 13. Drop Size Data from Island Beach, N. J.

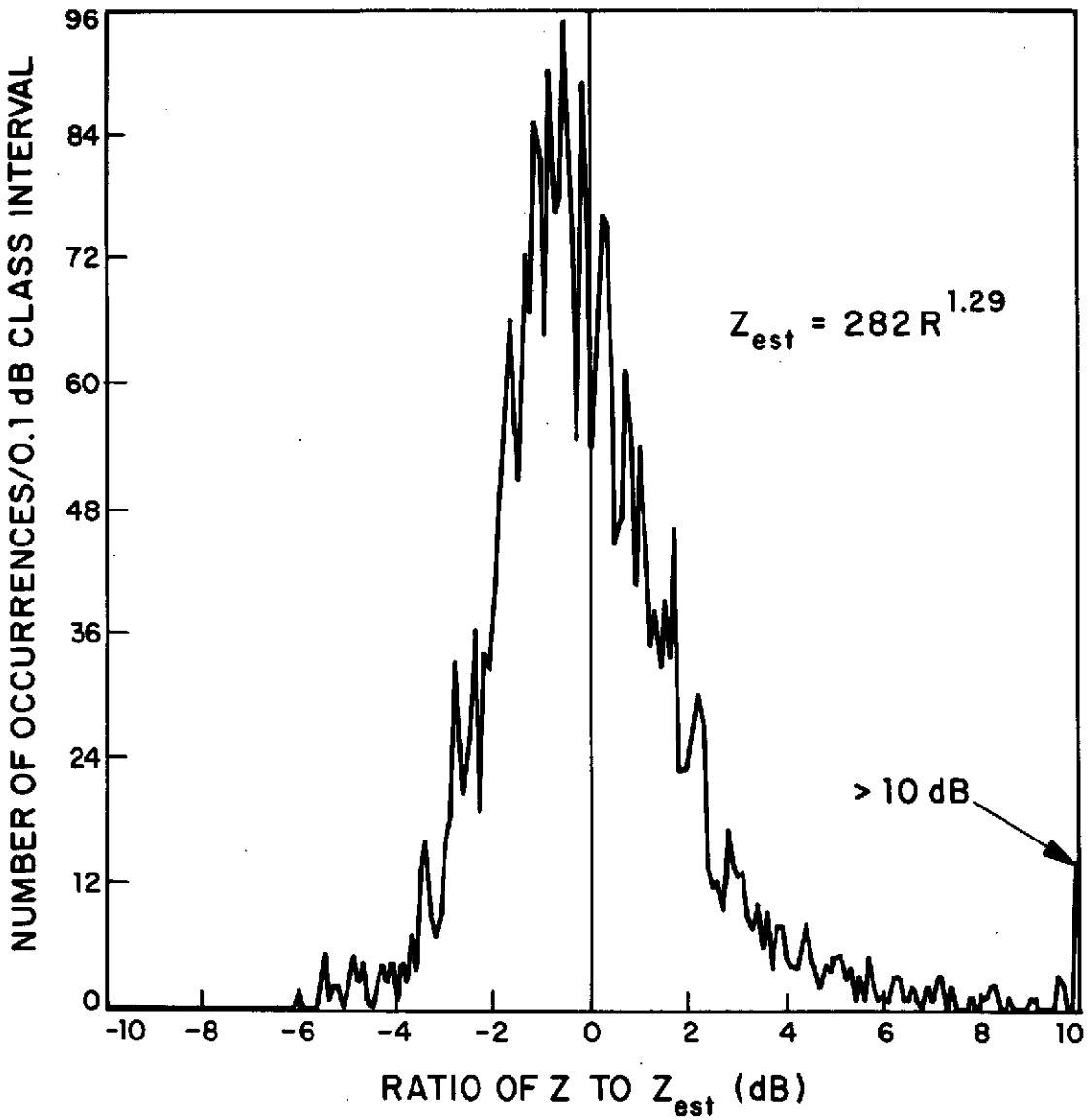

Figure 14. Empirical Density Function for Deviations from Regression Line

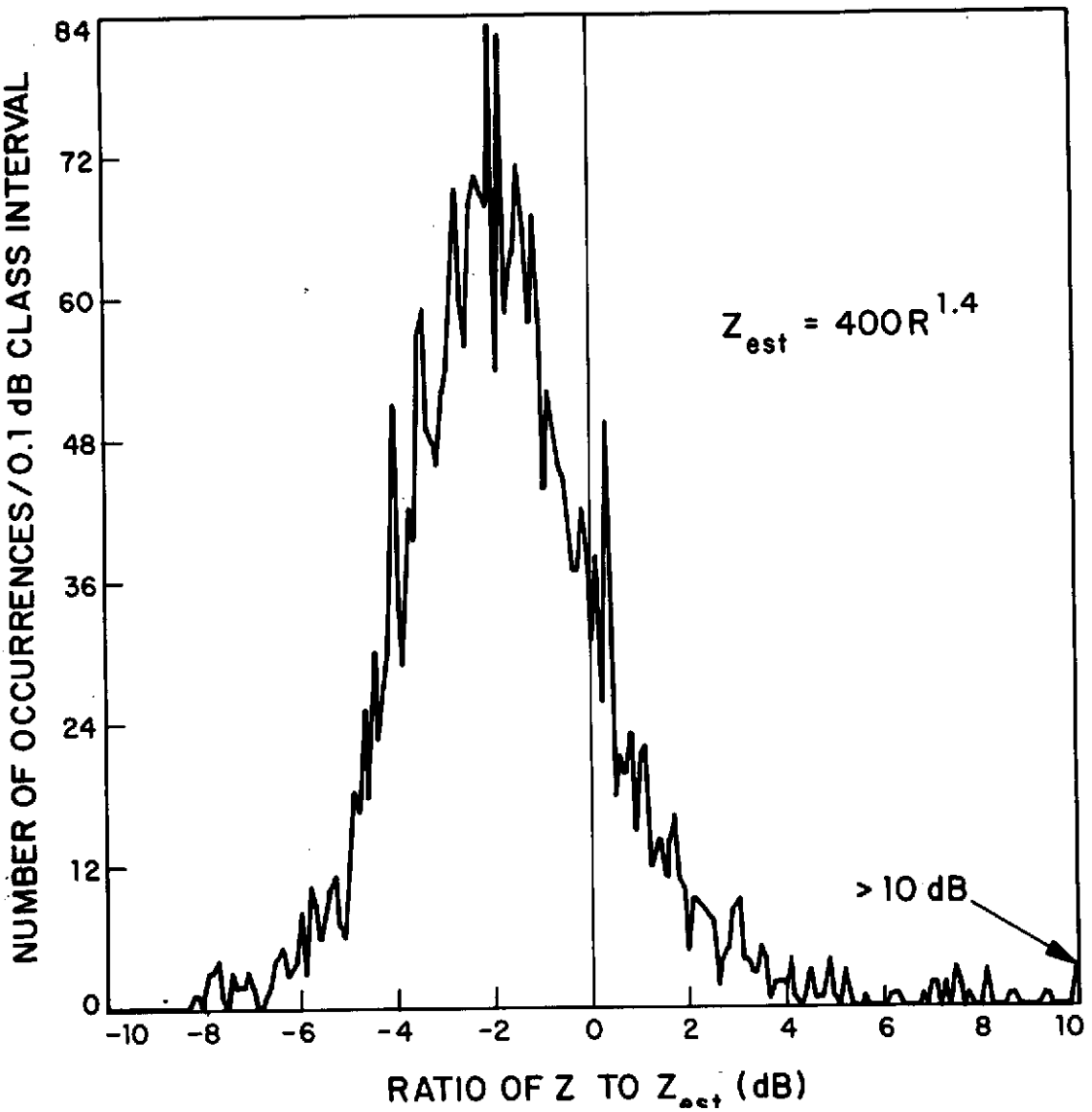

Figure 15. Empirical Density Function for Deviation from Laws and Parsons Model

20 mm/hr, the least squares line coincides with the log R class average values. The best estimate curve for use above 1 mm/hr therefore is the least squares line given by Equation (46). Above 20 mm/hr, this relationship would underestimate Z by approximately 1 dB. The $Z = 270\ R^{1.4}$ relationship would provide a better fit to the log R class average values above 20 mm/hr. For this relationship, half the averages lie above the curve and half below.

The least squares straight line for the North Carolina data of Equation (44) differs from the best estimate for New Jersey of Equation (45) by less than 0.3 dBz over the entire range of R and the rate stratified average $\langle \log Z \rangle$, $\langle \log R \rangle$ values for both North Carolina and New Jersey are nearly identical for rates less than 100 mm/hr. Since both the North Carolina and New Jersey data provide nearly identical Z/R relationships and are from areas within 600 km of the experiment area, the best estimate Z/R relationship for either location may be used. The relationship adopted for the analysis of the rain rate measurements is Equation (46). Using this relationship, for Z values above 42 dBz* corresponding to rain rates above 20 mm/hr, the Z estimate given the rain rate may be 1 dB low. The difference between Equation (46) and $270\ R^{1.4}$ is 1 dB at 20 mm/hr and 2 dB at 150 mm/hr. However, the assumption that raindrops are spherical (see Section 2.1.3.4) causes the Z value to be overestimated by 1 dB for rates above 20 mm/hr. The effect of drop shape therefore compensates for the underestimation caused by departure from the relationship of Equation (47). To account for these tendencies, the accuracy of the Z/R relationship is assumed to be ±1.0 dB.

The rms deviation about the estimation relationship, Equation (46), is 67 percent. The precision may be taken to be given by the maximum deviation from the relationship given by Equation (46), which is ±14.7 dB. The bistatic radar, however, samples a scattering volume larger than $3 \times 10^7\ m^3$. If each cubic meter within the scattering volume were independently related in terms of the random variation in $\bar{\eta}$ the precision estimate would be $\pm 3 \times 10^{-3}$ dB. Correlation distances for atmospheric turbulence are often estimated to be the order of 100 m and, assuming that the random variations in $\bar{\eta}$ are uncorrelated over distances of this order, approximately 30 independent samples of $\bar{\eta}$ will occur at any one instant of time. During a 1-min sample period each of the samples will change approximately four times, yielding 120 independent samples and a precision of ±1.3 dB. The latter estimate is adopted for the precision of the Z/R relationship given in Equation (46).

*Z values are given in dB relative to 1 mm^6/m^3.

3 CALIBRATION VERIFICATION AND MEASUREMENT ACCURACY

The bistatic radar system and rain gauge system were periodically calibrated during the high accuracy (Phase II) measurement period. The transmitter system calibration was verified by comparing the received signal levels with each other for each of the 10K paths. The rain gauge calibrations were verified by comparison with measurements made using other gauges.

3.1 BISTATIC RADAR SYSTEM

3.1.1 Wideband Radiated Power Measurements

The wideband radiated power measurements made periodically during Phase II of the experiment are described in Section R1:/3.5.3.* These measurements were used to test both the stability of transmitted power and of pointing angle. The transmitted power measurements were made by probing the field with a small antenna at distances between 100 and 200 ft, depending upon transmit antenna elevation angle. The pointing angle was measured by probing the field at the approximate position of the half-power points in the vertical and horizontal planes that included the expected position of the electrical boresight at the same distance as the transmitted power measurements. The actual pointing angle was computed by fitting the data to the known antenna pattern.

The estimated error in determining transmitted power was 0.5 dB and, because of possible errors in the relative positioning of the probe and the relative power measurements, the angle measurement repeatability is estimated to be $\pm 0.2^\circ$. The position of the actual probe reference location relative to the correct reference location was measured at the end of the experiment for the Eastville antennas. The probe position errors were found to be as large as 0.4°. The measurements were corrected for this error. The reference position was not measured at Fort Lee and the angular accuracy of the location of the Fort Lee probe position was assumed to be $\pm 0.4^\circ$.

The transmit antenna pointing angles are given in Figures 16(a) to 16(d). The error bars on the angle measurements are the sum of the repeatability and accuracy estimates given above. Also plotted are the antenna alignment and calibration measurements made throughout the year and the accuracy estimates

*Citations to Reference 1 materials are prefixed R1:/ throughout this report.

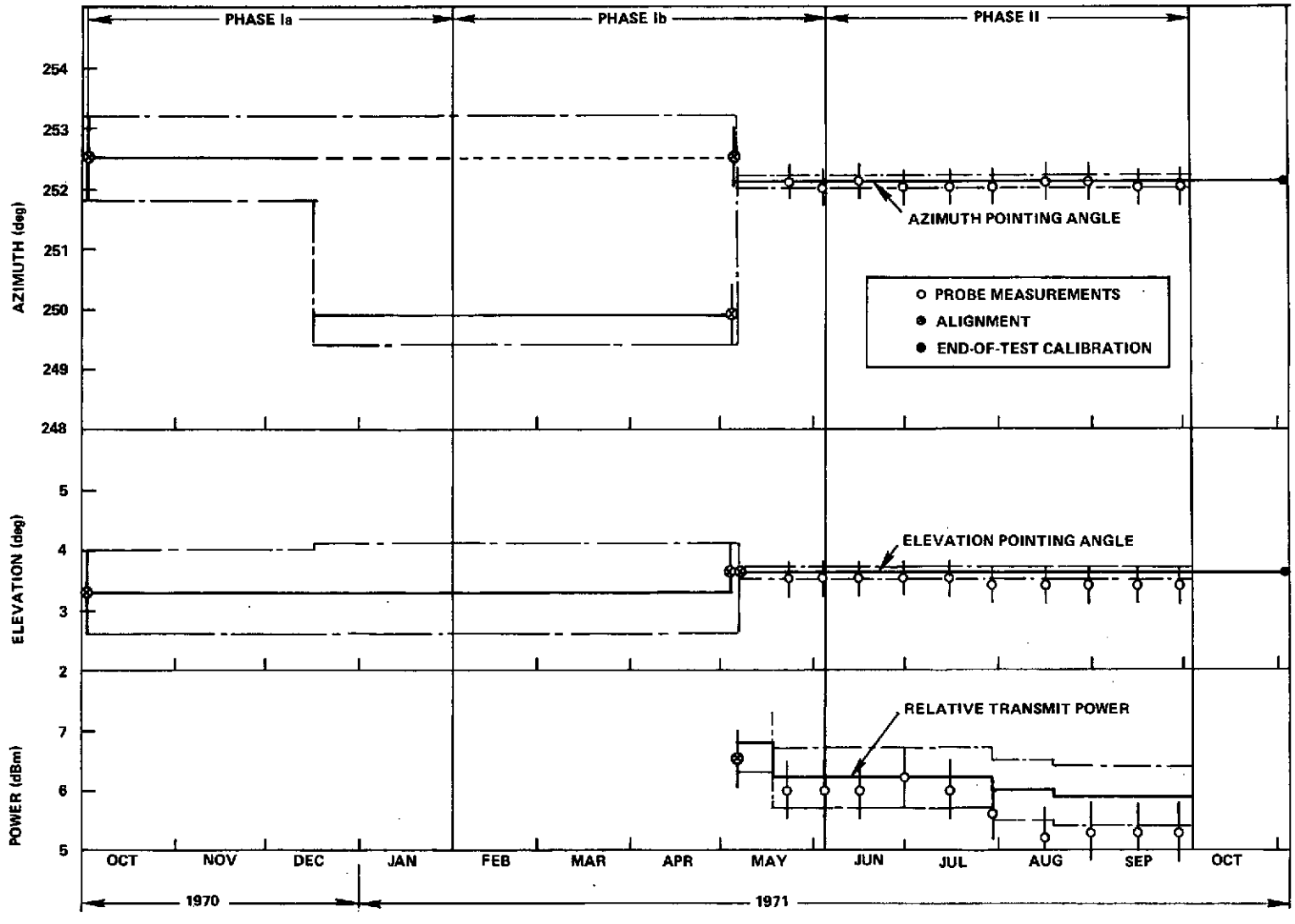

Figure 16a. Eastville 10K Pointing and Radiated Power Measurement Summary

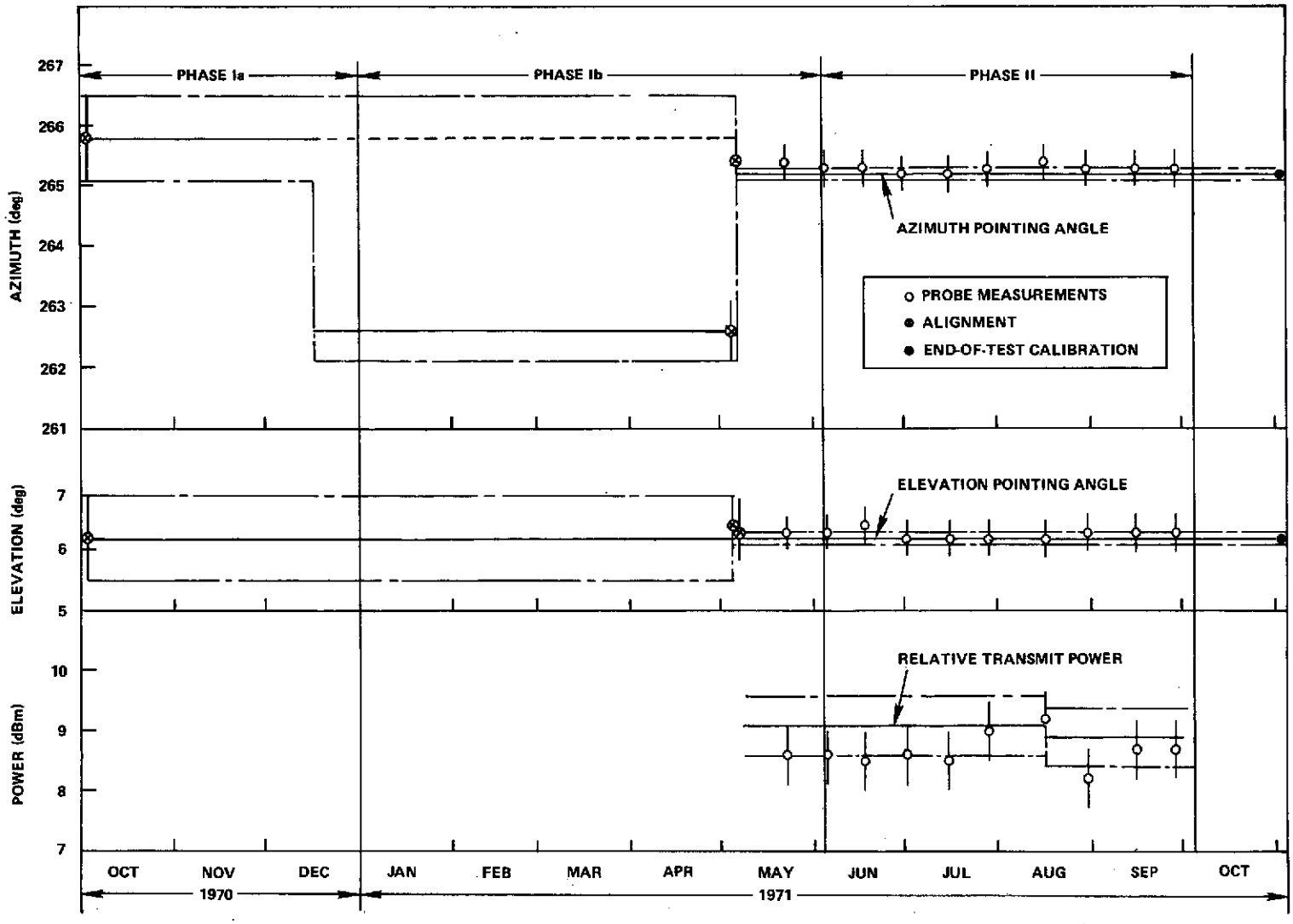

Figure 16b. Eastville 20K Pointing and Radiated Power Measurement Summary

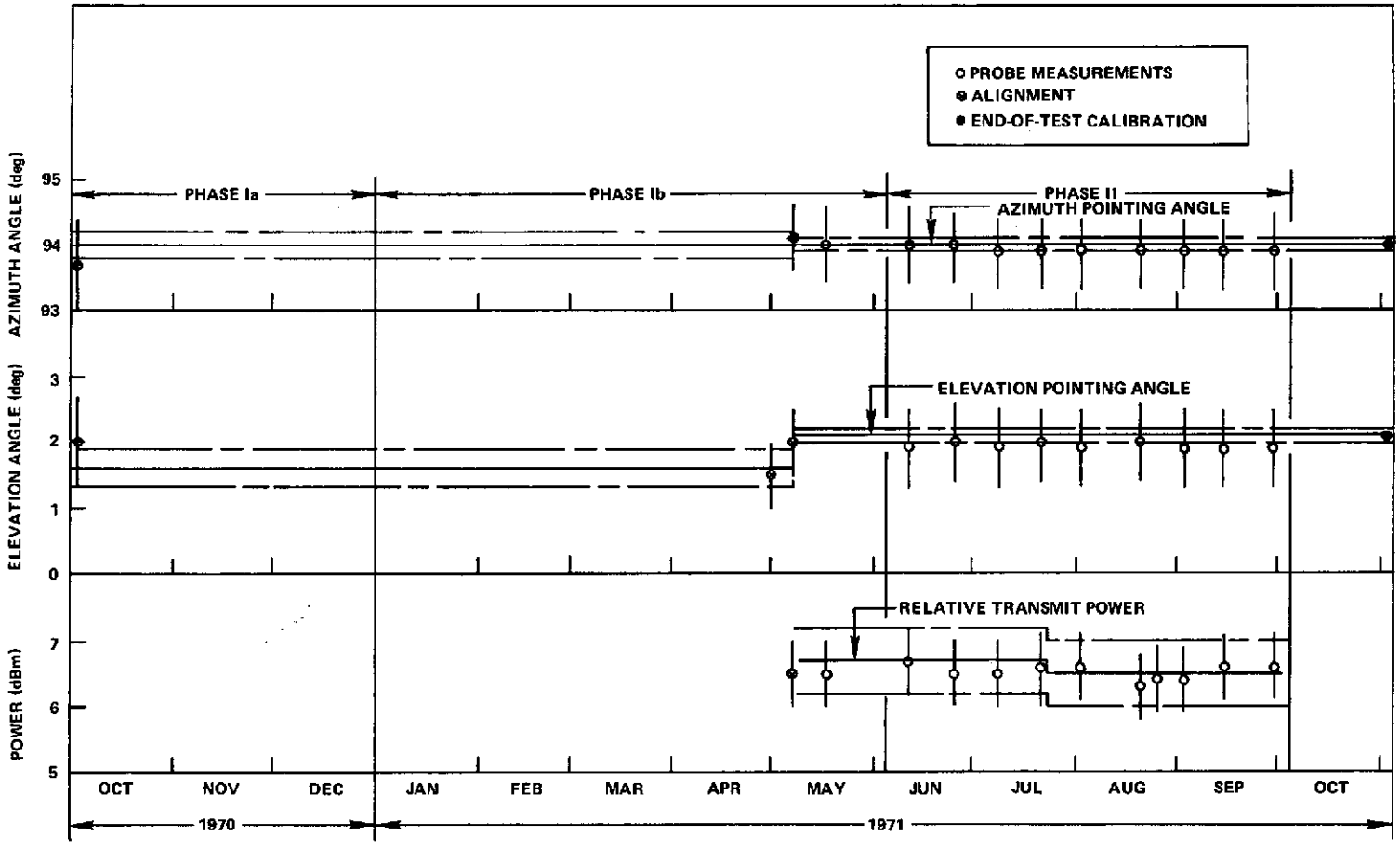

Figure 16c. Fort Lee 10K Pointing and Radiated Power Measurement Summary

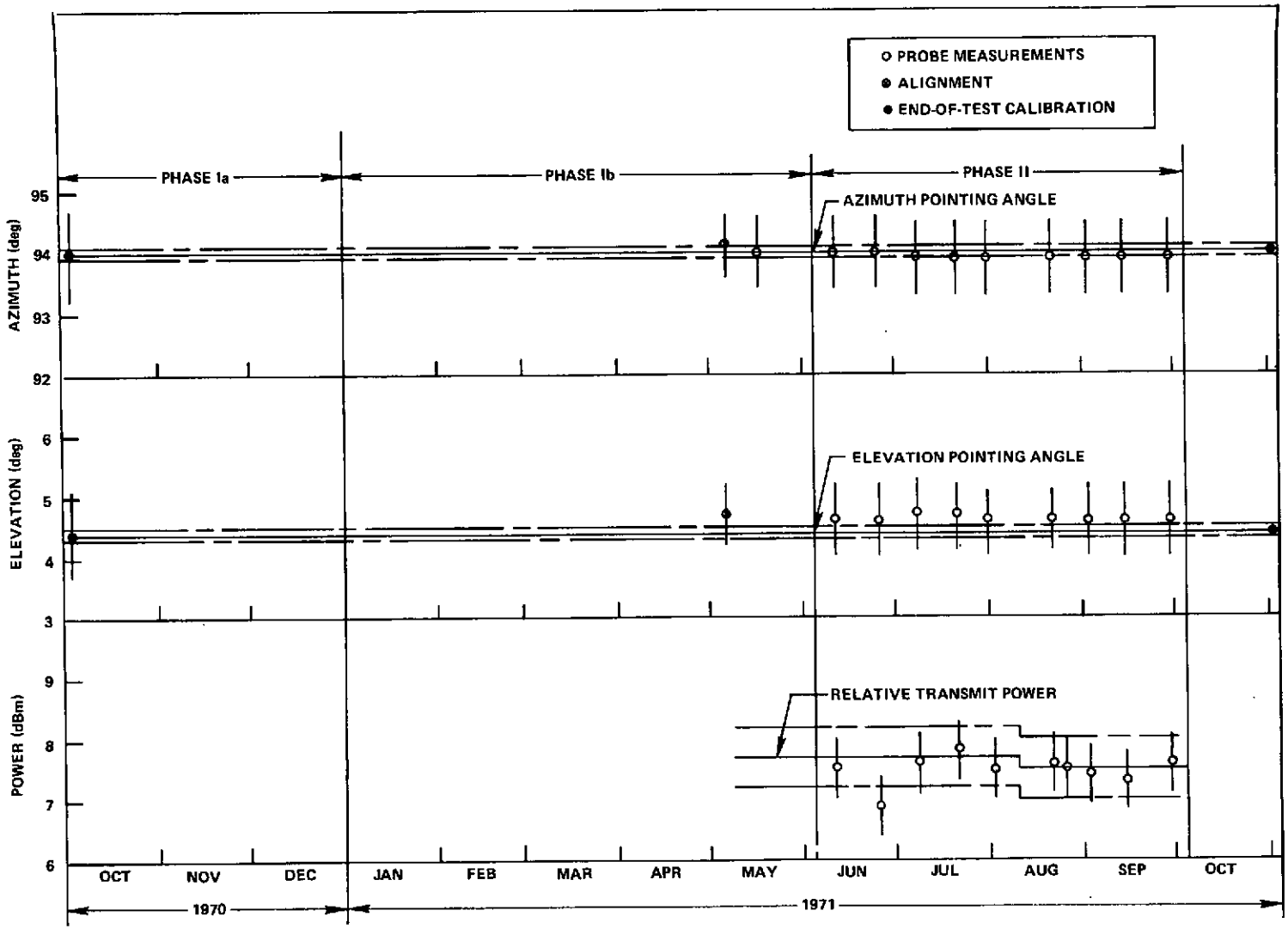

Figure 16d. Fort Lee 20K Pointing and Radiated Power Measurement Summary

for each of the measurements as estimated in Section R1:/3.1.4. The solid lines show the pointing angles used to compute the relationship between $\langle P_r \rangle$ and Z_e and to estimate possible errors in the relationship, as given in Table 6. The positioning accuracy values used are also shown. The measured pointing angles agreed with the estimated values for the entire Phase II period and show that no antenna motion occurred in Phase II. The position change data for Phase I for Eastville were estimated from comparisons between Z_e values for the 10KE and 10KF paths (see Section 3.1.2). In plotting the estimated position values, it was assumed that the antenna changed position and stayed at the new position. No data are available to either verify or refute this assumption. The error bands are widened to indicate that the antenna position was not accurately known. Interpretation of data from Eastville for the time period December 16, 1970, to May 7, 1971, must be done with caution, since the antenna may have moved even more and returned to the position measured in early May.

The transmitted power estimates and uncertainty bounds were computed from the line-of-sight transmission equation for the transmit antenna, probe antenna, antenna spacing, and receiver parameters that applied for each path, as discussed in Section R1:/3.5.3. The transmitted power estimates were corrected in accordance with Table 7 (compiled from Reference 1). With the exception of the low power reading for the 20KF transmitter on June 25, 1971, Fort Lee data all agree with the estimated values within the measurement accuracy of the probe system. The 10KE data agreed with the estimated value prior to July 26, 1971, and 20KE data agreed with the estimated value after July 26, 1971, with the exception of the single reading on August 30, 1971. Since the 10KE and 20KE transmitters were interchanged on July 26, the data show that F4 transmitter was about 0.5 dB low. A review of the daily calibration checks showed that the loop power monitor did not indicate low transmit power, but the power meter used outside the loop at the output of the 20-dB pad connected to the calibration switch (Figure R1:/3.1) showed a 0.5-dB change when the transmitters were interchanged. The loop power meter circuit was used to drive a relatively low input impedance dc amplifier ($\sim 2\ K\Omega$) and metering circuit errors were possible. The outside-the-loop meter was therefore used as the standard. A further review of the weekly calibration data showed that the F5 transmitter power (10KE) was 2 dB low on January 7, 1971, and 1 dB low between January 14 and February 12. Additional transmitter power correction factors were used for events that occurred during periods of low output power. With the transmitter power corrections (1 dB for Eastville F4 during Phase II) the wideband radiated power measurements agreed with the expected values.

Table 6
Antenna Pointing and Gain Values

	Initial						Final						
Path	Az (deg)	El (deg)	ΔEl[1] (deg)	ΔAz[1] (deg)	$\Delta\theta$[1] (deg)	$\Delta G_2(\hat{r}_2)$ (dB)	Az (deg)	El (deg)	ΔEl (deg)	ΔAz (deg)	$\Delta\theta$ (deg)	$\Delta G_2(\hat{r}_2)$	ΔG_2 for Beam Peak
10KE[2]	252.5	3.3	0.0	0.0	0.0	0.0	252.1	3.6	-0.4	+0.1	0.4	-0.6	0.0
20KE[2]	265.8	6.2	+0.1	0.0	0.1	-0.1	265.2	6.2	-0.1	+0.0	0.1	-0.1	-0.1
10KF	94.0	1.6	+0.2	0.0	0.2	-0.2[3]	94.0	2.1	-0.2	-0.1	0.2	-0.2[3]	-0.2
20KF	84.6	4.4	+0.3	+0.1	0.3	-0.4	84.6	4.4	+0.3	+0.1	0.3	-0.4	+0.1
Pointing and Gain Accuracy													
10KE	0.7	0.7	0.7	0.2	+0.7, -0.0	+0.0, -1.8	0.1	0.1	0.1	+0.1, -0.0	0.1	0.3	0.5
20KE	0.7	0.7	+0.6, -0.8	+0.1, -0.2	+0.6, -0.1	+0.1, -1.3	0.1	0.1	0.1	0.0	0.1	0.1	0.5
10KF	0.2	0.3	+0.3, -0.2	+0.2, -0.0	+0.3, -0.2	+0.2[3], -0.8	0.1	0.1	0.1	+0.1, -0.0	0.1	+0.1[3], -0.2	0.5
20KF	0.1	0.1	0.1	0.0	0.1	0.2	0.1	0.1	0.1	0.0	0.1	0.2	0.5

1 See Figure 10 for definitions

2 Pre-realignment 10K $-\Delta\theta = 0.6$, $\Delta G = 1.3$ dB; 20K $-\Delta\theta = 0.8^\circ$, $\Delta G = -2.2$ dB.

3 Does not include estimation of blockage by trees.

Table 7
Equipment and Processing Correction Factors

Path	Period (1970-71)	Events	Correction Factor (dB)				
			Trans. Line Loss	Trans. Spectra	Recv. Calib.	Data Process	Total
10KE	10/2-12/8	1-14	-0.6	0.0	0.0	-0.5	-1.1
	12/8-1/31	15-27	-0.6	0.0	-1.0	-0.5	-2.1
	1/31-4/5	28-46	-0.6	0.0	-1.0	+2.3	+0.7
	4/5-5/17	47-61	-0.6	0.0	-3.0	+2.3	-1.3
	5/17-6/4	62-67	0.0	0.0	-3.0	0.0	-3.0
	6/4-7/26	68-85a	0.0	0.0	-2.0	0.0	-2.0
	7/26-9/1	85b-98	+0.2	1.7	-2.0	0.0	-0.1
	9/1-10/2	100-105	+0.3	-0.1	-2.0	0.0	-1.8
20KE	10/2-12/8	1-14	+1.1	0.0	0.0	-0.5	+0.6
	12/8-1/31	15-27	+1.1	0.0	-1.0	-0.5	-0.4
	1/31-4/5	28-46	+1.1	0.0	-1.0	+2.3	+2.4
	4/5-6/4	47-67	+1.1	0.0	-3.0	+2.3	+0.4
	6/4-7/26	68-85a	+1.1	0.0	-2.0	+2.3	+1.4
	7/26-8/9	85b-90	+1.1	-0.1	-2.0	+2.3	+1.3
	8/9-8/15	91-92	+1.1	+1.5	-2.0	+2.3	+2.9
	8/16-10/2	93-105	+1.3	+1.5	-2.0	+2.3	+3.1
10KF	10/2-12/8	1-14	-0.7	0.0	0.0	-0.5	-1.2
	12/8-1/31	15-27	-0.7	0.0	-1.0	-0.5	-2.2
	1/31-4/5	28-46	-0.7	0.0	-1.0	+2.3	+0.6
	4/5-5/17	47-61	-0.7	0.0	-3.0	+2.3	-1.4
	5/17-6/4	62-67	-0.7	0.0	-3.0	0.0	-3.7
	6/4-7/26	68-85a	-0.5	0.0	-2.0	0.0	-2.7
	7/26-10/2	85b-105	-0.5	-0.1	-2.0	0.0	-2.8
20KF	10/2-12/8	1-14	+0.5	0.0	0.0	-0.5	0.0
	12/8-1/31	15-27	+0.5	0.0	-1.0	-0.5	-1.0
	1/31-4/5	28-46	+0.5	0.0	-1.0	+2.3	+1.8
	4/5-5/7	47-54	+0.5	0.0	-3.0	+2.3	-0.2
	5/7-6/4	55-67	+0.5	0.0	-3.0	+2.3	-0.2
	6/4-7/26	68-85a	+0.5	0.0	-2.0	+2.3	+0.8
	7/26-8/10	85b-90	+0.5	+3.0	-2.0	+2.3	+3.8
	8/10-8/17	91-92	+0.7	+3.0	-2.0	+2.3	+4.0
	8/18	93-94	+0.7	+1.8	-2.0	+2.3	+2.8
	8/19-8/24	95-97b	+0.7	+3.0	-2.0	+2.3	+4.0
	8/25-10/2	98-105	+0.7	+2.5	-2.0	+2.3	+3.5

3.1.2 Comparisons Between Simultaneous Measurements of Z_e Using the 10K Paths

Throughout the measurement year, scattering values from the 10KE and 10KF paths were simultaneously measured. Since the Z_e values should be identical for these paths, the scattergrams of $\langle \bar{P}_r \rangle$ for the 10KE versus that for the 10KF paths should aid in verifying the relative calibration error between the two transmitter sites.

A scattergram for event 81, on July 11, 1971 is given in Figure 17. During this event, the F5 transmitter at Eastville failed; within 3 minutes the F4 transmitter was switched to the 10KE antenna and the 10KE path was restored. The F5 and F4 data are reported separately, and a 1-dB correction was applied to the F4 data to correct the relative change in transmitter power prior to plotting. The Z_e values were determined using the correction factors and pointing angle data described above. In calculating Z_e, a 3.5-km cell size was adopted. This cell size is consistent with the models adopted by the CCIR (NASA, 1971) and provides a correction factor that is within 1 dB of the correct value for all cells larger than 2.0 km (see Figure 11). The data were read using method B and, from Table 3, have a precision of ±3 dB. For Eastville $\langle \bar{P}_r \rangle$ values above -110 dBm, all the comparison data points are within ±3 dB of the equal Z_e value line. Below that level, the data spread increases and, since the Z_e values are more than 10 dB below the peak Z_e value for the event, the cells may not be centered within the common volume or the 3.5-km cell size hypothesis may not apply and larger data spreads may occur.

The median line provides an estimate of the relationship between $\langle \bar{P}_r \rangle$ for 10KE and $\langle \bar{P}_r \rangle$ for 10KF, using the hypothesis that the $\langle \bar{P}_r \rangle$ values may differ only by a multiplicative factor (additive constant in dB) which depends solely on the transmitter calibration constants. For the scattergram given in Figure 17, the median line shows $\langle \bar{P}_r \rangle$ values on the 10KE path to be 1 dB greater than the $\langle \bar{P}_r \rangle$ values on the 10KF path for the same scattering cross section. The median of the ratios of $\langle \bar{P}_r \rangle$ for 10KE to $\langle \bar{P}_r \rangle$ for 10KF (differences in dB) was determined by positioning a line with unity slope (45°) on the scattergram so that half the data points were above the line and half below. The medians of the ratios for each event having 10 or more comparison points with $\langle \bar{P}_r \rangle$ for 10KE greater than -115 dBm are plotted in Figure 18. Using the medians of the ratios to estimate the relative radiated powers for the transmitter sites, the plotted data represent the changes in the relative radiated power values for the two sites.

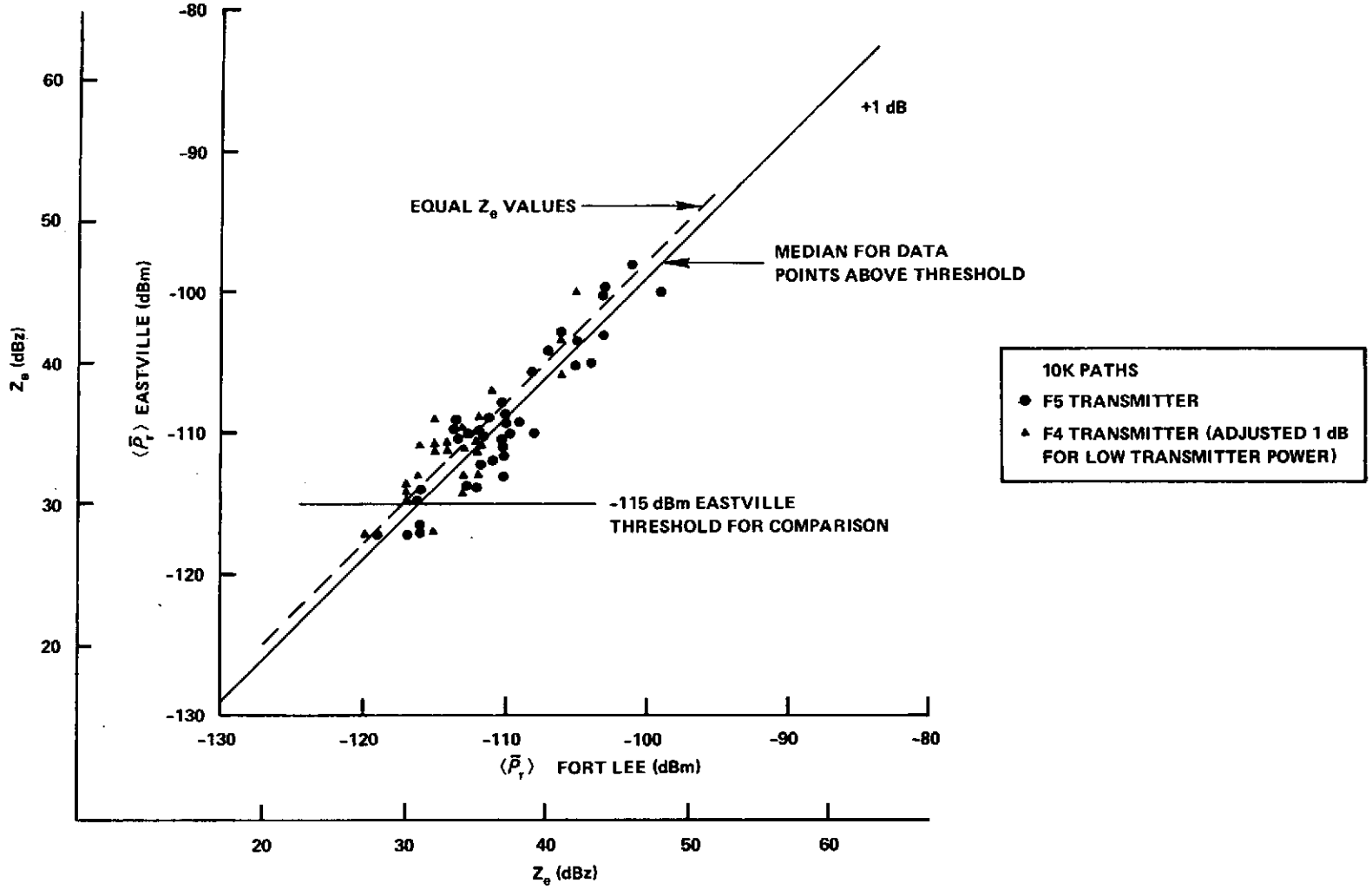

Figure 17. Scattergram of July 11, 1971 Event 81

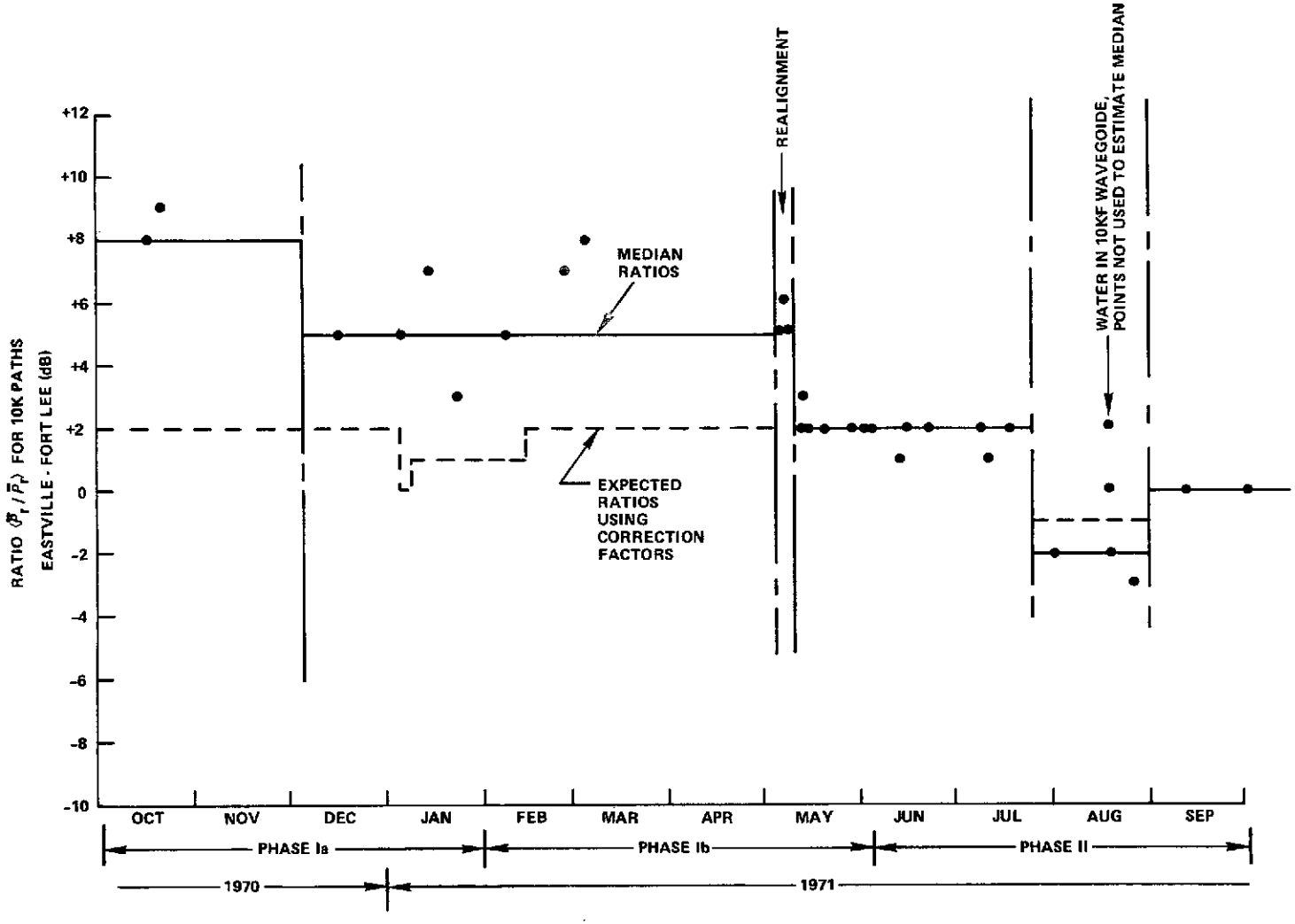

Figure 18. Medians of Scattergram Comparisons, 10K Paths

Assuming that the calibration constants remained the same over a period of time, the relative radiated power values may be used to verify the calibration constants and correction factors for the transmitter sites. The wideband radiated power measurements accomplished the same purpose except for the estimation of the correction factor for spectral broadening of the transmitted signal. The scattered power comparison measurements were made using the entire receiver system so the spectrum correction factors are included. Since the scattered signal is used, the calibration constants for transmit antenna pointing are also checked.

The expected values for the ratios of $\langle \bar{P}_r \rangle$ for the 10KE and 10KF paths are plotted on Figure 18. For comparison with the expected values, the median of the medians of the ratios is determined for each time period for which the expected ratios were constant. For time periods when the median of the medians of the ratios and the expected ratios were identical, only the median was plotted. During these time periods, the calibration values and correction factors were correct. This occurred for the time period May 10 to July 26 and September 1 to October 2. During the latter time period, neither the 10KE nor 10KF transmitters (F4 modified and F2, see Table R1:/3-11) had spectral broadening problems and the calibration and correction factors (including the 0.5 dB transmit power correction factor discussed in Section 3.1.1) are correct.

During the May 10 to July 26 time period, the F3 transmitter was used on the 10KF path. Spectral broadening problems were discovered for this transmitter in August and, in establishing the table of correction factors, the spectrum correction factor was applied from July 26 on. This date was selected because the transmitters on the 10K and 20K paths were interchanged on that day. The spectral correction factor was not used for earlier time periods due to a lack of information. In Table R1:/3-11, the spectrum error (accuracy) for the F3 transmitter was estimated at -0, +6 dB (accuracy of the correction factor), since spectral broadening could have occurred (accuracy values are repeated in Table 8 for reference). The $\langle \bar{P}_r \rangle$ comparisons show that no spectral broadening occurred prior to July 26, since the median of the medians agreed with the expected value. The Phase I and II transmitting system error estimates (Table R1:/3-9) for Fort Lee therefore must be revised, so the spectrum estimate is ± 0.1 dB, not -0, +6 dB.

During the time period July 26 to September 1, the spectral broadening problems were detected for the F4 transmitter (10KE). A correction factor of +1.7 dB (Table R1:/3-6) was estimated for this time period based upon two measurements of the transmitted spectrum. The measurements differed by 1.4 dB, so the average of the two measurements was used to estimate the correction factor and a ± 0.7 dB accuracy estimate was adopted. Neglecting the

Table 8
Equipment and Processing Errors

Path	Period (1970-71)	Events	Transmitting System		Receiving System		Data Processing Precision (dB)
			Accuracy (dB)	Repeatability (dB)	Accuracy (dB)	Repeatability (dB)	
10KE	10/2-12/8	1-14	±1.1	±0.5	+1.6, -3.9	+3.1, -5.1	±1.0
	12/8-1/25	15-25	±1.1	±0.5	±2.9	+3.1, -5.1	±1.0
	1/25-1/31	26-27	±1.1	±0.5	±1.9	±3.3	±1.0
	1/31-4/5	28-46	±1.1	±0.5	±1.9	±3.3	±5.0
	4/5-5/6	47-53c	±1.1	±0.5	±2.6	±1.3	±5.0
	5/6-6/4	54-67	±1.1	±0.4	±2.6	±1.3	±3.0
	6/4-7/26	68-85a	±1.1	±0.4	±1.8	±0.9	±3.0
	7/26-8/1	85b-91	±1.7	±0.4	±1.8	±0.9	±3.0
	8/1-9/1	92-98	±1.7	±0.4	±1.8	±0.9	±1.0
	9/1-10/2	100-105	±1.1	±0.4	±1.8	±0.9	±1.0
20KE	10/2-12/8	1-14	+4.0, -1.0	±0.5	+1.6, -3.9	+3.1, -5.1	±1.0
	12/8-1/25	15-25	+4.0, -1.0	±0.5	±2.9	+3.1, -5.1	±1.0
	1/25-1/31	26-27	+4.0, -1.0	±0.5	±1.9	±3.3	±1.0
	1/31-4/5	28-46	+4.0, -1.0	±0.5	±1.9	±3.3	±5.0
	4/5-5/6	47-53c	+4.0, -1.0	±0.5	±2.6	±1.3	±5.0
	5/6-6/4	54-67	+4.0, -1.0	±0.4	±2.6	±1.3	±4.0
	6/4-7/26	68-85a	+4.0, -1.0	±0.4	±1.8	±0.9	±4.0
	7/26-8/9	85b-90	±1.1	±0.4	±1.8	±0.9	±4.0
	8/9-10/2	91-105	±1.2	±0.4	±1.8	±0.9	±4.0
10KF	10/2-12/8	1-14	+7.0, -1.0	±0.5	+1.6, -3.9	+3.1, -5.1	±1.0
	12/8-1/25	15-25	+7.0, -1.0	±0.5	±2.9	+3.1, -5.1	±1.0
	1/25-1/31	26-27	+7.0, -1.0	±0.5	±1.9	±3.3	±1.0
	1/31-4/5	28-46	+7.0, -1.0	±0.5	±1.9	±3.3	±5.0
	4/5-5/6	47-53c	+7.0, -1.0	±0.5	±2.6	±1.3	±5.0
	5/6-6/4	54-67	+7.0, -1.0	±0.4	±2.6	±1.3	±3.0
	6/4-7/26	68-85a	+7.0, -1.0	±0.4	±1.8	±0.9	±3.0
	7/26-10/2	85b-105	±1.1	±0.4	±1.8	±0.9	±1.0
20KF	10/2-12/8	1-14	+7.0, -1.0	±0.5	+1.6, -3.9	+3.1, -5.1	±1.0
	12/8-1/25	15-25	+7.0, -1.0	±0.5	±2.9	+3.1, -5.1	±1.0
	1/25-1/31	26-27	+7.0, -1.0	±0.5	±1.0	±3.3	±1.0
	1/31-4/5	28-46	+7.0, -1.0	±0.5	±1.9	±3.3	±5.0
	4/5-5/6	47-53c	+7.0, -1.0	±0.5	±2.6	±3.3	±5.0
	5/6-6/4	54-67	±1.1	±0.4	±2.6	±3.3	±4.0
	6/4-7/26	68-85a	±1.1	±0.4	±1.8	±0.9	±4.0
	7/26-10/2	85b-105	±1.2	±0.4	±1.9	±0.9	±4.0

two data points for August 18, when water was detected in the transmission line at Fort Lee, the median of the medians and the expected values differed by 1 dB. For use in processing data, the spectrum correction factor for the July 26 to September 1 time period was increased by 1 dB to agree with the $\langle \bar{P}_r \rangle$ ratio measurements. The transmission line loss variation caused by water detected at Fort Lee was estimated by using the two data points on August 18. The line loss was increased by 3 dB so the two measurements straddle the expected value (see Figure 18).

Data for the time period prior to May 1 were difficult to interpret due both to a limited number of comparison values and to the uncertainty in pointing of the Eastville antennas. Using the pointing angles measured prior to realignment to estimate the change in median ratio expected due to antenna motion, an additional 1 dB correction factor (see Table 6 footnote) is required. During this time period, the 10KF transmit antenna was pointed 0.5° low. At the correct elevation angle, blockage by trees was expected to cause a 0 to 2 dB increase in path loss for the 10KF path. The post May 10 data showed good agreement without including a blockage correction factor, hence the correction factor is less than 1 dB. For the low antenna elevation angle, considerably more loss may occur. The median of the medians is between 3 and 6 dB higher (3 to 6 dB additional loss on the 10KF path) than the expected value. This implies that a tree-blockage correction factor is required for this time period. The data points seem to occur in two groups (as shown in Figure 18), one for October with a 6-dB difference, and one for December 16 on, with a large spread in data points. Postulating that motion of the Eastville antenna contributed to the large uncertainty in the median of the ratios, a 1-dB correction (-1 dB change in the ratio) was made to the data points, and the median difference between the corrected values and the expected values was used to estimate the 10KF antenna blockage correction. The blockage correction is 6 dB and the resultant best estimate ratio values using this correction factor and the 1-dB factor for antenna motion is shown on Figure 18. Other combinations of blockage and antenna pointing corrections are possible for this time period, but the values adopted provide an equal number of data points above and below the best estimate line.

The time period April 30 to May 10 was used to modify the sites for the change from the Phase I to Phase II transmitter configuration. During this time period the antennas were realigned, transmission lines changed, and a transmitter was added at the Fort Lee site. The data were obtained during this transition period for different antenna pointing combinations. Two of the data points (May 7 and 8) were taken after all the antennas were realigned; one of the points (May 6) is after the 10KE antenna was moved and before the 10KF antenna was moved. The probable explanation for the large, 3-dB discrepancy

in median values after realignment is additional loss in the Fort Lee transmission line, which was still in the process of being modified. For this time period, it was assumed that Fort Lee had 3-dB additional transmission loss, and the correction factors for data processing were modified accordingly. This correction factor was also applied for the May 6 event without an additional correction for blockage, although the 10KF antenna had not been realigned. This was done because the antenna guys were tightened on the 10KF antenna prior to May 6, and the 6-dB blockage factor may not apply and because the data were better fitted by using the 3-dB correction factor than the unknown but correct factor. The maximum Z_e value (after applying the 3-dB line loss correction) was 38 dBz. Only 7 min of data exceeded 32 dBz; therefore the errors in the empirical distribution and density functions for Phase Ib caused by using this correction factor are negligible.

Using the best estimated correction factors as determined above, the highest Z_e values for each event were compared. The values were the highest measured for each path for each event and were not necessarily simultaneous measurements. The scattergram of peak Z_e for 10KE versus peak Z_e for 10KF is given in Figure 19. Data for Phase I and II are separately displayed. The maximum deviation from the equal Z_e value line is 3 dB for Phase II and 6 dB for Phase I. These deviations are consistent with the reading precision of the methods used, indicating that after correction, the calibration factors for the two receiver sites were consistent with each other. Calibration errors that are identical for both sites may not be determined from the comparisons given above.

3.1.3 Calibration Factor and Measurement Accuracy Summary

The equipment correction factors and system measurement accuracy as initially estimated were presented in Tables 6, 7, and 8. As a result of the measurements reported above, the estimates were revised. The revised values are summarized below for easy reference. Sufficient data were not available to check the transmitter calibrations by comparison between $\langle \bar{P}_r \rangle$ for the 20 KE and 20KF paths. The revised estimates for these paths depend only upon the wideband radiated power measurements and the periodic outside-the-loop power measurements. In preparing the data correction factors, an additional -0.5 dB data processing correction factor was added so all the reported data in a 1-dBz interval will exceed the Z_e level given and be less than the value of the next level. (The $\langle \bar{P}_r \rangle$ values were obtained by rounding to the nearest decibel.) The data processing corrections therefore differ from those given in Table 3.

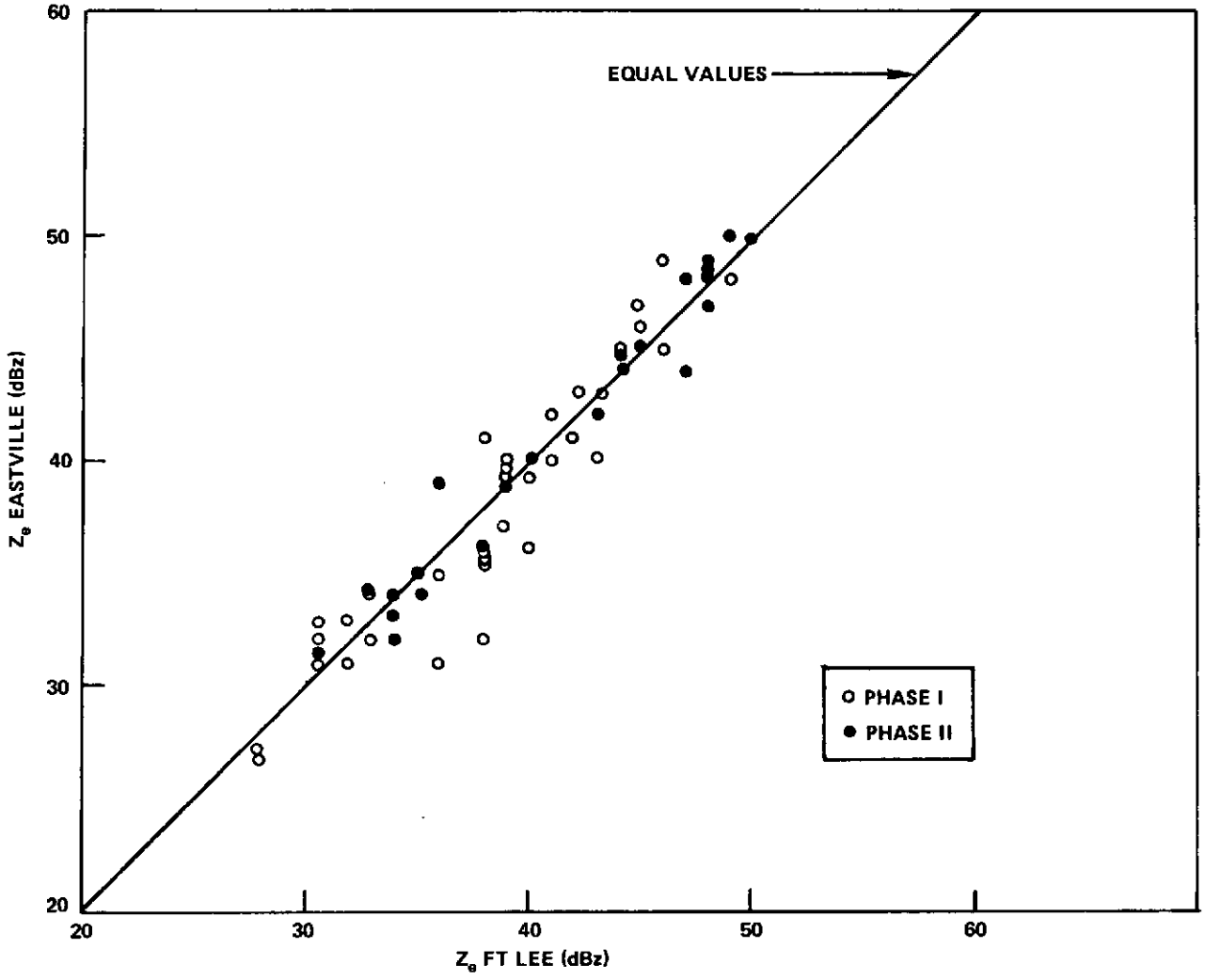

Figure 19. Comparison Between Peak Z_e Values Recorded in all Events, 10K Paths

The revised correction factors, errors, and scale constants are given in Tables 9(a) to (d). The revised scale constants were used to convert $\langle \bar{P}_r \rangle$ to Z_e for use in the construction of the empirical distribution and density functions reported below. The repeatability estimates also include the effects of Doppler shift and cell size as described in Section 2. An example of the error contributions from all sources is shown in Table 10 for the 10KE path during September 1 to October 2, 1971. The accuracy values listed for the 20K paths were determined by adding the values listed in Table 8 for the transmitting and receiving systems, the 0.5-dB uncertainty in the integral of the relative gain function for the receiving antenna as discussed in Section 2.1.2, and the antenna pointing uncertainty $\Delta G_2(r_2)$ in Table 6. A similar listing for the 10K paths for the time period between June 4 and July 26 would give ±3.7 dB for the accuracy of the 10KE path and +3.5, -3.6 dB for the 10KF path. The median of the scattergram comparison for May 10 through July 26 showed the transmitter calibration values to be correct with a maximum uncertainty of 0.4 dB (3σ, assuming Gaussian distribution in errors of reported scattergram median values). The accuracy values for the transmitter may be reduced from the ±1.4 dB value for the 10KE path, and the +1.2, -1.3 dB value for the 10KF path, to a value of ±0.4 dB plus any other contribution common to both transmitter sites.

The antenna gains at the transmitter sites were determined using a standard-gain horn with a gain uncertainty of ±0.2 dB. All other contributions to the transmitter calibration were independently determined at each site. The net transmitter accuracy value therefore was ±0.6 dB for both sites. The values given in Tables 9(a) and 9(c) are for a transmitter accuracy value of ±0.6 dB when the antenna pointing was known and ±1.6 dB when the line loss for hot measurement day or tree blockage had to be estimated from the median of the scattergram. The repeatability estimates also include the effects of Doppler shift and cell size as described in Section 2. An example of the error contribution for all sources is shown in Table 9(a) for the 10KE path for September 1 to October 2, 1971.

The accuracy, repeatability, and precision estimates are for the factors required to correct the data. The accuracies of the measurements after correction are the negatives of these values. For Phase II, the accuracy estimates may be prepared from Tables 9(a) to (d), using the highest values for the June 4 to October 2, 1971, time period. For the 10KE path, the accuracy was ±2.8 dB; for the 20KE path, +3.4, -6.4 dB; for the 10KF path, ±3.8 dB (±2.8 dB excluding event 90); and for the 20KF path, ±2.8 dB.

Table 9(a)
Revised Correction Factors and Error Estimates, 10KE Path

Period (1970-71)	Event	Scale Constant K_p[1] (dB)	Correction Factors						Revised Scale Constant (dB)[2]	Error Estimates		
			Transmitting Site				Receiving Site (dB)	Data Processing (dB)		Accuracy (dB)	Repeatability (dB)	Precision (dB)
			Line Loss (dB)	Spectrum (dB)	Power (dB)	Antenna (dB)						
10/2-12/8	1-14	144.7	-0.6	0.0	0.0	).0	0.0	+1.5	146	+2.6, -6.7	+3.3, -5.2	+4.0, -1.0
12/8-12/16	15	144.7	-0.6	0.0	0.0	).0	-1.0	+1.5	145	+3.9, -5.7	+3.3, -5.2	+4.0, -1.0
12/16-1/2	16-19	144.7	-0.6	0.0	0.0	+1.3	-1.0	+1.5	146	±5.0	+3.3, -5.2	+4.0, -1.0
1/2-1/7	20a-20c	144.7	-0.6	0.0	+2.0	+1.3	-1.0	+1.5	148	±5.0	+3.3, -5.2	+4.0, -1.0
1/7-1/14	21	144.7	-0.6	0.0	0.0	+1.3	-1.0	+1.5	146	±5.0	+3.3, -5.2	+4.0, -1.0
1/14-1/25	22-25	144.7	-0.6	0.0	+1.0	+1.3	-1.0	+1.5	147	±5.0	+3.3, -5.2	+4.0, -1.0
1/25-1/31	26-27	144.7	-0.6	0.0	+1.0	+1.3	-1.0	+1.5	147	±4.0	±3.5	+4.0, -1.0
1/31-2/5	28	144.7	-0.6	0.0	+1.0	+1.3	-1.0	+2.0[3]	147	±4.0	±3.5	±4.0
2/5-2/12	30	144.7	-0.6	0.0	0.0	+1.3	-1.0	+2.0[3]	146	±4.0	±3.5	±4.0
2/12-2/15	32	144.7	-0.6	0.0	+1.0	+1.3	-1.0	+2.0[3]	147	±4.0	±3.5	±4.0
2/15-4/5	33-46	144.7	-0.6	0.0	0.0	+1.3	-1.0	+2.0[3]	146	±4.0	±3.5	±4.0
4/5-5/5	47-53c	144.7	-0.6	0.0	0.0	+1.3	-3.0	+2.0[3]	144	±4.7	±1.9	±4.0
5/5-5/17	54-61	144.7	-0.6	0.0	0.0	+).6	-3.0	+2.0[3]	144	±3.7	±1.9	±4.0
5/17-6/4	62-67	144.7	0.0	0.0	0.0	+).6	-3.0	+2.0[3]	144	±3.7	±1.9	±3.0
6/4-7/26	68-85a	144.7	+0.0	+0.0	0.0	+).6	-2.0	+2.0	145	±2.9	±1.6	±3.0
7/26-8/1	85b-91	144.7	+0.2	+2.7	+1.0	+).6	-2.0	+2.0	149	±2.9	±1.6	±3.0
8/1-9/1	91-98	144.7	+0.2	+2.7	+1.0	+).6	-2.0	+2.0	149	±2.9	±1.6	±1.4
9/1-10/2	100-105	144.7	0.3	-0.1	+1.0	+).6	-2.0	+2.0	147	±2.9	±1.6	±1.4

1 Includes C_d = +0.5 dB for 3.5-km cell and $\int_0^{r_2} A\,ds + \int_{r_2}^{L} A\,ds$ = 0.4 dB for gaseous absorption

2 To be added to (P_r) to get Z (dBz)

3 Additional signal-level-dependent correction required, 0 dB at -115 dBm and +5 dB at -100 dBm (see Figure 8)

Table 9(b)
Revised Correction Factors and Error Estimates, 20KE Path

Period (1970-71)	Event	Scale Constant Kp[1] (dB)	Correction Factors						Revised Scale Constant (dB)[2]	Error Estimates		
			Transmitting Site				Receiving Site (dB)	Data Processing (dB)		Accuracy (dB)	Repeatability (dB)	Precision (dB)
			Line Loss (dB)	Spectrum (dB)	Power (dB)	Antenna (dB)						
10/2-12/8	1-14	144.8	+1.1	0.0	+1.0	+0.2	0.0	+1.5	149	+6.2, -6.7	+3.3, -5.2	+4.0, -1.0
12/8-1/25	15	144.8	+1.1	0.0	+1.0	+0.2	-1.0	+1.5	148	+7.4, -5.7	+3.3, -5.2	+4.0, -1.0
12/16-1/25	16-25	144.8	+1.1	0.0	+1.0	+2.3	-1.0	+1.5	150	+9.6, -6.6	+3.3, -5.2	+4.0, -1.0
1/25-1/31	26-27	144.8	+1.1	0.0	+1.0	+2.3	-1.0	+1.5	150	+8.6, -5.6	±3.5	+4.0, -1.0
1/31-4/5	28-46	144.8	+1.1	0.0	+1.0	+2.3	-1.0	+2.0[3]	150	+8.6, -5.6	±3.5	±4.0
4/5-5/5	47-53c	144.8	+1.1	0.0	+1.0	+2.3	-3.0	+2.0[3]	148	+9.2, -6.3	±1.9	±4.0
5/5-6/4	54-67	144.8	+1.1	0.0	+1.0	+0.2	-3.0	+4.3	148	+7.2, -4.2	±1.9	±4.0
6/4-7/26	68-85a	144.8	+1.1	0.0	+1.0	+0.2	-2.0	+4.3	149	+6.4, -3.4	±1.6	±4.0
7/26-8/9	85b-90	144.8	+1.1	-0.1	0.0	+0.2	-2.0	+4.3	148	±3.5	±1.6	±4.0
8/9-8/15	91-92	144.8	+1.1	+1.5	0.0	+0.2	-2.0	+4.3	150	±3.6	±1.6	±4.0
8/15-10/2	93-105	144.8	+1.3	+1.5	0.0	-0.2	-2.0	+4.3	150	±3.6	±1.6	±4.0

1 Includes C_d = +0.6 dB for a 3.5-km cell and $\int_0^{r_2} A\,ds + \int_{r_2}^{L} A\,ds = 0.1$ dB

2 To be added to (P_r) to get Z_e (dBz)

3 Additional signal-level-dependent correction required (see Figure 8)

Table 9(c)

Revised Correction Factors and Error Estimates, 10KF Path

Period (1970-71)	Events	Scale Constant Kp[1] (dB)	Correction Factors						Revised Scale Constant (dB)	Error Estimates		
			Transmitting Site				Receiving Site (dB)	Data Processing (dB)		Accuracy (dB)	Repeatability (dB)	Precision (dB)
			Line Loss (dB)	Spectrum (dB)	Power (dB)	Antenna (dB)						
10/2-12/8	1-14	146.9	-0.7	0.0	0.0	+6.4[3]	0.0	+1.5	154	+3.7, -6.0	+3.3, -5.2	+4.0, -1.0
12/8-1/25	15-25	146.9	-0.7	0.0	0.0	+6.4[3]	-1.0	+1.5	153	±5.0	+3.3, -5.2	+4.0, -1.0
1/25-1/31	25-27	146.9	-0.7	0.0	0.0	+6.4[3]	-1.0	+1.5	153	±4.0	±3.5	+4.0, -1.0
1/31-4/5	28-46	146.9	-0.7	0.0	0.0	+6.4[3]	-1.0	+2.0[4]	154	±4.0	±3.5	±4.0
4/5-5/7	47-54c	146.9	-0.7	0.0	0.0	+6.4[3]	-3.0	+2.0[4]	152	±4.7	±1.9	±4.0
5/7-5/10	55-58	146.9	+2.3	0.0	0.0	+0.4	-3.0	+2.0[4]	149	±4.7	±1.9	±4.0
5/10-5/17	59-61	146.9	-0.7	0.0	0.0	+0.4	-3.0	+2.0[4]	146	±3.7	±1.9	±4.0
5/17-6/4	62-67	146.9	-0.7	0.0	0.0	+0.4	-3.0	+2.0	146	±3.7	±1.9	±3.0
6/4-7/26	68-85a	146.9	-0.5	0.0	0.0	+0.4	-2.0	+2.0	147	±2.9	±1.9	±3.0
7/26-8/4	85b-89	146.9	-0.5	-0.1	0.0	+0.4	-2.0	+2.0	147	±2.9	±1.6	±3.0
8/4-8/5	90	146.9	+5.5[5]	-0.1	0.0	+0.4	-2.0	+2.0	153	±3.9	±1.6	±1.4
8/5-8/18	91-92	146.9	-0.5	-0.1	0.0	+0.4	-2.0	+2.0	147	±2.9	±1.6	±1.4
8/18-8/19	93-94	146.9	+1.5[5]	-0.1	0.0	+0.4	-2.0	+2.0	149	±3.9	±1.6	±1.4
8/19-10/2	95-105	146.9	-0.5	-0.1	0.0	+0.4	-2.0	+2.0	147	±2.9	±1.6	±1.4

1 Includes C_d = 1.2 dB for a 3.5-km cell and $\int_0^{r_2} A\,ds = \int_{r_2}^{L} A\,ds = 0.6$ dB

2 To be added to $\langle P_r \rangle$ to get Z_e (dBz)

3 Includes estimated 6-dB site shielding

4 Additional signal-level-dependent correction required (see Figure 8)

5 Water in transmission line

Table 9(d)
Correction Factors and Error Estimates, 20KF Path

Period (1970-71)	Events	Scale Constant K_p[1] (dB)	Correction Factors						Revised Scale[2] Constant (dB)	Error Estimates		
			Transmitting Site				Receiving Site (dB)	Data Processing (dB)		Accuracy (dB)	Repeatability (dB)	Precision (dB)
			Line Loss (dB)	Spectrum (dB)	Power (dB)	Antenna (dB)						
10/2-12/8	1-14	146.6	+0.5	0.0	0.0	+0.3	0.0	+1.5	149	+3.3, -5.6	+3.3, -5.2	+4.0, -1.0
12/8-1/25	15-25	146.6	+0.5	0.0	0.0	+0.3	-1.0	+1.5	148	±4.6	+3.3, -5.2	+4.0, -1.0
1/25-1/31	26-27	146.6	+0.5	0.0	0.0	+0.3	-1.0	+1.5	148	±3.6	+3.3, -5.2	+4.0, -1.0
1/31-4/5	28-46	146.6	+0.5	0.0	0.0	+0.3	-3.0	+2.0[3]	148	±3.6	±3.5	±4.0
4/5-5/7	47-54	146.6	+0.5	0.0	0.0	+0.3	-3.0	+2.0[3]	146	±4.3	±1.9	±4.0
5/7-6/4	55-67	146.6	+0.5	0.0	0.0	+0.3	-2.0	+4.3	149	±4.3	±1.9	±4.0
6/4-7/26	68-85a	146.6	+0.5	0.0	0.0	+0.3	-2.0	+4.3	150	±3.5	±1.6	±4.0
7/26-8/10	85b-90	146.6	+0.5	+3.0	0.0	+0.3	-2.0	+4.3	153	±3.7	±1.6	±4.0
8/10-8/17	91-92	146.6	+0.7	+3.0	0.0	+0.3	-2.0	+4.3	153	±3.7	±1.6	±4.0
8/17-8/19	93-94	146.6	+0.8	+1.8	0.0	+0.3	-2.0	+4.3	152	±3.7	±1.6	±4.0
8/19-8/24	95-97	146.6	+0.8	+3.0	0.0	+0.3	-2.0	+4.3	153	±3.7	±1.6	±4.0
8/24-10/2	98a-105	146.6	+0.8	+2.5	0.0	+0.3	-2.0	+4.3	152	±3.7	±1.6	±4.0

1 Includes C_d = 1.0 dB for 3.5-km cell and $\int_0^{r_2} A\,ds + \int_{r_2}^{L} A\,ds = 0.5$

2 To be added to (P_r) to get Z_e (dBz)

3 Additional signal-level-dependent correction required (see Figure 8)

Table 10
Estimated Errors From All Sources for 10KE
Path—September 1 to October 2, 1971

Error Sources	Accuracy (±dB)	Repeatability (±dB)	Precision (±dB)
Equipment calibration	2.0	1.0	
Transmit antenna pointing	0.4		
Statistical and processing			1.4
Integral of receiving antenna	0.5		
Beam filling (≥2 km)		1.0	
Doppler offset		0.5	
Nonspherical drop shape (1-dB low, compensates for high Z/R)			
TOTAL	2.9	1.6	1.4

3.2 RAIN GAUGE SYSTEM

3.2.1 Comparisons Between NWS and Rain Gauge Measurements

Rain gauge calibration and siting errors were discussed in Section R1:/4. The measurement accuracy of the type II and III gauges depended mainly on siting. The siting errors are caused by variations in wind flow about the gauge and by blockage of rain falling into the gauge. Both sources of error depend upon the prevailing wind conditions, which change with season. The siting errors were estimated by comparing the accumulations recorded by gauges with the NWS gauge accumulations recorded at Williamsburg, Norfolk, and Richmond, Virginia. The results of the comparisons for all of Phase I and for 10 events in Phase II were that the 5K, 10K, and 20K gauges reported between 7 and 25 percent lower accumulations, and a 25 percent error including the effects of siting, aerodynamic gauge errors, and calibration errors was assumed.

The NWS collects monthly accumulation data from 26 gauges within 100 km of the 10K gauge. These gauges include the Norfolk, Richmond, and Williamsburg gauges used in the analysis reported in Section R1:/4. The monthly accumulations for time periods that best approximate the phases of the experiment—October through January for Phase Ia, February through May for Phase

Ib, and June through September for Phase II—were tabulated for comparison with the type I, II, and III gauges used for the experiment. (See Appendix B for the tabulations and map showing gauge locations.) The data were reported in the Annual Summary of Climatological Data for Virginia (EDS, 1970 and 1971). The climatological data also reported average accumulations for sections (divisions) of the state. The Tidewater division included most of the NWS gauge sites, and the Tidewater average accumulations were used as reference for reporting accumulations. The measured accumulations for the NWS gauges and the type I, II, and III gauges, plotted on maps with center at the 10K gauge as percent differences from the Tidewater average, are given in Figures 20(a) to 20(d). Each of the figures is for a different time period.

The accumulations for the measurement year (Figure 20(a)) are all within 10 percent of the division average with the exception of the Langley Air Force Base gauge (the NWS network gauge closest to L8 indicating +14 percent), two NWS network gauges south of the 10K gauge, all the gauges on the Delmarva Peninsula (separated by dot-dashed line from the rest of the map), and the 10K gauge. Accumulations recorded on the Delmarva Peninsula for each of the time periods are consistent with each other and considerably lower than those recorded for the rest of the Tidewater District. The low values for the Delmarva Peninsula indicate that the rain climate there is different than for the mainland, the Chesapeake Bay causing showers to dissipate as they move out from the mainland. The two NWS network gauges that are more than 10 percent higher then the district average and more than 50 km south of the 10K gauge are consistent with each other and the general change in accumulation across the map. For the mainland, the map indicates the accumulation tended to increase from north to south. The Langley Air Force Base gauge accumulation was consistently high for each of the time periods, and the Newport News Press Building gauge just to the south of it was consistently lower. These departures probably represent siting and calibration errors. The station data for the Newport News Press Building gauge indicate that it was installed on a building and was significantly higher than the surrounding terrain. This gauge may suffer from the same siting problems as the 10K gauge (Section R1:/2. 2. 2. 2).

The 10K gauge accumulation was below that of the neighboring gauges with the exception of other type II or III gauges for each of the time periods. The accumulation was approximately 20 percent low for the entire year and ranged 30 to 40 percent low for Phase II (42 percent low in comparison with the L8 gauge) to 5 to 10 percent low for Phase Ib. The type I gauges were used only during Phase II and all had accumulations within 6 percent of the nearest neighbor gauge (discounting the Langley Air Force Base gauge, which tended to be high) and of the trend of the accumulations for the gauges in the area. The type I gauge accumulations were determined by measuring the volume of water collected

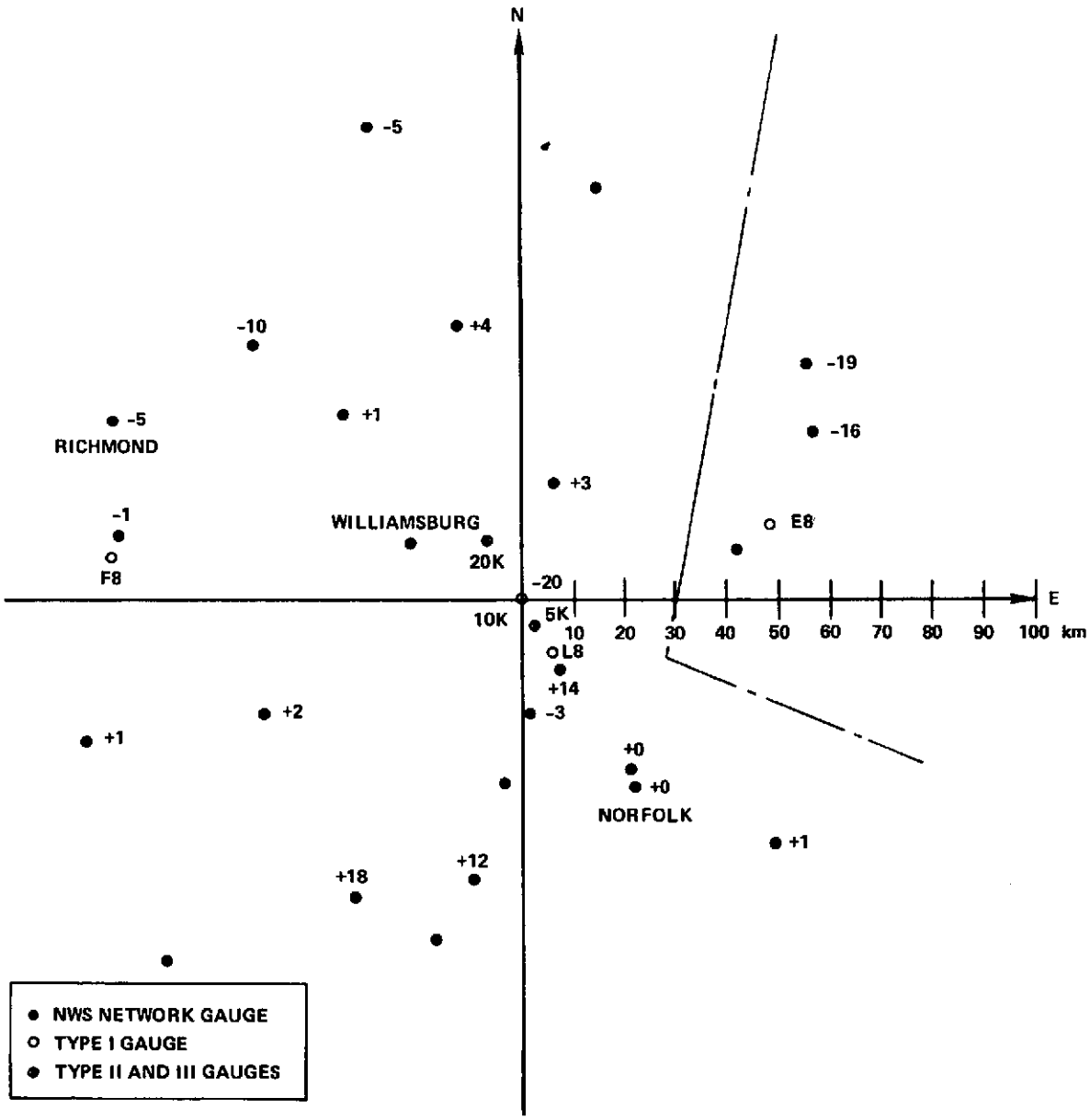

Figure 20a. Map of Percent Departure from Tidewater Division Average Entire Year

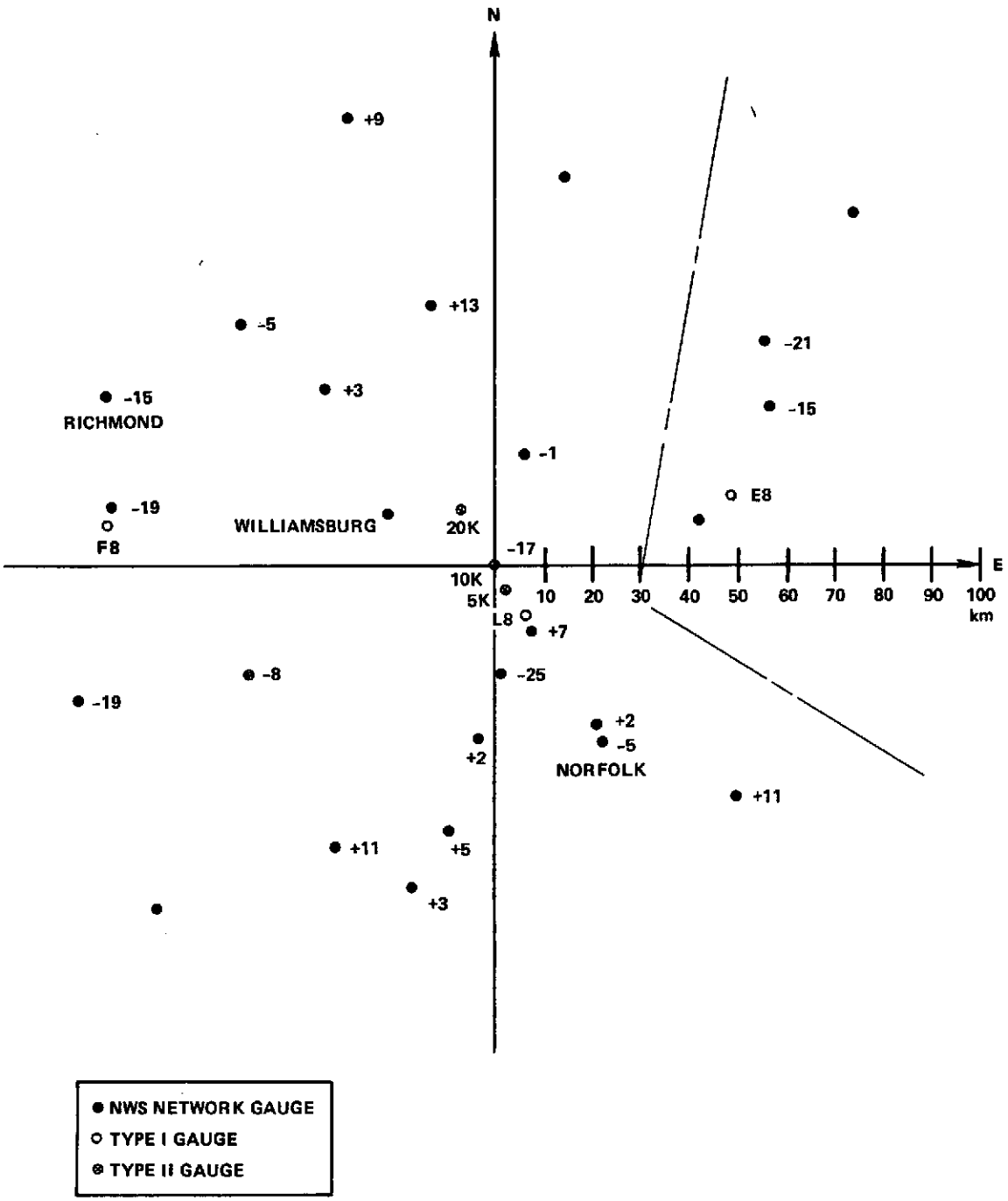

Figure 20b. Map of Percent Departure from Tidewater Division Average, Phase Ia

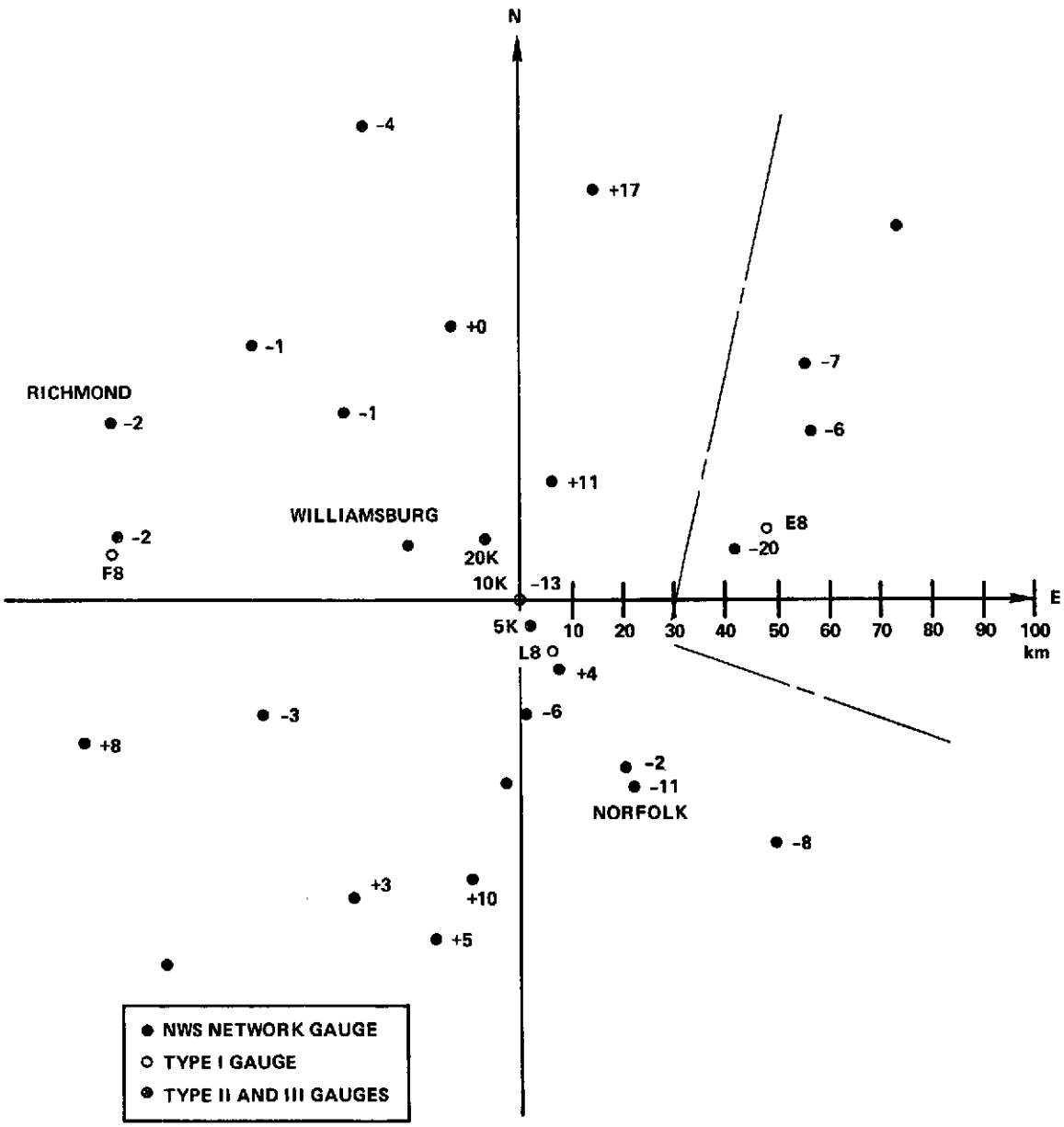

Figure 20c. Map of Percent Departure from Tidewater Division Average, Phase Ib

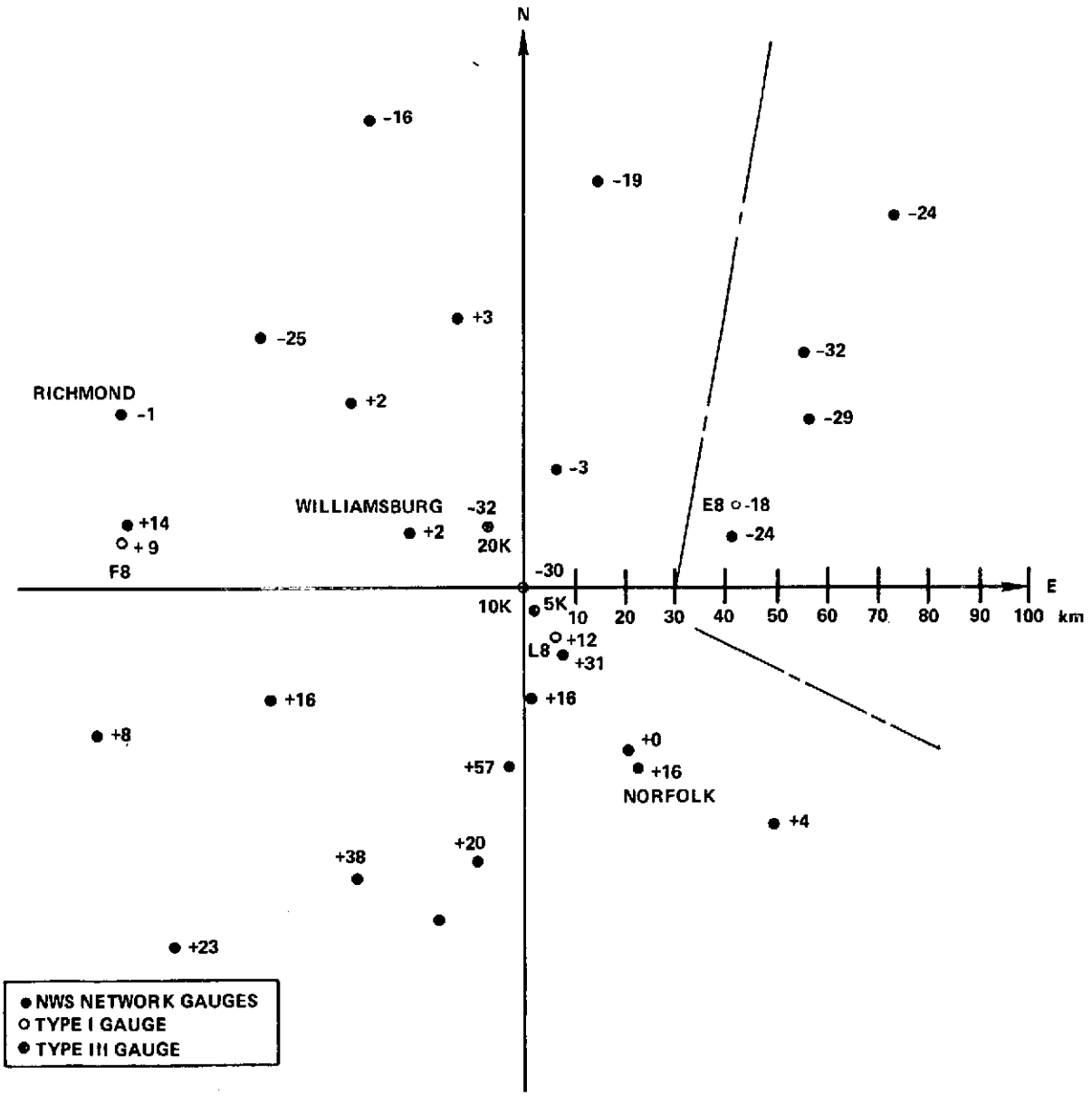

Figure 20d. Map of Percent Departure from Tidewater Division Average, Phase II

in the gauge housing for the time period of July through September and by integrating the rain rates determined using the recorded sequence of gauge tips for the month of June. The latter technique was also used during the July through September time period and was found to give accumulation estimates within 5 percent of the measured value. The type II and III gauge accumulations were all estimated by counting the number of tips that occurred and multiplying by the calibration constant for the gauge. The errors involved in estimating accumulation using this technique should not be more than the 5 percent error obtained with the type I gauge. The low accumulations for the type II and III gauges therefore are indicative of siting errors. Although siting errors are evident, they may not be simply corrected since the error may be rate dependent due to the dependence of error on wind conditions and possible correlations in wind conditions and rain rates.

3.2.2 Calibration Factor and Measurement Accuracy Summary

The gauge calibration factors are listed in Table R1:/2.5. These factors were determined on site by comparing the amount of water collected with the number of tips processed for each gauge. Due to siting error, the type II and III gauges accumulated less rain for a given time period than any of the nearby gauges. The accumulation comparisons are, however, not useful in gauge calibration at high rain rates because the siting errors may be dependent upon synoptic conditions as are rain rates. The siting errors may be rain rate dependent.

The errors in the estimation of Z using rain rate data depend both on gauge calibration and on the Z/R relationship. Equation (47) was used for this relationship. From the discussion in Section 2.2, the Z/R relationship of Equation (47) may underestimate Z by 1 dB and the effect of drop shape may cause an overestimation by 1 dB for rain rates above 20 mm/hr. The measurement accuracy for the gauge systems as given in Table R1:/4-1 therefore must be increased by ± 1 dB. For 100 mm/hr, the gauge accuracies are 1.7 dB for the type I gauge, ± 2.8 dB for the type II gauge, and ± 2.7 dB for the type III gauge, as summarized in Table 11.

The precision of the gauge measurements is given in Table R1:/5-2 and Table 11. The precision estimates must be increased by the uncertainty value for the Z/R relationship. Using the square root of the sum of squares (rss), the precision, including the Z/R relationship is estimated to be ± 1.4 dB for the type I gauge, ± 2.5 dB for the type II gauge, and ± 2.2 dB for the type III gauge.

Table 11
Rain Gauge Error Estimates (~100 mm/hr)

	Phase II		Phase I
	Type I Gauge (±dB)	Type III Gauge (±dB)	Type II Gauge (±dB)
Constant Components—Accuracy			
Calibration	0.5	0.9	1.0
Aerodynamics	0.2	0.3	0.3
Siting	-	0.5	0.5
Z/R relationship	1.0	1.0	1.0
Total accuracy (max)	1.7	2.7	2.8
Variable Components			
Reliability	0.3	2.7	2.7
Precision (reading)	0.5	1.8	2.1
Precision (Z/R relationship)	1.3	1.3	1.3
Total variable error (rss)	1.7	3.5	3.7

4 RESULTS OF MEASUREMENTS

Data were processed for each of the events listed in Appendix A using the revised scale factors given in Tables 9(a) to (d). Data for the bistatic radar system were tabulated and processed only when a 32-dBz threshold was exceeded. The threshold value corresponded to received power levels between 0 and -5 dB with respect to the -115 dBm threshold for useful measurements (true logarithmic operation). The rain gauge data were processed only when a 30-dBz (2.7 mm/hr) threshold was exceeded.

4.1 HOURLY SUMMARIES

Data for every operating hour for each system were investigated for evidence of rain and, for the bistatic radar system, for evidence of signals caused by propagation modes other than rain. Section R1:/2.5* gives the number of hours during which the bistatic scatter path signals were detected ($\langle \bar{P}_r \rangle$ greater than -125 dBm) for at least 1 min of the hour and the number of hours that the rain rate exceeded 1 mm/hr sometime during the hour. The data showed that bistatic signals were detected sometime during a total of 568 hr of the measurement year for the 10K paths and during 128 hr for the 20K paths. These data were useful for editing in preparation for the construction of empirical density and distribution functions.

Data were also obtained from the great circle paths (GC) either via the sidelobes of the 30-ft receiving antenna or the main and sidelobes of the horn receiving antennas. The hourly summary data for the GC paths into the 30-ft antenna sidelobes are summarized in Table R1:/2.7. The GC data showed considerably more occurrences of detected signals for the Eastville great circle path (GCE) than for the Fort Lee great circle path (GCF); 152 and 95 hr, respectively. The GCE path occurrences corresponded either to superrefractive conditions on the largely overwater Eastville to Langley path (ducting or terrain diffraction), or to rain scatter into the sidelobes of the receiver antenna for rain in the vicinity of the receiver site. The GCF path occurrences corresponded entirely to rain scatter into the receiving antenna sidelobes. Since the threshold for interference given in Section R1:/1 corresponds to the detected signal level criteria used in compiling the hourly summaries, mainlobe-to-sidelobe interference would have occurred for at least 1 min of each of the 95 hr logged for the GCF path.

*Citations to Reference 1 materials are prefixed R1:/ throughout this report.

The great circle path scatter system (Sections R1:/2.2.4 and R1:/3.3) monitored the same scattering paths as the 30-ft, receiving antenna system using three horn antennas, one pointed along the great circle path to Fort Lee, one pointed toward Eastville, and the third pointed in nearly the same direction as the 30-ft antenna (10° elevation rather than 13.5° elevation at the same azimuth). The hourly data summary for Phase II for the available path, horn receiving antenna combinations are given in Table 12. The summaries show that signals were nearly always present on the Eastville great circle path (EGCE) and were present over one-third of the time on the Fort Lee great circle path (FGCF). Data for the great-circle-to-horn-antenna paths where the horn antenna was directed along the receiver beams, EGCQ and FGCQ, consisted of either large signals propagating via the great circle path into the horn antenna sidelobes or rain scatter signals into the horn antenna from rain near the receiver site. Of the events recorded, 42 of the 67 hr of data for EGCQ corresponded to rain events, and 52 of the 62 hr for FGCQ corresponded to rain events. Of the hours not corresponding to rain events, 5 hr corresponded to simultaneous occurrences for both paths suggestive of rain scatter that did not occur either over the Langley site (no L8 data), or in the scattering volumes (no 10K, 20K, 10KE, 10KF, 20KE, or 20KF data). The F20KQ occurrences corresponded either to rain events or to FGCQ events that were probably rain caused. The other paths were difficult to interpret due to errors in antenna switching or data recording.

Data for both the great circle path system and the great circle-to-sidelobes of the 30-ft antenna paths were inspected for an indication of possible contamination of the 10K and 20K rain scatter data by other propagation mechnisms. High level signals were recorded on the great circle paths during periods without rain. During these time periods, no signals (peaks) were detected above -115 dBm on the 10KE, 10KF, 20KE, or 20KF paths. For the processing thresholds used, only rain scatter was observed on the 10K or 20K paths.

4.2 ANALYSIS OF SELECTED EVENTS

During Phase II, data were continuously recorded for the 10K paths. An example of the recorded data for the 10KE and 10KF paths is given in Figure 21. Simultaneous 10K gauge recordings are also shown. The data are from event 100, an isolated thundershower that occurred on September 11, 1971. Shown on the figure are the quantized $\langle \bar{P}_r \rangle$ values obtained every 10 s (method A) and the calculated 1-min average $\langle \bar{P}_r \rangle$ values for both the 10KE and 10KF paths. Shown also are the averaged rain rate between tips for the 10K gauge and the rate averaged for each successive minute from the first tip. The original chart records for both the bistatic radar system and rain gauge system are shown in Figure R1:/5-2 and R1:/5-5, respectively. The processed

Table 12
Hourly Data Summary for Great-Circle-Path System

Period (1971)	EGCE[1] Data (hr)	E20KF[1] Data (hr)	EGCQ Data (hr)	E20KQ Data (hr)	FGCF Data (hr)	F20KE Data (hr)	FGCQ Data (hr)	F20KQ Data (hr)	Duration of Period (hr)
June	600	1	17	5	347	7	10	10	720
July[2]	439	96[2]	29	12	289	6	21	12	744
August	625	147[3]	16	20	218	1	20	6	744
September	608	—	10	4	125	5	9	6	720
October	41	—	—	2	15	—	4	—	48
Phase II	2263	244[3]	67	42	948	19	62	31	2904

1 Path notation is of the form: transmitter site–path–receiving horn antenna. EGCQ specifies Eastville great circle antenna as transmit antenna and the horn directed along the 30-ft receiving antenna beam as receiver.

Transmitter site: Eastville (E) or Fort Lee (F)

Path: Via the 20° (6-km height) scattering volume (20K) or great circle path (GC)

Receiving horn antenna: Directed toward Eastville (E) or Fort Lee (F) along 30-ft antenna beam (Q).

2 Great circle receivers inoperable for 83 hr during month of July.

3 Appear to be in error, data for EGCE and E20KF are nearly identical from July 26 to August 9.

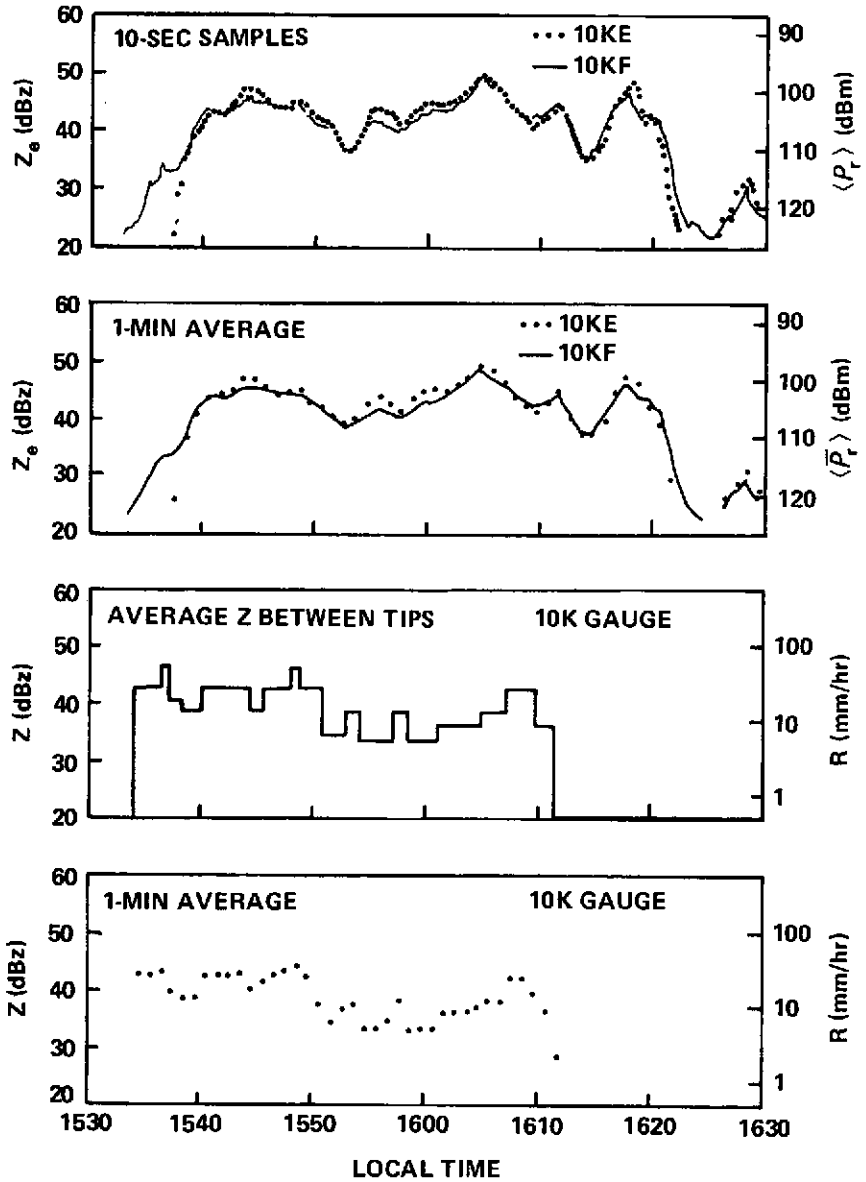

Figure 21. Reflectivity Estimate Time History, Event 100

rain gauge data shown here are identical to those originally shown in Figure R1:/5-6, except that $Z = 270\ R^{1.3}$ was used to relate Z to rain rate for Figure 21, and $Z = 200\ R^{1.6}$ was used for Figure R1:/5-6.

The bistatic radar data show nearly identical Z_e values for both paths (the revised scale constants for the 10KE and 10KF paths were identical during the month of September). The 10KE values tend to be higher than the 10KF values at the relative received signal maxima and lower at the minima. From Figure 11, this is expected for cells with a horizontal width less than 3.5 km. The 3.5-km width value was assumed for the computations of the revised scale constants. For cells that cross the receiver beam at a distance from the center of the common volume, the 10KF signal level should exceed the 10KE level. This behavior is noted between 1533 and 1538 local time (LDT) and from 1620 to 1626 LDT.

The difference in Z_e values at the relative maxima may be due to either calibration error or occurrences of cell sizes smaller than the assumed 3.5 km. Radiosonde data from four NWS stations surrounding the scattering volume at Dulles Airport, Wallops Island, Cape Hatteras, and Greensboro, N. C., show that the wind speed and direction varied little from 1 to 7 km altitude and had an average value of 10 m/s from 200° azimuth for the four stations at 3-km height. Using this value to approximate cell motion, the cells crossed the narrow receiver beam at an angle of 80° with a speed of 10 m/s. Since the receiver beamwidth at the scattering volume is 0.15 km, which is less than one-tenth the expected cell size, the received signal level time history may be used to estimate cell size (assuming that the cell translates through the volume and does not grow or decay while translating). The half-power received signal points (-3 dB relative to the Z_e maxima) are separated by time intervals between 1.5 and 3.5 min, corresponding to widths between 0.9 and 2.1 km. The peak estimated Z_e values are 3.3 dB low for the 10KE path and 4.3 dB low for the 10KF path for a 0.9-km cell width, and 0.9 and 1.3 dB low for the 10KE and 10KF paths, respectively, for a 2.1-km cell width. The relative Z_e estimates for the two paths will also vary from 0.4 to 1 dB, as is observed in the data on Figure 21. The data for event 100 indicate that the cell size estimate was in error and that the calibration values were correct. Since the 1-min averaged value was of interest, the Z_e value averaged over the minute will be slightly less than the peak value (0.4 dB for a 1.5-min apparent cell width with the center of the cell in the center of the 1-min averaging interval and less for longer cell passage times). The relative error due to a misestimate in the percentage filling of the scattering volume (horizontal cell size) will be the same.

The rain gauge records show little similarity in the structure of the observed Z time history. The records show that it rained at the surface at

about the same time scattered signals were observed from the common volume. The 10K gauge was placed near the scattering volume subpoint. With a 10 m/s horizontal wind, rain traversing the common volume will land at the surface approximately 4 km away from the subpoint (assuming a 7 m/s fall velocity for rain drops). Due to the variation of drop fall velocities with size, changes in wind with height, and natural modification of the drop size distribution as the drops fall, it is possible to associate a rain rate measurement at a point on the surface only with a Z_e estimate for a point at some height above the surface in a statistical manner. The observed histograms, or number density, of Z_e values for the 10KE path (10KE bistatic) and the 10K gauge are shown in Figure 22 for this event. Also shown is the number density for the L8 gauge, which was located 12.5 km from the 10K gauge.

The number densities display little regularity or agreement with each other. The sample size for a single event is not sufficient for the comparison of number densities of Z_e obtained from the bistatic radar data and Z from the rain gauge data. In an attempt to remove some of the fluctuations in the 10K rain gauge data caused mainly by data reading and processing (see Section R1:/5-2) the number densities were averaged over adjacent 4-dBz intervals. The average number densities for the 4-dB-wide intervals (category* averages) are depicted by the solid lines. An examination of the 10K gauge data reveals spikes in the number densities at 38, 40, and 42 dBz. The spikes correspond to the quantization steps used to measure the time between tips, 0.04, 0.03 and 0.02 hr. The 4-dB-wide intervals average over the quantization intervals, reducing in part the quantization error.

The data in Figure 21 show that relatively rapid changes of Z_e were detected over time periods as short as a minute. For Z_e values below 40 dBz, 12 dB/min changes were observed; between 40 and 50 dBz, 5 dB/min changes were observed. These changes are approximately linear (in dB) and have Ξ values of 16 and 3, respectively. From Section 2.1, corresponding measurement errors as large as 1.3 and 0.2 dB would have occurred for the other processing methods (B, C, D, E and G).

*The category notation is that of Austin (1971), with category 6 corresponding to Z_e values between 30 and 34 dBz, and higher category numbers for higher Z_e value class intervals.

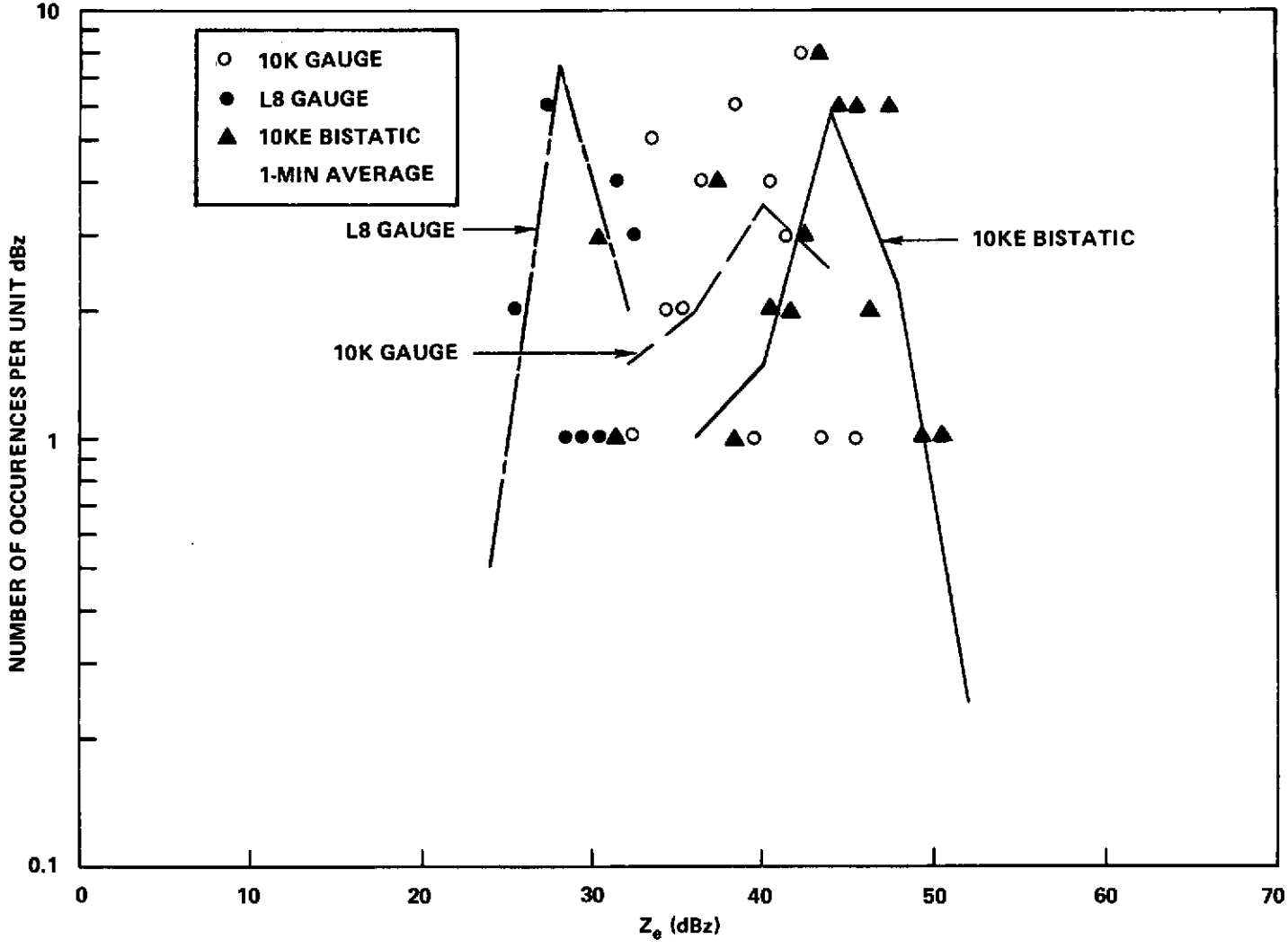

Figure 22. Number Density for Reflectivity Estimates for September 11, 1971 Event 100

Data for an isolated shower observed on May 5, 1971 (event 54) is shown in Figure 23. These data show a change of 12 dB in 1 min while the signal increased for the second peak and a decay of 13 dB in 1 min after the peak passed. The average wind speed at height was 20 m/s at an angle of 40° to the receiver beam. Assuming that the cell translates with the wind at height (3 km), the cell would have a half scattering intensity width of 2 km. For this day, measurements by methods other than A would be in error during the rise and fall of the signal and the measurement is in error by 0.9 dB due to the limited horizontal extent of the cell.

Data for an isolated thundershower observed on June 12, 1971 are shown in Figure 24. On this day, the wind speed varied between 6 and 10 m/s between 3-and 6-km height. The wind was from an azimuth of 310° and cell motion was essentially along the receiver beam. For this case, the peak Z_e values were in near agreement for the 10KE and 10KF paths. Since the cell motion is parallel to the largest dimension of the scattering volume, it is difficult to directly estimate cell size although the 2.5-min duration suggests a size on the order of 1.5 km. The estimated Z_e time history between 1820 and 1840 LDT is indicative of the differences in response of both bistatic scatter paths for cells not centered in the common volume but located close to the common volume along the receiver beam. Analysis of this data for Z_e estimates below 38 dBz is difficult, since the common volume is not filled in accordance with the assumption of a centered 3.5-km wide cell. If it is assumed that the highest Z_e value for a particular event represents cell passage close to the center of the scattering volume, then data for levels 10 to 20 dB below the peak level may correspond to occurrences of cells not centered in scattering volume. The data in the scattergram for July 11, 1971, event 81, shown in Figure 17 are also indicative of this effect since the scattergram broadens for Z_e values 10 dB below the peak. The scattergram for the peak values for each event, Figure 19, also shows a tendency toward broadening for values below 38 dBz, suggestive of cells missing the scattering volume center.

The several examples of data from single events show that data from more than one event must be combined to provide information about the statistical relationship between rain gauge measurements on the surface and scattering measurements made at heights of several kilometers above the surface. The data also show that the rain cells may be smaller than the 3.5-km horizontal size assumed in computing the revised scale constants, although the scattergrams show that 3.5 km is correct on average (providing the peak reflectivity estimates are for cells centered in the common volume). The data also show that reflectivity estimates below approximately 38 dBz may be contaminated by nearby cells that are just outside the common volume.

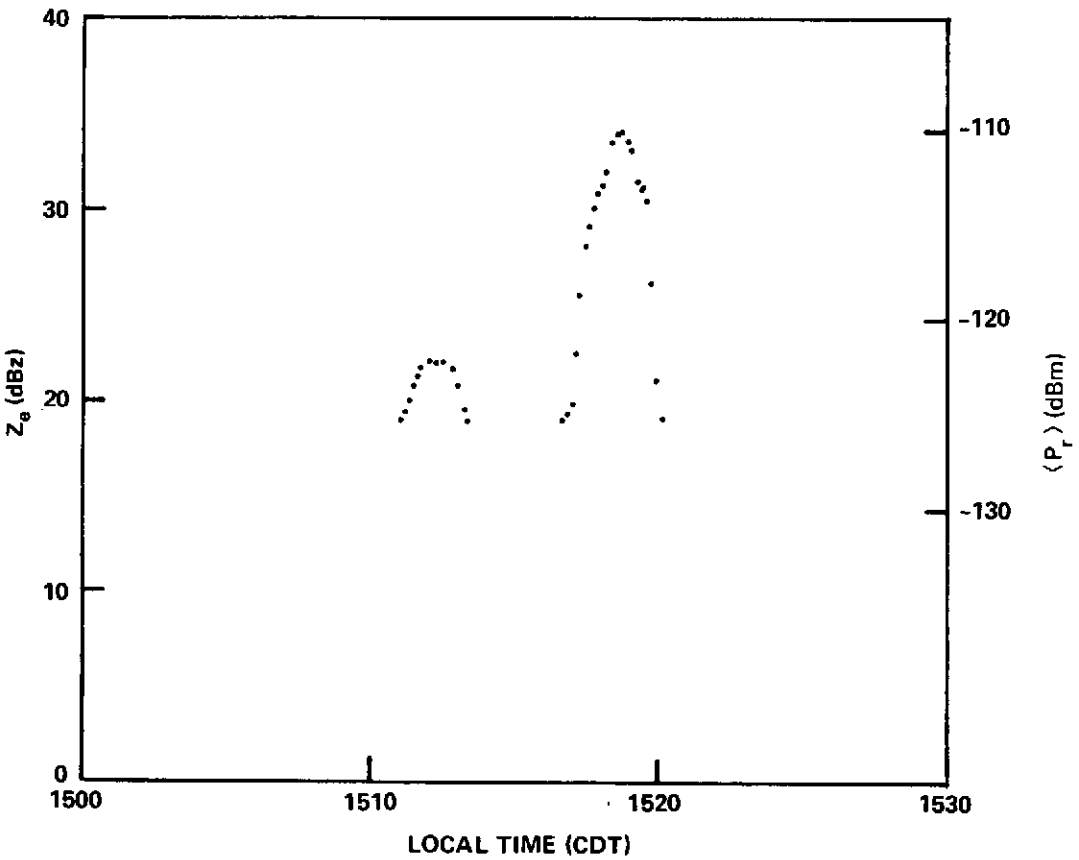

Figure 23. Reflectivity Estimates for Bistatic Radar 10KE Path for May 5, 1971 Event 54

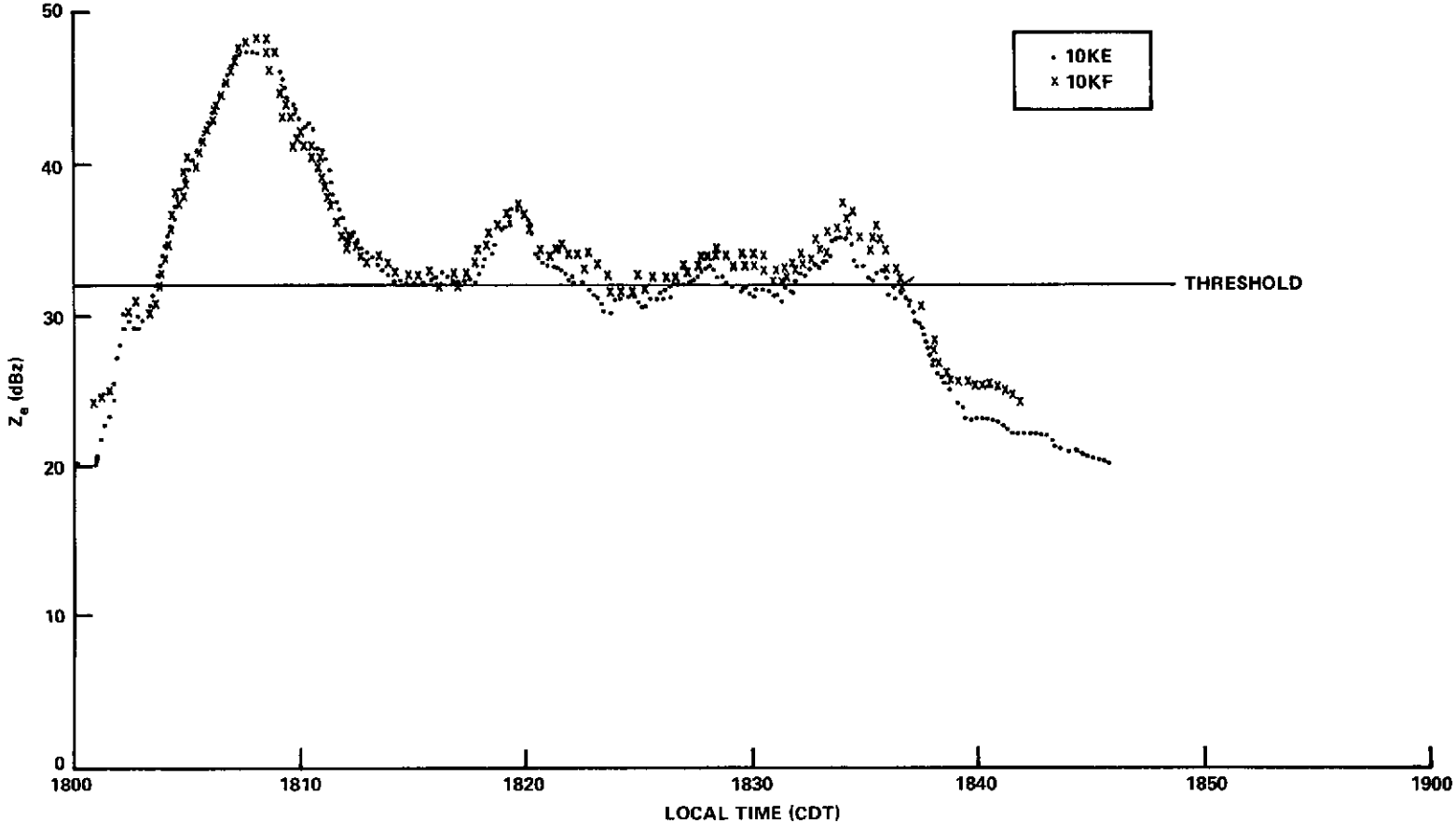

Figure 24. Reflectivity Measurements of June 12, 1971 Event 71

4.3 ANALYSIS OF DATA FROM PHASE II

4.3.1 Equivalent Reflectivity Number Densities

The combined bistatic radar reflectivity estimates for all Phase II measurements are summarized in the number density histograms given in Figure 25. Due to both the errors caused by changes in system behavior (repeatability) and data processing (precision) the individual density values for a given Z_e class (intervals 1-dBz width) show a spread about some best estimate value. The a priori error was less than ±3.5 dB for the 10K paths and 4.3 dB for the 20K paths (precision and repeatability for each component were combined by summing squares—see Table 10). The expected standard deviation due to errors in Z_e is approximately 1.2 dB for the 10K paths and 1.5 dB for the 20K paths (one-third of the maximum values, assuming a Gaussian distribution of errors and a maximum error approximately three times the standard deviation). By averaging over four adjacent Z_e class intervals (category average) a smoothed estimate is provided as shown by the lines in the figure.

4.3.2 Combination of Measurement Errors

The effect of measurement error may be assessed by approximating the measured number density by an exponential density function. The approximate density (best fit by eye) is

$$\hat{p}(z) = ce^{-az} \quad (30 \leqslant z \leqslant 50) \tag{47}$$

where

$\hat{p}(z)$ = approximation to the measured number density

$z = 10 \log Z_e$

a, c = constants

For both the 10KE and 10KF paths, $a \simeq 0.2$. The error distribution is assumed to be Gaussian with a 1.5-dB standard deviation. The measured density function is the convolution of the error density function and the true density function that

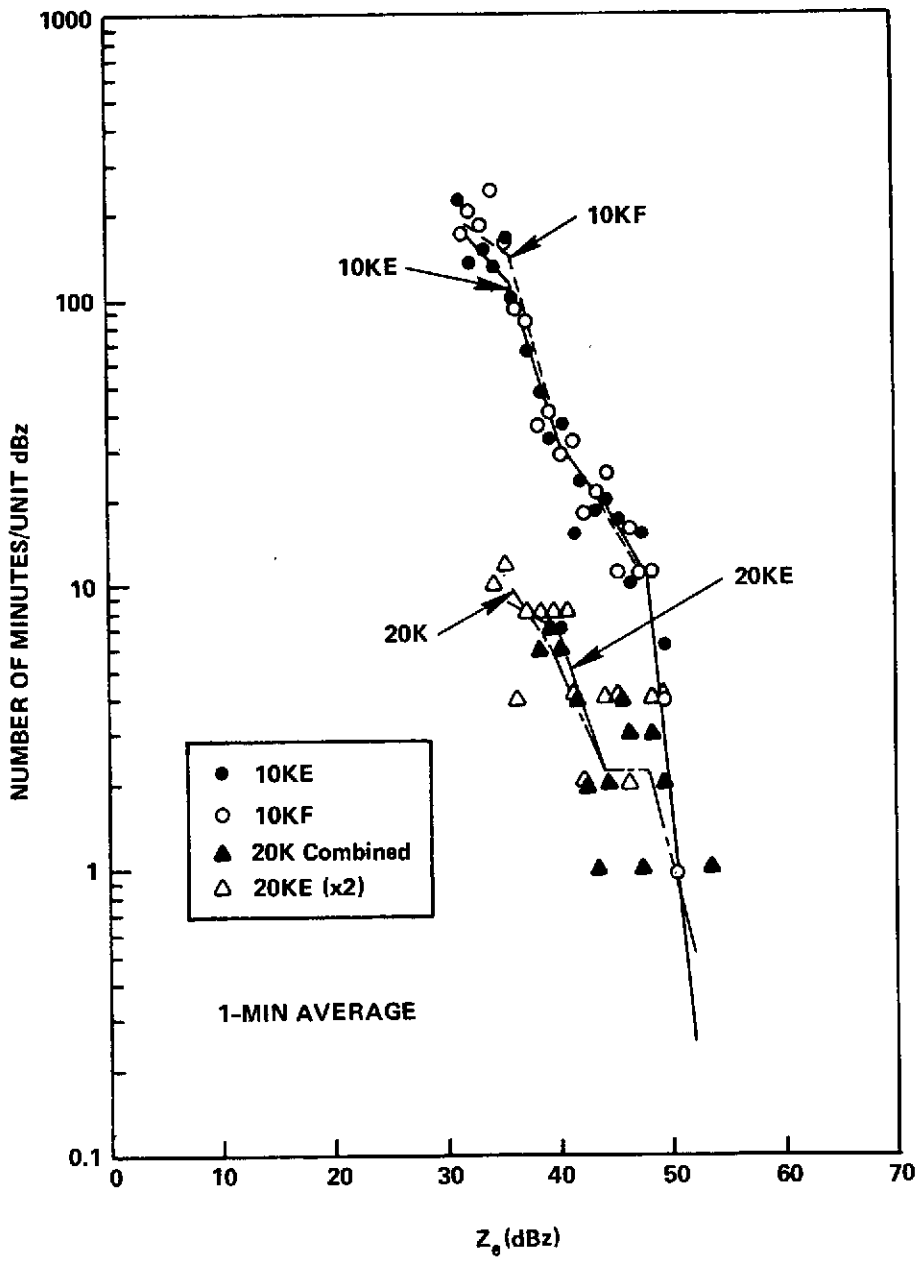

Figure 25. Number Density for Reflectivity Estimates for Bistatic Radar Data of Phase II

is to be estimated:

$$\hat{p}(z) = \int_{z_{min}}^{z_{max}} p_e(x - z)\, p(x)\, dx$$

$$= \int_{z_{min}}^{z_{max}} p(x)\, \frac{e^{-(x - z)^2/2\sigma^2}}{\sqrt{2\pi\sigma^2}}\, dx \qquad (48)$$

where σ = standard deviation of the error distribution and z_{min}, z_{max} are the extreme values of z. Equation (48) is an integral equation that must be solved for $p(\hat{z})$. Noting that the convolution of an exponential distribution and a Gaussian distribution is an exponential distribution

$$\hat{p}(z) = ce^{-az} = \int_{z_{min}}^{z_{max}} c'e^{-ax}\, \frac{e^{-(x - z)^2/2\sigma^2}}{\sqrt{2\pi\sigma^2}}\, dx$$

$$= c'e^{-az}\, e^{a^2\sigma^2/2}\, \frac{1}{2}\left[\text{erf}\,(z_{max} - z + \sigma^2 a) - \text{erf}\,(z_{min} - z + \sigma^2 a)\right]$$

where erf is the error function (see Abramowitz and Stegun, 1964), and c is the constant for the true exponential distribution to be estimated. The term $\sigma^2 a \simeq 0.5$, hence for z near midrange, the arguments of the error functions

may be replaced by $\pm\infty$ and

$$c \sim c' e^{\frac{a^2\sigma^2}{2}}$$

For the a and σ values assumed, the true number density is 9.4 percent lower than the measured number density for the same z value. The identification of Z_e with each class interval is also in error by the possible uncertainty in system calibration (accuracy), which is a constant error throughout each phase of the experiment. For Phase II, the 10K path Z_e measurement accuracy is ± 2.9 dB. For the exponential distribution, the 9 percent number density estimate error is equivalent to an increase of 0.2 dB in Z_e for the same number density or an overestimate of Z_e by 0.2 dB. The effect of the variable component of the measurement error is to decrease the experiment accuracy by 0.2 dB.

The effective error in estimating Z_e for the 20K path is roughly the same, because a is approximately the same, although c differs by nearly an order of magnitude. The data for 20K combined were obtained by summing the number densities for the separate 20KE and 20KF paths. The data were combined in this manner to compensate for the alternate sampling of the 20K scatter volume. For a large enough number of samples, the density function obtained by combining the two data sets should be equal to twice the number density values for each of the data sets, providing that the true (parent) density function is stationary. The 20KE values shown in Figure 25 represent twice the measured number density values for alternate minute observations of the 20K scattering volume. The category averages show differences of as much as 2 dB due to either the effect of sampling or the misalignment of cells and the common volume. The category averages for the 10K paths show departures as large as 2 dB only at the low Z_e value extreme of the empirical density function where cell, scattering volume misalignment and scattering volume size differences are responsible for the 10KF overestimates. Since the 20K path-category average differences occur at relatively high Z_e values, it is assumed that sampling effects are responsible, and the combined density function rather than twice the individual density functions will be used to represent the data.

4.3.3 Reflectivity Number Densities

The rain gauge data were also summarized using empirical number density functions. The data for the two type I rain gauges located at the receiver site, L8 and L19 gauges, are shown in Figure 26. The variable component of the measurement error has a standard deviation of 0.5 dB (repeatability ±0.3 dB, Section R1:/4.4; precision ±1.3 dB for the Z/R relationship, Section 2.2; precision ±0.3 dB for chart reading, Section R1:/5.2 and Table 12). The variable component of the measurement error is one third that of the measurement error of the bistatic radar system and the spread of the number density values about the category averages is somewhat less. Figure 27 shows data from the type I gauges at each of the sites. Since the L19 and L8 category averages were essentially identical except for the high Z_e values, where the L8 gauge has higher accuracy, the L8 gauge category average was used for comparison. The F8 (Fort Lee) and E8(Eastville) category averages again provide a good fit to the empirical density functions. The differences between the F8, E8, and L8 category averages are primarily due to sampling rain at the surface at sites spaced by many tens of kilometers. The E8 gauge shows a trend toward a lower number density for Z_e values below 40 dB. This is presumably the effect of siting on the Delmarva Peninsula, where total rain accumulations are generally less than those for the rest of the Tidewater District of Virginia. The difference between the L8 and F8 gauges for Z_e values above 48 dBz may be climatic or may be due to sampling; insufficient data are available for analysis.

Figure 28 depicts the number densities and category averages for the type III gauges that operated during all of Phase II. The category average for the L8 gauge is again included for comparison. The type III gauge data evidence a greater spread in data points about the category average, due primarily to the difficulties experienced in reading the data (Section R1:/5.2). Although the L8 and 20K gauges were each only 12.5 km from the 10K gauge, considerable differences are observed in the category averages. Both the type III gauges appear to underestimate the L8 gauge data (Z_e values) by 3 dB. This is due primarily to siting and is larger than the 2-dB difference estimated on the basis of accumulation measurements (42 percent, see Section 3.2). The type III data also have large spikes corresponding to the time quantization intervals of the reading process. The spikes are indicated on the figure.

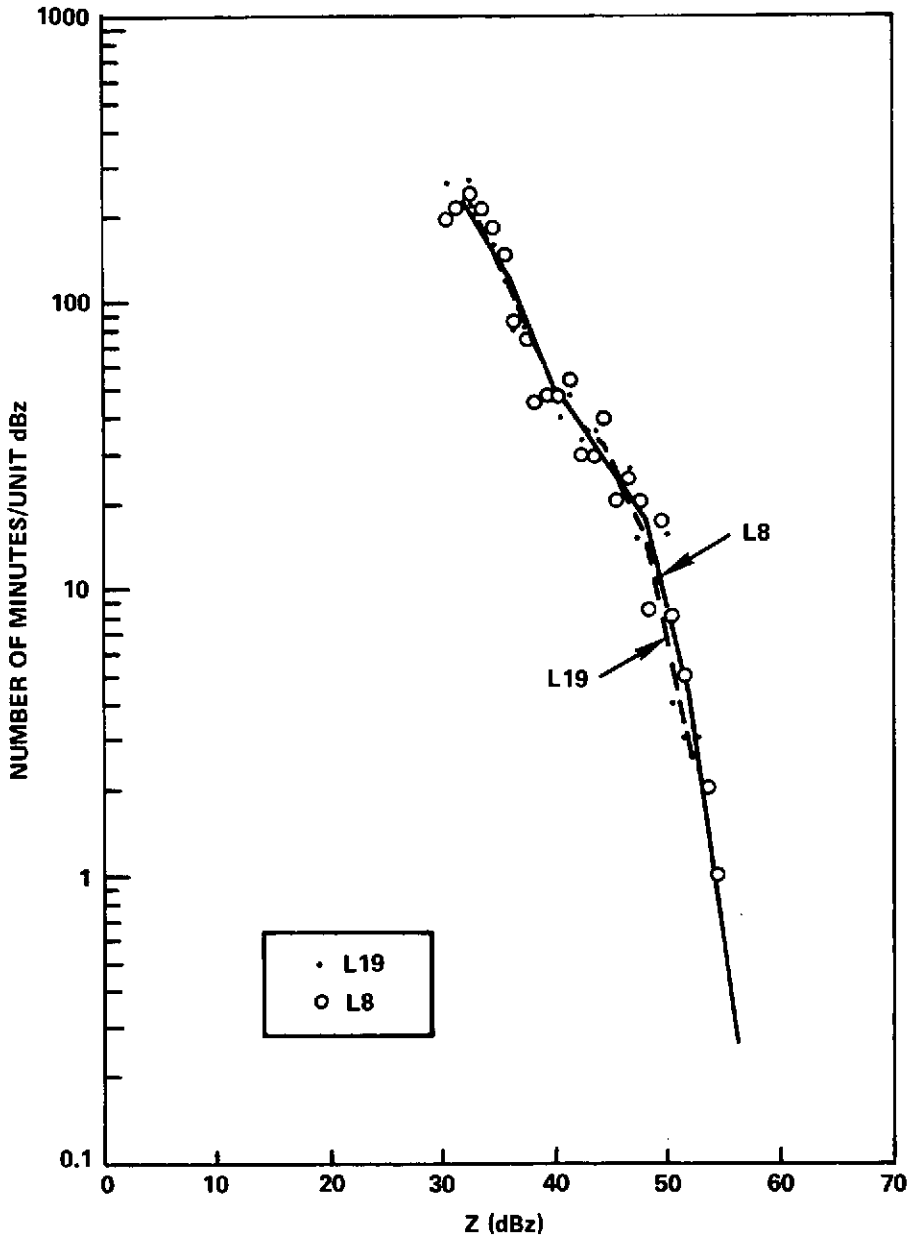

Figure 26. 1-Minute Average Rain Gauge Densities in Phase II

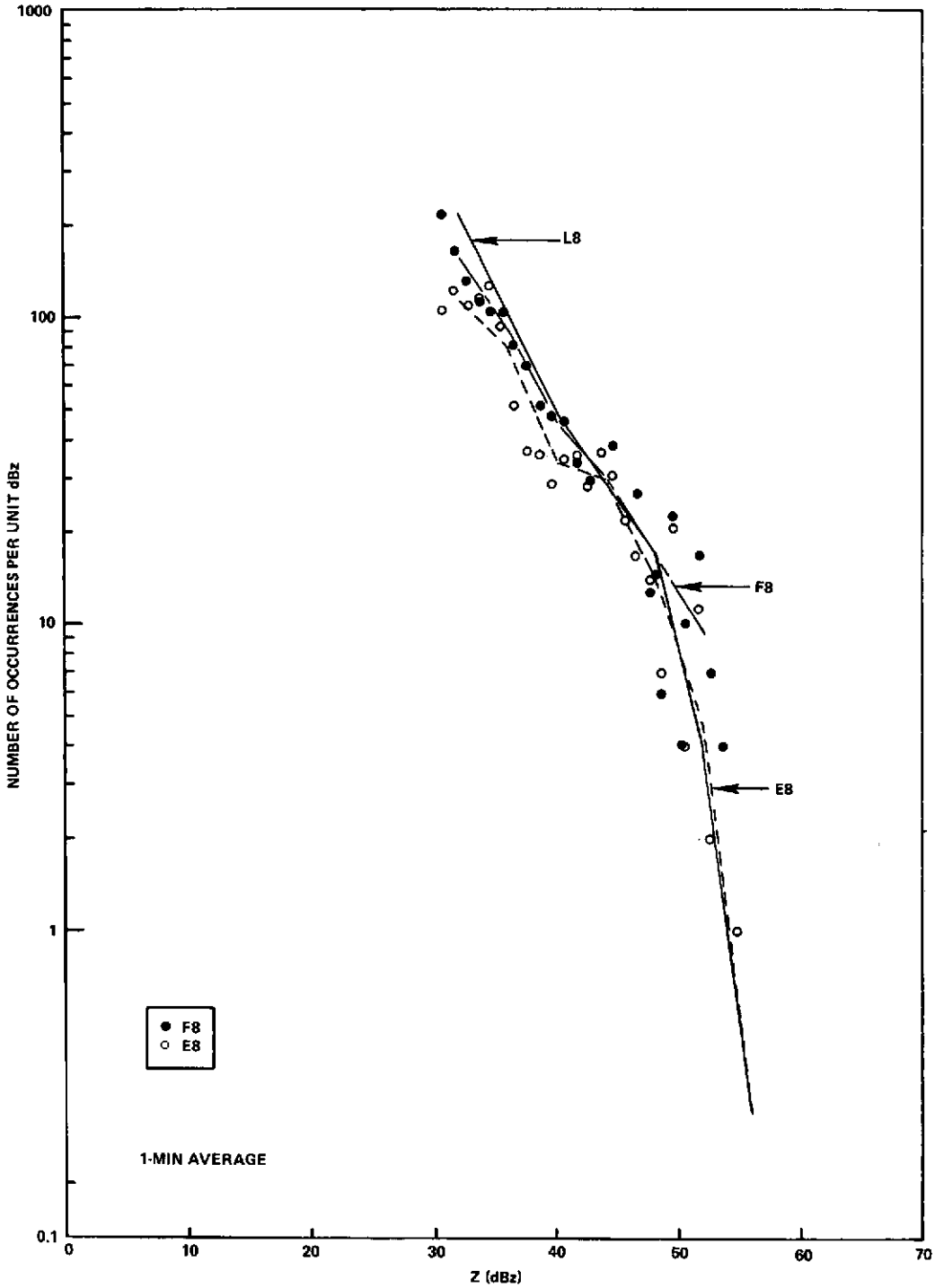

Figure 27. 1-Minute Average of Type I Gauges in Phase II

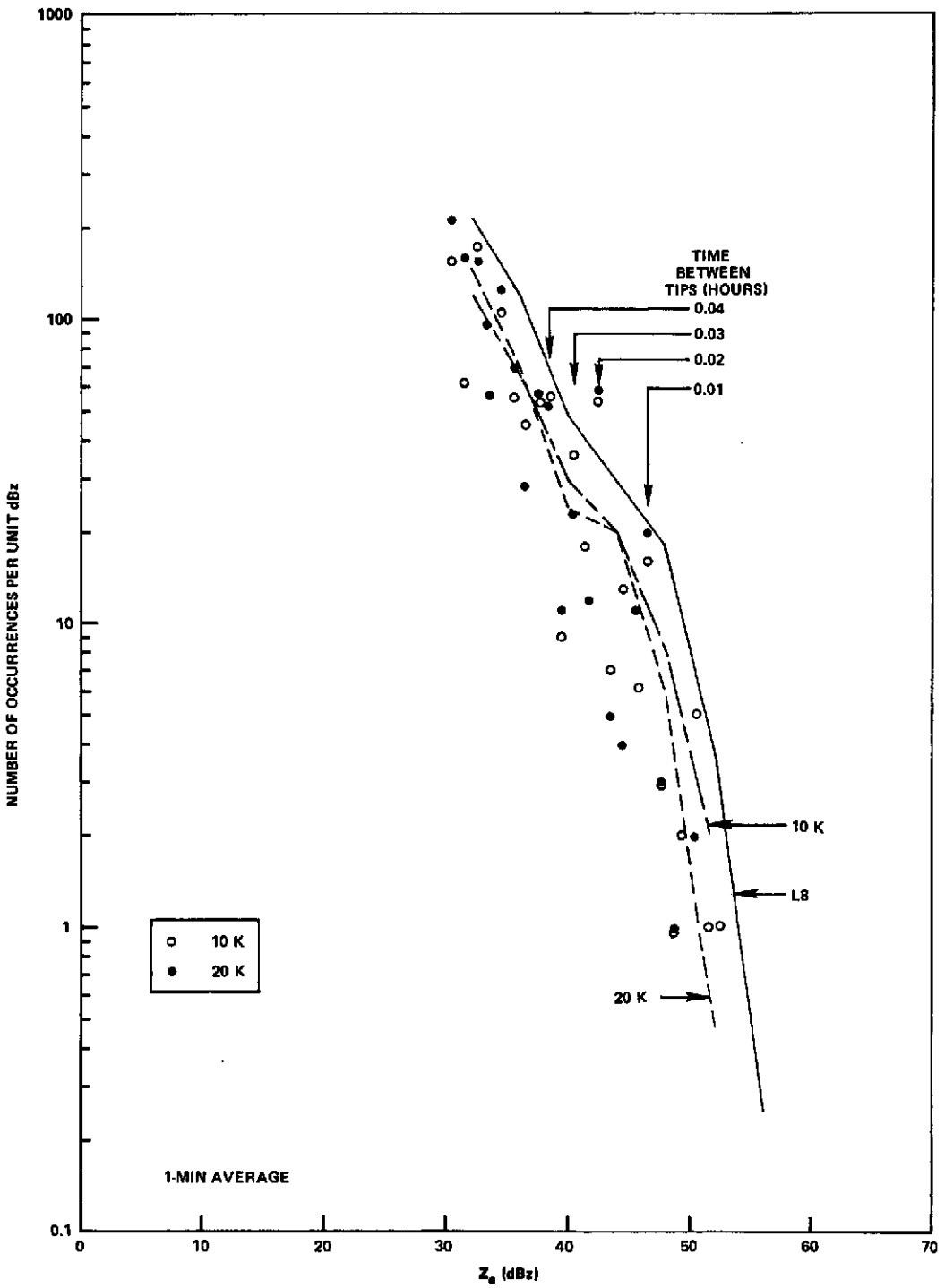

Figure 28. 1-Minute Average of Type III Gauges in Phase II

4.3.4 Comparison Test for Number Densities

Each of the number densities may be compared to determine if they represent samples from the same distribution. The use of rain gauge data for the prediction of scattering effects is predicated on the hypothesis that, for a sufficient number of samples, the densities for Z values estimated from rain gauge data and of Z_e estimated from the bistatic radar data are identical. The measured densities may be compared using a chi-square goodness-of-fit test (Von Mises, 1964). To remove the effects of time quantization, the chi-square tests were performed on the number densities (histograms) pooled by category (four times the category average). The histograms were compared using the chi-square goodness-of-fit of Pearson with the pooled number density of the L8 gauge used in the role of the known distribution. Since the reference histogram values of the L8 gauge were not adjusted prior to comparison, the test function

$$F^2 = \sum_{i=7}^{12} \frac{(f_i - F_i)^2}{F_i} \tag{49}$$

where

f_i = pooled number density of distribution to be tested

F_1 = pooled number density for the L8 gauge

was compared with $\chi^2_{6,0.05}$ (chi-square distribution, six degrees of freedom).

If $F^2 \leq \chi^2_{6,0.05}$, the number densities were judged to be identical at 0.05 level of significance (probability equal to 0.05 that two samples from the same distribution are judged to have been obtained from different distributions). Only the data for Z_e classes between 34 and 54 dBz were used in the distribution tests. The Z_e values below 34 dBz were not included due to the possible effects of receiver nonlinearity and to the relatively long integration time between tips (5.5 min for type III gauges and 3 min for type I gauges at 34 dBz). Using this test, the L8 and L19 gauge number densities were found to be identical, as shown in Table C-5 of Appendix C (identical density functions are tagged with

the word "yes" in the test row of each table). Using the 10KE bistatic radar data as reference, the 10KF density was found to be identical with the 10KE density if Z_e values greater than 38 dBz were used (test using categories 8 through 11 and $\chi^2_{4,0.05} = 9.5$). All other combinations of measured density functions were found to be different.

The measurement systems were independently calibrated and have calibration errors (accuracy) estimated to be ±3.8 dB (maximum) for the 10K bistatic radar scatter paths, ±2.7 dB for the type III gauges, and ±1.7 dB for the type I gauges. Since the L8 gauge has the smallest calibration error, it was used as reference. The number density plots (Figure 28) show that a relative shift of 3 dB in the calibration of the type III gauges relative to the L8 gauge would bring the data into better alignment (implying calibration errors greater than 1.7 dB (2.7 dB was not used, since the 2.7-dB value includes the effect of errors in the Z/R relationship for rain rates in excess of 5.6 mm/hr). Using a 3-dB shift in calibration (recalibration by increasing Z measured by the 10K and 20K gauges by 3 dB for each recorded number density value), the chi-square goodness-of-fit tests were again repeated (Table C-5, Appendix C). For this test, the data had been used to adjust the calibration constant, therefore the number of degrees of freedom for the test is reduced by one. The recalibrated (shifted) 10K gauge density was found to be identical to the L8 gauge data but the shifted 20K gauge density remained different. A 1-dB change in the 10K path (bistatic) calibration constants also appeared to bring the L8 gauge and 10KE bistatic data into better agreement. With this shift (or any other shift), the density functions (bistatic radar-to-rain gauge comparisons) were again found to differ.

The category averages for each of the rain gauges used in the experiment and the NWS tipping bucket gauge at Norfolk* are shown in Figure 29. The test values are given in Appendix C. The densities for the bistatic radar data and the L8 and 10K gauges are given in Figure 30. In this figure, the 10K gauge data excluding event 80 are also shown. Event 80 was excluded because a power failure occurred at the receiver site; consequently, both the bistatic radar data and the L8 gauge data for Event 80 were not included in the comparison. The 10KF bistatic radar data are not shown since they are almost identical to the 10KE data.

*Data reduced from NWS gauge records by the Weather Radar Research Project Staff, Department of Meteorology, Mass. Institute of Technology.

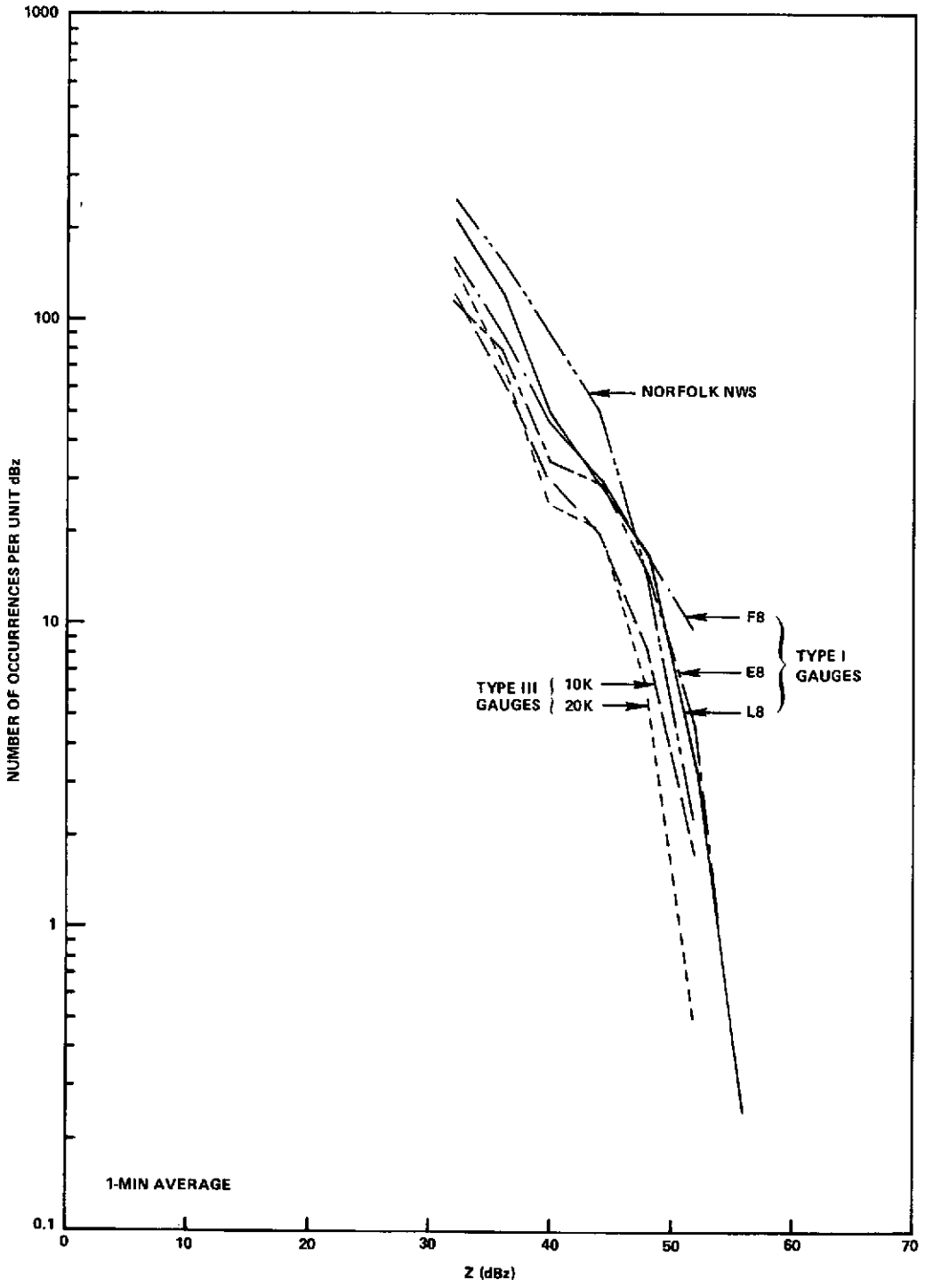

Figure 29. Gauge Densities for Phase II

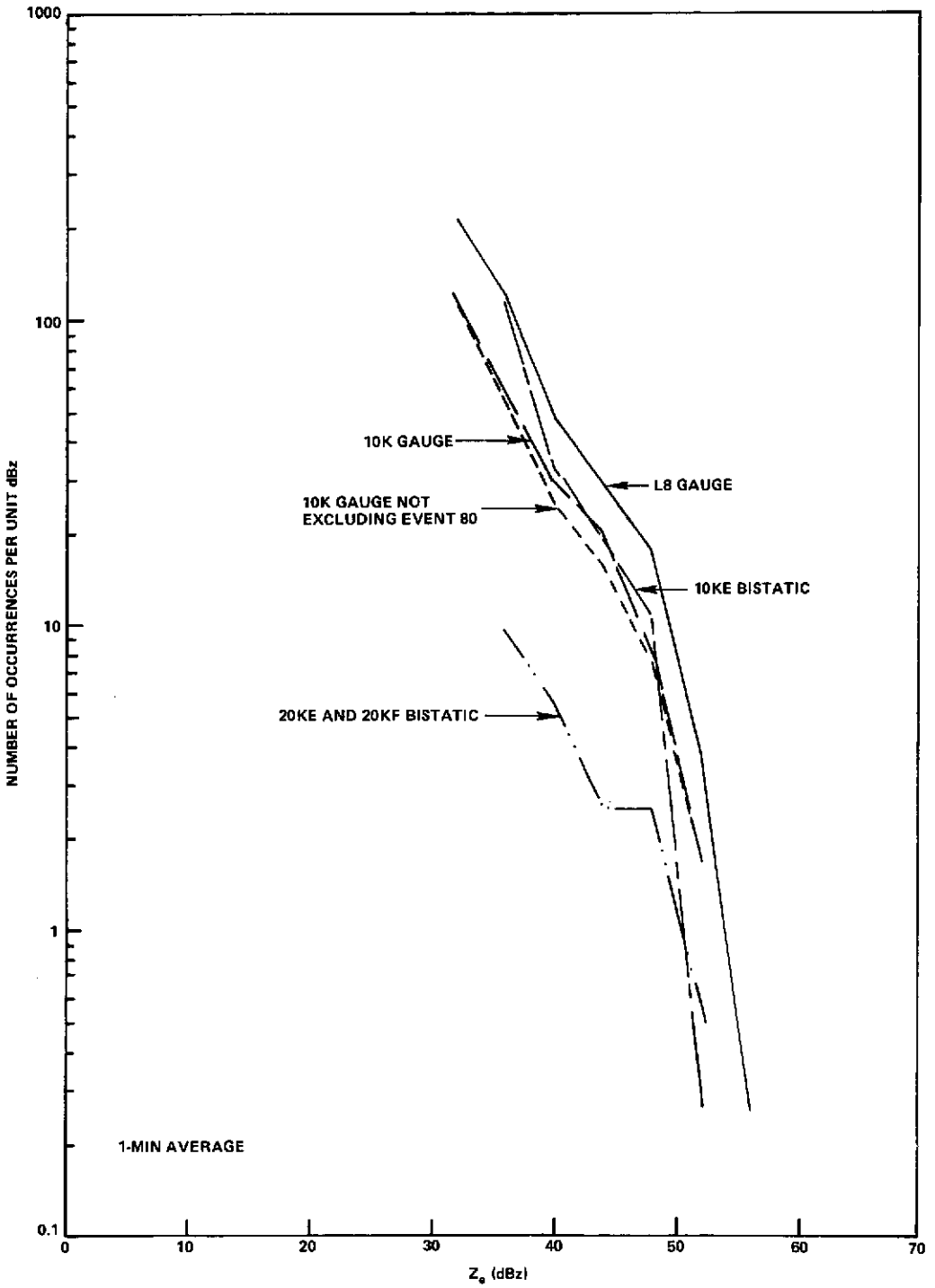

Figure 30. Estimated Reflectivity Densities for Phase II

4.3.5 Comparison of Number Densities by Rain Type

The events that occurred in Phase II were due either to thundershowers or to tropical storm Doria and hurricane Ginger. Both Doria and Ginger (events 98b, 104, and 105) caused considerably more rain along the coast than inland. These storms may also have a different distribution of reflectivity with height. To determine whether the rain gauge and bistatic radar densities were identical for either of the two storm types observed, thundershowers and tropical storms, the number densities for Doria and Ginger were compiled separately from all other data. The data for Doria and Ginger are given in Figure 31 for the bistatic radar system, Figure 32 for the rain gauges, and Figure 33 for both the bistatic radar and rain gauge systems. Again, the measured 10KE bistatic density function is identical with the 10KF density for Z_e values greater than 38 dBz, and the L8 gauge density is identical to the L19 gauge density. All other combinations indicate different distributions.

The Phase II data excluding tropical storm Doria and hurricane Ginger are given in Figures 34 to 36. The 10KE and 10KF bistatic radar data densities test to be different for Z_e values greater than 34 dBz (categories 7 to 11) but test to be identical for Z_e values greater than 38 dBz (categories 8 to 11). The L8 and L19 gauge densities again are shown to be identical (see Table C-6, Appendix C). The data further show that after recalibration by increasing Z_e for the 10KE path by 1 dB, the L8 gauge density and 10KE bistatic radar density are identical for Z_e values above 42 dBz. The agreement above a set threshold reflects the importance of cells that do not pass through the center of the scattering volume. The rain gauge measurements are for a single point on the surface. The bistatic radar data are for a scattering volume that is large in comparison with the sampling volume of the rain gauge (product of orifice area, drop fall velocity, and integration time). The cells several kilometers distant from the center of the scattering volume still contribute to the received signal (see Section 2.1.2) but not to the rain rate. This may be one of the causes of the lack of agreement in number densities for both rain rate and scatter measurements at the low rain rates (large cell offsets). A second source of density difference may be in the natural change in reflectivity with height.

The recalibrated 10KF bistatic radar data, although agreeing with the recalibrated 10KE data, was judged by the goodness-of-fit tests to be different from the L8 gauge data. The difference persisted for all Z_e thresholds. Agreement would be obtained if a less severe test were used, say at a 0.01 rather than 0.05 level of significance. The other comparisons still show the densities to be different at an 0.01 level of significance. The disagreement between the L8 gauge and 10KF bistatic radar data at the 0.05 level of significance and the agreement between the L8 and 10KE data above 42 dBz again show the effect of scattering volume size. For different cell sizes, the

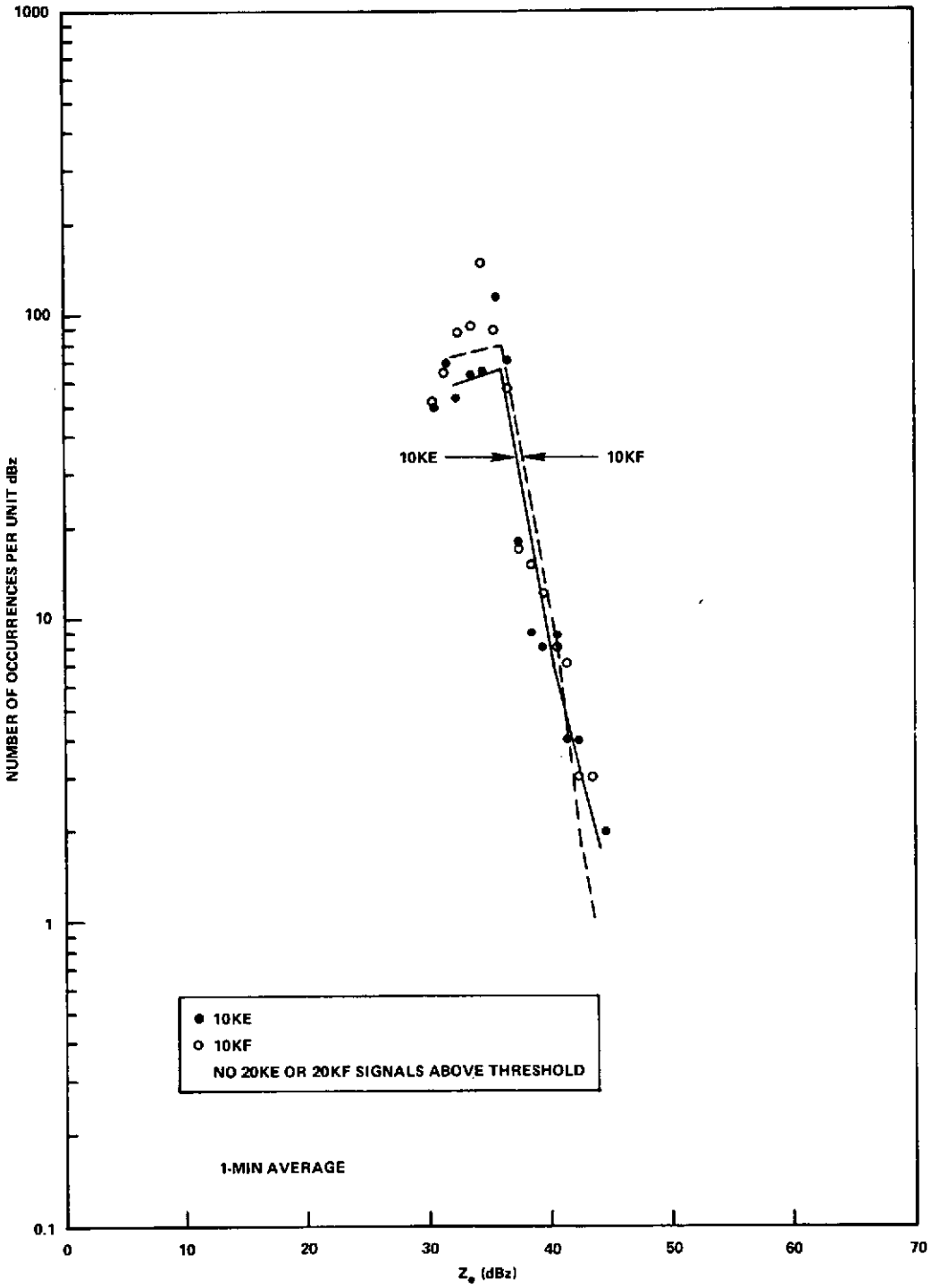

Figure 31. Bistatic Radar Densities for Tropical Storm Doria and Hurricane Ginger

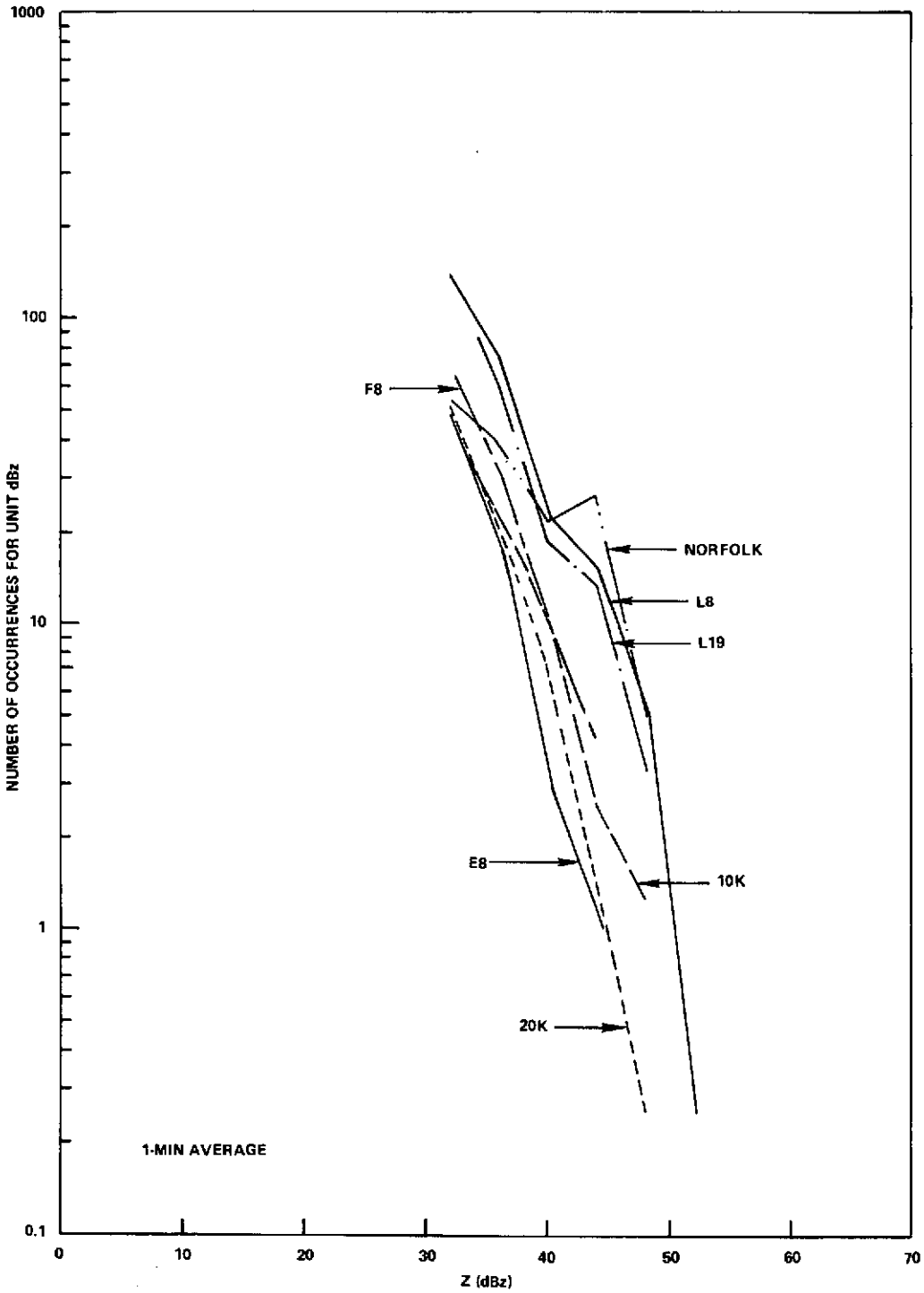

Figure 32. Gauge Densities for Tropical Storm Doria and Hurricane Ginger

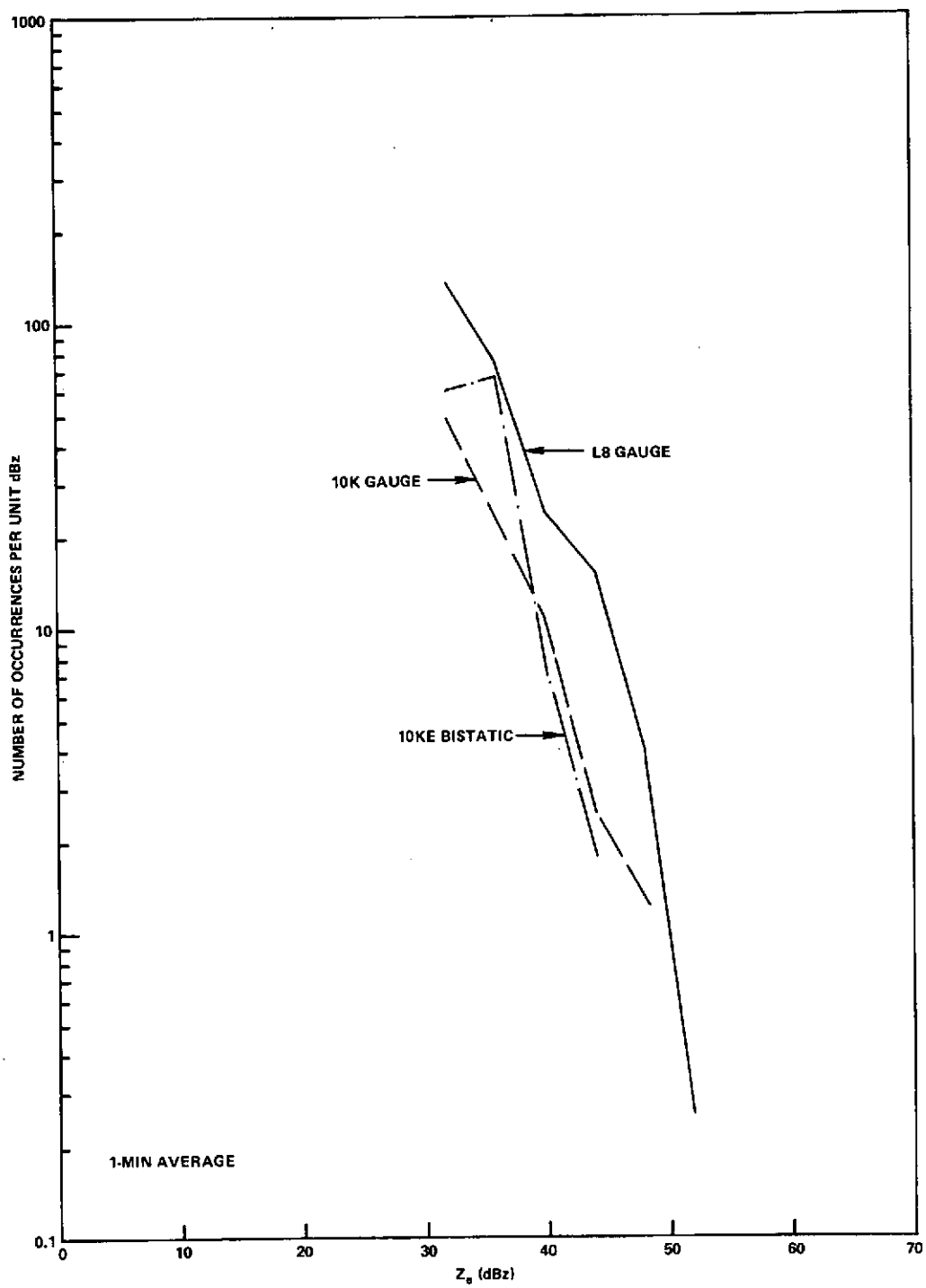

Figure 33. Estimated Reflectivity Densities for Tropical Storm Doria and Hurricane Ginger

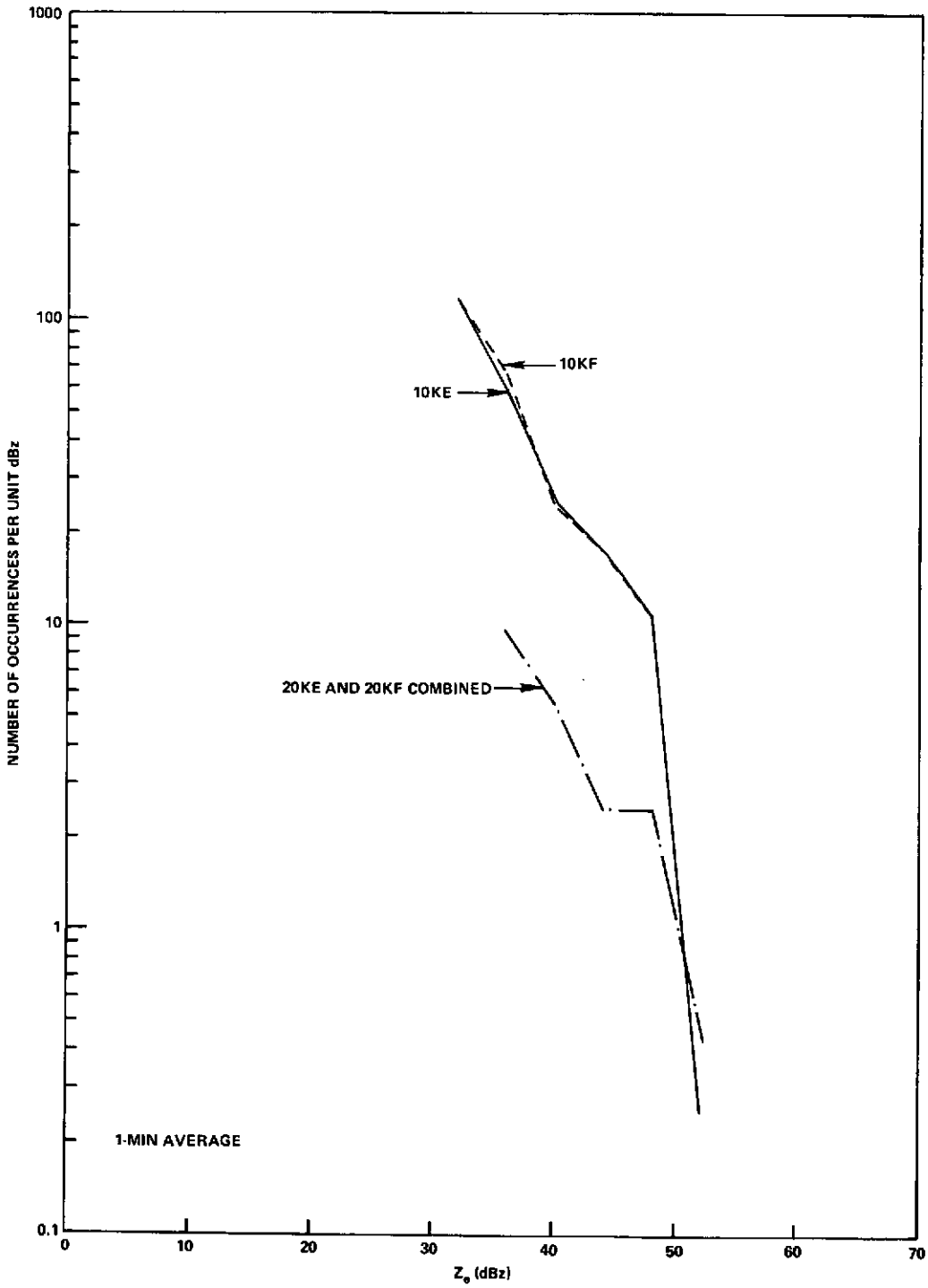

Figure 34. Bistatic Radar Densities for Phase II (Excluding Tropical Storm Doria and Hurricane Ginger)

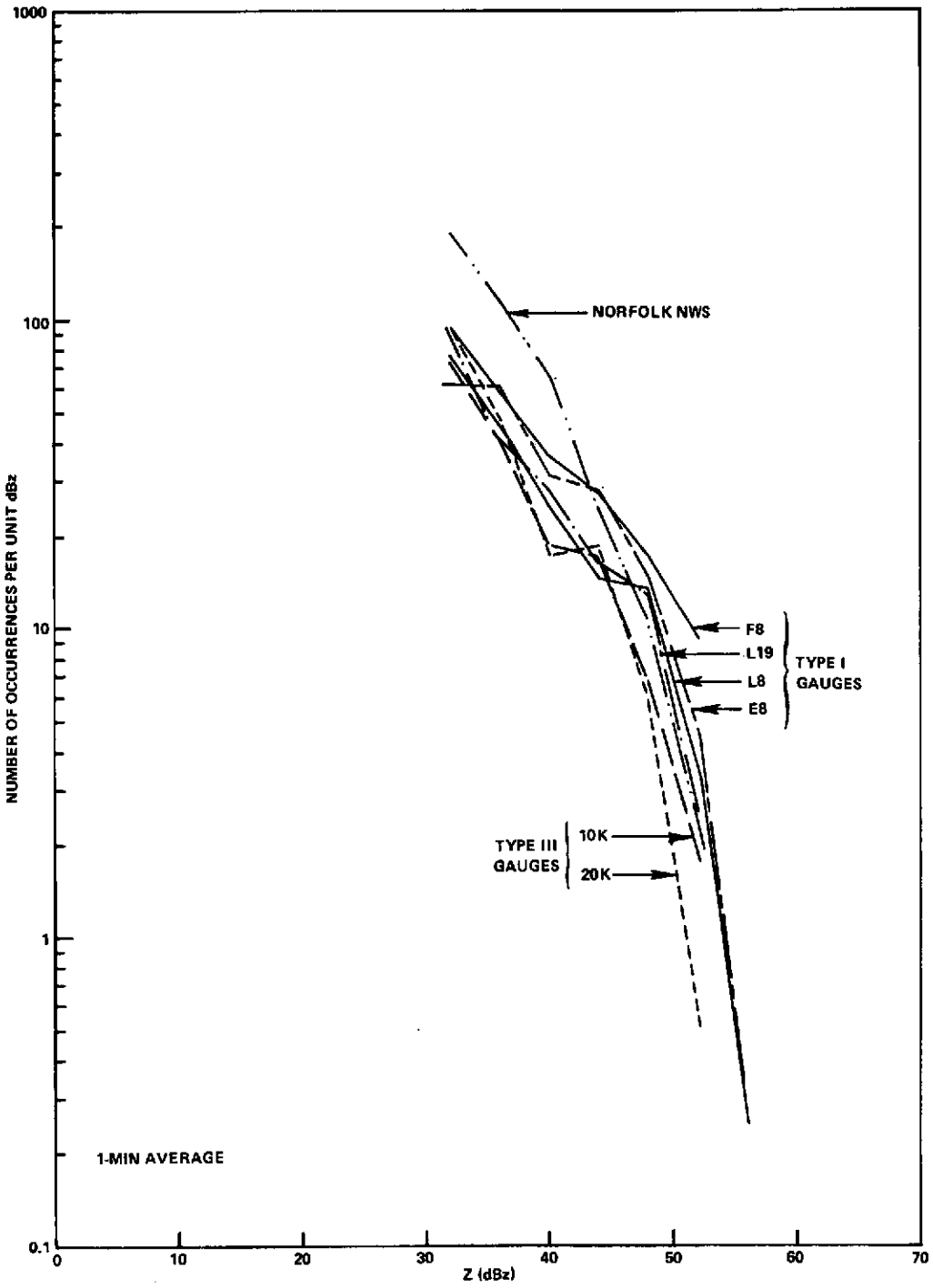

Figure 35. Gauge Densities for Phase II (Excluding Tropical Storm Doria and Hurricane Ginger)

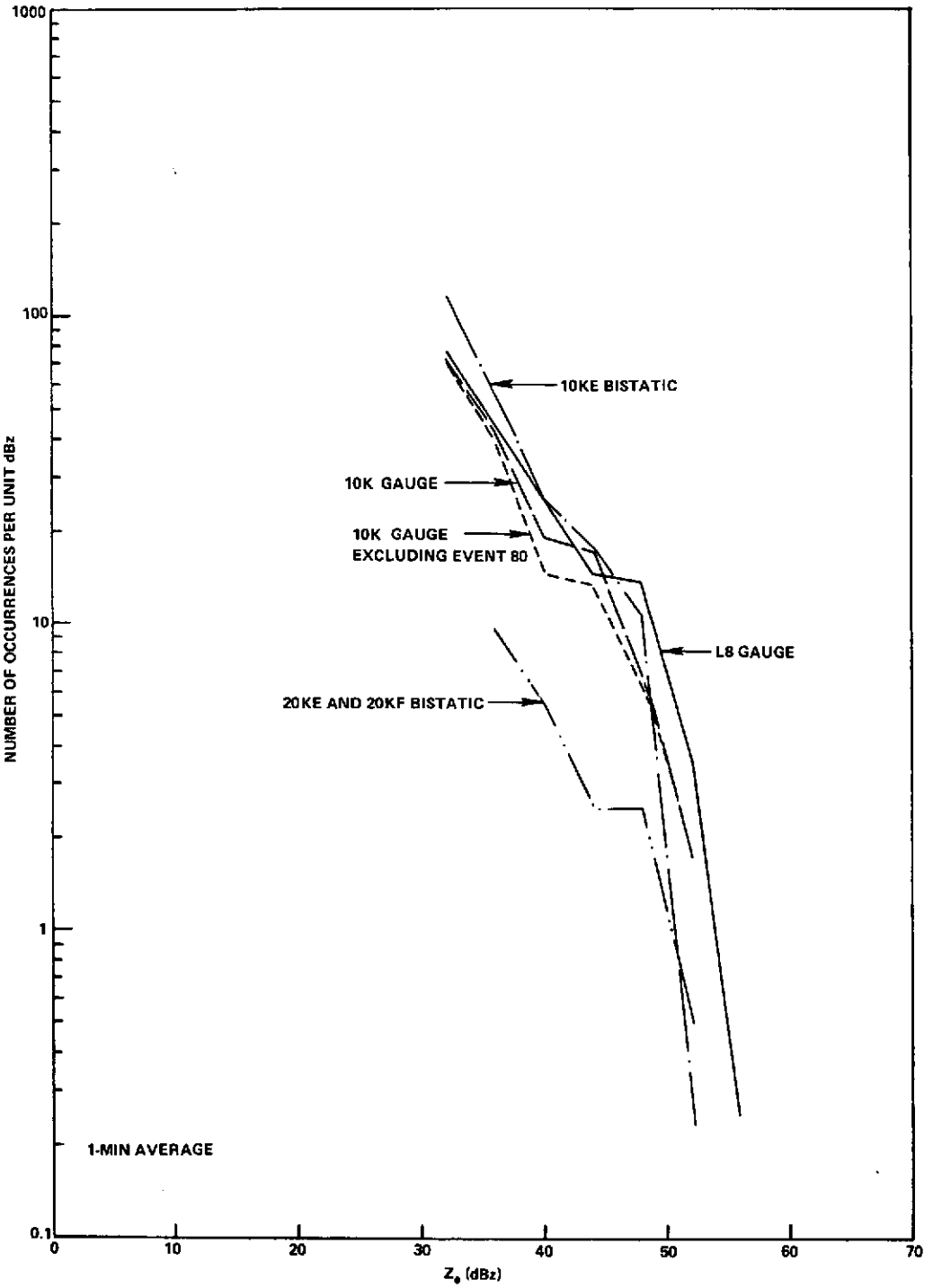

Figure 36. Estimated Reflectivity Densities for Phase II (Excluding Tropical Storm Doria and Hurricane Ginger)

relative errors in the Z, Z_e comparison are reasonably small for the 10KE path but are larger for the 10KF path (see Figure 11). The relatively large number of occurrences of low Z_e values for the 10KF path as compared with the 10KE path also point to the same scattering volume size effect.

Although agreement was not obtained between the 10K gauge and L8 gauge densities for data excluding Doria and Ginger, the results of comparison between the 10K gauge and the 10KE path show that both distributions are identical for Z_e greater than 42 dBz (after recalibration). The 10K gauge data, however, were different from the L8, 20K, and 10KF data at the 0.05 level of significance, although they were identical to the 10KF data at an 0.01 level of significance for Z_e greater than 42 dBz. Figure 37 shows the category averages after rescaling Figure 36. The density functions are all within a region 3 dB wide, although only the L8–10KE and 10K–10KE comparisons indicate that the parent distributions were identical (at the 0.05 level of significance). Figure 38 gives the empirical distribution functions for the data presented in Figure 37. Although the L8 and 10KE data were judged to be identical and the 10K and 10KF data were judged to be different, the data as presented in distribution function form appear to show the opposite to be true. This illustrates the difficulty in using distribution functions to compare measurements without additional statistical testing.

4.4 ANALYSIS OF DATA FOR THE ENTIRE YEAR

Data for Phase I were less reliable because only 1 out of every 4 min were sampled, the 10KE and 10KF antennas were not properly aligned, and the type II and III gauges were not adequately sited. The data for Phase Ia for the two type II gauges, the 5K and 10K gauge, the Norfolk NWS gauge and both the 10KE and 10KF bistatic scatter paths are given in Figure 39. The data were not adjusted (recalibrated) because of differences in the physical state of the bistatic radar system and expected differences in the rain gauge siting (see Section 3.2). The bistatic radar data densities were constructed by multiplying the observed number densities by four to provide an estimate of the actual number densities. This requires a sufficiently large sample size so that events such as Event 54 (see Figure 23) do not cause large errors because of their limited duration. In these data, the 10K gauge overestimates the Z_e values measured on the 10KE path, the 5K gauge underestimates the Z_e values, and the Norfolk gauge—although located over 40 km away—provides a reasonable estimate for Z_e values between 36 and 44 dBz. The 10KE and 10KF paths show greater dissimilarity than in Phase II, due to antenna alignment and calibration difficulties. The 10K gauge data, even if recalibrated, would provide a significant overestimate (larger than measurement error) of the bistatic radar data.

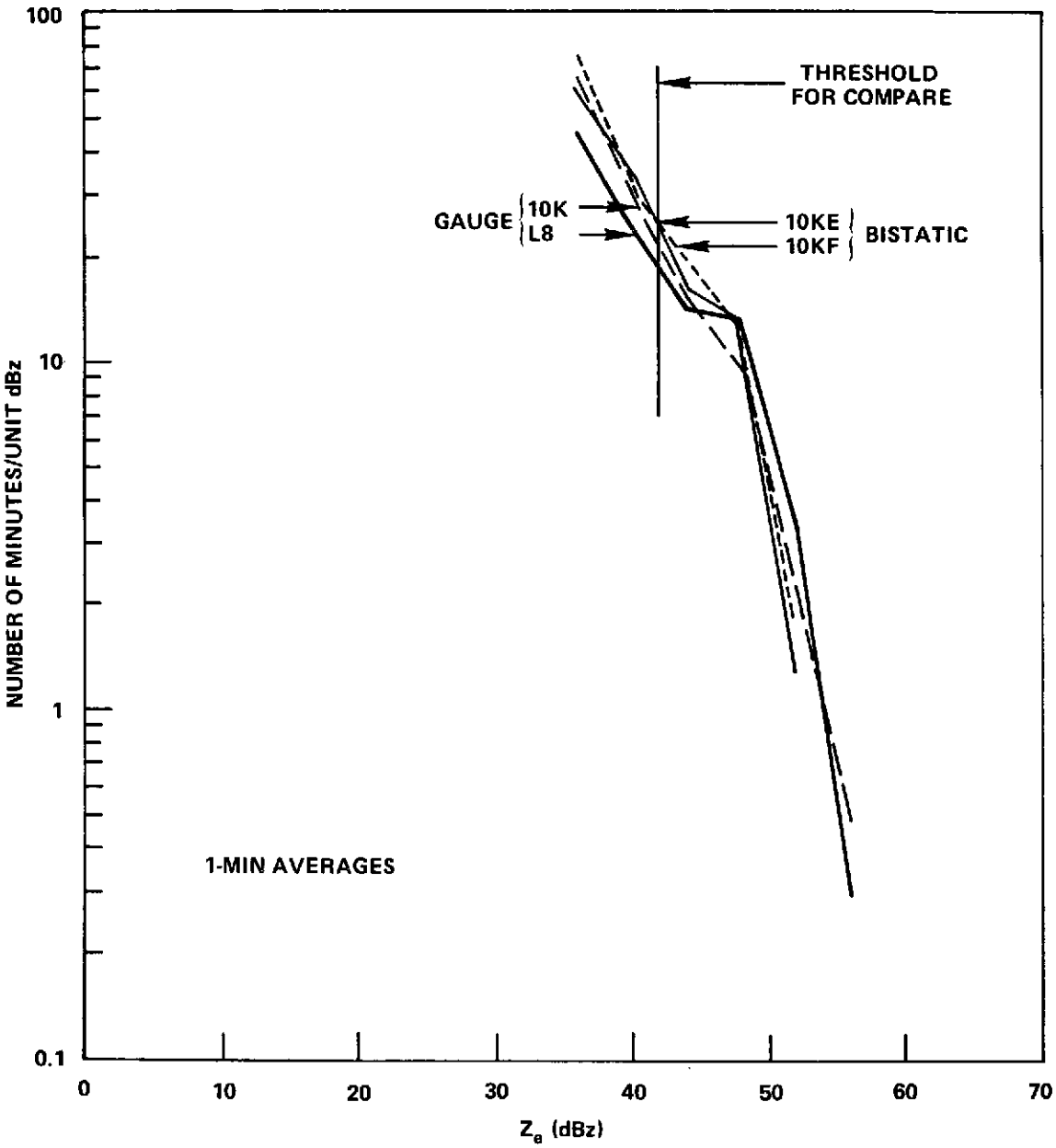

Figure 37. Empirical Density Function for Estimated Reflectivity After Recalibration for Phase II (Excluding Tropical Storm Doria and Hurricane Ginger)

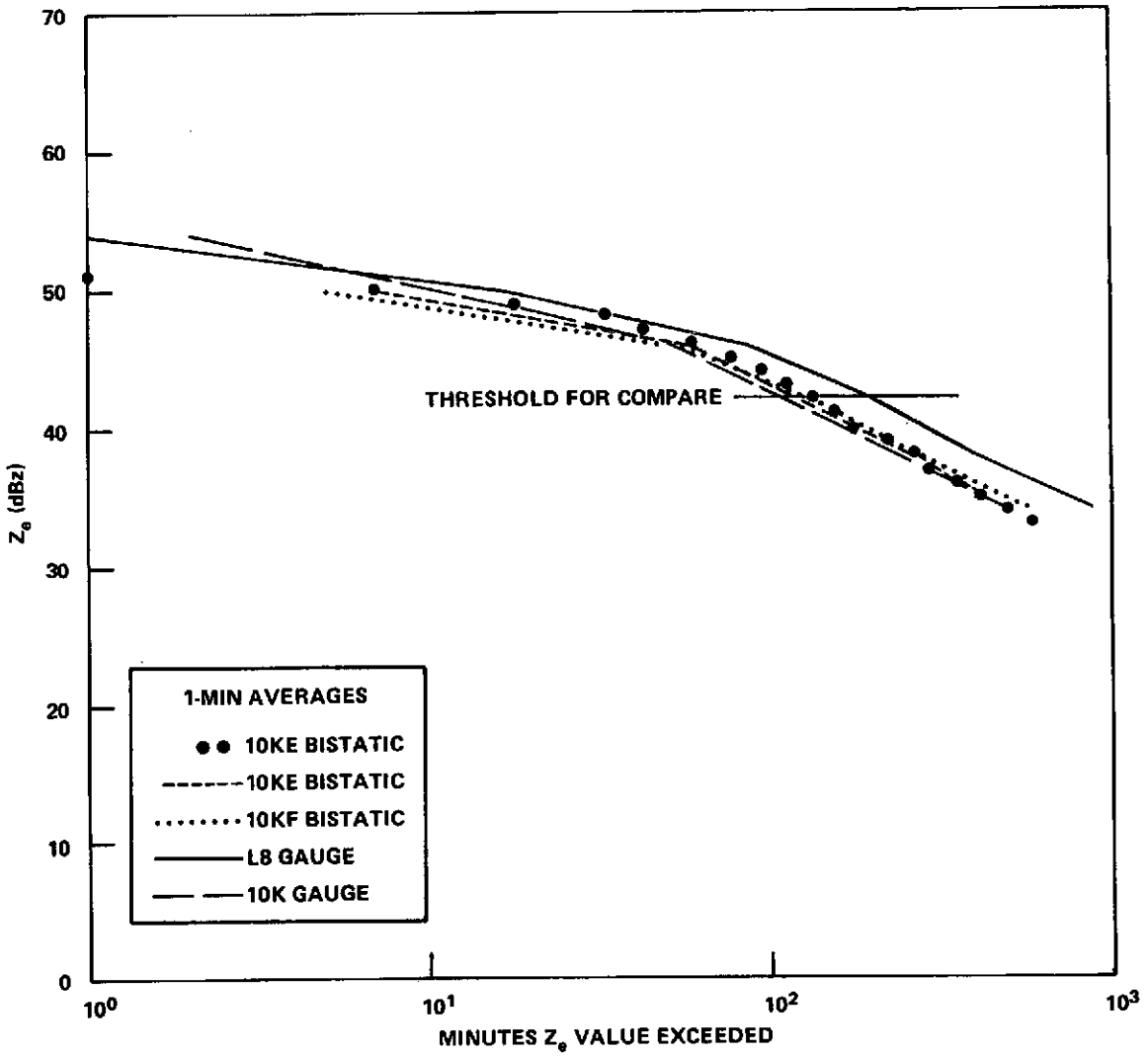

Figure 38. Empirical Distribution Function for Estimated Reflectivity After Recalibration for Phase II (Excluding Tropical Storm Doria and Hurricane Ginger)

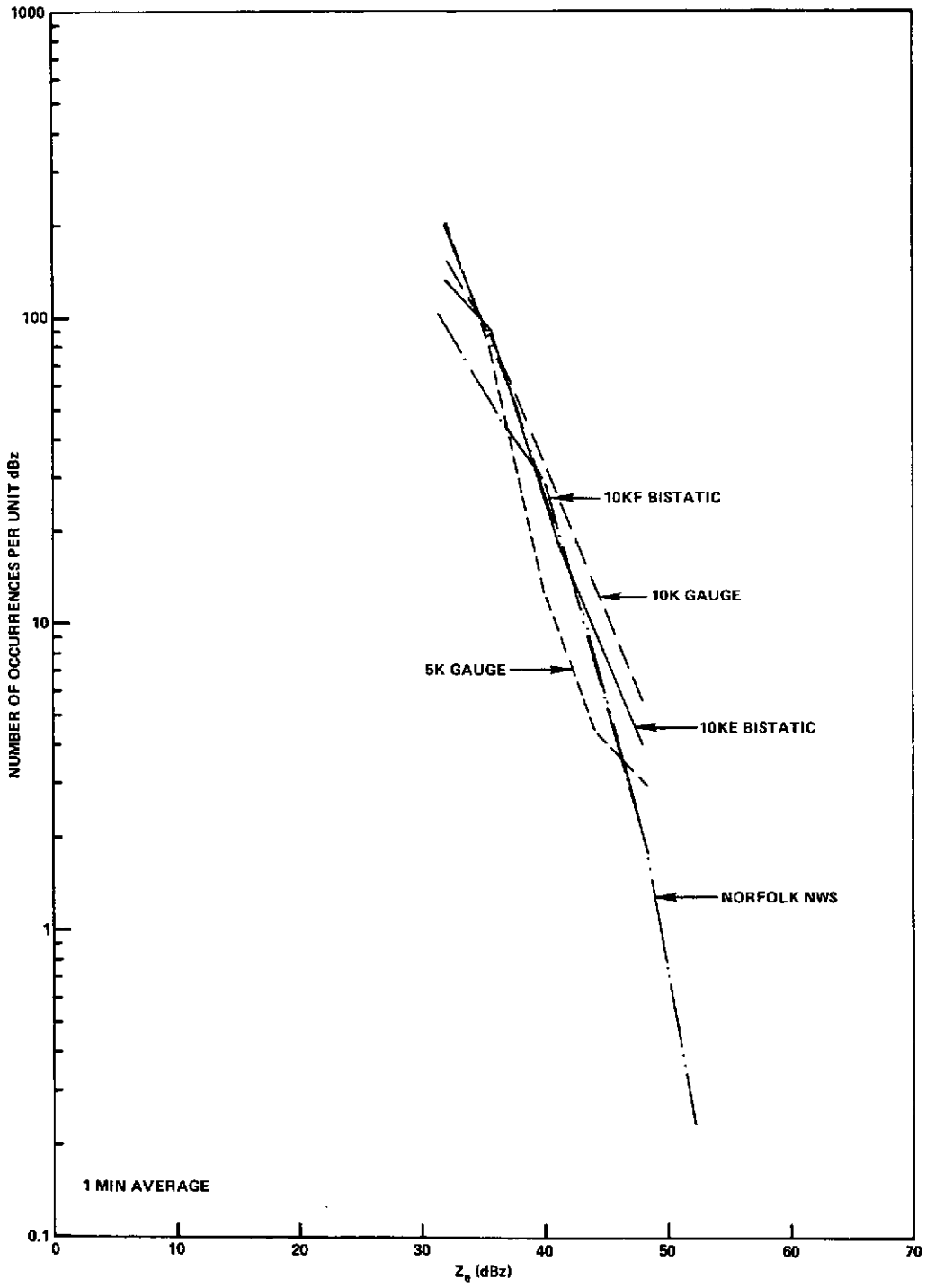

Figure 39. Reflectivity Estimate Densities for Phase Ia

The events comprising Phase Ia were both for showery rain associated with frontal passage and for widespread rain. The widespread winter rains were sometimes accompanied by snow, and when snow was observed at the surface, the gauge data were not processed. However, the bistatic radar data for snow events were processed. For seven widespread rain events with rain at the surface, the melting layer (0°C isotherm) between the surface and the 3-km scattering volume height, and snow in the scattering volume, the number densities indicated in Figure 40 were observed. For these data, the 10K gauge measurements significantly overestimate the scattering cross sections per unit volume observed in the snow even without recalibration. The success of prediction based upon surface rain gauge data therefore depends strongly upon the rain type and the location of the melting layer. The measured number densities for Phases Ia and Ib (Figure 41)—which were composed of relatively more showery rain with melting levels above the 10K scattering volume than occurred in Phase Ia—show that the 10K gauge data overestimates the 10KE and 10KF path data for Phase Ia and either underestimates the path data (10KF) or is nearly the same as (10KE) the path data for Phase Ib. From the analysis for Phase II, the relative agreement between the scattering data and 10K gauge data must depend upon the mix of storm types.

The number densities for an entire year are shown in Figure 42. The data show reasonable, although apparently fortuitous, agreement between the 10KE, 10KF, 10K gauge, and Norfolk NWS gauge data despite the calibration, siting, and pointing errors discussed above. In Figure 42, the CCIR prediction for rain climate 1, which includes the Tidewater District of Virginia, is also shown (CCIR, 1972; NASA, 1971). The CCIR model tends to overestimate the number densities for Z_e values in excess of 40 dBz (as does the Norfolk data) although it is in reasonable agreement with the Norfolk data for Z_e values below 48 dBz.

The empirical distribution functions for each phase of the experiment and the year are given in Figures 2 to 4 of Section 1 and Figures 43 to 45. The empirical distribution functions are the cumulative summations of the histograms (number densities) given above.

5 COMPARISON WITH PREVIOUS MEASUREMENTS AND PREDICTION TECHNIQUES

5.1 PREVIOUS MEASUREMENTS

Doherty (1964) reported on a bistatic radar, surface rain rate comparison experiment conducted in Ottawa, Ontario. In his experiment, the scattering volume was approximately 250 m above the surface. The rain gauge was located on the surface just below the scattering volume. The rain rate averaged

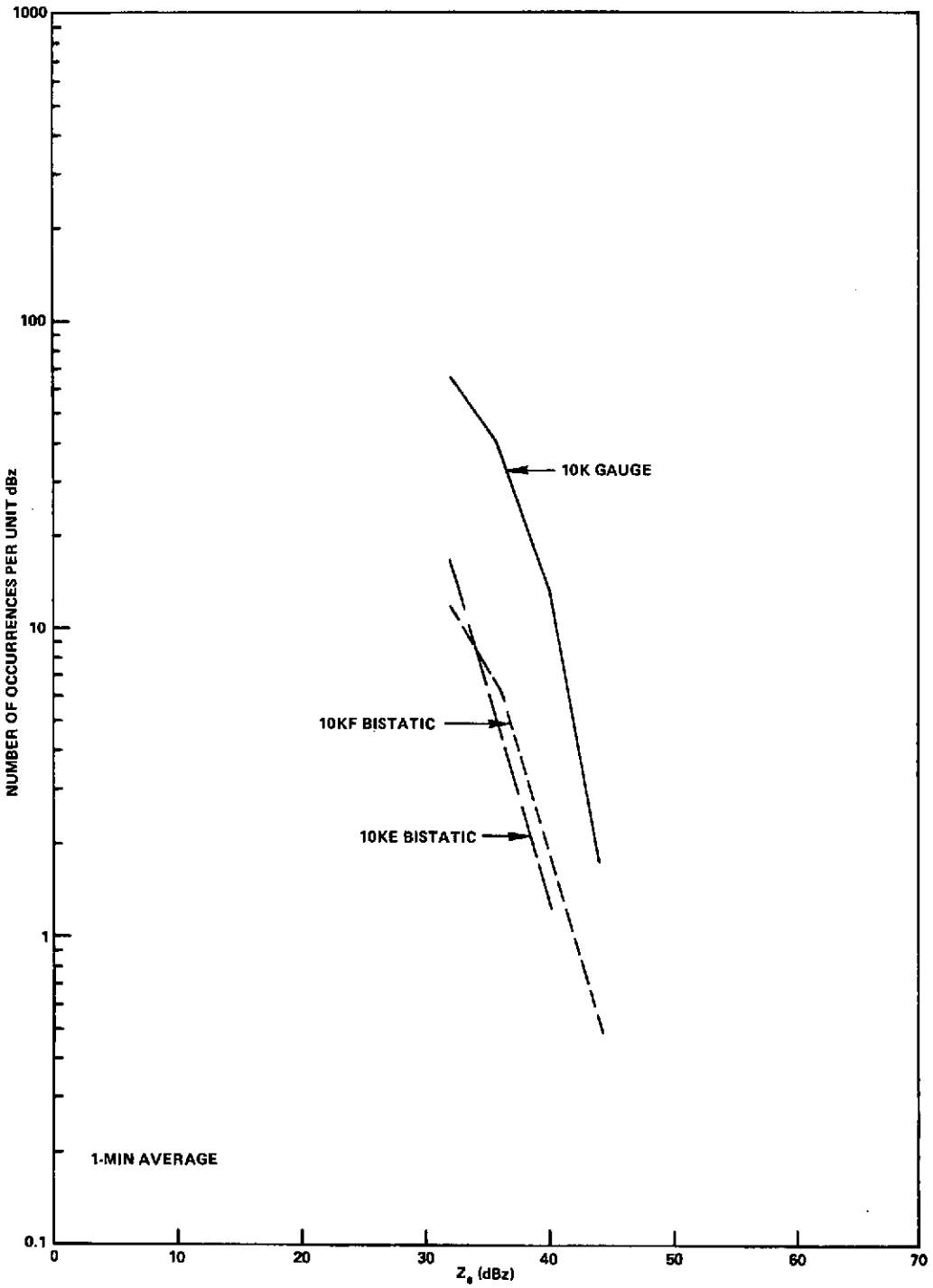

Figure 40. Reflectivity Estimate Densities for Phase Ia

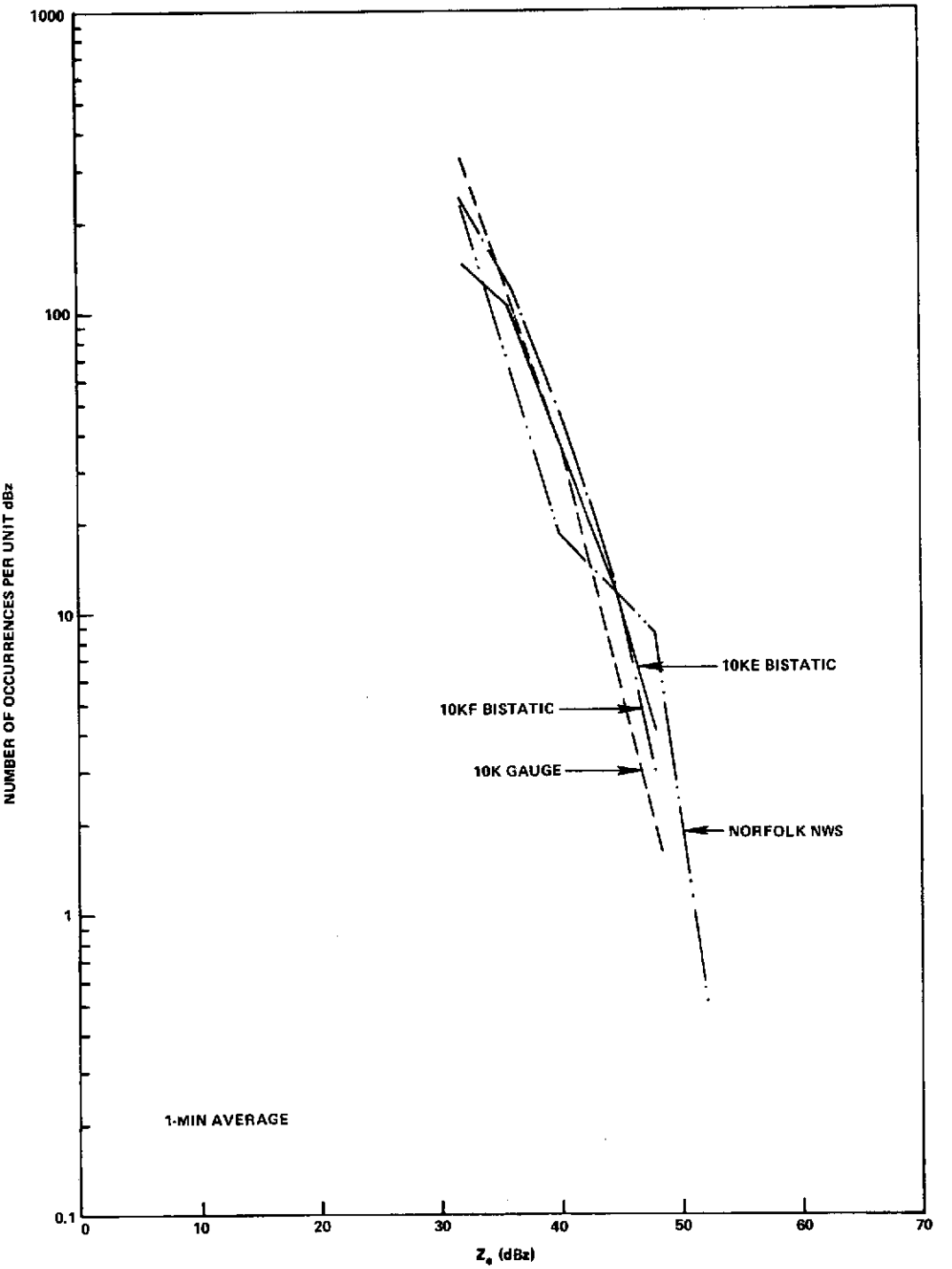

Figure 41. Reflectivity Estimate Densities for Phase Ib

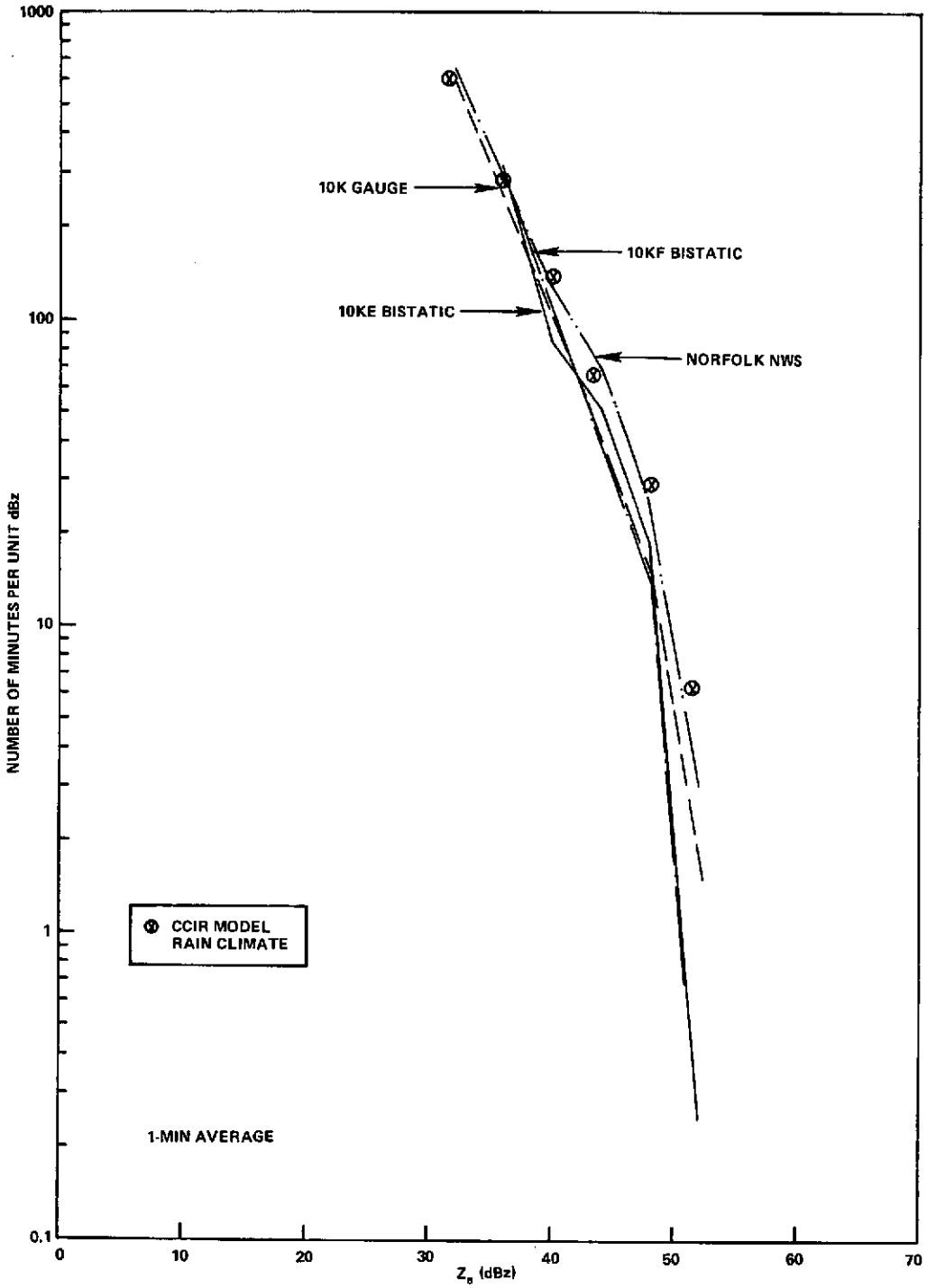

Figure 42. Reflectivity Estimate Densities for Full Year (October 1970—October 1971)

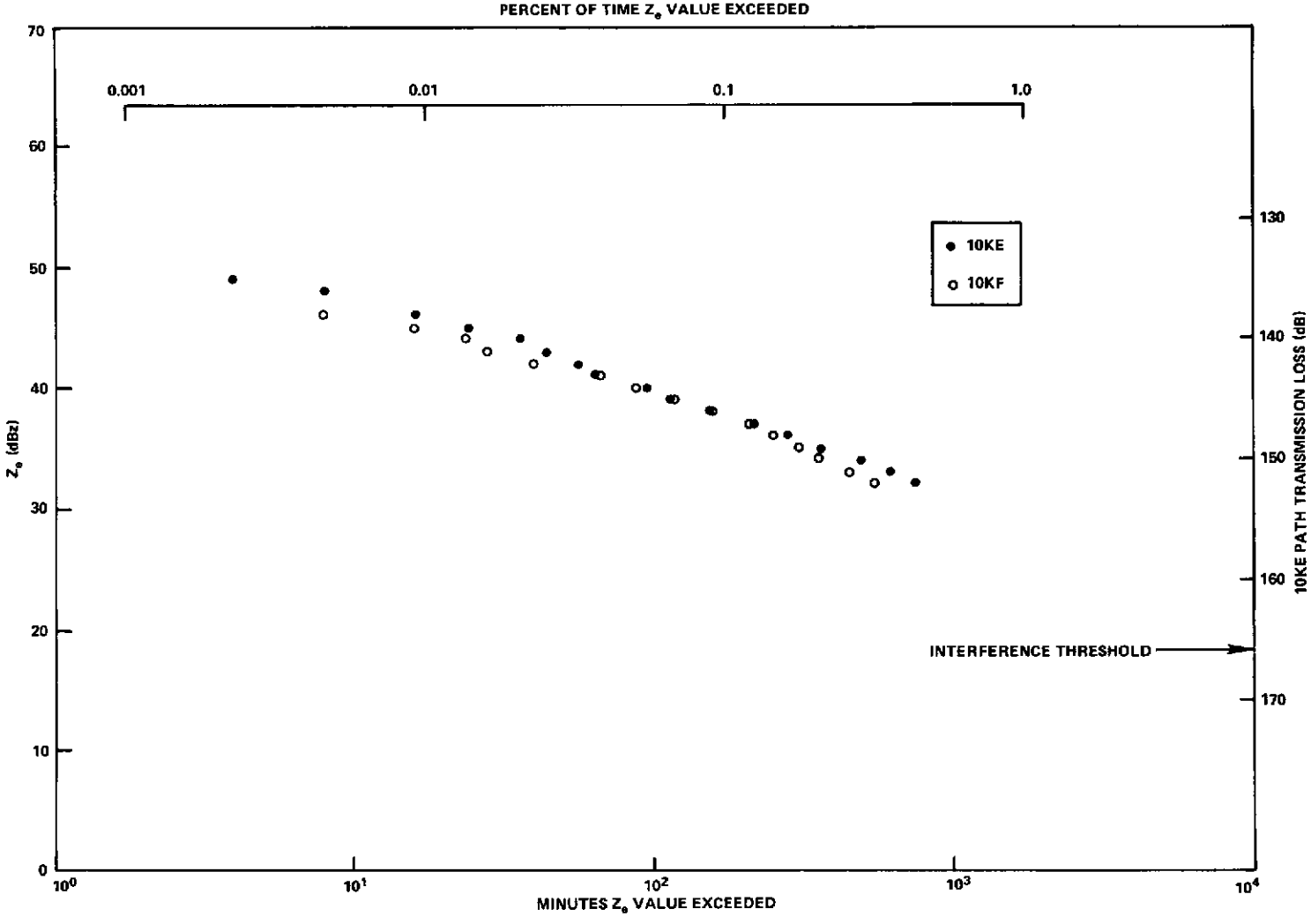

Figure 43. Bistatic Radar Distribution for Phase Ia

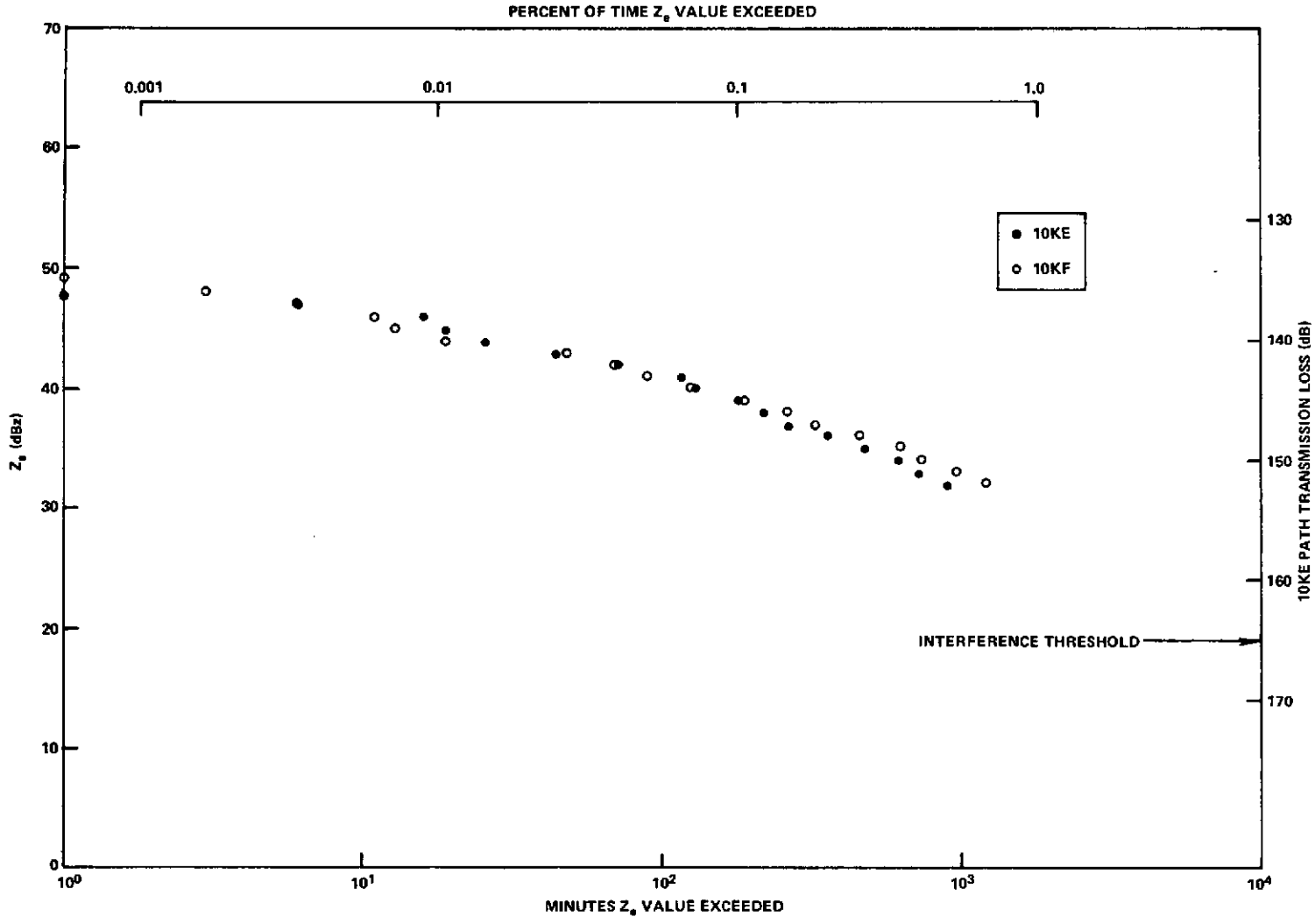

Figure 44. Bistatic Radar Distribution for Phase Ib

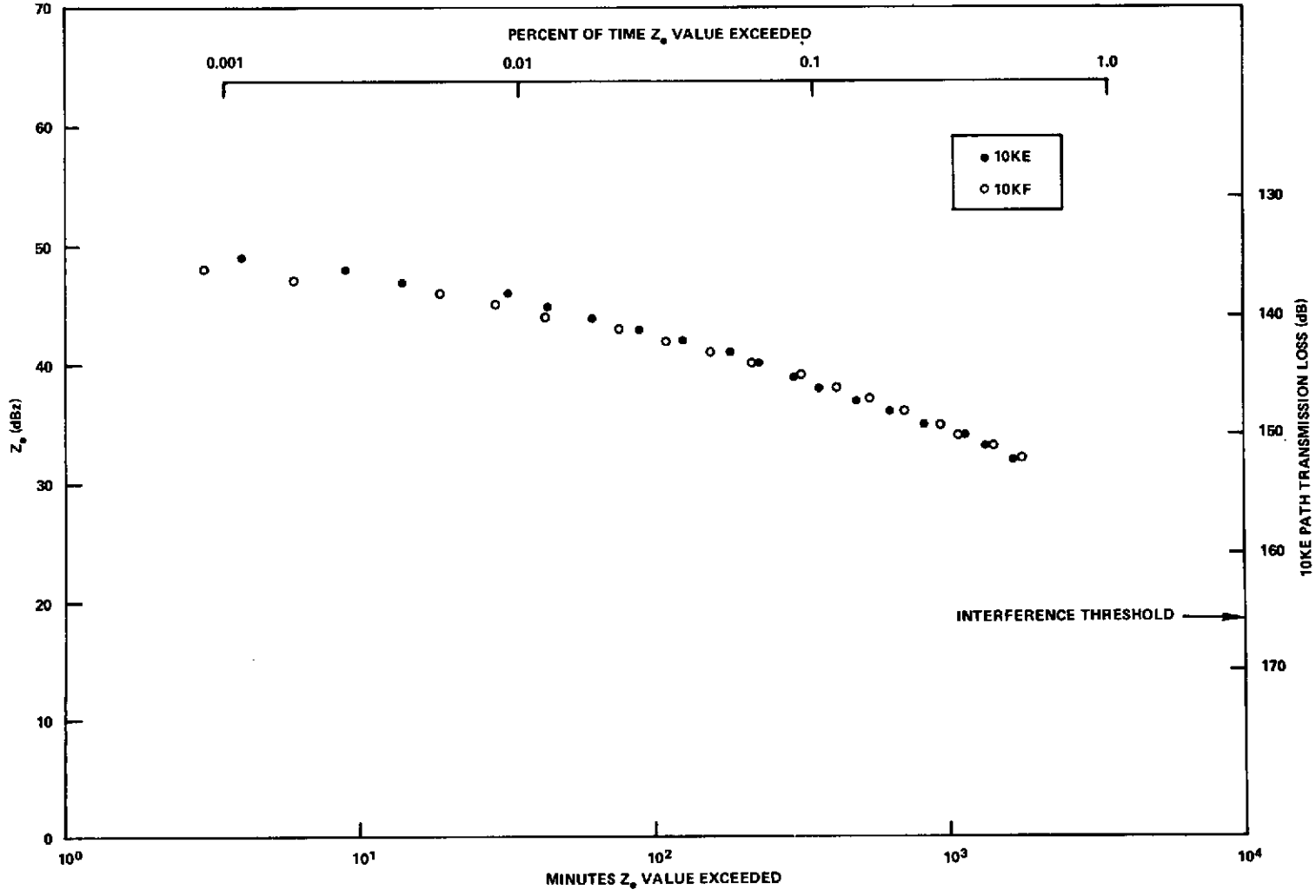

Figure 45. Bistatic Radar Distribution for Phase I

between tips of the rain gauge and the Z_e values averaged linearly over the same time period were statistically compared to provide a best estimate Z/R relationship. The Z/R relationship determined for all data observed during the summer of 1962 was estimated to be $Z_e = 244\ R^{1.39}$ for Z_e measured at X-band. The Z/R relationship determined from a comparison of the bistatic radar and rain gauge data is in agreement, considering possible measurement errors, with the Z/R relationships generally determined by using drop size measurements (see Section 2.2). Doherty showed that the bistatic scattering measurements of Z_e at heights just above the surface agreed with values computed using the surface rain gauge measurements. The Virginia Precipitation Scatter Experiment showed that for thundershowers in Virginia, the agreement may be extended to heights above 3 km. However, for widespread rain, no agreement is observed when the scattering volume is above the melting layer.

Carey and Kalagian (1970) reported on the POPSI experiment, which was an attempt to provide a statistical measurement of the Z/R relationship for scattering volume heights ranging from 0.7 to 9.4 km. The bistatic radar system used by Carey and Kalagian sampled each scattering volume for 5 min once every 3 hr. The 5-min median value for the logarithm of the received signal was determined for each observation and tabulated in the form of empirical distribution functions for comparison with surface rain rate data. Surface rainfall distributions were tabulated using 15-min average rain rates from seven rain gauges located from 10 to 170 km from the scattering volumes. A relationship for Z to R of $Z_e(p) = 127.7\ [R(p)]^{2.26}$ was found by comparing points of equal percentage of the time, p, on both the pooled distribution function for all the bistatic radar data and the pooled distribution function for all the rain gauge data.

The Carey and Kalagian analysis suffers because the final estimated Z/R relationship compares a sparse set of Z_e samples from a large number of different spatial locations with a complete set of samples from a small number of widely separated rain gauge sites. The distributions from each of the rain gauge sites were different because of the wide separation between gauges and differences in proximity to the New Jersey coast. The distributions from the individual scattering volumes must be different due to differences in both height and scattering volume size. Finally, large errors may have occurred due to the relatively long time used in determining the median value of the received signal and the average of surface rain rate. In contrast to the results of the POPSI experiment, the experiment reported by Doherty and the Virginia Precipitation Scatter Experiment show good agreement with Z/R relationships based upon drop size calculations. The latter experiments also compared a complete data set obtained at a single spatial position with a complete data set for a second single spatial position. Finally, the latter experiments used relatively short averaging times.

Buige and Rocci (1970) reported on a series of bistatic scatter measurements conducted in West Virginia. Four years of data from the 6-GHz experiment described by Buige and Rocci are reported in CCIR (1972). The measurements were made in rain climate 2. The recorded transmission loss values were compared with computations based upon Equation R1:(4)* with correction only for logarithmic receiver processing with $\Xi = 1$ (see Section 2.1) and the CCIR model for Region 2. The data showed agreement with the model within 3 dB (the expected accuracy of the Buige and Rocci measurements). The CCIR model for region I also agreed with the Virginia Precipitation Scatter Experiment data (within +6, -3 dB, see Figure 3) indicating similar results.

Buige and Rocci made measurements at both 2000 ft (0.6 km) and 6000 ft (1.8 km) above the local terrain (4000 and 8000 ft above mean sea level, respectively) and tabulated 5-min medians of the logarithm of the received signal. In addition to normal calibration and measurement errors, their data should tend to underestimate the actual 5-min median transmission loss values due to changes in the scattering volume within the 5-min period. The effect of change will be most pronounced at the lower Z_e values, perhaps explaining why the Buige and Rocci results tend to be overestimated by the CCIR model at low Z_e values. By way of contrast, the agreement between the CCIR model and the Virginia Precipitation Scatter Experiment data is better at lower Z_e values. This behavior is to be expected, because at low rain rates the CCIR models are identical for all rain climates. Buige and Rocci did not make direct comparisons with rain gauge data with a 5-min integration time. They attempted a comparison using hourly averaged data and the empirical relationship between distributions of 5-min and hourly integrated data proposed by Bussey (1950). They found that after transforming the hourly data to a 5-min average distribution, the standard $Z = 200\ R^{1.6}$ relationship (see Section 2.2) overestimated the transmission loss and that a new $Z_e = 23\ R^{2.0}$ should be used. If, however, they had used $Z = 270\ R^{1.3}$, which appears to be a better Z/R relationship for the Virginia/West Virginia area as determined by drop size distribution methods, their data (Figure 16 of Buige and Rocci, 1970) would have fitted the rain gauge data between 0.01 and 0.5 percent of the time. It would have been lower than the rain gauge estimates for more than 0.5 percent of the time—by an amount typical of one to two orders of magnitude change of reflectivity within the 5-min period ($10 < \Xi < 100$). Although Buige and Rocci proposed a new Z/R relationship for use in estimating interference, it is more likely that the proposed Z/R relationship compensates for use of the 5-min median of the logarithm of the received signal for preparation of the Z_e values.

*Citations to Reference 1 materials are prefixed R1: throughout this report.

5.2 PREDICTION TECHNIQUES

Three major problems are of interest in the prediction of density or distribution functions of reflectivity:

- Change in reflectivity with height for a given percent of the time
- Change in reflectivity at a point on the surface with integration time for a given percent of time
- Prediction of reflectivity at the surface for a particular integration time using available climatological data.

These problems arise because the available climatological data mainly consists of yearly or monthly accumulations of rain rate.

One of these problems—change in reflectivity with height—was considered by Austin (1971, Section IV-B) and is implicit in the analysis performed above, where it was found that only thundershowers had identical Z and Z_e distributions for Z_e measured at 3-km height and Z estimated from surface data. Austin summarized the available weather radar data by noting that the distributions for thunderstorm rain will be essentially independent of height for all altitudes between the surface and the 0° isotherm, and for widespread rain (extratropical cyclones) the distribution will be identical for all heights below 0.5 km below the 0° isotherm. She also noted that above the 0° isotherm, the reflectivity value for a given percent of the time will decrease with increasing height. This behavior is born out by results of the Virginia Precipitation Scatter Experiment given above. Insufficient data are currently available to construct a set of conditional distribution functions useful for calculating the change in reflectivity with height for use in predicting interference. The 20K path measurements do, however, show that the CCIR models predict too large a Z_e value at heights above the 0°C isotherm (melting level), which is nowhere as high as the rain cell heights used in the models (except in regions where hail is common—such as areas of Wyoming, Colorado, and South Dakota).

Another problem—estimating the distribution function for one integration time given measurements made with another (longer) integration time—is important for applications in the United States, where hourly rainfall accumulation data are readily available for a large number of stations. Bussey (1950) considered this problem and, from point rain-rate data obtained in Washington, D. C., using 1-min and 60-min integration times, proposed an empirical relationship between points of equal probability of occurrence of the instantaneous (1-min) and clock hourly empirical distribution functions (Section R1:/5.2).

This relationship was used by Buige and Rocci to prepare 5-min average rain rate estimates for comparison with their transmission loss measurements. The Bussey model assumes that a unique transformation exists between the 1- and 60-min average distribution functions. The transformation most likely depends upon rain and synoptic type and the relative rain accumulation for each type. For the Washington, D. C., and Virginia areas, the Bussey transformation or a similar transformation based upon a longer record of data should hold on average. The Bussey transformation applied to the clock hour averages of the 10K gauge data is shown in Figures 46 and 47. The Bussey transformation provides a very good estimate of the clock 5-min averaged data based on the clock hourly data (the chi-square test shows densities to be identical). The 1-min and clock 5-min averaged number densities, however, are different.

The 1-min, clock 5-min, and clock hourly averaged data for the L8 and 10K gauges for Phase II are shown in Figures 48 and 49, respectively. The 1-min number densities were compared with the 5-min number densities for these gauges and all the other gauges used during Phase II (see Tables D-8 and D-9 in Appendix D). Using the 1-min data as reference, the clock 5-min data have identical number densities (using chi-square test) with the exception of E8 and Norfolk NWS gauges (the gauges located near the coast). The 1962 West Concord data reported by Austin similarly had identical number densities for clock 1/2-, clock 1-, and clock 5-min averages for summer showers and thundershowers. Apparently, the 1- and 5-min average number densities are identical for showery rain but not for all rain types. The E8 and Norfolk gauges experienced both showery and widespread rain moving along the Virginia coast during Phase II, and exclusion only of tropical storms Doria and hurricane Ginger did not leave only showery rain. The equivalence of the clock 1-min and clock 5-min distributions in thunderstorm rain allows one to use the 5-min excessive-precipitation data reported by first-order NWS stations in estimating the expected 1-min average distributions. As an example, the empirical number density for Norfolk NWS excessive-precipitation data and Richmond NWS excessive-precipitation data averaged over the years 1963 to 1970 is shown in Figure 44 (EDS, 1963-1970).

The Norfolk yearly accumulation (October 1970 to October 1971) was 1063 mm and the Tidewater District average accumulation was 1062 mm. The average annual accumulation for the years 1931 to 1960 for Norfolk was 1141 mm. The average annual accumulation for the years 1963 to 1970 was 1018 mm. Thus, the measurement year had a slightly higher accumulation than the previous eight years, but was low in comparison with the 1931 to 1960 30-year average. During the previous eight years, the highest annual accumulation was 1466 mm and the lowest was 677 mm, showing that rather large excursions are possible and that the measurement year can be considered typical. The 5-min

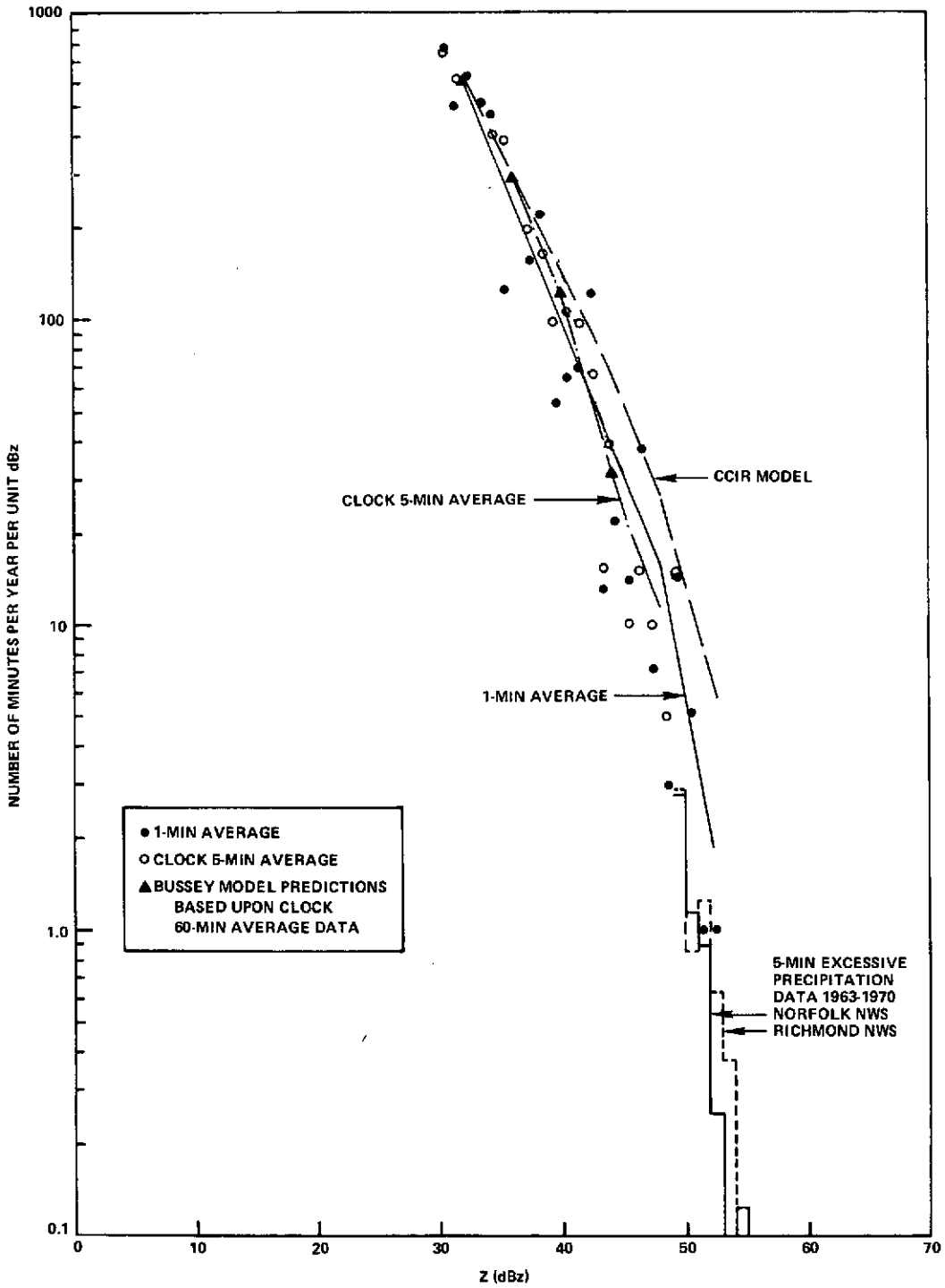

Figure 46. 10K Gauge Density for Entire Year

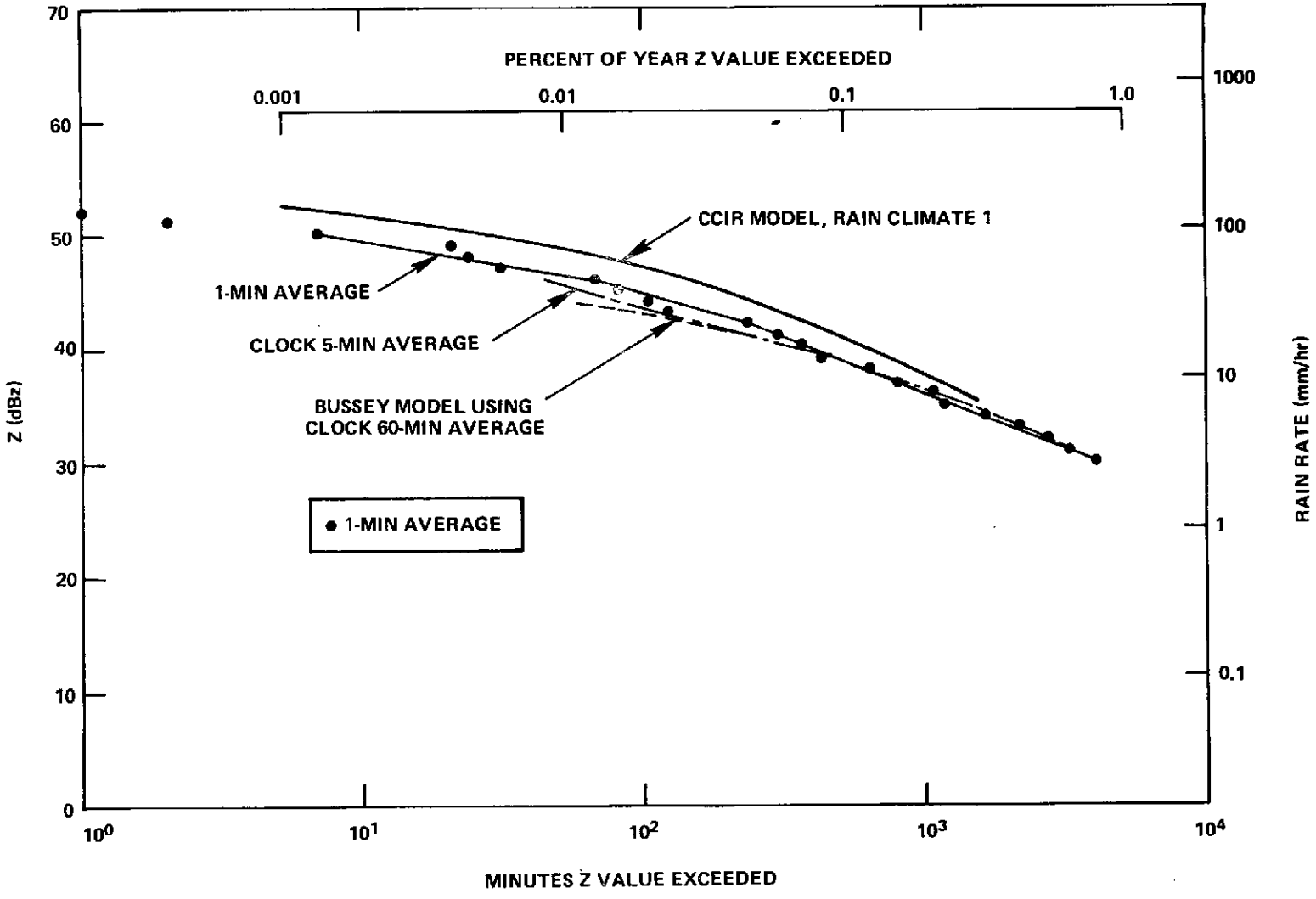

Figure 47. Comparison of Predictions, 10K Gauge Full Year Empirical Distribution Function

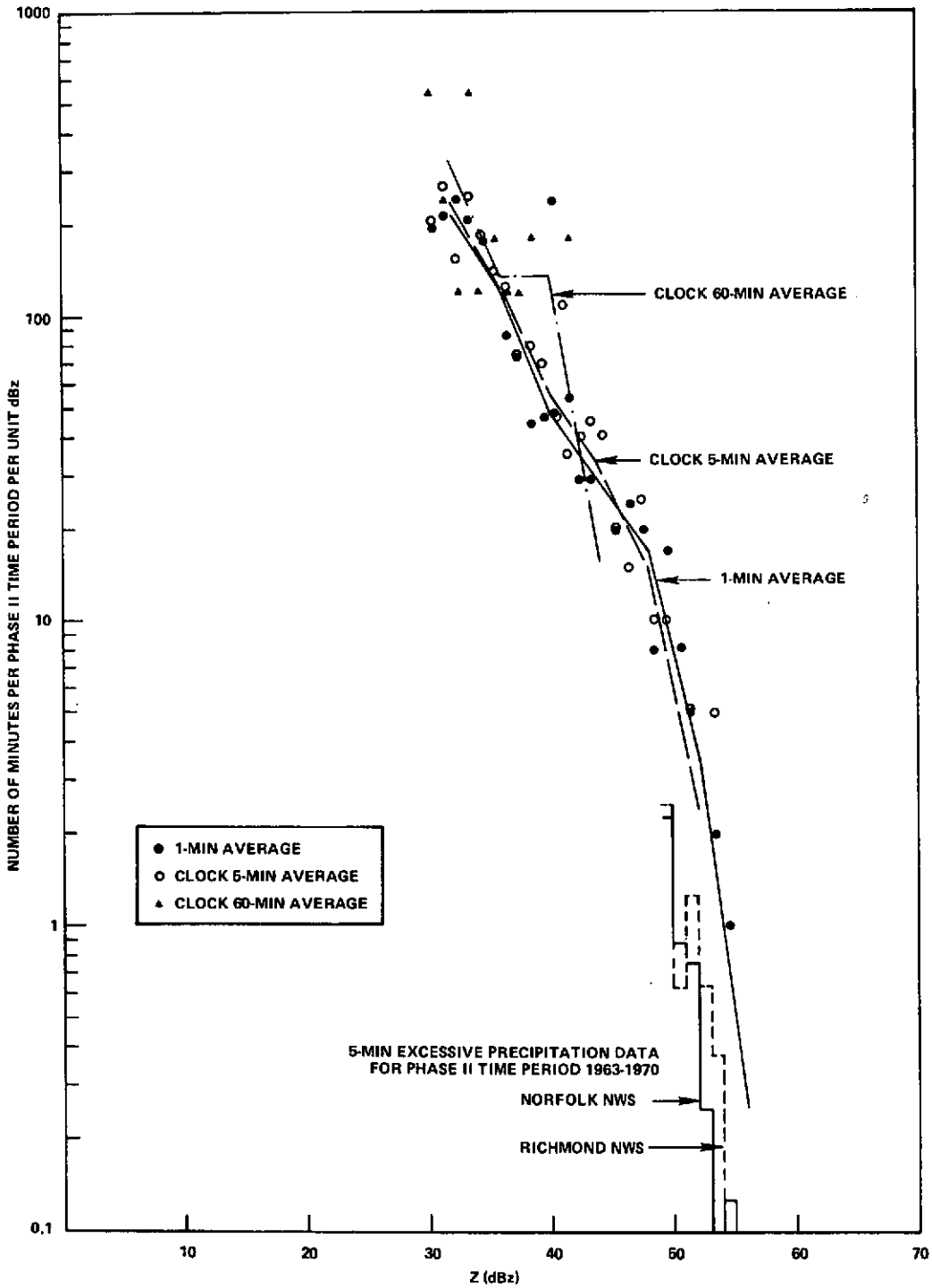

Figure 48. L8 Gauge Density for Phase II

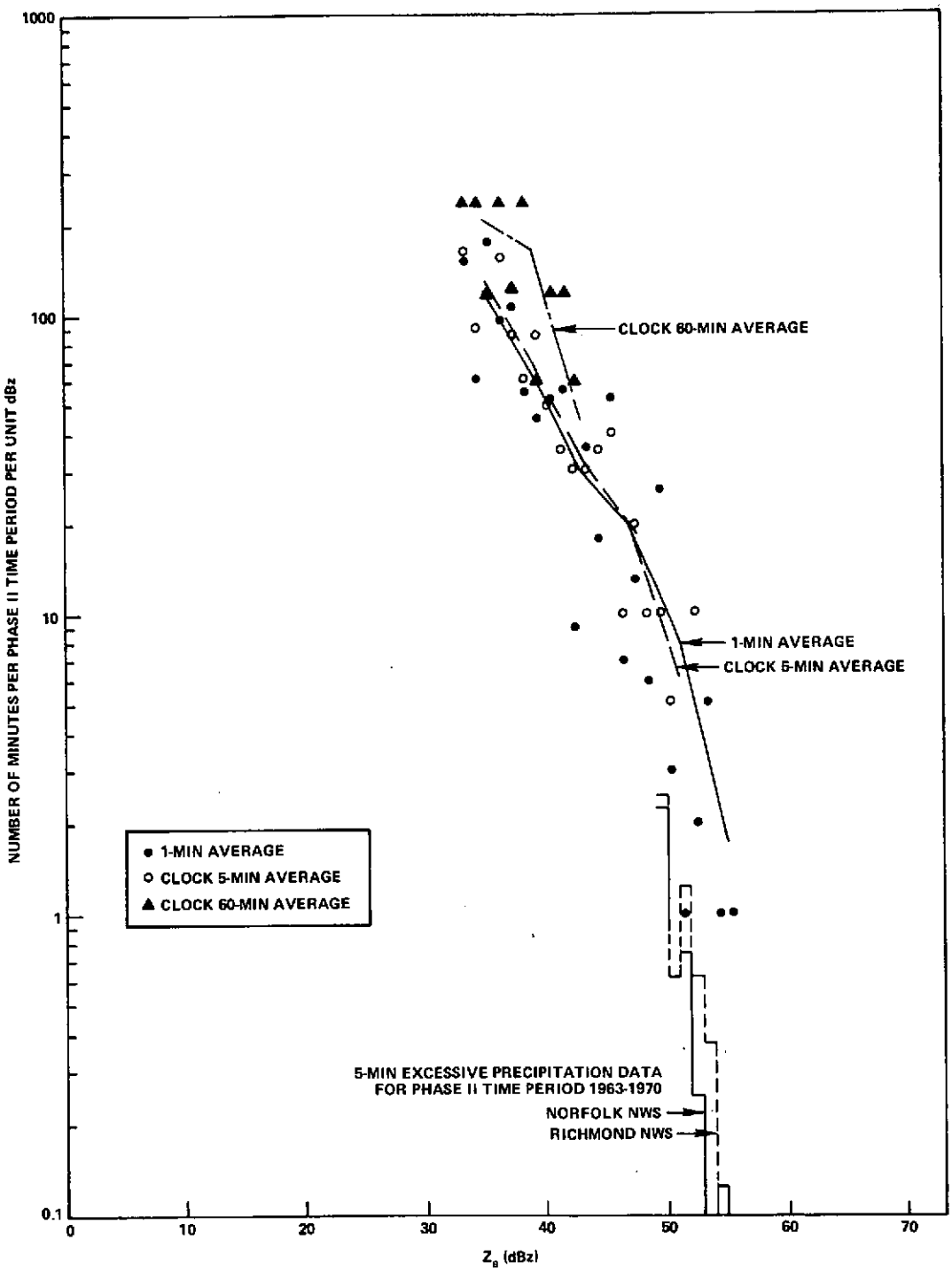

Figure 49. 10K Gauge Density for Phase II

excessive-precipitation data for the previous eight years also shows reasonable agreement with the measured 10K gauge number density for the year for both 1-min and clock 5-min averaging. Although the data appear to represent a typical year, the CCIR model appears to overestimate both the 1-min and clock 5-min number densities.

The CCIR model was developed in response to the problem of estimating the rain rate at a point, using climatological data. Overestimation by the CCIR model is to be expected since it applies to all of rain climate 1, which includes regions of much higher annual accumulation in both Florida and Georgia. The 10K gauge data were not adjusted by the 3-dB calibration correction as was required for the summer data. The readjustment was not performed on the data for the entire year due to possible variability in siting errors as shown by the accumulation comparison in Section 3.2.1. The 5-min excessive-precipitation data for the Phase II time period only for the years 1963 to 1970 are shown in both Figures 48 and 49. In Figure 49, the data were shifted by the required 3 dB. Both the L8 and 10K data show that the average excessive-precipitation data for the Phase II time period averaged over the previous eight years consistently underestimate both the 1-min and clock 5-min empirical density functions for Z values above 49 dBz. The data for the measurement year therefore have higher Z values than are typical for the Tidewater District, and some adjustment is required to the 10K gauge density function for the measurement year. A 3-dB adjustment as used for Phase II, however, would cause larger differences between the 10K gauge density and the 10KE and 10KF bistatic densities. This is to be expected, because the bistatic radar and rain gauge densities agreed only for thundershower rain. The 3-dB recalibration also would cause the CCIR model to underestimate the Z values for percentages of the year greater than 0.01. Comparisons between 1 year of measurement data and climatological data should be used with caution because of large changes in annual rain accumulations and in annual rain rate extremes.

ACKNOWLEDGMENTS

This experiment was a joint effort of the Goddard Space Flight Center (GSFC) of the National Aeronautics and Space Administration (NASA) and the Institute for Telecommunication Sciences of the Office of Telecommunications of the Department of Commerce (ITS). The multi-agency steering committee — assisted by advisors and chaired by NASA — consisted of the Office of Telecommunications Policy (OTP), Federal Communications Commission (FCC), Department of Commerce (DoC), and NASA. The GSFC Project Manager was Dr. Jerome Eckerman. Principal investigators were Phillip L. Rice of ITS and Dr. Robert K. Crane of MIT Lincoln Laboratory. ITS personnel designed, fabricated, installed, operated, and maintained the equipment under the

direction of Paul Wells. Data processing was performed at ITS under the direction of Robert Hubbard and at GSFC under the direction of Stanley Neuder. Coordination of the ITS effort was provided by Joseph Hull. Coordination of the GSFC effort was provided by Francis X. Downey with the support of Edward Levine of Computer Sciences Corporation (CSC). The NASA Headquarters program manager was Jerome Freibaum of the Communications Science Branch, Communications Programs, Office of Applications (Dr. Richard B. Marsten, Director).

The following individuals provided support and equipment for the experiment:

S. Sokol, NASA/Langley Research Center
H. Fine and R. Carey, Federal Communications Commission
N. Novack, NASA/Wallops Island
W. Fansler, U. S. Army Satellite Communications Agency

Organizations that participated in field operations were:

Institute for Telecommunication Sciences
Fairchild Industries
Computer Sciences Corporation
Dynamics Corporation of America
NASA/Langley Research Center

The data processing was done by:

Institute for Telecommunication Sciences
NASA/Goddard Space Flight Center
Westinghouse Electric Corporation
Computer Sciences Corporation
Operations Research Institute
MIT Lincoln Laboratory

The author wishes to express his appreciation to S. Neuder of GSFC and J. Elliott of CSC for contributions to this report. Lastly, the author would like to express appreciation for the support and encouragement of the GSFC Technical Officer, J. Eckerman.

REFERENCE

1. Levine, E., R. K. Crane, F. X. Downey, and P. Wells. Virginia Precipitation Scatter Experiment—Experiment Description. NASA/GSFC X-750-73-54. August 1972.

SOURCES

1. Abramowitz, M. and I. A. Stegun. Handbook of Mathematical Functions with Formulas, Graphs, and Mathematical Tables. Applied Math. Series 55, National Bureau of Standards. U. S. Government Printing Office, 1964.

2. Atlas, D. "Advances in Radar Meteorology," in Advances in Geophysics 10, H. E. Landsberg and J. Van Mieghem eds. Academic Press, New York. 1964.

3. Austin, P. M. Some Statistics of the Small Scale Distribution of Precipitation. NASA/GSFC X-751-72-149. July 1971.

4. Buige, A. and B. Rocci. Precipitation-Scatter Measurement at 6, 12, and 18 GHz. Tech. Memo CL-55-70, COMSAT Laboratories. December 1970.

5. Bussey, H. E. Microwave Attenuation Statistics Estimated from Rain fall and Water Vapor Statistics. Proc. IRE 38, 781-785. 1950.

6. Carey, R. B., and G. S. Kalagian. Detailed Analysis of Precipitation Data, FCC/USAF POPSI Project. Report R-7003, Research Division, Federal Communications Commission. December 1970.

7. CCIR. Determination of Coordination Distance. Report 382, CCIR Documents of the XI Plenary Assembly, Oslo, 1966, Vol. IV. International Telecommunication Union, Geneva. 1967.

8. CCIR. Influence of Scattering from Precipitation on the Siting of Earth and Terrestrial Stations, Report 339-1 (Rev. 72); and Simplified Propagation Model for the Determination of Coordination Distance in the Frequency Range 1-40 GHz, Report AC/5, Conclusions of the Interim Meeting of Study Group 5 (Propagation in Non-Ionized Media), International Telecommunication Union, Geneva. 1972.

9. Crane, R. K. Microwave Scattering Parameters for New England Rain. Tech. Report 426, MIT Lincoln Laboratory. October 1966.

10. Crane, R. K. A Comparison Between Monostatic and Bistatic Scattering from Rain and Thin Turbulent Layers. Tech. Note 1970-29, MIT Lincoln Laboratory. October 1970.

11. Crane, R. K. Description of the Avon-to-Westford Experiment. Tech. Report 483, MIT Lincoln Laboratory. April 1971a.

12. Crane, R. K. "Propagation Phenomena Affecting Satellite Communication Systems Operating in the Centimeter and Millimeter Wavelength Bands," Proc. IEEE 59, 173-188. 1971b .

13. Crane, R. K. Analysis of Data from the Avon-to-Westford Experiment. Tech. Report 498, MIT Lincoln Laboratory, January 1973.

14. Doherty, L. H. "Z/R Relationships Deduced from Forward Scatter Doppler Measurements," J. Atmospheric Sci. 21, 683-697. 1964 .

15. Donaldson, R. J., Jr., G. M. Armstrong, K. J. Banis, and R. M. Dyer. "Measurement of Wind Gradients in Convective Storms by Doppler Radar," Preprints 15th Weather Radar Conference, pp. 22-26. Amer. Meteorol. Soc.. October 1972.

16. EDS. Climatological Data, National Summary, Annual. Environmental Data Service, U. S. Dept. of Commerce, Vols. 14-21. 1963-70 .

17. EDS. Climatological Data, Virginia, Annual Summary. Environmental Data Service, U. S. Dept. of Commerce, Vol. 80, No. 13 1970 and Vol. 81, No. 13. 1971 .

18. Feller, W. An Introduction to Probability Theory and Its Applications, II. J. Wiley and Sons, New York. 1966.

19. Hubbard, R. W., J. Hull, P. Wells, and P. L. Rice. An Experimental Study of the Temporal Statistics of Radio Signals Scattered by Rain. Tech. Report OT/TRER-33, Institute for Telecommunication Sciences. 1971 .

20. Laws, J. O. and D. A. Parsons. "The Relationship of Raindrop-Size to Intensity." Am. Geophys. Union Trans. 24, 452-460. 1943.

21. Marshall, J. S. and W. Hitschfeld. "Interpretation of the Fluctuating Echo from Randomly Distributed Scatters, Part I," Can. J. Phys. 31, 962-994. 1953 .

22. Marshall, J. S. and W. McK. Palmer. "The Distribution of Raindrops with Size," J. Meteorol. 5, 165-166. 1948 .

23. McCormick, G. C. and A. Hendry. "The Study of Precipitation Backscatter at 1.8 cm with a Polarization Diversity Radar," Preprints 14th Weather Radar Conference, 225-230. Amer. Meteorol. Soc. November 1970.

24. McCormick, G. C. and A. Hendry. "Results of Precipitation Backscatter Measurements at 1.8 cm with a Polarization Diversity Radar," Preprints 15th Weather Radar Conference, 35-38. Amer. Meteorol. Soc. October 1972.

25. Mueller, E. A. and A. L. Sims. Raindrop Distributions at Franklin, North Carolina. Tech. Report TR-ECOM-02071-RR3, Illinois State Water Survey, (Urbana). September 1967a.

26. Mueller, E. A. and A. L. Sims. Raindrop Distributions at Island Beach, New Jersey. Tech. Report TR-ECOM-02071-RR2, Illinois State Water Survey. September 1967b.

27. Nathanson, F. E. and J. P. Reilly. Experiments Regarding Temporal, Spatial, and Frequency Correlation Characteristics of Radar Precipitation Clutter. Memo MRT-0-124, Applied Physics Laboratory, Johns Hopkins University. 1967.

28. NASA. Interference Due to Rain, NASA/GSFC X-750-71-211 (Rev.). August 1971.

29. Pruppacher, H. R. and R. L. Pitter. "A Semi-empirical Determination of the Shape of Cloud and Rain Drops," J. Atmospheric Sci. 28, 86-94. 1971 .

30. Rogers, R. R. Interpretation of the Fluctuating Echo from Randomly Distributed Scatters, Part 4. Scientific Report MW-63, Stormy Weather Group, McGill University. September 1969.

31. Silver, S. Microwave Antenna Theory and Design, MIT Rad. Lab. Series, Vol. 12. Dover (reprint), New York. 1949.

32. Van de Hulst, H.C. Light Scattering by Small Particles. J. Wiley, New York 1957.

33. Von Mises, R. Mathematical Theory of Probability and Statistics. Academic Press, New York 1964.

APPENDIX A
RAIN EVENT LIST
AND SUMMARY OF HOURS OF OBSERVATION
BY GAUGE TYPE AND PERIOD

APPENDIX A
RAIN EVENT LIST
AND SUMMARY OF HOURS OF OBSERVATION
BY GAUGE TYPE AND PERIOD

Table A-1
Rain Events and Hours of Observation by Gauge Type

Event	Start Day	Start Time	Stop Day	Stop Time	Duration (hr)	Type II, III (hr)	10K Paths (hr)	20K Paths (hr)	Type I (hr)
1	10/ 3/70	2100		2400	3	3	2	1	
2	10/16/70	0500		1100	6	5	6	--	
3	10/21/70	0100		2100	20	8	16	3	
4	10/22/70	2000	10/23/70	0200	6	3	4	--	
5a	10/26/70	1900		2200	4	4	--	--	
5b	10/27/70	0900		1000	1	1	--	--	
6	10/30/70	1300		1700	4	3	3	--	
7a	11/ 3/70	0700		0800	1	1	--	--	
7b	11/ 3/70	1700		2000	3	3	2	1	
8	11/ 4/70	1600	11/ 5/70	0400	12	9	--	--	
9	11/10/70	1600	11/11/70	1600	24	23	19	1	
10	11/13/70	0100		0300	2	2	1	--	
11	11/14/70	2100	11/15/70	1200	15	5	5	1	
12a	11/17/70	1900		2100	2	--	1	2	
12b	11/18/70	1800		2400	6	6	2	1	
13	11/20/70	1400		1700	4	4	3	--	
14	11/30/70	0300	12/12/70	1000	7	1	3	--	
15a	12/11/70	1900		0300	8	--	5	--	
15b	12/12/70	1200		1600	4	4	4	--	
16	12/16/70	0700		2200	15	15	11	--	
17a	12/21/70	0800		2000	12	10	9	--	
17b	12/22/70	1600		1800	2	--	2	--	
18	12/23/70	0700		1500	8	3	7	--	
19	12/31/70	1500		2200	6	6	4	--	
20a	1/ 4/71	0800		0900	1	--	1	--	
20b	1/ 4/71	1700		1800	1	1	--	--	
20c	1/ 5/71	0000		1300	13	6	9	--	
21	1/ 8/71	2200	1/ 9/71	0700	9	snow	9	--	
22	1/13/71	2000	1/14/71	2000	18	11	13	--	
23	1/15/71	0700		1400	7	3	6	--	
24a	1/22/71	1500		1600	1	--	1	--	
24b	1/23/71	0200		0900	7	5	7	--	
25	1/24/71	0900		2300	14	5	12	--	
26	1/30/71	1700		2000	3	1	2	--	
27	1/31/71	0200		0800	6	3, snow	6	--	

Table A-1 (continued)

Event	Start Day	Start Time	Stop Day	Stop Time	Duration (hr)	Type II, III (hr)	10K Paths (hr)	20K Paths (hr)	Type I (hr)
28	2/ 3/71	1900	2/ 5/71	1200	41	snow	16	--	
30	2/ 7/71	1300		2100	8	8	7	1	
31	2/ 8/71	1200		2200	3	3	inop.*	inop.*	
32	2/13/71	0200		1900	17	16	14	--	
33	2/20/71	0700		0900	2	2	2	--	
34	2/21/71	2300	2/22/71	0200	3	--	3	--	
35	2/22/71	1100		2300	12	7	9	--	
36	2/26/71	1500	2/27/71	0400	13	7	9	1	
37a	3/ 1/71	2200		2300	1	--	1	--	
37b	3/ 2/71	0500		1500	10	4	7	--	
38a	3/ 3/71	0200	3/ 4/71	0100	23	21	15	1	
38b	3/ 4/71	1000		1300	3	3	--	--	
39	3/ 7/71	0300		0800	5	2	4	--	
40	3/10/71	1800		2000	2	2	1	--	
41	3/15/71	1400		1800	4	3	3	1	
42	3/19/71	1000		1900	9	5	4	--	
43	3/22/71	2100	3/23/71	0400	7	4	4	--	
44	3/26/71	0900		1400	14	snow	10	1	
45	3/29/71	0600		2000	15	12	7	--	
46	4/ 2/71	1600	4/ 3/71	0400	12	7	10	--	
47	4/ 5/71	2200	4/ 6/71	2200	24	20	14	--	
48	4/ 7/71	1000		1300	3	2	1	--	
49	4/17/71	2000		2300	3	--	3	--	
50	4/21/71	2100		2200	1	--	1	--	
51	4/23/71	1400		1900	5	2	4	1	
52a	4/26/71	1700		1800	1	--	1	--	
52b	4/28/71	0300		0500	2	--	2	--	
53a	5/ 2/71	1500		2300	8	6	5	1	
53b	5/ 3/71	0700		0800	1	--	1	--	
53c	5/ 3/71	1500		1600	1	--	1	1	
54	5/ 5/71	1500		1600	1	--	1	--	
55	5/ 6/71	1400		1900	5	--	4	--	
56	5/ 7/71	0500		0900	4	2	4	--	
57	5/ 7/71	2300	5/ 8/71	0300	4	3	4	--	
58	5/ 8/71	1700		1900	2	--	2	--	
59	5/13/71	0600		1200	6	4	6	4	
60	5/13/71	1700	5/14/71	0300	10	1	5	2	
61	5/15/71	1300	5/16/71	1000	21	5	15	--	

*Inoperative

Table A-1 (continued)

Event	Start Day	Start Time	Stop Day	Stop Time	Duration (hr)	Type II, III (hr)	10K Paths (hr)	20K Paths (hr)	Type I (hr)
62	5/20/71	2100	5/21/71	0500	8	3	4	7	
63a	5/27/71	1600		1700	1	--	1	--	
63b	5/27/71	2300	5/30/71	1900	71	35	35	1	37
63c	5/31/71	0300		0500	2	2	2	--	--
63d	5/31/71	1100		1200	1	--	1	--	--
67	6/ 2/71	1600		2200	6	1	6	1	3
68	6/ 4/71	1600	6/ 5/71	0300	11	3	4	4	1
69	6/ 7/71	2000		2300	3	--	2	3	--
70	6/ 8/71	1700		1800	1	--	1	1	--
71	6/12/71	1600		1900	3	2	2	2	4
72a	6/14/71	1800		1900	1	--	--	1	--
72b	6/15/71	0100		0900	8	--	3	--	5
73	6/15/71	2000	6/16/71	1800	22	4	12	--	7
74	6/21/71	2000		2400	4	--	2	3	1
75	6/22/71	1500		1900	4	1	2	4	--
76	6/23/71	0900		2200	13	--	8	2	5
77	6/30/71	1500		1600	1	--	--	1	--
78	7/ 6/71	1400		2400	10	3	8	2	7
79	7/ 9/71	1600		2100	5	2	3	2	1
80	7/10/71	1400		1600	3	3	2 inop. 1	2 inop. --	2 inop. --
81	7/11/71	1700		2400	7	7	3	3	4
82	7/19/71	1400		1800	4	2	3	4	4
83	7/21/71	1200		1400	2	--	2	--	--
84	7/24/71	2300	7/25/71	0300	4	--	3	2	2
85a	7/25/71	1800		2100	3	--	3	--	--
85b	7/26/71	1400		1500	1	1	--	--	--
86a	7/27/71	1600		2000	4	4	4	3	5
86b	7/28/71	1900		2100	--	--	--	--	2
87	7/29/71	1200		1600	4	3	2	3	8
88	7/30/71	1700		1900	2	--	2	1	3
89	7/31/71	1100		1600	5	3	1	5	5
90	8/ 4/71	1800	8/ 5/71	0300	9	9	7	8	8
91	8/11/71	1800	8/12/71	0700	13	--	2	3	6
92	8/14/71	0900		1300	--	--	--	--	3
93	8/18/71	0700		1100	3	2	1	2	5
94	8/18/71	1600		2100	5	5	2	3	5
95	8/19/71	2000		2300	3	2	--	--	2
96	8/22/71	1700		1800	1	--	1	1	--

Table A-1 (continued)

Event	Start Day	Start Time	Stop Day	Stop Time	Duration (hr)	Type II, III (hr)	10K Paths (hr)	20K Paths (hr)	Type I (hr)
97	8/23/71	1900		2100	--	--	--	--	2
98a	8/26/71	1100		1400	3	--	3	--	3
98b	8/26/71	2300	8/27/71	2200	23	20	15	6	27
100	9/11/71	1500		2000	5	5	5	4	6
101	9/12/71	1100		2000	9	7	7	4	11
102a	9/13/71	1800		2000	2	2	1	--	--
102b	9/21/71	1200		1300	1	--	--	1	--
103	9/22/71	0900		1200	3	2	1	--	6
104	9/30/71	0700	10/ 1/71	1900	36	23	27	17	38
105a	10/ 2/71	0300		0700	4	4	--	--	4
105b	10/ 2/71	1900		2100	2	2	--	--	3

Table A-2
Total Hours of Observation by Period and Gauge Type

	Start Event	Stop Event	No. of Events	Duration	Type II, III (hr)	10K Paths (hr)	20K Paths (hr)	Type I (hr)
Oct 70	1	6	7	44	27	31	4	
Nov 70	7a	14	10	77	54	37	6	
Dec 70	15a	19	7	55	38	42	--	
Jan 71	20a	27	11	80	35	66	--	
Feb 71	28	36	8	99	59	60	2	
Mar 71	37a	45	11	93	56	56	3	
Apr 71	46	52b	8	51	31	36	1	
May 71	53a	63d	16	146	61	91	16	37
Jun 71	67	77	12	77	11	42	22	26
Jul 71	78	89	13	54	28	35	25	41
Aug 71	90	98b	8	60	38	31	23	61
Sept 71	100	104	6	37	27	26	19	39
Oct 71	104	105b	2	25	18	15	7	29
Phase Ia	1	27	35	256	154	176	10	
Phase Ib	28	67	44	395	208	249	23	
Phase II	68	105b	40	247	121	143	95	193
Year			119	898	483	568	128	193

Table A-3
Start and Stop Dates for Each Phase

Phase	Day Start	Day Stop	Event Start	Event Stop
Ia	3 Oct 1970	31 Jan 1971	1	27
Ib	3 Feb 1971	2 Jun 1971	28	67
II	4 Jun 1971	2 Oct 1971	68	1056

30 Oct. 1973

APPENDIX B
GAUGE ACCUMULATIONS BY EVENT, TIME PERIOD, AND PHASE

APPENDIX B
GAUGE ACCUMULATIONS BY EVENT TIME PERIOD, AND PHASE

Table B-1
Gauge Accumulations by Event (millimeters)

Event	5K	10K	20K	L8	E8	F8	NWS Williamsburg	NWS Norfolk	NWS Richmond
1	0.51	0.76	1.27				--	--	--
10/4 /70*	--	--	0.25				--	--	--
10/15/70	--	--	--				--	1.02	1.27
2	7.11	8.13	6.35				--	5.59	2.79
3	9.14	16.00	13.72				--	13.46	18.03
10/22/70	--	0.25	--				--	--	--
4	1.02	0.76	0.76				20.30	10.41	2.54
10/23/70	0.25	--	--				10.16/mia.	--	--
10/25/70	--		0.25				X	--	--
5a	1.02	0.51	2.79				X	--	--
5b	--	0.51	0.51				X	--	0.25
10/29/70	0.76	--	0.76				X	1.78	--
6	1.27	1.02	1.52				X	0.76	14.48
11/ 1/70	--	--	--				--	0.25	0.76
11/ 2/70	--	--	--				--	2.79	--
7a	--	--	0.76				--	--	0.51
7b	0.25	3.56	0.58				17.78	2.79	--
11/ 4/70	--	--	0.25				2.54	1.78	0.25
8	2.54	4.06	4.83				7.62	1.78	5.59
9	42.42	41.40	51.05				53.34	37.08	35.56
11/12/70	0.25	--	--				--	--	--
10	0.25	0.76	--				2.54	--	4.06
11/13/70	--	--	0.25				--	--	--
11	7.87	5.33	14.73				27.94	0.25	21.85
12b	9.65	9.65	5.33				2.54	3.05	--
11/19/70	0.25	--	--				--	--	--
13	1.02	4.83	4.83				2.54	9.40	5.33
14	0.51	inop.	inop.				--	--	2.29
15a	--	--	inop.				--	--	0.25
15b	2.03	2.29	X**				2.54	0.51	7.87
16	36.32	45.47	X				35.56	44.70	32.77
17a	17.02	16.51	X				17.78	19.81	13.97
12/22/70	--	--	X				--	0.25	--
18	2.54	1.78	X				X	3.30	0.25
12/24/70	--	--	X				X	--	1.78
12/25-26/70	--	--	X				X	0.25	0.51
19	20.07	17.53	X				X	7.62	25.66
20a	--	--	X				X	--	0.51
20b	0.51	0.51	X				X	1.78	--

*Date is used when rain rate does not exceed value for event criterion.
**X = inoperable or missing.

Table B-1 (continued)

Event	5K	10K	20K	L8	E8	F8	NWS Williamsburg	NWS Norfolk	NWS Richmond
20c	22.60	14.22	X				X	42.93	11.43
21	snow	snow	X				X	21.08	8.83
22	6.35	6.60	5.84				X	2.03	7.11
23	4.83	3.56	5.33				X	6.86	3.56
1/17/71	--	--	--				X	--	0.25
1/18/71	--	--	--				X	--	0.25
24b	4.83	4.57	5.08				X	5.84	2.29
25	9.65	7.87	6.10				X	11.18	2.79
1/25/71	0.25	--	0.25				X	--	--
1/26/71	0.25	0.51	X				X	0.51	--
26	3.81	4.07	X				X	5.33	2.03
27	snow	snow	X				X	4.83	1.27
2/ 1/71	--	--	X				--	0.51	--
28	snow	snow	X				17.78	29.2	13.96
30	40.13	49.02	39.62				33.02	13.46	34.80
31	3.81	4.51	4.06				5.08	3.05	10.92
32	37.08	38.35	24.89				33.02	18.54	19.81
1/17/71	--	--	--				2.54	--	--
2/18/71	--	--	0.25				--	--	--
33	0.51	0.76	1.02				--	1.52	0.76
34	--	--	--				--	0.76	--
35	5.08	4.83	4.32				5.08	11.68	17.53
36	6.86	11.94	12.45				15.24	12.45	13.21
37b	3.33	3.33	3.81				2.54	2.79	2.33
3/ 2/71	0.25	--	--				--	--	--
38a	32.00	34.54	30.99				30.48	26.41	25.40
38b	--		--				--	--	--
39	0.25	1.27	0.76				2.54	0.25	0.76
40	1.02	1.02	0.51				--	0.51	0.25
3/11/71	0.51	0.25	0.25				--	--	--
3/13/71	--	--	--				--	0.51	--
41	2.54	4.83	3.95				12.70	13.97	4.57
42	3.81	5.33	5.84				2.54	3.56	5.84
3/20/71	--	0.51	--				--	--	--
43	3.56	3.81	4.06				2.54	1.52	4.82
44	snow	snow	snow				10.16	35.05	22.10
45	4.83	5.59	4.06				5.08	13.97	2.29
3/30/71	0.25	--	--				--	--	--
46	9.65	10.67	10.67				10.16	18.19	4.83

Table B-1 (continued)

Event	5K	10K	20K	L6	E8	F8	NWS Williamsburg	NWS Norfolk	NWS Richmond
47	36.83	X	X				27.94	27.68	39.12
48	0.76	1.02	X				--	3.56	--
4/ 8/71	--	--	X				2.54	--	--
4/14/71	--	0.25	X				--	--	--
49	--	--	X				--	--	0.25
50	--	--	X				--	0.25	--
51	1.02	0.25	X				--	5.08	--
52b	--	--	X				--	--	0.51
53a	6.86	3.81	X				7.62	11.94	--
53b	--	--	X				--	0.76	--
55	--	--	X				27.94	--	0.51
56	1.27	2.54	X				2.54	--	1.78
57	X	13.72	X				12.70	7.37	11.12
58	X	0.25	X				2.54	17.53	4.83
5/11/71	X	0.25	X				--	--	--
59	X	17.53	X				20.32	8.13	16.36
60	X	15.49	X				10.16	5.59	2.29
61	X	26.42	X				30.48	23.88	55.63
62	9.66	6.60	8.64				10.16	--	1.78
5/21/71	--	0.51	0.51				--	4.83	--
63a	--	--	--				--	--	0.25
63b	60.96	32.51	64.01	65.04	25.32	39.50	58.42	33.25	78.48
63c				--	--	--	--	0.25	--
67	8.13	9.14	1.02	20.53		--	--	--	0.76
68	1.02	3.05	3.05	0.98	X	X	12.70	13.46	0.25
69	--	--	--	X	1.72	3.29	--	--	12.19
71	2.03	2.03	1.02	16.88	2.01	2.39	2.54	6.10	--
6/13/71	--	--	--	--	--	--	--	--	1.78
72a	--	--	--	--	--	--	--	--	13.97
72b	--	--	0.51	X	X	5.17	2.51	0.51	25.40
73	5.08	6.10	4.06	11.56	5.97	18.23	10.16	19.81	22.60
74	0.51	1.02	1.02	X	0.86	1.00	5.08	--	1.02
75	--	1.02	1.52	--	--	--	7.62	--	16.51
76	1.52	1.02	0.51	1.37		5.86	2.54	12.95	7.87
6/25/71	--	--	--				2.54	--	--
6/26/71	--	--	--				--	2.03	--
6/28/71	--	--	--				--	--	1.78
77	--	--	--				2.54	--	--
7/ 2/71	--	--	--				--	1.02	--

Table B-1 (continued)

Event	5K	10K	20K	L8	E8	F8	NWS Williamsburg	NWS Norfolk	NWS Richmond
7/ 3/71	--	--	--				2.54	--	--
78	1.02	3.56	5.08	16.79	16.78	1.46	12.70	15.75	6.10
79	10.67	15.25	4.06	3.15			--	5.84	--
80	35.05	18.29	7.62	25.50			15.25	2.03	25.65
81	21.34	22.86	18.29	36.21	40.05	22.11	33.02	27.94	--
7/16/71	--	--	--				--	--	14.99
7/17/71	--	--	--				--	3.56	--
82	4.57	5.59	6.60	17.12	4.72	10.12	10.16	6.86	--
7/20/71	--	--	--				--	0.25	--
84	0.51	0.51	--	2.43			--	0.51	1.78
85a	--	--	--	--			--	--	5.84
85b	--	--	1.52				5.08	0.51	3.81
86a	2.54	11.18	6.10	3.27	3.23	38.39	2.54	44.70	0.25
86b	--	--	--	0.51			--	4.57	--
87	2.03	1.52	3.56	0.78	M	1.97	17.78	0.25	10.92
88	X	--	0.51	0.51	4.44	1.26	--	2.54	6.60
89	X	16.76	16.26	22.07	10.97	18.72	20.32	5.84	35.81
8/ 1/71	X	--	--				2.54	--	2.54
90	X	8.13	19.81	11.49		68.87	17.78	0.76	33.02
91	X	--	0.51	0.27	2.00	43.49	2.54	--	8.38
92	X	0.51	--	0.21	0.78		--	9.65	--
8/16/71	X	--	--	--			5.08	--	--
93	X	4.06	8.13	4.22	9.85	0.73	17.78	6.35	2.03
94	X	7.11	7.62	8.14	0.72	2.53	27.94	7.37	6.35
95	X	2.54	9.15		12.14		12.70	3.26	5.08
96	X	--	--				--	0.51	--
97	X	--	--		11.20		--	7.62	--
98a	X	--	--				--	6.86	--
98b	X	41.66	41.66	74.99	118.27	31.31	50.80	78.74	36.33
9/ 8/71	--	--	0.51				--	--	--
9/ 9/71	--	--	--			2.54		--	--
9/10/71	--	--	0.51				--	--	--
100	6.60	22.36	15.75	2.14	5.40	1.51	7.62	18.54	17.27
101	22.35	31.50	28.96	40.04	12.96	33.86	43.18	28.19	22.35
9/13/71		--	0.51				--	--	--
102a	1.52	--	7.11	6.09	0.28	1.83	2.54	--	--
9/14/71	--	--	0.51				--	--	--
102b	--	--	0.51			2.2	--	--	8.38
103	3.56	1.52	0.51	0.82	0.28	8.28	5.08	3.30	0.25

Table B-1 (continued)

Event	5K	10K	20K	L8	E8	F8	NWS Williamsburg	NWS Norfolk	NWS Richmond
104	46.23	22.86	29.97	98.46	21.91	38.34	15.24	164.6	38.86
105a	4.57	--	3.05	7.99			--	12.45	7.37
105b		9.65					--	6.10	0.25
Oct '70	21.08	27.94	28.18				X	33.02	39.36
Nov '70	65.01	69.59	87.11				116.84	59.4	76.20
Dec '70	77.98*	83.58*	X				X	76.44	76.20
Jan '71	53.08*	41.91*	X				X	102.37	47.18
Feb '71	93.47*	109.41*	86.61				101.6	91.17	110.99
Mar '71	52.07*	57.15*	55.45*				68.58	98.54	68.06
Apr '71	48.26	X	X				40.64	55.36	44.71
May '71	X	86.6	X				149.9	113.53	173.03
June '71	18.29	23.38	12.71	X	X	X	48.23	54.86	104.13
July '71	X(77.73)	95.52	69.6	128.34	80.19	94.03	119.39	122.17	111.75
Aug '71	X	64.01	86.88	99.32	154.96	137.16	137.16	117.6	93.74
Sept '71	80.3	78.2	84.9	155.54	40.83	88.56	76.2	138.7	
Phase Ia	217.15*	223.02*	X				X	271.00	241
Phase Ib	X	346.55**	X				361	359	397
Phase II	X	261.72	254	420	306	407	381	483	370
Year	X	831.29	X				X	1063	1008

*Data above did not include snow days. Including snow, values were: Phase Ia (5K) 232, (10K) 236; Phase Ib (10K) 350.

**Includes 36.83 mm accumulation from gauge 5K for event 47 when gauge 10K was inoperable.

Table B-2
Gauge Accumulations and Deviations From Tidewater District

	Accumulations by Phase (millimeters)					Percent Deviation From Average				
Gauge	Ia	Ib	I	II	Year	Ia	Ib	I	II	Year
10K*	236	350	586	262	848	-17	-13	-15	-30	-20
20K*	--	--	--	254	--	--	--	--	-32	--
5K*	232	--	--	--	--	-18	--	--	--	--
L8*	--	--	--	420	--	--	--	--	+12	--
LAF8	305	419	724	491	1215	+7	+4	+5	+31	+14
Williamsburg	--	361	--	381	--	--	-11	--	+2	--
Newport News	214	378	592	435	1027	-25	-6	-14	+16	-3
Driver	290	--	--	586	--	+2	--	--	+59	--
Bohannon	281	449	729	361	1090	-1	+11	+6	-3	+3
Diamond Spring	290	398	688	374	1062	+2	-2	0	0	0
Urbana	322	402	724	385	1108	+13	0	+6	+3	+4
West Point	292	401	693	381	1074	+3	-1	+1	+2	+1
Wakefield	262	393	655	432	1087	-8	-3	-5	+16	+2
Soffolk L. K.	299	444	743	447	1190	+5	+10	-8	+20	+12
Nassawadox	240	380	620	267	887	-15	-6	-10	-29	-16
E8	--	--	--	306	--	--	--	--	-18	--
Cheriton	--	323	--	284	--	--	-20	--	-24	--
Norfolk	271	359	630	433	1063	-5	-11	-8	+16	0
Walkerton	270	409	679	282	961	-5	-1	-1	-25	-10
Hopewell	229	398	628	425	1053	-19	-2	-9	+14	-1
F8	--	--	--	407	--	--	--	--	+9	--
Holland	314	415	729	519	1249	+11	+3	+6	+38	+18
Wallaceton	292	425	716	--	--	+3	+5	+4	--	--
Burgess	--	174	--	303	--	--	+17	--	-19	--
Painter	225	377	602	255	857	-21	-7	-13	-32	-19
Parramore	--	230	--	--	--	--	-43	--	--	--
Backbay	315	373	688	388	1076	+11	-8	0	+4	+1
Warsaw	310	388	698	316	1013	+9	-4	+1	-16	-4
Richmond	241	397	638	370	1008	-15	-2	-7	-1	-5
Stony Creek	230	438	668	405	1073	-19	+8	-3	+8	-1
Boykins	--	--	--	460	--	--	--	--	+23	
Nelsonia	--	--	--	233	--	--	--	--	-24	
Tidewater aver.	284	404	688	374	1062	--	--	--	--	--
Norfolk*	228	282	510	473	983	-20	-30	-26	+26	-7

*Tipping-bucket gauge, accumulation determined by counting tips.

30 Oct. 1973

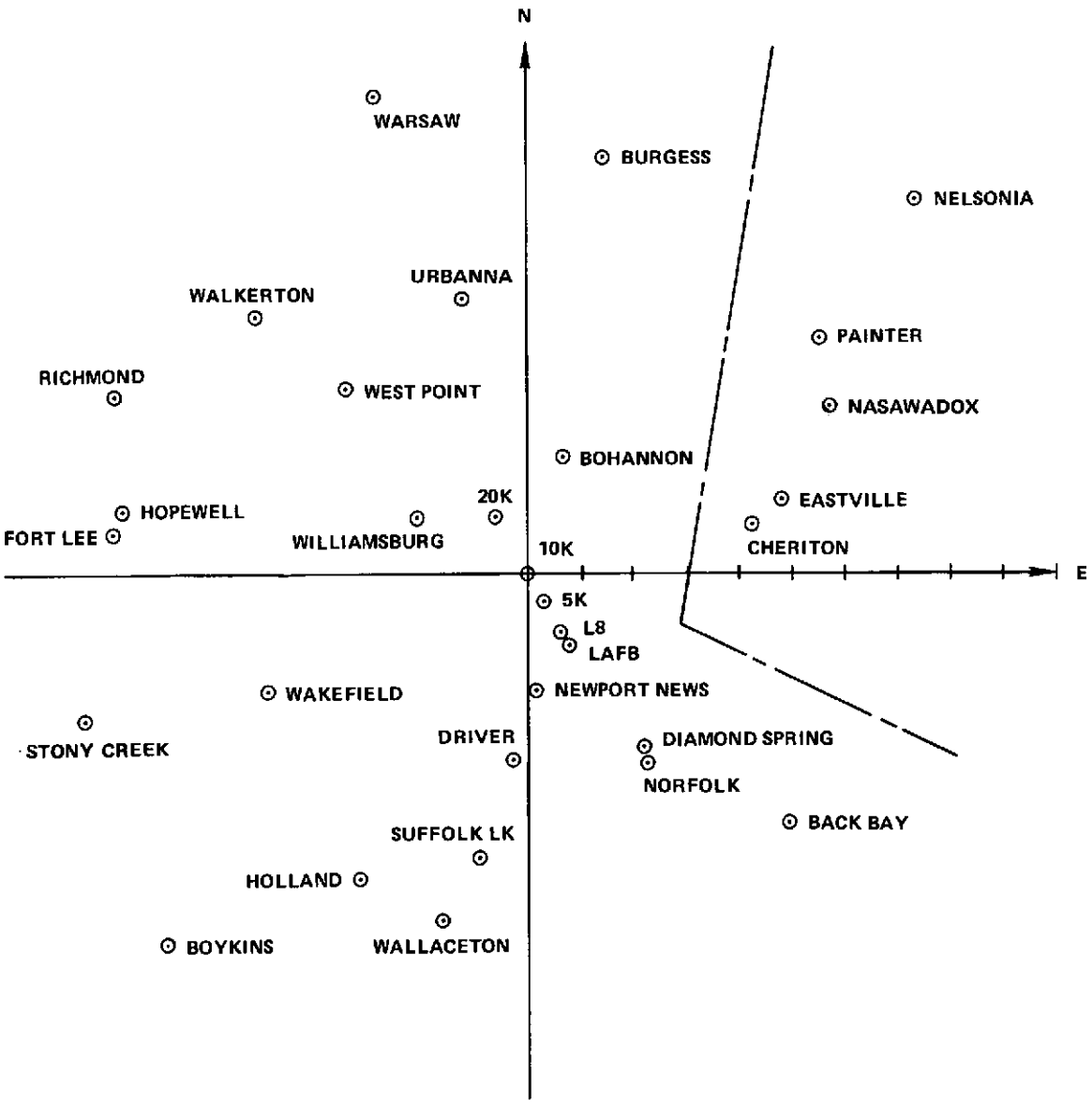

Figure B-1. Map of NWS Gauges and Type I and Type II Gauges, Tidewater District, Virginia

APPENDIX C
DISTRIBUTION FUNCTIONS FOR BISTATIC RADAR DATA AND NUMBER-DENSITY COMPARISONS

APPENDIX C
DISTRIBUTION FUNCTIONS FOR BISTATIC RADAR DATA AND NUMBER-DENSITY COMPARISONS

Table C-1
Distribution and Density Function for 1-minute Averages- 10K Eastville Summary

Z_e (dBz)	Distribution * by Phase					Density ** by Phase				
	Ia	Ib	I	II	Year	Ia	Ib	I	II	Year
30										
31										
32	760	902	1662	1005	2667	148	180	328	136	464
33	612	722	1334	869	2203	116	105	221	150	371
34	496	617	1113	719	1832	132	138	270	130	400
35	364	479	843	589	1432	84	125	209	168	377
36	280	354	634	421	1055	60	90	150	100	250
37	220	264	484	321	809	68	49	117	68	185
38	152	215	367	253	620	40	36	76	47	123
39	112	179	291	206	497	16	49	65	33	98
40	96	130	226	173	399	36	13	49	37	86
41	64	117	181	136	317	8	46	54	15	69
42	56	71	127	121	248	12	27	39	23	62
43	44	44	88	98	186	8	18	26	18	44
44	36	26	62	80	142	12	7	19	20	39
45	24	19	43	60	103	8	3	11	17	28
46	16	16	32	43	75	8	10	18	10	28
47	8	6	14	33	47	0	5	5	15	20
48	8	1	9	18	27	4	1	5	11	16
49	4		4	7	11	4		4	6	10
50				1	1				1	1

* Number of minutes Z_e value is exceeded.

** Number of minutes Z_e value is observed.

Table C-2
Distribution and Density Function for 1-minute Averages-
10K Fort Lee Summary

Z_e (dBz)	Distribution * by Phase					Density ** by Phase				
	Ia	Ib	I	II	Year	Ia	Ib	I	II	Year
30										
31										
32	548	1207	1755	1230	2985	92	249	341	206	590
33	456	958	1414	1024	2438	96	220	314	187	501
34	360	738	1098	837	1935	43	116	164	241	405
35	312	622	934	596	1530	60	162	222	159	381
36	252	460	712	437	1149	40	135	175	94	269
37	212	325	537	343	880	56	63	119	86	205
38	156	262	418	257	675	28	72	100	37	137
39	128	190	318	220	538	40	65	105	41	146
40	88	125	213	179	392	20	36	56	29	85
41	68	89	157	150	307	28	19	47	32	79
42	40	70	110	118	228	12	22	34	18	52
43	28	48	76	100	176	4	29	33	21	54
44	24	19	43	79	122	8	6	14	25	39
45	16	13	29	54	83	8	2	10	11	21
46	8	11	19	43	62	8	5	13	16	29
47		6	6	27	33		3	3	11	14
48		3	3	16	19		2	2	11	13
49		1	1	5	6		1	1	4	5
50				1	1				1	1

* Number of minutes Z_e value is exceeded.

** Number of minutes Z_e value is observed.

Table C-3
Distribution and Density Functions for 1-minute Averages—
20K Eastville

Z_e (dBz)	Measured Distribution*			2X Measured Distribution*			2X Measured Density**		
	I	II	Year	I	II	Year	I	II	Year
30									
31									
32									
33									
34	10	41	51	20	82	102	8	10	18
35	6	36	42	12	72	84	4	12	16
36	4	30	34	8	60	68	4	4	8
37	2	28	30	4	56	60		8	8
38	2	24	26	4	48	52		8	8
39	2	20	22	4	40	44		8	8
40	2	16	18	4	32	36		8	8
41	2	12	14	4	24	28	2	4	6
42	1	10	11	2	20	22		2	2
43	1	9	10	2	18	20			
44	1	9	10	2	18	20		4	4
45	1	7	8	2	14	16		4	4
46	1	5	6	2	10	12		2	2
47	1	4	5	2	8	10			
48	1	4	5	2	8	10	2	4	6
49		2	2		4	4		4	4
50									

* Number of minutes Z_e value is exceeded.

** Number of minutes Z_e value is observed.

Table C-4
Distribution and Density Functions for 1-minute Averages—
20K Fort Lee

Z_e (kHz)	Measured Distribution*			2X Measured Distribution*			2X Measured Density**		
	I	II	Year	I	II	Year	I	II	Year
30									
31									
32									
33									
34									
35									
36									
37									
38	8	18	26	16	36	52	6	2	8
39	5	17	22	10	34	44	6	6	12
40	2	14	16	4	28	32	2	4	6
41	1	12	13	2	24	26		4	4
42	1	10	11	2	20	22		2	2
43	1	9	10	2	18	20		2	2
44	1	8	9	2	16	18			
45	1	8	9	2	16	18	2	4	6
46		6	6		12	12		4	4
47		4	4		8	8		2	2
48		3	3		6	6		2	2
49		2	2		4	4			
50		2	2		4	4		2	2
51		1	1		2	2			
52		1	1		2	2			
53		1	1		2	2		2	2

* Number of minutes Z_e value is exceeded.

** Number of minutes Z_e value is observed.

Table C-5
Phase II Number-Density Comparison For All Data

CAT.	L8 Gauge	L19 Gauge	10K Gauge	20K Gauge	E8 Gauge	F8 Gauge	Norfolk NWS Gauge	10KE Bistatic	10KF Bistatic	20K Bistatic
					Category Average (1/4 Pooled Number Density)					
7	121.0	109.5	64.3	70.3	78.3	89.5	155.3	116.5	145.0	9.5
8	48.3	48.3	29.8	24.5	34.0	45.3	87.8	33.0	34.8	5.5
9	29.3	31.0	19.5	20.3	29.8	30.5	50.5	19.5	18.8	2.5
10	17.3	16.3	8.0	6.0	14.8	17.3	14.3	10.5	10.5	2.5
11	3.8	2.5	1.8	0.5	4.5	9.3	2.3	0.3	0.3	0.5
12	0.3	0.0	0.0	0.0	0.3	0.0	0.0	0.0	0.0	0.0
Σ	220.0	206.6	123.7	121.6	161.7	191.9	310.2	179.8	209.4	20.5
					F^2 TEST ($\Sigma \leq \chi^2_{6,.05} = 12.6$)					
7	-	4.37	107.4	85.0	60.3	32.8	38.9	0.7	19.0	411.0
8	-	0.08	28.3	46.9	16.9	0.7	129.2	19.4	15.1	15.7
9	-	0.39	12.3	11.1	0.0	0.2	61.0	13.1	15.1	98.0
10	-	0.23	20.0	29.5	1.4	0.0	2.1	10.7	10.7	50.6
11	-	1.78	4.2	11.5	0.5	31.8	2.4	12.9	12.9	11.5
12	-	1.20	1.2	1.2	0.0	1.2	1.2	1.2	1.2	1.2
Σ	-	8.05	173.4	185.2	79.1	66.7	234.8	58.0	74.0	724
Test		Yes	No	No	No	No	No	No	No	No
					Best Fit Shifted Category Average					
Shift	-	-	+3dB	+3dB	-	-	-	+1	+1	
7	-	-	110.8	124.3	-	-	-	137.0	170.3	
8	-	-	52.0	51.8	-	-	-	46.3	48.3	
9	-	-	29.0	26.5	-	-	-	19.0	24.0	
10	-	-	13.0	10.3	-	-	-	13.3	12.3	
11	-	-	2.8	1.5	-	-	-	1.8	1.3	
12	-	-	0.5	0.0	-	-	-	0.0	0.0	
Σ	-	-	208.1	214.4	-	-	-	217.4	256.2	
					F^2 Test On Shifted Data ($\Sigma \leq \chi^2_{5,.05} = 11.1$)					
7	-	-	3.4	0.4	-	-	-	8.5	80.4	
8	-	-	1.1	1.0	-	-	-	0.3	0.0	
9	-	-	0.0	1.1	-	-	-	14.5	3.8	
10	-	-	4.3	11.3	-	-	-	3.7	5.8	
11	-	-	1.1	5.6	-	-	-	4.2	6.6	
12	-	-	0.5	1.2	-	-	-	1.2	1.2	
Σ	-	-	10.4	20.6	-	-	-	32.4	97.8	
Test	-	-	Yes	No	-	-	-	No	No	

Table C-6
Phase II Number-Density Comparison For Data Not Including Tropical Storm Doria and Hurricane Ginger

CAT.	L8 Gauge	L19 Gauge	10K Gauge	20K Gauge	E8 Gauge	F8 Gauge	Norfolk NWS Gauge	10KE Bistatic	10FE Bistatic	20K Bistatic
					Category Average (1/4 Pooled Number Density)					
7	46.0	41.0	41.5	48.5	61.3	59.2	116.3	57.5	66.2	9.5
8	25.4	28.8	19.0	17.5	31.3	36.6	66.0	25.5	24.3	5.5
9	14.3	16.7	17.3	18.8	28.8	27.3	24.0	17.8	17.3	2.5
10	13.3	13.0	6.8	5.8	14.8	17.3	10.3	10.5	10.5	2.5
11	3.5	2.5	1.8	0.5	4.5	9.3	2.3	0.3	0.3	0.5
12	0.3	0.0	0.0	0.0	0.0	0.0	0.0	0.0	0.0	0.0
Σ	102.8	102.0	86.4	91.1	141.0	149.7	218.9	111.6	118.6	20.5
					F^2 TEST ($\Sigma \leq \chi^2_{6,.05} = 12.6$ for identical distributions)					
7	-	2.2	1.8	0.5	9.1	15.2	429.7	11.5	35.5	115.8
8	-	1.8	6.5	9.8	5.5	19.8	259.6	0.0	0.2	62.4
9	-	1.6	2.5	5.7	58.8	47.3	26.3	3.4	2.5	38.9
10	-	0.0	12.7	16.9	0.7	4.8	2.7	2.4	2.4	35.0
11	-	1.1	3.3	10.3	1.1	38.0	1.6	11.7	11.7	10.3
12	-	1.2	1.2	1.2	0.0	1.2	1.2	1.2	1.2	1.2
Σ	-	7.9	28.0	44.4	75.2	126.3	721.1	30.2	53.5	263.6
Test		Yes	No	No	No	No	No	No	No	No
					Best Fit Shifted Category Average					
Shift			+3dB	+3dB				+1dB	+1dB	
7	-	-	67.5*	77.8*	-	-	-	59.8	75.8	
8	-	-	30.3	36.3	-	-	-	35.3	32.5	
9	-	-	16.0	20.0	-	-	-	16.3	20.8	
10	-	-	10.0	8.8	-	-	-	13.3	12.3	
11	-	-	2.3	1.5	-	-	-	1.8	1.8	
12	-	-	0.5	0.0	-	-	-	0.0	0.0	
Σ	-	-	126.6	144.4	-	-	-	126.5	142.7	
					F^2 TEST ($\Sigma \leq \chi^2_{5,.05} = 11.1$)					
7			40.2	87.9	-	-	-	16.6	77.2	
8			3.8	18.7	-	-	-	15.4	7.9	
9			0.8	9.1	-	-	-	1.1	11.8	
10			3.3	6.1	-	-	-	0.0	0.3	
11			1.6	4.6	-	-	-	3.3	5.5	
12			0.5	1.2	-	-	-	1.2	1.2	
Σ			50.2	127.6	-	-	-	37.6	103.9	
Test			No	No	-	-	-	No	No	

Shifted 10K Gauge Reference (10K Not Including Event 80, $\Sigma \leq \chi^2_{5,.05} = 11.1$)

	10KE	10KF	20K	L8
7	3.5	4.1	6.3	27.4
8	3.3	0.6	4.8	3.2
9	0.0	5.8	4.0	0.7
10	4.4	2.1	0.6	4.4
11	0.4	1.7	1.1	2.5
12	2.0	2.0	2.0	0.3
	13.6	16.3	18.8	51.6
Test	No	No	No	No

*NOT INCLUDING EVENT 80

30 Oct. 1973

APPENDIX D
DISTRIBUTION FUNCTIONS FOR RAIN GAUGES AND NUMBER-DENSITY COMPARISON TESTS FOR DIFFERENT INTEGRATION TIMES

APPENDIX D
DISTRIBUTION FUNCTIONS FOR RAIN GAUGES AND NUMBER-DENSITY COMPARISON TESTS FOR DIFFERENT INTEGRATION TIMES

Table D-1
10K Gauge Summary—1-minute Average

Z†	Distribution * by Phase					Density ** by Phase				
	Ia	Ib	I	II	Year	Ia	Ib	I	II	Year
30	1158	1924	3082	976	4058	203	426	629	144	773
31	955	1498	2453	832	3285	125	307	432	70	493
32	830	1191	2021	762	2783	131	321	452	172	624
33	699	870	1569	590	2159	153	252	405	96	501
34	546	618	1164	494	1658	137	224	361	105	466
35	409	394	803	389	1192	26	42	68	55	123
36	383	352	735	334	1069	105	122	277	45	272
37	278	230	508	289	797	68	35	103	52	155
38	210	195	405	237	642	66	96	162	56	218
39	144	99	240	181	421	25	19	44	9	53
40	119	80	199	172	371	8	21	29	36	65
41	111	59	170	136	306	33	17	50	18	68
42	78	42	120	118	238	44	24	68	53	121
43	34	18	52	65	117	4	2	6	7	13
44	30	16	46	58	104	4	5	9	13	22
45	26	11	37	45	82	4	4	8	6	14
46	22	7	29	39	68	4	7	11	26	37
47	18		18	13	31	4		4	3	7
48	14		14	10	24	2		2	1	3
49	12		12	9	21	12		12	2	14
50				7	7				5	5
51				2	2				1	1
52				1	1				1	1

* Number of minutes Z value is exceeded.

** Number of minutes Z value is observed.

† $Z = 270\ R^{1.3}$, expressed in dB relative to $Z = 1\ mm^6/m^3$.

Table D-2
5K Gauge Summary—1-minute Average (Phase Ia)

Z†	Distribution *	Density ** by Phase
30	1215	394
31	821	163
32	658	149
33	509	145
34	364	144
35	220	25
36	195	92
37	103	23
38	80	32
39	48	9
40	39	6
41	33	3
42	30	7
43	23	3
44	20	2
45	18	6
46	12	8
47	4	4

* See D-1
** See D-1
† See D-1

Table D-3
20K Gauge Summary—1-minute Average (Phase II)

Z†	Distribution *	Density **
30	1069	212
31	857	160
32	697	155
33	542	56
34	486	126
35	360	70
36	290	28
37	262	57
38	205	52
39	153	11
40	142	23
41	119	12
42	107	60
43	47	6
44	41	4
45	37	11
46	26	20
47	6	3
48	3	1
49	2	0
50	2	2

* See D-1
** See D-1
† See D-1

Table D-4
L8 Gauge Summary—1-minute Average (Phase II)

Z†	Distribution *	Density **
30	1728	193
31	1535	211
32	1324	238
33	1086	207
34	879	181
35	698	144
36	554	85
37	469	74
38	395	45
39	350	47
40	303	47
41	256	54
42	202	29
43	173	29
44	144	39
45	105	20
46	85	24
47	61	20
48	41	8
49	33	17
50	16	8
51	8	5
52	3	0
53	3	2
54	1	1

* See D-1
** See D-1
† See D-1

Table D-5
L19 Gauge Summary—1-minute Average (Phase II)

Z†	Distribution *	Density **
30	1760	259
31	1501	223
32	1278	264
33	1014	188
34	826	158
35	668	119
36	549	80
37	469	81
38	388	45
39	343	58
40	285	39
41	246	47
42	199	33
43	166	35
44	131	29
45	102	27
46	75	26
47	49	15
48	34	8
49	26	16
50	10	4
51	6	3
52	3	3

* See D-1
** See D-1
† See D-1

Table D-6
F8 Gauge Summary—1-minute Average (Phase II)

Z†	Distribution *	Density **
30	1397	219
31	1178	166
32	1012	132
33	880	132
34	767	113
35	664	104
36	560	81
37	479	70
38	409	52
39	357	48
40	309	47
41	262	34
42	228	29
43	199	30
44	169	39
45	130	24
46	106	27
47	79	13
48	66	6
49	60	23
50	37	10
51	27	17
52	10	6
53	4	4

* See D-1
** See D-1
† See D-1

Table D-7
E8 Gauge Summary—1-minute Average

Z†	Distribution *, Phase I	Density **, Phase II
30	1100	106
31	994	122
32	872	109
33	763	117
34	646	129
35	517	95
36	422	52
37	370	37
38	333	36
39	297	29
40	268	35
41	233	36
42	197	29
43	168	37
44	131	31
45	100	22
46	78	17
47	61	14
48	47	7
49	40	21
50	19	4
51	15	12
52	3	2
53	1	0
54	1	1

* See D-1
** See D-1
† See D-1

Table D-8
Phase II Summary for Clock 5-minute and Clock 60-minute Averages

	Distribution *				Density **			
Z†	5-min 10K	60-min 10K	5-min L8	60-min L8	5-min 10K	60-min 10K	5-min L8	60-min L8
30	1045	1560	1850	2580	160	240	205	540
31	885	1320	1645	2040	90	240	270	240
32	795	1080	1375	1800	125	120	155	120
33	670	960	1220	1680	155	240	245	540
34	515	720	975	1140	85	120	190	120
35	430	600	785	1020	60	240	140	180
36	370	360	645	840	85	60	125	120
37	285	300	520	720	50	120	75	120
38	235	180	445	600	35	120	80	180
39	200	60	365	420	30	60	70	0
40	170		295	420	30		45	240
41	140		250	180	35		35	180
42	105		215		40		40	
43	65		175		10		45	
44	55		130		20		40	
45	35		90		10		20	
46	25		70		10		15	
47	15		55		5		25	
48	10		30		0		10	
49	10		20		10		10	
50			10					
51			10				5	
52			5					
53			5				5	

* Number of observations Z value is exceeded.
** Number of observations Z value is observed.
† —See D-1

Table D-9
Phase II Number-Density Comparisons
for Various Integration Times

Category Average							
Category	10K	20K	L19	L8	E8	F8	Norfolk
6	120.5	145.8	233.5	212.3	113.5	157.5	245.3
7	64.3	70.3	109.5	121.0	78.3	89.5	155.3
8	29.8	24.5	47.3	48.3	34.0	45.3	87.8
9	19.8	20.3	31.0	29.3	29.8	30.5	50.5
10	8.0	6.0	16.3	17.3	14.8	17.3	14.3
11	1.75	0.5	2.5	3.75	4.5	9.3	2.25
12				0.25	0.25		
Clock 5-minute Average							
6	132.5	156.3	241.3	232.5	202.5	172.5	266.3
7	70.0	72.5	117.5	122.5	81.3	95.0	192.5
8	32.5	33.8	58.8	56.3	37.5	47.5	117.5
9	20.0	16.3	33.8	33.8	32.5	33.8	45.0
10	6.25	3.75	12.5	15.0	15.0	16.3	1.25
11			2.5	2.5	3.75	8.75	1.25
*F^2	3.3	5.2	3.8	3.9	56.7	1.8	21.0
Test	yes	yes	yes	yes	no	yes	no
Clock 60-minute Average							
6	210.0	210.0	315.0	315.0	255.0	300.0	450.
7	168.8	135.0	180.0	135.0	90.0	120.0	315.
8	45.0	30.0	105.0	135.0	75.0	60.0	60.
9				15.0	30.0	45.0	30.
10						15.0	

* F^2 Test Sum ($F^2 < \chi^2_{6, 0.05} = 12.6$)

APPENDIX E
SYMBOLS

SYMBOLS

Symbol	Definition
A	specific attenuation
a	hydrometeor size parameter
$\mathcal{A}$	amplitude of V
C	constant defined in Equation (5)
C_d	scattering volume size and location correction factor
C_p	data processing correction factor
C_R	equipment constant
C_s	scattering process correction factor
C_θ	antenna-pattern-related constant
D	effective length of scattering volume along receiver beam when volume is filled
d	rain cell width between half scattering intensity points
D	diameter of circular aperture of antenna
E_1	exponential integral
$\underset{\sim}{E}^i$	incident electric field vector
$\underset{\sim}{E}^s$	scattered electric field vector
$\hat{e}_1, \hat{e}_2, \hat{e}_3$	unit vectors along the principal axes of a spheriod
f	intermediate parameter in the calculation of α_i

SYMBOLS (continued)

Symbol	Definition
f_c	carrier frequency
f_d	Doppler frequency
f_ℓ	local oscillator frequency
f_1	normalized complex pattern function, receive antenna
f_2	normalized complex pattern function, transmit antenna
G_1	receive antenna gain (peak)
G_2	transmit antenna gain (peak)
g_1	normalized gain function (directivity) of receive antenna
g_2	normalized gain function (directivity) of transmit antenna
H	receiver bandpass response function
i	$\sqrt{-1}$
K	phase shift and path loss
k	wave number
$\underset{\sim}{L}$	position vector of receiver relative to transmitter
L_i	intermediate parameter in the calculation of α_i
ℓ_1	receiver line loss factor
ℓ_2	transmitter line loss factor
m	polarization mismatch factor

SYMBOLS (continued)

Symbol	Definition
n	index of refraction of medium
P_m	median value of P_r for a measurement interval
P_r	instantaneous received power
P_t	transmitter power
P_2'	transmitter power delivered to antenna 2 (transmit)
$\langle P_1 \rangle$	lowest value of $\langle P_r \rangle$ in a measurement interval
$\langle P_2 \rangle$	highest value of $\langle P_r \rangle$ in a measurement interval
P_m	$10 \log_{10} P_m$
P_r	$10 \log_{10} P_r$
p	percent of time
R	rain rate
$\underset{\sim}{r}$	position vector of scatterer relative to transmitter
$\underset{\sim}{r}_1$	position vector of center of scattering volume relative to receiver
$\underset{\sim}{r}_2$	position vector of center of scattering volume relative to transmitter
$\underset{\sim}{r}_0$	position vector of scatterer relative to transmitter at reference or start time
R	ratio of major to minor axis of the spheroid
s	position variable for line integral
$\underset{\approx}{S}$	scattering amplitude tensor

SYMBOLS (continued)

Symbol	Definition
S_1, S_2, S_3, S_4	scattering amplitudes
t	time
t_0	reference or start time
U	scattering volume
U'	scattering volume for filled beams
u	imaginary part of V
$\hat{u}_1$	polarization vector of receive antenna (unit vector in direction of electric field vector)
$\hat{u}_2$	polarization vector of transmit antenna
V	voltage into logarithmic amplifier
$\underset{\sim}{v}$	hydrometeor velocity
v_v	hydrometeor velocity of fall
W	instantaneous intermediate frequency (IF)
w	real part of V
$\underset{\approx}{x}$	$\underset{\approx}{x} = \underset{\sim}{r}$, positive vector of scatterer relative to transmitter
y	range from receiver, or dummy variable
y'	position of scatterer along receiver beam relative to center of scattering volume
Z	reflectivity

SYMBOLS (continued)

Symbol	Definition
Z_e	equivalent reflectivity
Z_v	an effective Z value for use with spheroidal scatterers
z	10 log Z
Z_0	characteristic impedance of free space
α	antenna efficiency
$\alpha_1, \alpha_2, \alpha_3$	elements of polarizability tensor for polarization along the principal axis
β	scattering cross section per unit volume
β'	scattering cross section per unit volume averaged over the scattering volume
$\beta_{\|}$	scattering cross section per unit volume for polarization parallel to the plane of scattering
$\beta_{\perp}$	scattering cross section per unit volume for polarizations perpendicular to the plane of scattering
δ	position of cell center along receiver beam relative to center of scattering volume
ϵ	dielectric constant
$\hat{\xi}_1, \hat{\xi}_2$	unit vectors in plane of scattering and perpendicular to $\hat{r}_1$, $\hat{r}_2$, respectively
η	scatterer number density
θ_1	half-power beamwidth of receive antenna
θ_2	half-power beamwidth of transmit antenna

SYMBOLS (continued)

Symbol	Definition
κ	$(\epsilon - 1)/(\epsilon + 2)$, where ϵ is dielectric constant for water
λ	wavelength (cm)
$\underset{\sim}{\nu}$	Doppler response vector
Ξ	ratio of highest to lowest $\langle P_r \rangle$ for a measurement interval
$\hat{\xi}_1, \hat{\xi}_2$	unit vectors perpendicular to plane of scattering and perpendicular to $\hat{r}_1$, $\hat{r}_2$, respectively
$\underset{\sim}{\rho}$	position vector of receiver relative to scatterer
σ_η^2	variance of η
Ψ	phase of V
ψ	azimuthal angle about the direction of the receive antenna main lobe; scattering angle
Ω	solid angle over θ and ψ
Ω_m	solid angle subtended by scattering value
ω	radian frequency (instantaneous) of received signal
ω_c	radian carrier frequency
ω_d	radian Doppler frequency
ω_ℓ	radian local oscillator frequency